Novel Diagnostic Approaches to Characterizing the Performance of the Wisconsin Inertial Electrostatic Confinement Plasma

David R. Boris

July 2009

UWFDM-1366

Ph.D. thesis.

FUSION TECHNOLOGY INSTITUTE

UNIVERSITY OF WISCONSIN

MADISON WISCONSIN

Novel Diagnostic Approaches to Characterizing the Performance of the Wisconsin Inertial Electrostatic Confinement Plasma

David R. Boris

Fusion Technology Institute
University of Wisconsin
1500 Engineering Drive
Madison, WI 53706

http://fti.neep.wisc.edu

July 2009

UWFDM-1366

Ph.D. thesis.

Novel Diagnostic Approaches to Characterizing the Performance of the Wisconsin Inertial Electrostatic Confinement Plasma

by

David R. Boris

A dissertation submitted in partial fulfillment of

the requirements for the degree of

Doctor of Philosophy

(Nuclear Engineering and Engineering Physics)

at the

UNIVERSITY OF WISCONSIN – MADISON

2009

Abstract

The following research has been conducted in pursuit of a doctoral degree from the Engineering Physics Department at the University of Wisconsin – Madison. The work detailed below relates to the University of Wisconsin inertial electrostatic confinement (IEC) fusion project. The primary focus of this research regards plasma diagnostic development and implementation plus their use in understanding plasma conditions in IEC devices. This work has lead to significant advancements in the understanding of IEC operation. The research contributions of this thesis are detailed below.

A method for converting the kinetic energy of high energy protons to electricity using a silicon based PIN diode direct conversion device was developed and tested. The operation of such a device is similar to that a photovoltaic cell with the photons replaced by high energy protons from fusion. This work ultimately showed that silicon based devices cannot withstand the materials damage caused by high energy protons long enough to have viable lifetimes. A 3 MeV Tandem linear accelerator was used to simulate a reactor relevant flux of fusion protons on the silicon PIN diode.

A plasma diagnostic to measure concentrations of molecular deuterium ions in the edge plasma region of the UW-Inertial Electrostatic Confinement (IEC) Fusion Device was developed and implemented. This diagnostic relied on measuring the phase velocity of multi-species ion acoustic waves in the source plasma of the UW-IEC device. It was concluded that the source plasma, when run with a deuterium fill gas, is dominated (>50% by ion density) by D_3^+ ions.

A diagnostic for the measurement of energetic deuterium velocity spectra within the intergrid region of an inertial electrostatic confinement fusion device was developed and

implemented. The diagnostic functioned by measuring the Doppler shift imparted to high energy fusion protons from the deuterium reactants within the device. This work resulted in the ability to measure, for the first time, the high energy deuterium spectra within an IEC device. This diagnostic was used to document how the deuterium spectra within the UW-IEC device change over a wide range of device parameters. In all cases the deuterium energy spectra indicated that a dominant fraction of the energetic deuterons had energies between 10-20 keV for cathode potentials between 50 kV – 100 kV.

A technique to resolve the location of the fusion reactions along a chord through the center of an inertial electrostatic confinement fusion device has been developed and implemented. The location of the fusion reaction is determined by using two opposed silicon charged particle detectors and recording the difference in arrival time between the high energy proton and triton resulting from a D-D fusion reaction. Due to conservation of momentum these fusion products will travel in opposite directions. Thus detectors placed on opposite sides of the IEC reaction chamber will be able to discern the position, within their line of sight, of the fusion reaction that birthed the detected fusion products. Preliminary results from this diagnostic indicate that 50% of the fusion reactions occur within the 10 cm radius cathode of the UW-IEC device.

A magnetic deflection energy analyzer and Faraday trap diagnostic have been used to make measurements of divergent D^- flow in the inertial electrostatic confinement experiment at the University of Wisconsin – Madison. Deuterium anion current densities as high as 8.5 $\mu A/cm^2$ have been measured at the wall of the UW-IEC device, 40 cm from the surface of the device cathode with a detector assembly of admittance area $0.7cm^2$. Energy spectra obtained using a magnetic deflection energy analyzer diagnostic

indicate the presence of D_2^-, and D^- ions produced through thermal electron attachment near the device cathode, as well as D^- ions produced via charge transfer processes between the anode and cathode of the device.

Acknowledgments

Perhaps the most important thing one learns on the path to completion of a doctoral thesis is that research is not done in a vacuum and no investigator labors alone. I am privileged to have earned my degree in the company of great minds and great friends. I would first like to thank my formal advisor Professor Gerald Kulcinski whose guidance and encouragement, throughout my time here at the University of Wisconsin, has been essential.

I think that all doctoral students would agree that PhD's are attained through the assistance of many advisors, some of them fellow graduate students and some of them professors. In that spirit I would like to thank my colleagues at the University of Wisconsin Fusion Technology Institute, whom I also consider my advisors. First, Professors John Santarius and Gil Emmert who have been instrumental to the completion of this work, also my fellow IEC experimental researchers past and present, Bob Ashley, Richard Bonomo, Brian Egle, Eric Alderson, David Donovan, Sam Zenobia, Gabriel Becerra, Craig Schuff, Lauren Garrison, Carlos Paz-Soldan, John Sorebo, Dr. Ross Radel, Dr. Greg Piefer, Dr. Ben Cipiti, and Kunihiko Tomiyasu. You all have contributed to an environment that, in my mind, exemplifies the proper mixture of collegial support and scientific skepticism necessary for excellent research to flourish. Also I would like to recognize all those who worked on the IEC before my time here at UW, since their research paved the way for our current work.

I would also like to acknowledge the world-wide community of IEC researchers. Through the US-Japan IEC exchange I have had exposure to many exciting new ideas and also exposure to rich cultures that otherwise I may never have experienced. The

many contacts I have made, both in the United States and abroad, through this annual meeting, will be invaluable for the rest of my career.

Lastly, I would like to thank my loved ones. Without their continuous love and support I could never have reached this goal. My mother Elizabeth, my father Dave, my sister Megan and my girlfriend Bethany, have been a source of strength throughout this process. Thank you for standing by me and encouraging me through those times when I doubted that I would ever end up writing the Acknowledgements section of my thesis. I dedicate this thesis to you all.

Table of Contents

Table of Figures

Chapter 1

Chapter 2

Chapter 3

Chapter 4

Chapter 5

Chapter 6

Chapter 7

Table of Tables

Chapter 4

Chapter 5

Chapter 6

Chapter 7

Chapter 1: Introduction

1.1 Inertial Electrostatic Confinement Fusion

The inertial electrostatic confinement (IEC) fusion concept was first patented by Farnsworth[1] in the 1960's and was advanced by Hirsch[2] shortly after Farnsworth's initial patent. The concept focuses on confining light ions using large negative electrostatic potentials in a spherically symmetric geometry, and was inspired by theoretical work done by Elmore, Tuck and Watson[3] in the late 1950s. By placing a smaller, negatively biased, spherical cathode grid inside a grounded anode grid, ions produced outside the anode can be accelerated to fusion relevant energies. This confinement approach produces a non-Maxwellian plasma with increased ion density toward the center of the spherical geometry (See Figure 1.1-1).

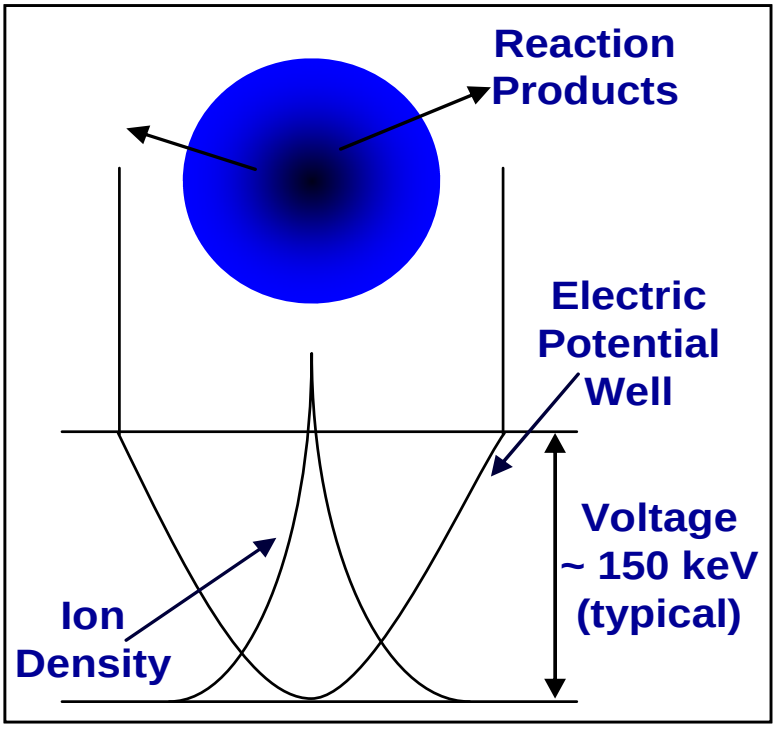

Figure 1.1-1: A depiction of an electrostatic potential well with a radially focused ion population

The IEC concept is of particular interest in the arena of non-electric applications of fusion, such as neutron sources for clandestine materials detection (explosives, chemical agents, fissile materials, etc.), and high energy proton sources for medical isotope production. The gridded IEC concept has been extensively investigated by research groups around the world. The University of Wisconsin[4], the University of Illinois Urbana-Champagne[5], and Los Alamos National Lab all have current research endeavors underway in the United States. This work has led to the first use of an IEC device to detect fissile material[6], high current pulsed operation[7], produce thrust for possible satellite station keeping[8], and experimental verification of the periodically oscillating plasma sphere concept[9]. In addition, Kyoto University[10], Kansai University[11], and Tokyo Institute of Technology[12] in Japan have research initiatives investigating the performance and applications of gridded IEC devices, including the first active testing of an IEC device as a means to detect anti-personnel land-mines. The University of Sydney[13] in Australia has also made important diagnostic contributions to IEC research with a focus on using IEC like devices as an alternative to conventional ion thrusters[14].

Gridded IEC devices have historically produced neutrons at rates on the order of 10^7 to 10^8 neutrons/s with deuterium fuel. Two different regimes of operation seem to be responsible for these fusion rates, the low pressure regime pioneered by Hirsch, and the high pressure regime which has been dominant in essentially all other IEC experiments. Hirsch operated in neutral gas pressure regimes of 0.1 mTorr to 8 mTorr and reported observations of virtual anode and cathode formation within the highly focused core of his device. He also noted increasing neutron production at lower background gas pressures. These characteristics are unique to Hirsch's experiments and indicate the possibility of a

beam-beam mode of operation. All other IEC devices seem to be dominated by interactions between fast ions and neutrals with background gas, yielding fusion rates that increase sub-linearly with background gas pressure. Both experimental work and modeling efforts at the University of Wisconsin-Madison have confirmed this beam background mode of operation[15,16]. As a result, recent work at UW has focused on trying to reproduce the results of the Hirsch experiment[17] and seeking to better understand the fundamental differences inherent to his work. This work detailed in this thesis, in an effort to better characterize the operation of IEC devices, has led to the development of an array of new diagnostics in the UW-IEC lab which allow for the characterization of the plasma in both the source region and the intergrid region. This thesis will focus on the construction and implementation of diagnostic advancements made over the last few years, on the original IEC device, referred to as HOMER, at the University of Wisconsin – Madison.

1.2 Improvements to Diagnostic Capability on the HOMER IEC Device

1.2-a Diagnostics on the source of the HOMER IEC Device

Modeling the atomic and molecular physics interactions that occur in the beam – background dominated mode that most gridded IEC devices operate in requires detailed knowledge of the composition of the source plasma from which the streaming ions are extracted. In order to achieve this, a diagnostic to measure the mass of the ion species present in the source region of the HOMER IEC device was developed and implemented.

The diagnostic uses ion acoustic waves to measure the ion mass inherent to the source region plasma. Since the plasma contains three molecular species of deuterium,

only the concentration weighted reduced ion mass can be measured, but this is nonetheless very useful for determining the ion species present in HOMER's plasma source region. The diagnostic utilizes electron temperature measurements coupled with direct phase velocity measurements of ion acoustic waves propagating in the IEC source region to determine the concentration weighted reduced ion mass. A picture of an ion acoustic wave plotted in time and space is shown in Figure 1.2-1. (More explanation can be found in Chapter 4 sections 3-5.)

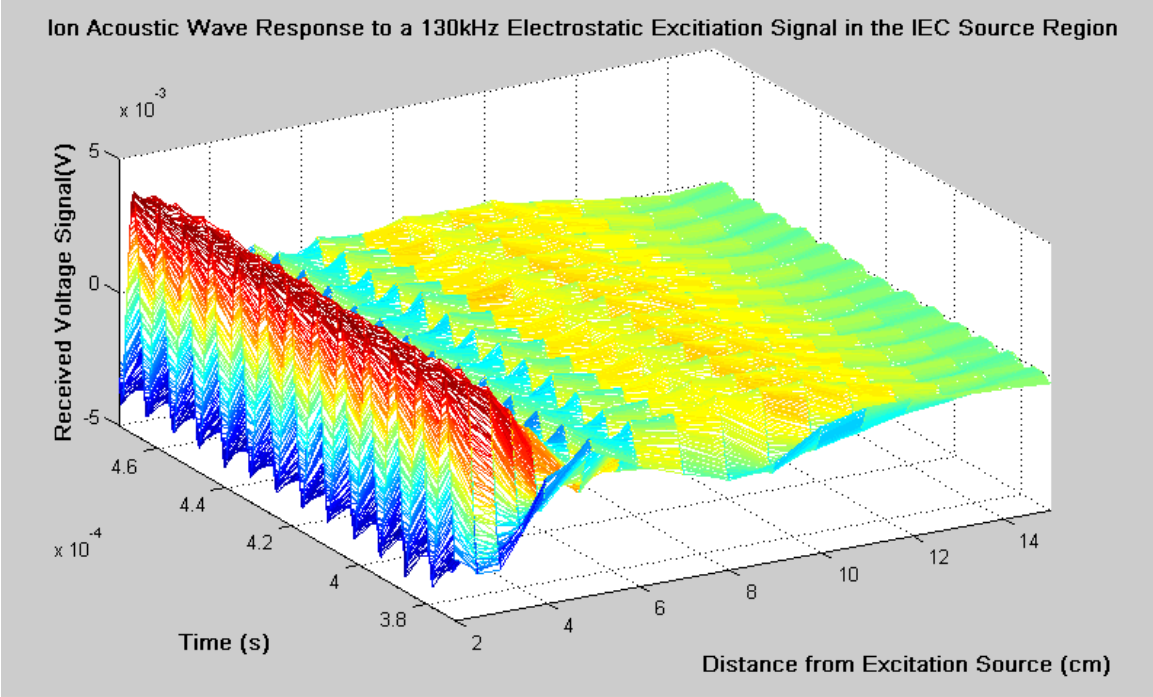

Figure 1.2-1: Amplitude of an ion acoustic wave varying in time and space. (T_e = 3.0 eV)

With this technique the concentrations of molecular deuterium ions were inferred for a variety of source region parameters with the results of the study indicating that the HOMER source region was dominated by D_3^+ ions.

1.2-b The Fusion Ion DOppler Diagnostic (FIDO)

The FIDO diagnostic plays an even more important role in understanding the HOMER IEC device, as it allows one to measure the line averaged energy distribution of the deuterium reactants within the intergrid region. The FIDO diagnostic uses the Doppler shifted fusion products from the D(d,p)T fusion reaction to measure the center of mass velocity of D-D nuclear collisions that result in fusion. It uses two narrow irises to constrict the view of a charged particle detector to a narrow conical view factor through the center of the device. The device's most important feature is its powerful, localized, variable magnetic field which serves to bend the fusion products leaving the IEC device to an angle where they can be detected free of X-ray noise by the silicon charged particle detector at the end of the FIDO bending arm. This provides the opportunity, for the first time, to do high resolution energy spectroscopy on both the proton and triton fusion products leaving an IEC device. An image of the FIDO diagnostic is shown below in Figure 1.2-2.

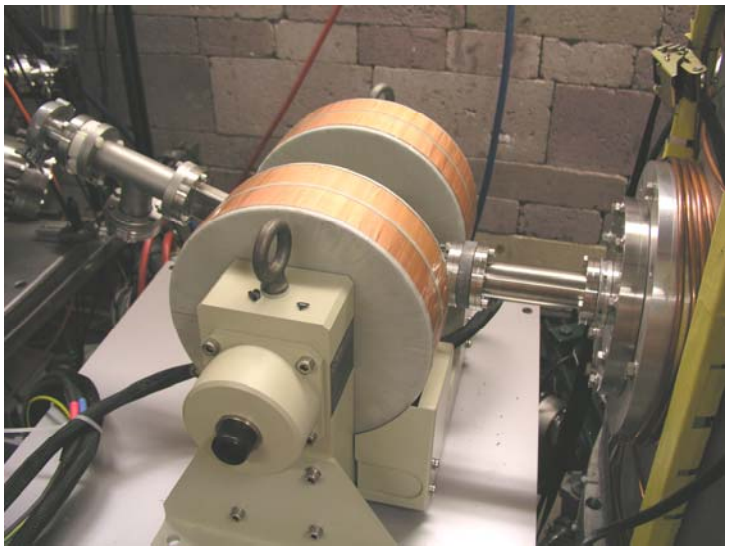

Figure 1.2-2: The FIDO diagnostic mounted to the side of the HOMER vacuum vessel.

With this diagnostic the UW-IEC group, for the first time, is able to determine how varying experimental parameters affect the energy distribution of the deuterium reactants. By enabling these measurements, FIDO provides a powerful tool for optimizing the performance of HOMER or any IEC device. Indeed FIDO was used for just that purpose and allowed the UW-IEC group to determine the optimal grid configuration within the system to maximize neutron rates. In addition to optimizing the grid geometry within the HOMER IEC device, FIDO has also been used to quantify the effect that varying cathode voltage, cathode current, and background gas pressure has on the energy spectra of fast deuterium reactants within the HOMER IEC.

1.2-c Diagnostics to measure deuterium anions within the HOMER IEC Device

The University of Sydney in Australia has also made substantial contributions to IEC research with optical spectroscopy diagnostics. One of their major findings is indications of divergent ion flow in their IEC experiment[18,19]. These findings led to speculation amongst the University of Wisconsin IEC group that a contribution from negative ions could explain this apparent divergent ion flow.

A magnetic deflection energy analyzer was constructed using an identical magnet to the one in operation on FIDO. By orienting the magnetic field such that deuterium anions would be bent 20º into a charged particle detector, while all positive particles would be bent away from the detector, detection and energy analysis of the negative ion flux leaving the HOMER IEC device could be performed. This approach yielded the detection of a substantial flux of deuterium anions with a broad and highly structured energy spectrum. Confirmation of the presence of deuterium anions was achieved using

a Faraday trap, a simple metallic charge collection plate with a secondary electron suppression mesh.

The discovery of the substantial fraction of deuterium anion current within the HOMER IEC device has major implications for future modeling efforts of IEC devices. In addition it may open up a new arena of applications for the IEC device as a possible alternative to conventional ion thrusters.

1.2-d Fusion Product Time of Flight Diagnostic

The last contribution to IEC diagnostics that will be discussed in this thesis is the fusion product time of flight (FPTOF) diagnostic. With this diagnostic it is possible to obtain data on both the energy distribution of fusing deuterium nuclei, and spatial distribution of the D(d,p)T fusion reactions occurring within the HOMER IEC device. Characterization of the spatial distribution of fusion reactions within IEC devices has been performed previously using collimated charged particle detectors by Nadler, Thorson, and Masuda[20,21,22] but never in conjunction with high resolution energy spectroscopy. In addition, all previous spatial profiling was done by taking line averaged readings with a collimated charged particle detector and then applying an Abel inversion or similar procedure to the signals. The FPTOF diagnostic utilizes the FIDO diagnostics capability to measure both protons and tritons from the same fusion reaction and couples this to the measured difference in arrival times of the two particles at opposite ends of the IEC chamber. This enables a determination of the spatial location where the fusion reaction that birthed the fusion products occurred. (Schematic shown below in Figure 1.2-3.)

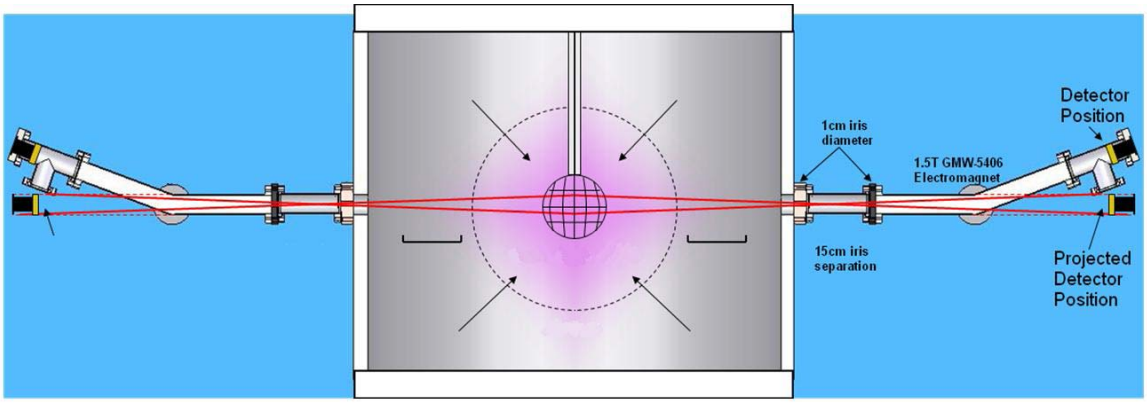

Figure 1.2-3: Schematic of TOF setup includes two identical FIDO diagnostic setups on opposite sides of the HOMER IEC device.

With the utilization of sub-nanosecond timing electronics, spatial resolution < 1 mm is achievable. Fine spatial resolution coupled with the high resolution energy spectroscopy this diagnostic provides will allow definitive measurements of any significant potential profiles present in the cathode region. The work detailed in this thesis proves the principle of the FPTOF diagnostic and demonstrates the capability of at least ~2 cm spatial resolution.

1.3 Direct Conversion of High Energy Protons with PIN Diodes

Additional research detailed in this thesis focuses on the use of silicon PIN (p-type, intrinsic, n-type) junction diodes as a means of converting high-energy protons to electricity. PIN diodes are the standard junction design for betavoltaic research, devices that convert beta particles to electricity, and for photovoltaic research. In this research the efficiency of the PIN diode as a conversion device will be investigated as well as how the PIN diode responds to damage from proton irradiation. This work will provide a better understanding of whether or not a solid-state device has any unique applications in the conversion of the kinetic energy of high-energy fusion protons to electricity.

In order to test the viability of this technology as a means of converting fusion protons to electricity a 3 MeV Pellatron linear accelerator was used to simulate a high fluence of D-D protons on a sample PIN diode. The response of the semiconductor to increasing fluence was measured.

Chapter 1 References

[1] P.T. Farnsworth, "Electric Discharge Device for Producing Interaction Between Nuclei" U.S. Patent #3,258,402, patented June 28, (1966).

[2] R.L. Hirsch, "Inertial Electrostatic Confinement of Ionized Fusion Gases," J. Appl. Phys. 38, 4522 (1967)

[3] W. C. Elmore, J. L. Tuck, and M. K. Watson, "On the inertial electrostatic confinement of a plasma," Physics of Fluids, 2, 239 (1959)

[4] J.F. Santarius, G.L. Kulcinski, et al, "An Overview of University of Wisconsin Inertial Electrostatic Confinement Fusion Research," Fusion Science Tech. 47, 1238 (2005).

[5] G. H. Miley, J. Sved, "The IEC-A plasma target based neutron source," Appl. Radiat. Isot. 48, 1557 (1997).

[6] R.F. Radel, G. L. Kulcinski, et al, "Detection of Highly Enriched Uranium Using a Pulsed D-D Fusion Source," Fusion Sci. Tech. 52, 1087 (2007).

[7] J.H. Nadler, G.H. Miley,. M. Coventry,. M. Williams,. B. Jurczyk,. R. Stubbers, Y. Nam, "High Current Pulsed IEC Operation," *Proceedings - Symposium on Fusion Engineering*, p 209-212, (1999)

[8] G. H. Miley, H. Momota, L. Wu, M. P. Reily, V. L. Teofilo, R. Burton, R. Dell, W. A. Hargus, "IEC thrusters for space probe applications and propulstion," *AIP Conference Proceedings*, v. 1103, p164-174 (2009)

[9] J. Park, R. A. Nebel, S. Stange, and S. Krupakar Murali, "Experimental Observation of a Periodically Oscillating Plasma Sphere," Phys. Rev. Lett. 95, 015003 (2005).

[10] K. Yoshikawa, K. Masuda, Teruhisa Takamatsu, Seiji Shiroya, Tsuyoshi Misawa, Eiki Hotta, Masami Ohnishi, Kunihito Yamauchi, Hodaka Osawa and Yoshiyuki Takahashi, "Research and Development of a Compact Discharge-driven D-D Fusion Neutron Source for Explosive Detection," Nucl. Instr. Meth. Phys. Res. B 261, 299 (2007).

[11] H. Osawa, T Kawame, S Yoshioku, M Ohnishi, 20th IEEE/NPSS Sym. Fusion Eng., SOFE 03, 316 (2003).

[12] K. Yamauchi, Masato Watanabe, Akitoshi Okino, Toshiyuki Kohno, Eiki Hotta, Morimasa Yuura, "Pulsed Operation of a Compact Fusion Neutron Source Using a High-Voltage Pulse Generator Developed for Landmine Detection," Fusion Sci. Tech. 47, 1229 (2005).

[13] J. Khachan and S. Collis, “Measurements of ion energy distributions by Doppler shift spectroscopy in an inertial-electrostatic confinement device”Phys. Plasmas, 8, 1299 (2001).

[14] L. Blackhall, and J. Khachan, “A simple electric thruster based on ion charge exchange” J. Phys. D: Appl. Phys. 40 2491–2494 (2007)

[15] S. K. Murali, B. B. Cipiti, J. F. Santarius, G. L. Kulcinski, “Study of Fusion regimes in an Inertial Electrostatic Confinement Device Using the New Eclipse Disk Diagnostic,” Physics of Plasmas, 13, 053111 (2006)

[16] G.A. Emmert and J.F. Santarius, “Atomic and Molecular Effects on Spherically Convergent Ion Flow II: Multiple Molecular Species” (in preparation, 2009).

[17] B. J. Egle, "Construction and Initial Results from the Six Ion Gun Fusion Experiment", Proceedings of the 10th U.S. - Japan Workshop on Inertial Electrostatic Confinement Fusion (2008)

[18] J. Kipritidis, J. Khachan, M. Fitzgerald, and O. Shrier, “Absolute densities of energetic hydrogen ion species in an abnormal hollow cathode discharge,” Physical Review E, 77, 066405 (2008)

[19] O. Shrier, J. Khachan, S. Bosi, M. Fitzgerald, and N. Evans, “Diverging ion motion in an inertial electrostatic confinement discharge” Physics of Plasmas, 13, 012703 (2006)

[20] J. H. Nadler, G. H. Miley, Y. Gu, T. Hochberg, “Characterization of an Inertial Electrostatic Confinement Glow Discharge Neutron Generator” Fusion Technology, 21, 1639-1643 (1992)

[21] T. A. Thorson, R. D. Durst, R.J. Fonck, A.C. Sontag, “Fusion Reactivity Characterization of a Spherically Convergent Ion Focus” Nuclear Fusion, Vol. 38, No. 4 (1998)

[22] Fujimoto, T., Oishi, T., Zen, H., Masuda, K., Yoshikawa, K. “Intensity Distribution of D-^{3}He Fusion Reaction Rate in an IEC Device” Fusion Engineering, SOFE (2007)

Chapter 2: The University of Wisconsin IEC Experiment

A schematic of the HOMER IEC device at the University of Wisconsin – Madison is shown below in Figure 2-1. The HOMER IEC device is contained within an aluminum vacuum vessel measuring 65 cm in height and 91 cm in diameter. The vacuum system (not shown below) consists of an oil free Varian Triscroll roughing pump that backs up a Varian V550 Macrotorr turbomolecular pump. This system allows for base pressures in the low 10^{-6} Torr range. Pressure is measured in the HOMER IEC device with a Varian Sentorr ion gauge.

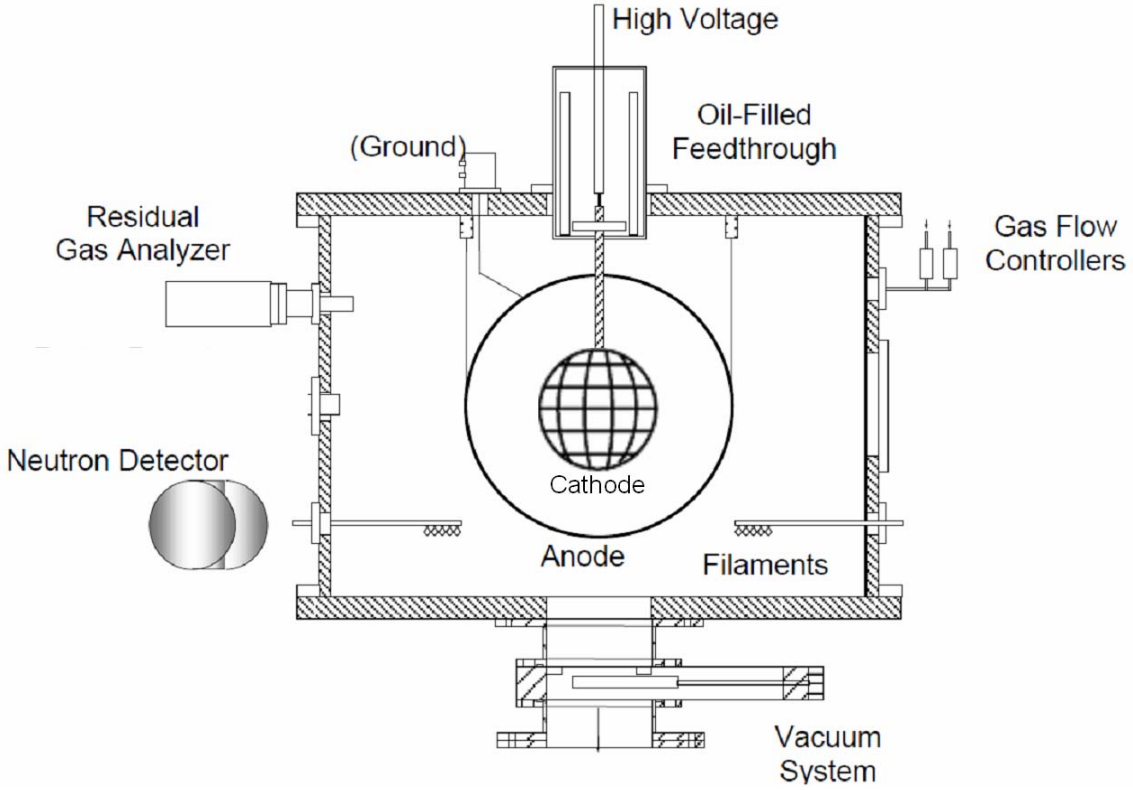

Figure 2-1: Schematic of the HOMER IEC device showing high voltage system, gas feeds, vacuum diagnostics, and neutron detector.

The HOMER IEC device can be filled with the necessary fuel gas through the use of three MKS Mass-Flo® controllers which allow independent control of the partial

pressures of deuterium, helium-3, and helium-4 gas in the vacuum chamber. The flow controllers allow volumetric flow rates up to 50 sccm (standard cubic centimeters per minute). These adjustable flow rates coupled with an adjustable gate valve over the turbomolecular pump allow a wide range of operating pressures between 0.25 mTorr – 5 mTorr. Monitoring of the partial pressures of the fuel gases and contaminant gases is performed with a Stanford Research Systems CIS 200® residual gas analyzer.

Cathode and anode configurations are another important consideration within the HOMER IEC device. Mounted to the vacuum vessel lid is an adjustable anode mount that allows anodes of varying radii to be mounted within the device. Anodes are typically constructed in a latitude and longitude pattern out of stainless steel wire. The anode is typically held at ground potential. The cathodes within the device are mounted to a molybdenum rod that connects to the high voltage power supply outside the chamber through a boron nitride, insulating vacuum feedthrough. Connection to the high voltage power supply is made in an oil filled cylinder on top of the vacuum vessel.

The typical design for an IEC cathode is either a symmetric triangular or lat-long design (shown below in Figure 2-2).

(a) 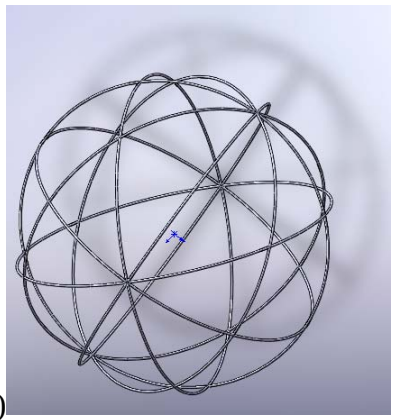 (b) 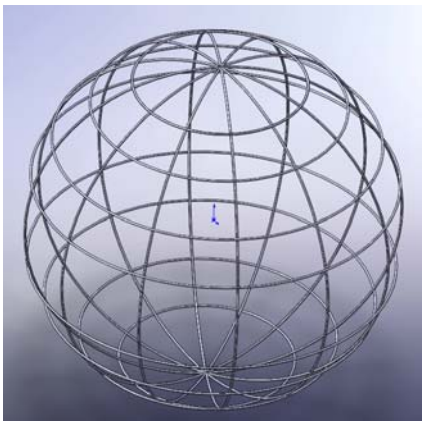

Figure 2-2: (a) equilateral cathode design (b) lat-long cathode design

Cathode diameters may vary between 5 cm – 20 cm although smaller and larger cathode diameters are possible in the current HOMER configuration. Nominally the cathodes are made of a tungsten-rhenium alloy, with typical wire thicknesses of 0.1 cm. The cathodes are attached to the molybdenum rod within the boron nitride insulator by inserting the collection of cathode wires at the apex of the grids into a series of custom made fastening holes within a molybdenum nut that is threaded onto the bottom of the molybdenum rod within the high voltage stalk. The high voltage stalk and the fastening nut are shown below in Figure 2-3.

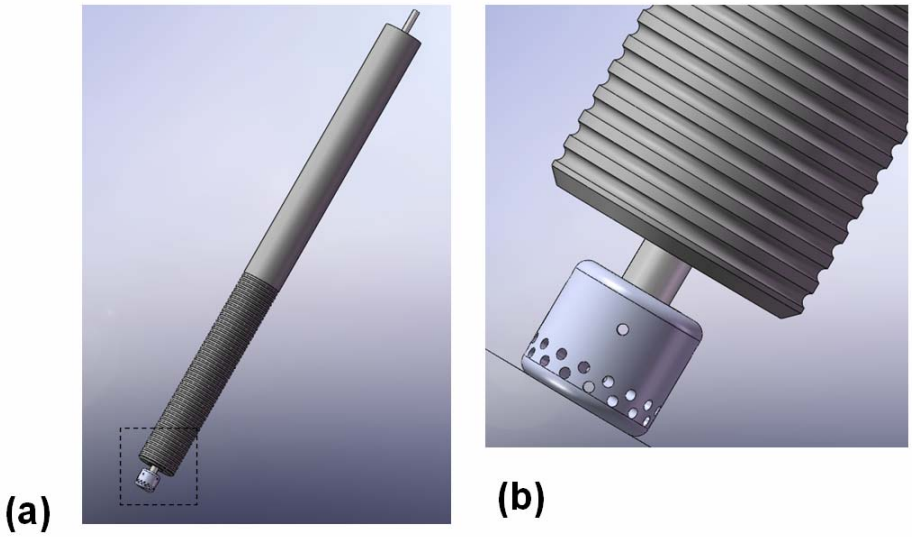

Figure 2-3: Schematic of (a) high voltage stalk (b) fastening nut for cathode mounting (CAD work courtesy of B. Egle)

The high voltage power supply used for the HOMER IEC device is a steady state, DC, 200 kV, 75 mA Hipotronics® power supply. The supply is connected to the chamber through a series of resistors totaling 250 kΩ. The resistors reside in an oil bath to prevent arcing. The resistors serve to stabilize the system during voltage surges. It

should be noted that the 200 kV, 75 mA supply will soon be replaced by a 300 kV, 150 mA power supply from Phoenix Nuclear Labs in Middleton, WI.

The source plasma in the HOMER IEC device is provided by six 200 W light bulb filaments which are heated and biased to produce an electron beam generated plasma outside the anode. A 0 – 120 V rectified variable transformer provides heating power to the filaments. Bias is applied to the filaments with a similar 0 – 120 V variable transformer connected to a 4x step up transformer, and rectified by a diode bridge and high voltage capacitor rated for 800 V and 1000 µf. The schematic of this circuit is shown below in Figure 2-4.

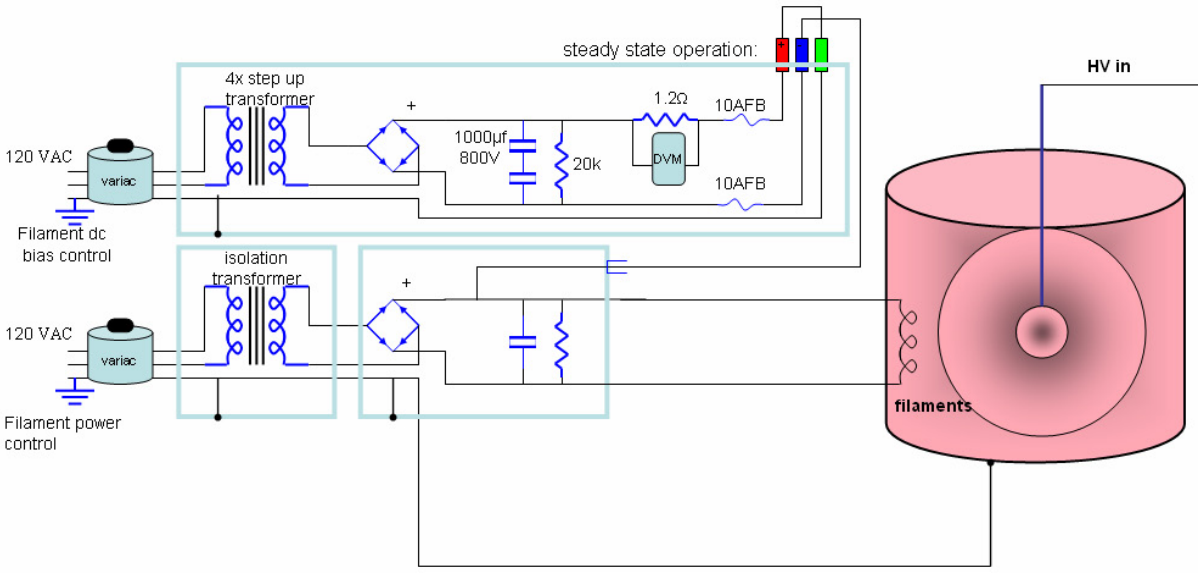

Figure 2-4: IEC source region filament control circuit[1].

In addition to the diagnostics detailed in this thesis a helium-3 filled neutron detector is also used to monitor the fusion rate within the device. The neutron detector is calibrated to a Pu-Be neutron source placed in the center of the IEC device for

calibration. This provides a calibration for the fusion rate within the HOMER IEC device. The neutron detector is located ~2 m from the vacuum vessel.

The HOMER IEC chamber, diagnostics, and high voltage power supply are all located within a radiation shielded facility. The radiation facility has 1.5 m thick concrete walls with a 1 tonne, 5cm thick, lead door serving to shield the entrance to the control room. Radiation monitors record the X-ray and neutron radiation levels within the room and an interlock system prevents the high voltage from being operated while the lead door is open.

Chapter 2 References

[1] R. P. Ashley – UW-Madison FTI – private communication 2007

Chapter 3: Direct Conversion of High Energy Protons to Electricity

3.1: Previous Work in Charged Particle Direct Conversion

To date there have been no known attempts made to convert the kinetic energy of high energy protons to electricity using solid-state devices. However, over the past 30 years, there has been a great deal of work done investigating the use of solid-state devices to convert the energy in beta particles to electricity. This field of research contains a useful knowledge base in that it also focuses on the conversion of high-energy charged particles to electricity.

Betavoltaics operate on the same principle as the proton radiation cell described previously, except that the charged particles inducing ionizations in the semiconductor junction are beta particles. The principle of these devices has been proven on numerous occasions. They have exhibited power densities on the order of 1-10mW/cm^3, and have shown overall efficiencies on the order of 2% using silicon technology[1, 2,3]. At the University of Wisconsin-Madison research was performed on the use of betavoltaics as a power source for MEMS devices. The device constructed produced 70 pW of power at an efficiency of 1%[4].

Recently work has also been conducted on the use of SiC betavoltaics that has shown the promise of increased conversion efficiency from the use of wide bandgap semiconductors. This study on SiC betavoltaic devices indicates a conversion efficiency of 4.5% with peak power outputs of 0.58uW, see Figure 3.1-1[5]. This efficiency is comparable to that of radioisotope thermal generators that utilize thermo-electric or thermionic conversion techniques.

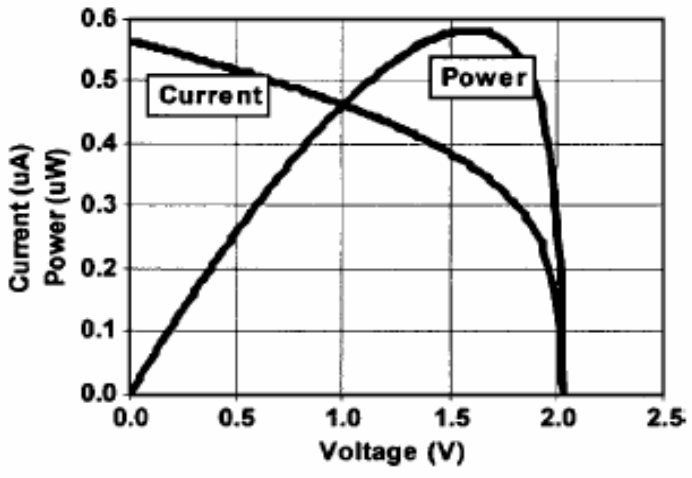

Figure 3.1-1: Output Current and Power from a SiC Betavoltaic Device[5]

In the years from 1968-1974, engineers at Donald W. Douglas Labs in Richland WA developed a betavoltaic battery design known as the Betacel (see Figure 3.1-2). These silicon based batteries exhibited efficiencies of 2% and power outputs in the range of 10 μW. These designs were even considered for use as pacemaker batteries in the early 1970's. It is probable that these efficiencies could be made slightly higher by increasing the number of incident charged particles. A detailed theoretical calculation of the efficiency of converting high-energy charged particles to electricity will be presented in the Theory section of this paper.

It is likely that these efficiencies will be very similar to the efficiency of a proton-based direct conversion system. While these efficiencies are low, with proper optimization, solid state direct conversion devices may yet be useful in some applications such as energy conversion space based fusion energy systems, due to their light weight and competitiveness with current space based energy conversion modules.

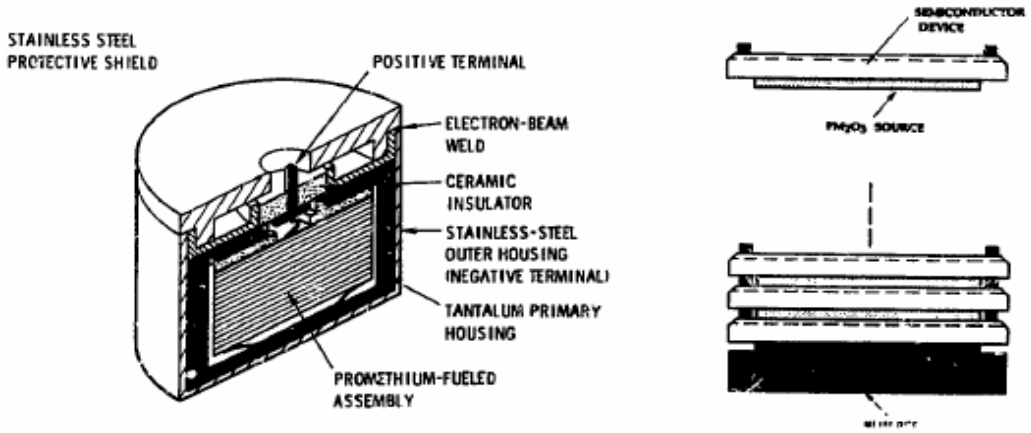

Figure 3.1-2: Construction of a Betacel Betavoltaic Battery [1]

3.2: Theory: Charged Particle Direct Conversion

3.2-a: Radiation Cell Theory

The PIN (P-type, Intrinsic, N-type) junction diode has long been used in the field of solar energy research as a means to create power by harnessing sunlight. The only difference in the application of PIN junctions to the conversion of high-energy protons to electric power is the form of radiation that is being converted to electricity. The theory behind proton radiation cells is very similar to the theory of photovoltaic operation.

The power produced by a proton radiation cell is due to electron/hole pairs excited by high-energy protons as they are slowed down in the silicon matrix mainly through electronic stopping. The current in the form of charge carriers generated in the PIN junction is given by[2]:

$$I_{gen} = \frac{A\gamma e E_p}{E_{pair}} \qquad (3\text{-}1)$$

where A is the surface area of the junction exposed to protons, γ is defined as the proton flux (protons-cm^{-2}-s^{-1}), e is the electronic charge, E_{pair} is the energy required to create e$^-$ /hole pair (3.62eV in Si), and E_p is the energy of the incident proton. In addition to the current generated by proton irradiation there is also a *dark current* present at all times in the PIN junction that is related to thermal excitation of charge carriers in the diode. The *ideal diode equation* defines the dark current in the PIN junction as follows:

$$I_{dark} = I_s \left[\exp\left(\frac{V}{V_{th}} \right) - 1 \right] \tag{3-2}$$

Here V_{th} is defined as the thermal voltage (0.025eV at 300K ambient temperature) and I_s is defined as the saturation current[6]. The saturation current is given below.

$$I_s = \frac{AeL}{\tau} \frac{n_0^2}{n_{maj}} \exp\left({-E_g}/{V_{th}} \right) \tag{3-3}$$

Here n_{maj} represents the number of majority carriers present in the intrinsic region of the PIN diode, and E_g is the band gap energy of the semiconductor material. L is the charge carrier diffusion length, which is defined in terms of the diffusion coefficient of charge carriers in the semiconductor material. The quantity n_0 is given by the following expression[7].

$$n_0 = 2.546 \times 10^{19} \left(\frac{m_{de} m_{dh}}{m_0^2} \right)^{3/4} \left(\frac{T}{300K} \right)^{3/2} \tag{3-4}$$

Where m_{de} and m_{dh} represent the density of states values for electron and hole effective mass, and m_0 is the electron mass. Also τ, from equation 3, represents the average carrier lifetimes of the electrons and holes in the semiconductor material. These values were assumed to be ~$1x10^{-4}$ s in the intrinsic region[8]. The carrier lifetime is affected by two factors, the impurity concentration of the semiconductor material and also the number of defects present in semiconductor material. The doping concentration affects the number of either acceptors or donors present for charge carrier recombination. Similarly defects present charge carriers with additional sites for recombination, and defect-aided recombination is most relevant in damaged semiconductor materials and polycrystalline semiconductor materials.

The total current produced in the PIN junction diode is the net sum of the I_{gen} and I_{dark}

$$I_{out} = I_{gen} - I_{dark} = \frac{\gamma e E_p}{E_{pair}} - I_s \left[\exp\left(\frac{V}{V_{th}} \right) - 1 \right] \tag{3-5}$$

With the I_{out} set to zero an expression for the open circuit voltage, V_{OC}, can be obtained. Similarly the short-circuit current (I_{sc}) can be obtained by assuming zero voltage drop across the PIN diode. These two expressions are given below:

$$V_{OC} = V_{th} \ln\left(\frac{\gamma e E_p}{E_{pair} I_s} + 1 \right) \tag{3-6}$$

$$I_{sc} = I_{gen} + I_s \approx I_{gen} \tag{3-7}$$

The I_{sc} in most cases can be considered equal to I_{gen} since the saturation current is usually very small when compared to the current generated by irradiation. Also note that V_{OC} is dependent on I_s in that smaller I_s values lead to larger relative open-circuit voltages for a given semiconductor material. This is significant because wide bandgap semiconductors have vanishingly small saturation currents that lead to higher relative values of V_{OC} for wide bandgap materials. The importance of this will be revisited in the theoretical efficiency calculations presented later in this section.

For the case of the idealized PIN diode, where the device is considered to be a perfect rectifier, the power output from the device can be expressed as the product of the short-circuit current and the open circuit voltage. However, no diode behaves as a perfect rectifier. To account for the leakage currents, internal resistances and contact resistances inherent in real devices a form factor, denoted FF, is introduced to account for the non-idealities of experimental diodes. Figure 3.2-1 shows that the power output from a radiation cell can be obtained from an I-V trace taken during irradiation, where the increasing area above the I-V curve represents the power output from the device at different fluxes of charged particles. From Figure 3.2-2 it is clear that the maximum power output of a real diode is some fractional value of the possible output from an ideal diode, which is defined by V_{OC} and I_{sc}. The ratio of the maximum power output of a real diode to the product of V_{OC} and I_{sc} is the form factor, FF. Thus the efficiency of a radiation cell can be defined as follows:

$$\eta = \frac{I_{sc} V_{OC} FF}{P_{in}} = \frac{V_{OC} I_{sc} FF}{\gamma e E_p} \tag{3-8}$$

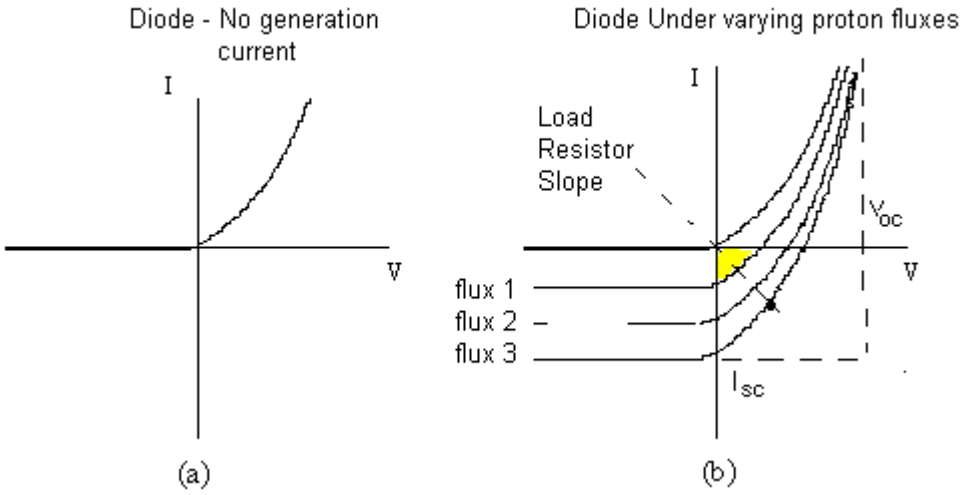

Figure 3.2-1: Radiation Cell I-V Characteristics under Irradiation

From Figure 3.2-2 the *form factor*, *FF*, would be the ratio of the area denoted $P_{max\text{-}real}$ to the area denoted P_{ideal}. For experimental purposes an I-V trace like the examples shown above can be obtained by connecting the radiation cell to a variable resistor and varying the load resistance in series with the diode during irradiation.

From work done by Klein[9] we find that the following expression relates the E_g to E_{pair}. Where E_g is the band-gap energy of the material used to make the radiation cell.

$$E_{pair} = 2.8E_g + \varepsilon \qquad (0.5eV \le \varepsilon \le 1.0eV) \qquad (3\text{-}9)$$

This expression is supported by the empirical data shown in Figure 3.2-3 that relates the energy necessary to create an electron hole pair the band gap energy of various semiconductor materials[9]. From combining equations 3-8 and 3-9 it is readily apparent

that the efficiency of any radiation cell is dependent on the ratio of V_{OC} to E_{pair}. The upper bound on the value of V_{OC} is set by the band gap energy, E_g.

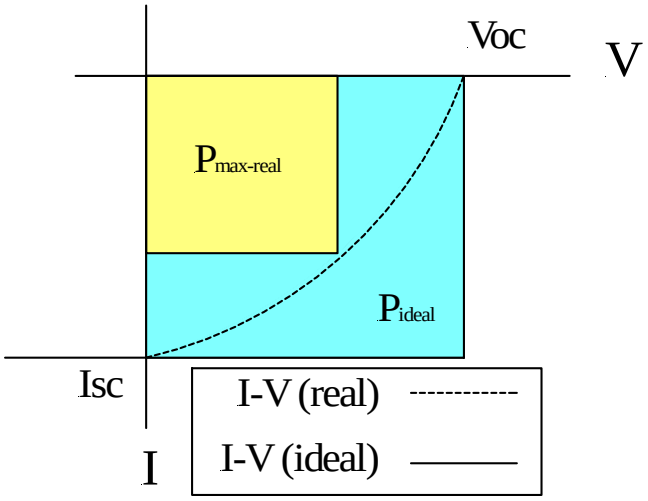

Figure 3.2-2: Real and Ideal Power Output Characteristics of a Radiation Cell I-V Trace

Since wider bandgap materials can support values of V_{OC} that are closer to E_g, it becomes apparent that wider bandgap semiconductors would be more efficient when used as a radiation cell. When the calculation of energy conversion efficiency (equation 3-7) is carried out for several different semiconductor materials, the theory shows that wider bandgap materials, such as SiC and diamond (E_g of 3.0 eV and 5.5 eV respectively), are indeed more efficient than more narrow band materials such as Si and Ge (E_g of 1.1 eV and 0.7 eV respectively).

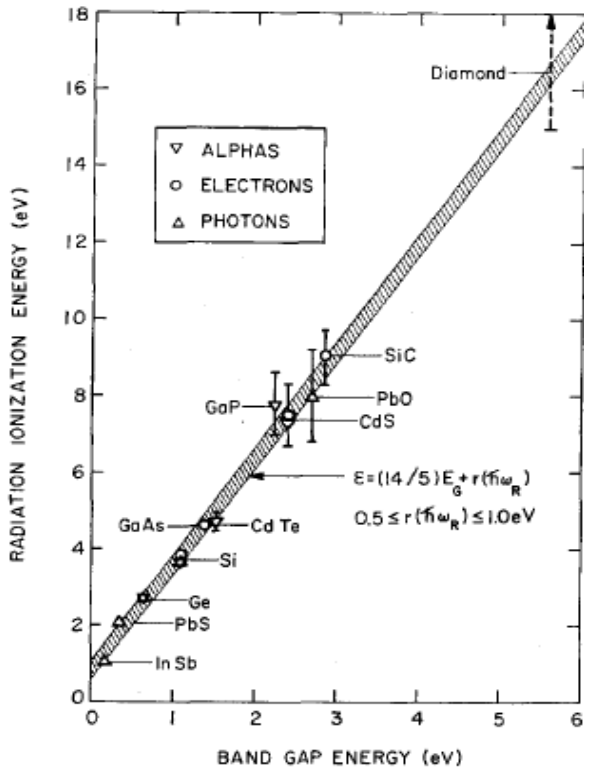

Figure 3.2-3: Electron/Hole Pair Production Energy for Varying Semiconductors[9]

The results of the calculation are shown in Figure 3.2-4. In this calculation a form factor of 0.8 was assumed since this is typical for most high quality photovoltaic devices that are manufactured today. The calculation assumes that the incident radiation is in the form of 3.02 MeV protons with fluxes that vary from $1x10^{10}$ protons cm^{-2} s^{-1} to $1x10^{14}$ protons cm^{-2} s^{-1}. The temperature of the semiconductor material was assumed to be held at room temperature (300 K) which may not be realistic for the higher proton fluxes presented here[10, 11, 12, 13, 14, 15, 16, 17, 18, 19]. The efficiency of proton collection by the radiation cell is assumed to be 100% for the purposes of this calculation.

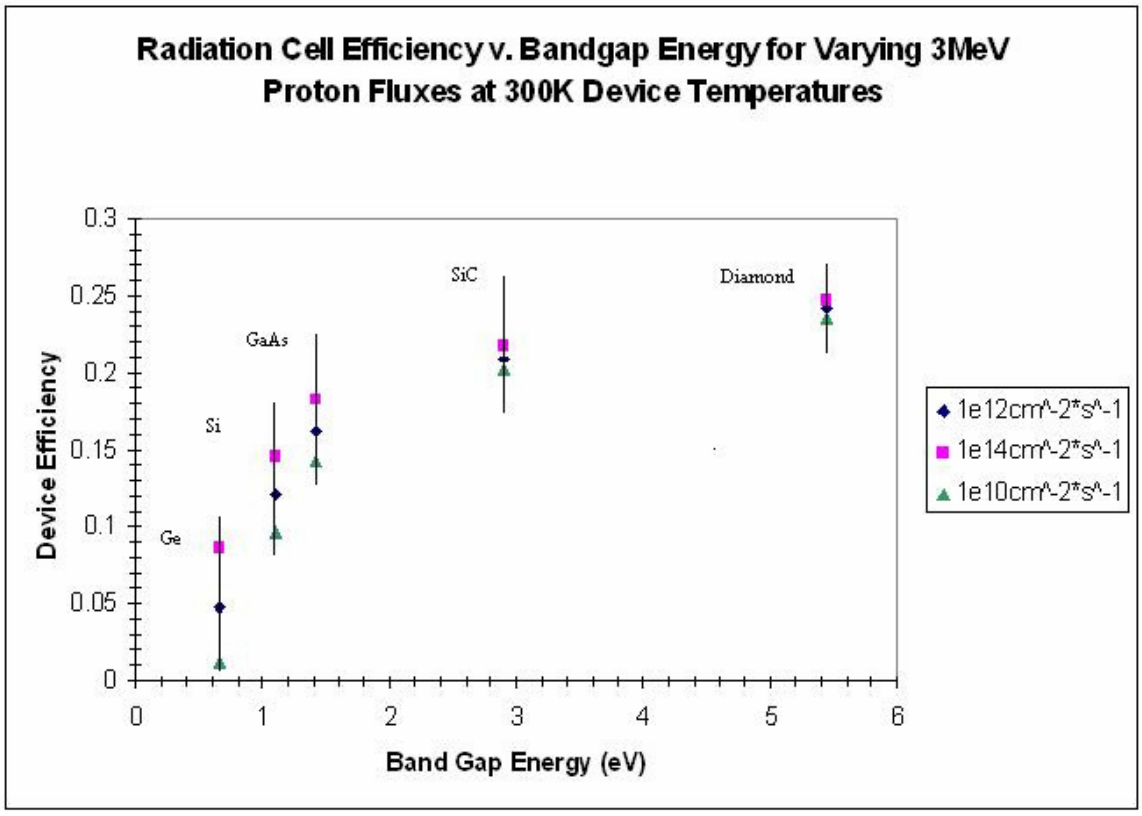

Figure 3.2-4: Radiation Cell Efficiency Dependence on Semiconductor Band Gap Width

From Figure 3.2-4, diamond is shown to be the most attractive semiconductor material from the standpoint of radiation cell conversion efficiency. It appears to be possible to produce radiation cells capable of conversion efficiencies above 20% if high quality modules can be produced from either SiC or diamond. This calculation of efficiencies for varying band gap energies is based on a similar study done by Olsen regarding the efficiency of beta-voltaic devices[2].

3.2-b: Radiation Damage in Semiconductors

A major concern surrounding the possibility of using semiconductors for converting the kinetic energy of fusion protons to electricity lies in the radiation damage

caused by the protons as they traverse the PIN junction diode. Although only a small fraction of the proton energy is lost to proton-Si atom collisions, damage would build up in the lattice very quickly under the high proton fluences expected in a D-D or D-^{3}He fusion reactor. Because of this, an understanding of the radiation resistance of PIN junction conversion devices is imperative.

The main detrimental effect of proton irradiation on semiconductor devices is the lattice displacement that occurs from direct knock-on collisions that occur between high energy protons and lattice atoms. These collisions result in an increase in the number vacancies and interstitials present in the semiconductor matrix. These interstitials and vacancies act as recombination centers and thus add an increased recombination current to the parasitic saturation current already present in the undamaged device. Thus the total reverse current, I_R, in a PIN diode that has undergone radiation damage is given by the sum of the saturation current discussed previously and recombination current.

$$I_R = I_s + I_{rec} \tag{3-10}$$

Eventually this effect will reduce the device efficiency to the point where it is no longer an effective means of electricity production. It should be noted that any semiconductor device that undergoes radiation damage suffers detrimental effects from an increase in recombination centers. Eventually, under very high doses of charged particles, at low temperatures, the semiconductor material may even begin to amorphize. This begins to occur near 0.5 dpa (displacements per atom) in most semiconductor materials[10].

Damage such as this can be repaired in a material by annealing the substance. One model for the annealing of radiation damage in silicon begins with the assumption

that equal concentrations of vacancies and interstitials are produced from a charged particle interaction in the silicon lattice. The charged particle interaction raises the concentrations of vacancies and interstitials well above the equilibrium concentrations inherent in the solid. Once the vacancies and interstitials are present in the solid they will either annihilate each other through recombination, migrate to sinks in the system, migrate to defects in the lattice and form stable structures (voids or dislocation loops for example), or form divacancies and di-interstitials. The changes in concentration of vacancies and interstitials in the lattice are governed by rate equations that depend on the activation energies of the phenomena mentioned previously. Let: V_1 be the concentration of monovacancies, V_2 be the concentration of divacancies, C_V be the concentration of vacancy clusters, J_V be the concentration of pre-existing defects that trap vacancies, I be the concentration of interstitials, C_I be the concentration of interstitial clusters (such as dislocation loops), J_I be the concentration of pre-existing defects that trap interstitials. In this analysis all the concentrations are considered normalized to the atomic density of the solid. The rate equations governing the population of interstitials, vacancies, and defect clusters are as follows[20]:

$$\frac{dV_1}{dt} = -R_1 V_1 I - R_5 (J_V - C_V) - R_7 V_1^2 + R_6 C_V + R_8 V_2 \tag{3-11}$$

$$\frac{dI_1}{dt} = -R_1 V_1 I - R_2 I - R_3 I (J_I - C_I) + R_4 C_I \tag{3-12}$$

$$\frac{dC_I}{dt} = -R_4 C_I + R_3 I (J_I - C_I) \tag{3-13}$$

$$\frac{dC_V}{dt} = -R_6 C_V + R_5 V_1 (J_V - C_V) \tag{3-14}$$

$$\frac{dV_2}{dt} = -R_8 V_1^2 + R_7 V_1^2 \qquad (3\text{-}15)$$

The various reaction constants R_1 through R_8 are defined as:

- The rate of vacancy-interstitial annihilation is $R_1 = \alpha_1 \exp(-E_I / kT)$ where α_1 is the interstitial jump frequency and E_I is the activation energy of interstitial migration.
- The rate of interstitial loss to interstitial sinks is $R_2 = \alpha_2 \exp(-E_i / kT)$ where α_2 is related to the jump frequency of interstitials and the concentration of interstitial sinks.
- The rate of interstitial loss to complex interstitial structures is R_3 and it is the same as R_1 because both loss rates depend solely on the interstitial jump frequency.
- The rate of interstitial complex decomposition is given by $R_4 = \alpha_4 \exp\left(-\frac{E_i + B_{Ci}}{kT}\right)$ where α_4 is a characteristic decomposition frequency and B_{Ci} is the binding energy of the interstitial complex.
- The rate of vacancy loss to vacancy complexes is given by $R_5 = \alpha_5 \exp(-E_V / kT)$ where α_5 is related to the vacancy jump frequency and E_V is the activation energy of vacancy migration.
- The rate of vacancy complex decomposition is given by $R_6 = \alpha_6 \exp\left(-\frac{E_V + B_{Cv}}{kT}\right)$ where α_6 is a characteristic decomposition frequency and B_{Cv} is the binding energy of the vacancy complex.

- The rate of divacancy formation is given by R_7, which is the same as R_5, since divacancy formation depends only on the migration of vacancies.
- The rate of divacancy decomposition is given by $R_8 = \alpha_8 \exp\left(-\frac{E_V + B_{V2}}{kT}\right)$ where α_8 is the characteristic rate of divacancy decomposition and B_{V2} is the binding energy of divacancies.

The formation and decomposition of all these defects are governed by characteristic activation energies that govern the extent to which these defects are mobile in the crystal lattice. The system of rate equations shown above is a highly coupled system that is quite difficult to solve. Data exists however that indicates that at temperatures above 500 ºC much of the defects can be annealed out of the crystal lattice[21]. The rate at which the annealing occurs will follow an Arrhenius relation based on the fact that all the processes governing defect annealing also follow an Arrhenius relation.

3.3: Charged Particle Direct Conversion - Experimental Setup

The initial attempts at converting high-energy fusion protons to electricity were performed on the UW-IEC device. The experiments involved a 10 cm^2 wafer of 500 μm thick silicon placed in view of the IEC cathode. The silicon wafer was placed behind a 300 μm thick lead shield to ensure that only protons from the D-^{3}He reaction could penetrate the wafer. Unfortunately, due to the inherently low efficiencies of a silicon radiation cell and the low proton flux from the IEC, it proved impossible to detect signal over the background noise present in the system. Significant steps were taken to reduce the background noise as much as possible. Background signal consisted of other forms

of ionizing radiation produced by the IEC, namely high-energy secondary electrons and bremsstrahlung X-rays produced by the impact of those electrons on the wall of the vacuum vessel. Magnetic shielding was used to stop secondary electrons from interacting with the silicon wafer. The 300 μm thick lead shield reduced the X-ray flux incident on the detector by a factor of ten. Attempts to measure the short-circuit current produced in the wafer showed that the current produced by background effects was less than 5 nA. Despite these efforts in shielding the silicon wafer from alternative forms of ionizing radiation, no evidence of D-^{3}He protons was ever seen in measurements of the short circuit current. When the 300 μm lead shield was removed, successful conversion experiments were performed on secondary electrons from the IEC cathode. Proving that the PIN junctions manufactured do indeed perform as radiation cells.

To prove the principle of using a solid-state device as a means to convert high-energy protons to electricity future experiments were performed in the University of Wisconsin Ion Beam Lab. These experiments utilized 3 MeV protons produced from a Pelletron Linear Accelerator[22], see Figure 3.3-1, to simulate D-D fusion protons. The significantly higher proton fluxes achievable on the accelerator made data collection a great deal easier. The experiments in the ion beam lab focused on measuring the efficiency of using a silicon PIN junction diode to convert the kinetic energy of high-energy protons to electricity.

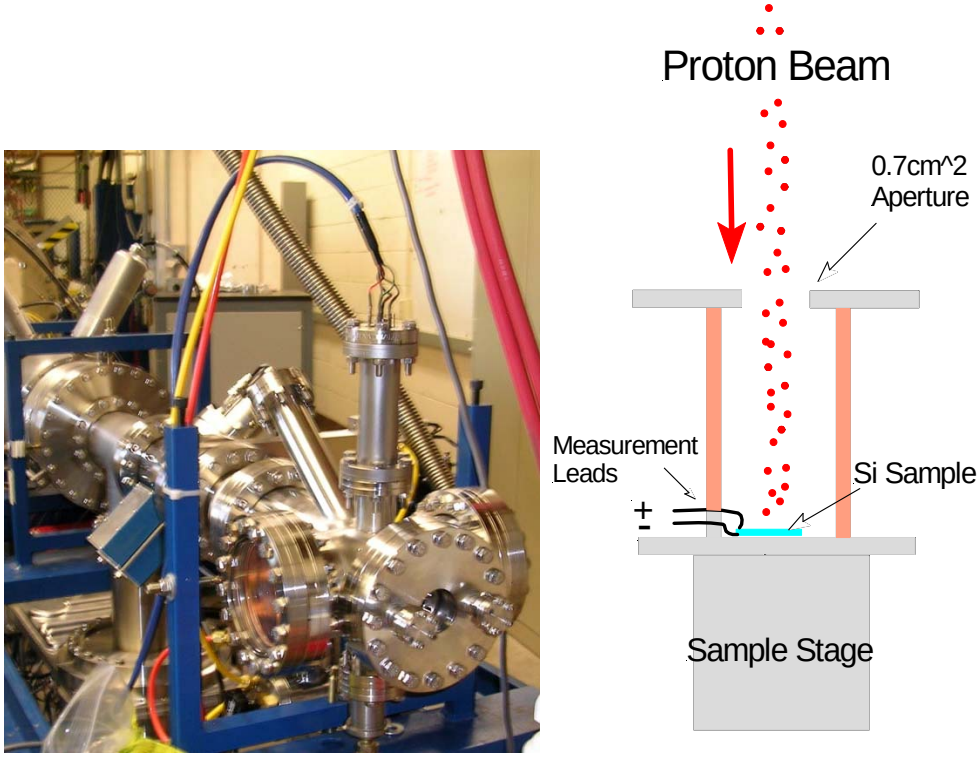

Figure 3.3-1: The Radiation Damage Stage in the UW-Ion Beam Lab

These experiments depended on an experimental set up that allows the proton fluence on the silicon wafer to be controlled with some precision. At low temperature in particular the SRIM™ computational data predicted the device to fail at proton fluences as low as $1x10^{13}cm^{-2}$. This prediction is based on the assumption that failure will occur two orders of magnitude below the predicted amorphization damage level of 0.5 dpa. These predictions for device failure were made using the ion transport code TRIM™ from the SRIM package, and the resulting simulations will be addressed later in this paper. Since such low fluences are necessary for these experiments correspondingly low proton currents on the order of 5-20 nA of beam current must be used for these experiments. While the irradiations were in progress I-V traces were taken using the setup shown in Figure 3.3-3. The I-V traces allowed for the conversion efficiency of the PIN diode to be

measured as a function of proton fluence. This was the means through which the lifetime of the device was characterized, when the operating conversion efficiency droped below $1/10^{th}$ of the initial conversion efficiency the PIN diode was deemed inoperable.

In order to characterize changes in efficiency during irradiation a Labview program was written that measures the voltage and current produced by the PIN diode while the proton beam was in operation. The PIN diode is in series with a variable load resistance that allowed I-V traces to be taken. The maximum power output of each trace was then compared to the input power from the proton beam for a constantly updated measurement of the efficiency versus fluence. The setup is shown below in Figures 3.3-2 and 4-3.

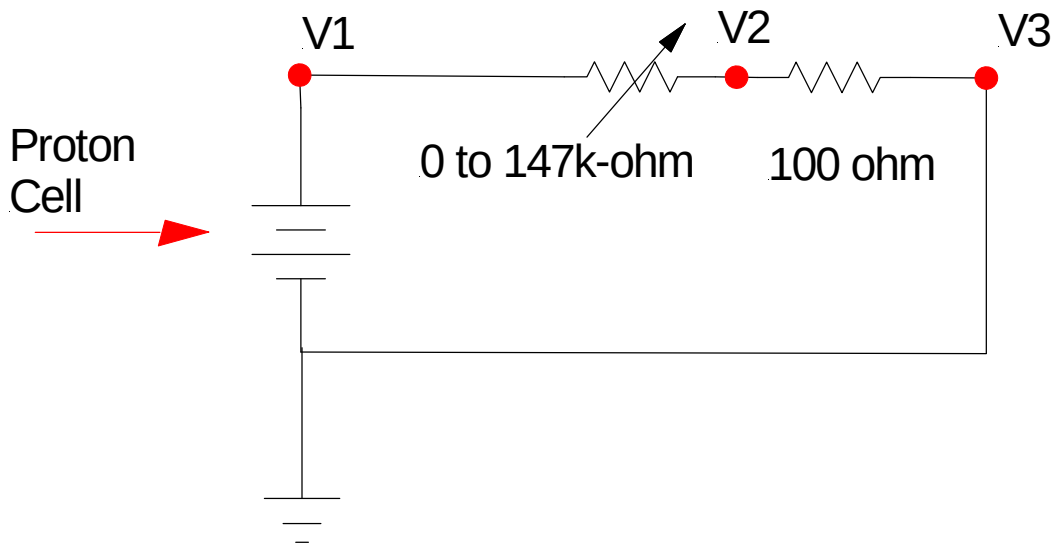

Figure 3.3-2: I-V Trace Setup with Voltages V1-V3 Sent to Labview for Signal Processing

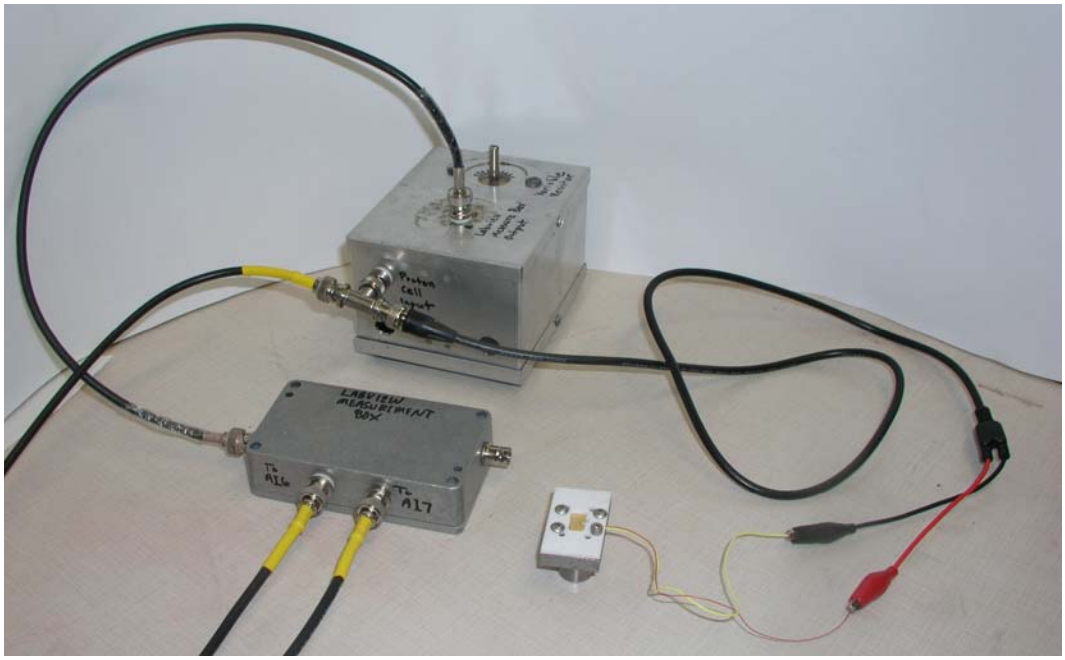

Figure 3.3-3: Data Acquisition Setup with Yellow Co-axial Cables Connecting to Labview

The voltage difference measured across the 100 Ω resistor (V2-V3) allowed for current measurements to be made while the variable resistor produced the variable load necessary for an I-V trace to be taken.

3.4: Charged Particle Direct Conversion - Results

3.4-a: SRIM Simulation of Proton Damage in Silicon

In order to better understand the effects that high energy proton impacts would have on a PIN junction diode the ion transport code SRIM™[23] was used to simulate lattice damage in silicon. SRIM™ is a group of programs, which calculate the stopping, and range of ions (10 eV - 2 GeV/amu) into matter using a full quantum mechanical treatment of the collisions between incident ions and target atoms. SRIM™ takes into account long-range electronic interactions between incident ions and all of the target atoms. Collisions between incident ions and target atoms are modeled by screened

Coulomb collisions that include the effects of overlapping electrons shells. TRIM™ is the most robust program contained within the SRIM™ package. TRIM™ is a Monte Carlo program that simulates the transport of energetic ions through solid or gaseous targets. TRIM™ is capable of handling the transport of ions through targets with as many as eight different material layers. It will calculate both the final 3-dimensional distribution of the ions in the target and also all phenomena associated with the ion's energy loss. Target damage, sputtering, ionization, and phonon production are all accounted for in TRIM simulations.

TRIM™ simulations were done for 3 MeV protons normally incident to 100 μm of silicon. The TRIM™ simulation used $1x10^{6}$ particle histories and generated a relatively smooth plot of displacements per ion per unit depth. This was integrated to achieve total displacements per ion, which could then be transformed into the unit dpa using the known atom density of solid silicon, $4.98x10^{22}\,cm^{-3}$. Figure 3.4-1 shows the expected dpa as a function of depth in the silicon as a result of proton bombardment.

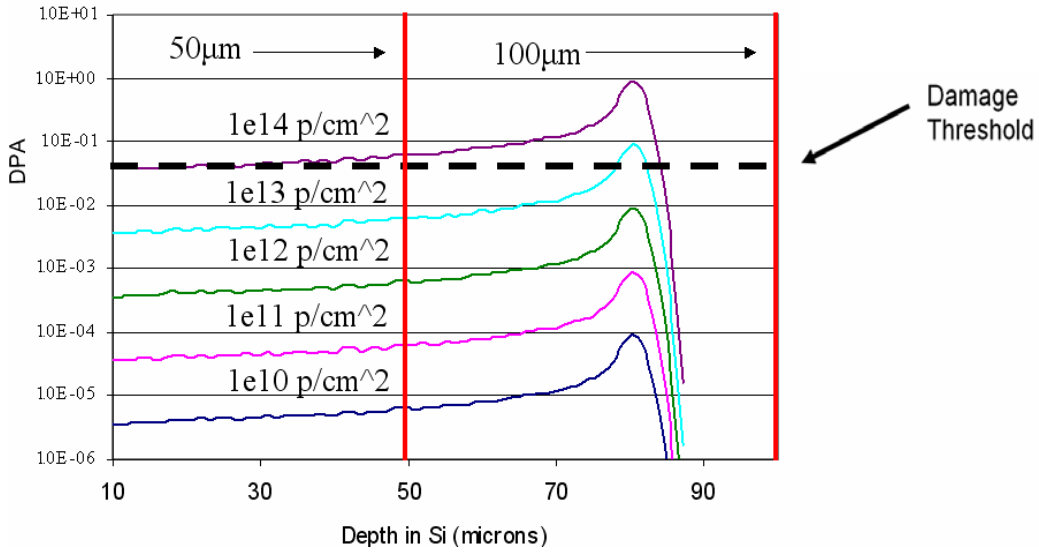

Figure 3.4-1: The calculated displacements per atom (DPA) as a function of depth in silicon for varying proton fluence. The black dotted line represents the expected damage threshold for device operation.

The damage threshold shown in Figure 3.4-1 is an estimate of the damage level at which the device will cease to function effectively. It is based on the expectation that an amorphous layer will form in the silicon at ~0.5 dpa, and that the device will cease to function at a damage level 10x less than that. Once an amorphous layer has formed charge carrier transport across the junction is impossible. The figure also shows the two possible junction thicknesses, for future experiments proposed for the UW Ion Beam Lab. Since most of the damage from the proton irradiation occurs between depths of 60 µm to 80 µm, a 50 µm thick PIN junction should endure less damage than a 100 µm thick junction, thus resulting in longer lifetime. However, TRIM™ also shows that a significant amount of the ionization done by the incident protons also occurs in the range of 60 µm to 100 µm. So the conversion efficiency should also be noticeably reduced in the 50 µm thick PIN junction as opposed to the 100 µm thick junction (See Figure 3.4-2). This trade off between enhanced lifetime and lower efficiency for thinner PIN junctions will need to be characterized in future experiments.

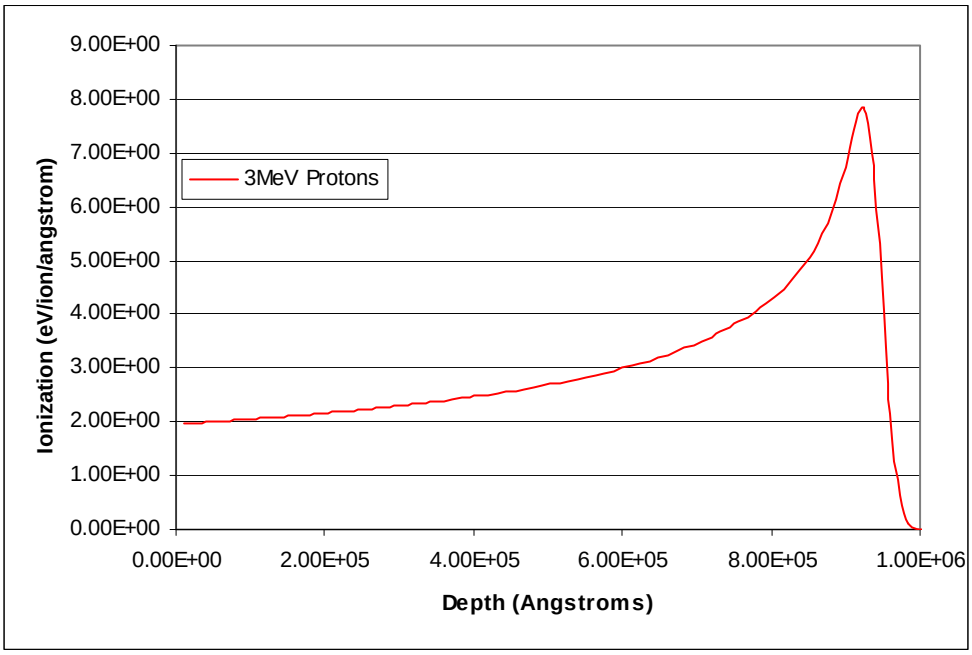

Figure 3.4-2: Energy to Charge Carrier Production through electronic stopping by 3MeV protons in silicon as a function of depth

3.4-b: Conversion Efficiency and Power Output vs. Fluence in Si PIN diode

Experiments performed with a 500 μm thick PIN junction diode have been performed in the UW Ion Beam lab. The PIN diode was irradiated with 3 MeV protons at a flux that was determined to be between $1x10^{10}$ and $5x10^{10}$ protons/cm^2-s. The maximum achieved conversion efficiency for the device was between 0.2% and 0.8%. The uncertainty for η is due to uncertainty in the flux of protons incident on the face of the PIN junction diode. It should be noted that the form factor for this PIN diode was 0.35, a relatively low value. With a more efficient design form factors of 0.7-0.8 may be attainable that could raise the efficiency somewhat further. The maximum achieved power output per unit area from the PIN diode was 40 μW/cm^2.

Figures 3.4-3 and 3.4-4 show the resulting decays in efficiency and power output with increased proton fluence.

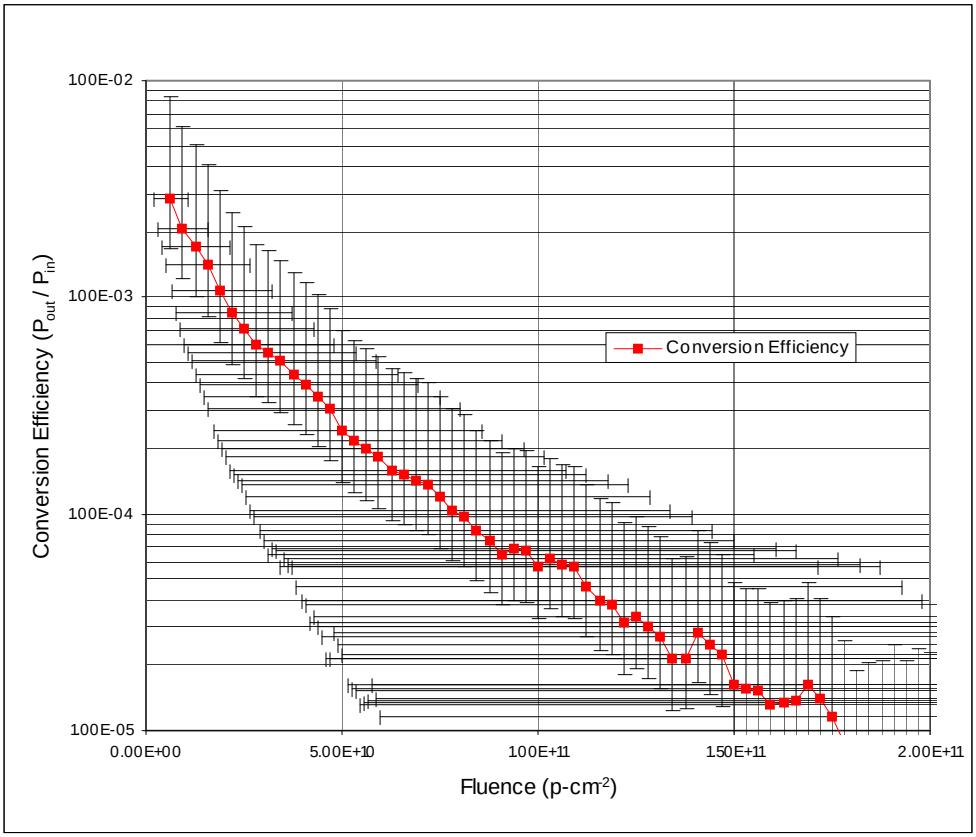

Figure 3.4-3: Conversion Efficiency verses proton fluence for a silicon, 500 μm thick, PIN junction diode.

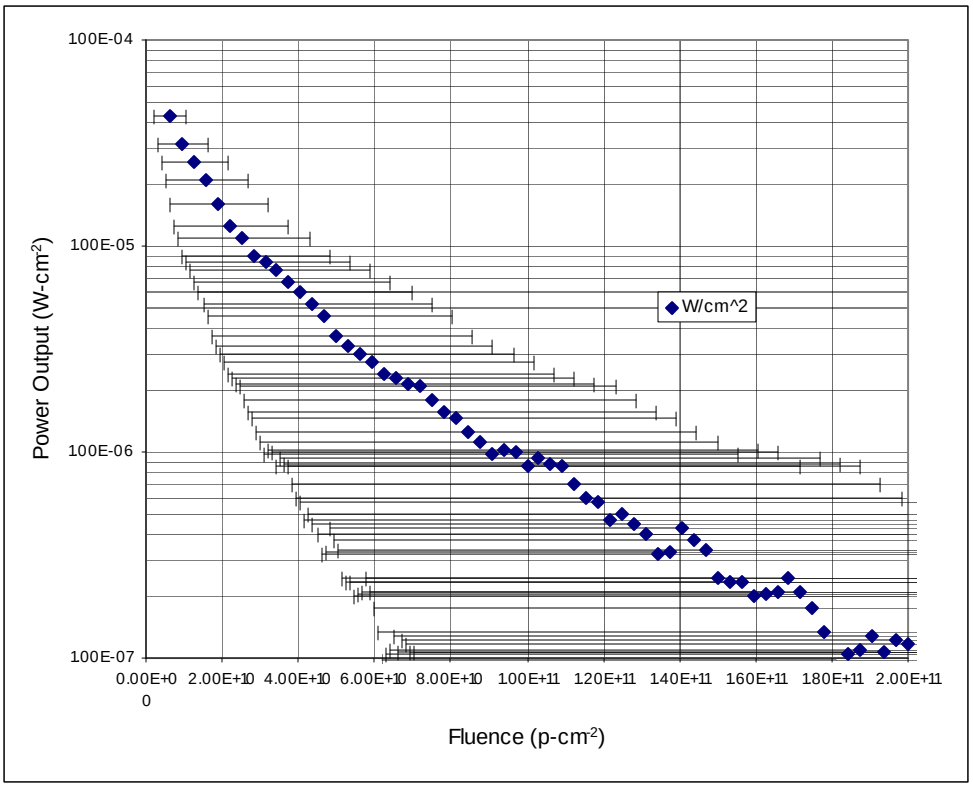

Figure 3.4-4: Power output per unit area as a function of proton fluence for a silicon, 500 μm thick, PIN diode.

As is shown in the above figures the performance of the PIN diode degraded rapidly with proton fluence. Even under the modest proton fluxes applied in this experiment the device lasted only a few seconds before the power output and conversion efficiency had fallen by two orders of magnitude. This shows that at room temperature the device is very sensitive to lattice damage. The data and TRIM simulation, from Figure 3.4-1, together indicate that silicon based charged particle direct conversion devices undergo a factor of 100 power output reductions for damage levels as low as $1x10^{-3}$ dpa. This is lower than the expected damage threshold by over two orders of magnitude. Future experiments under the same exposures should be performed at higher PIN junction temperatures.

Chapter 3 References

[1] L.C. Olsen, "Review of Betavoltaic Energy Conversion" *Proceedings of the 12th Space Photovoltaic Research and Technology Conference*, 256-267, (1993)

[2] L.C. Olsen, "Betavoltaic Energy Conversion" *Energy Conversion*, 13, 4, 117-127 (1973)

[3] P. Rappaport, et. al., "The Electron-Voltaic Effect in p-n Junctions Induced by Beta-Particle Bombardment," *Physical Review*, 93, 246 (1953)

[4] A. Lal, and J. P. Blanchard, *IEEE Spectrum*, September, p36-41, (2004)

[5] C. J. Eiting et al, "Demonstration of Radiation Resistant High Efficiency SiC Betavoltaic" *Applied Physics Letters*, 88, 064101 (2006)

[6] M. Shur, *Introduction to Electronic Devices*, John Wiley & Sons, New York, NY (1996)

[7] L.C. Olsen, "Advanced Betavoltaic Energy Conversion," *Energy Conversion*, 13, 4, 117-127, (1973)

[8] Davis, J.R., Jr., Rohatgi, A., Hopkins, R.H., Blais, P.D., Rai-Choudhury, P., McCormick, J.R., and Mollenkopf, H.C., *IEEE Trans. Electron. Devices*, 27, 677 (1980)

[9] C.A. Klein, "Bandgap Dependence and Related Features of Radiation Ionization Energies in Semiconductors," *Journal of Applied Physics*, 39, 4, 2029 (1968)

[10] S. Wolf, R.N. Tauber, *Silicon Processing in VLSI Era: Vol. 1*, Lattice, Sunset Beach, CA (1986)

[11] Jacoboni C., F. Nava, C. Canali and G. Ottaviani, "Electron drift velocity and diffusivity in germanium" *Phys. Rev. B* 24, 2, 1014-1026 (1981)

[12] Morin F. J., "Lattice Scattering Mobility in Germanium," *Phys. Rev.* 93, 1, 62-63 (1954)

[13] Li, S. S. and W. R. Thurber, "The dopant density and temperature dependence of electron mobility and resistivity in n-type silicon," *Solid State Electronics.* 20, 7, 609-616 (1977)

[14] Dorkel, J. M. and Ph. Leturcq, "Carrier mobilities in silicon semi-empirically related to temperature, doping and injection level," *Solid State Electronics.* 24, 9, 821-825 (1981)

[15] Rode, D. L., *Semiconductors and Semimetals*, R. K. Willardson and A. C. Beer, eds., Academic Press, N.Y., vol. 10, (1975)

[16] Wiley, J. D., *Semiconductor and Semimetals*, R. K. Willardson and A. C. Beer, eds., Academic Press, N.Y., vol. 10, p. 91 (1975)

[17] Nava, F., C. Canali, C. Jacoboni, L. Reggiani, and S. F. Kozlov, "Electron effective masses and lattice scattering in natural diamond," *Solid State Community* 33, 475-477 (1980)

[18] Reggiani, L., D. Waechter, and S. Zukotynskii, "Hall-coefficient factor and inverse valence-band parameters of holes in natural diamond," *Phys. Rev.* B 28, 6, 3550-3555 (1983)

[19] Shatter, W.J., H.S. Kong, G.H. Negley, J.W. Palmour, "Carrier mobility model for simulation of SiC-based electronic devices," *Inst. Phys. Conf. Ser.* 137, 155, (1994)

[20] L. Lazanu, I. Lazanu "Annealing of radiation inducted defects in silicon in a simplified phenomenological model," *Nuclear Instruments and Methods in Physics Research Section B: Beam Interactions with Materials and Atoms*, Volume 183, Issues 3-4, October, 383-390, (2001)

[21] R. Pourier et al, "Annealing Mechanisms of Divacancies in Silicon," *Proceedings of the 22nd International Conference on Defects in Semiconductors*, Århus, Denmark, (2003)

[22] National Electrostatics Corporation – www.pelletron.com (9/15/2006)

[23] Available at http://www.srim.org/

Chapter 4: Ion species measurements in the IEC source region

4.1: Previous Work

4.1-a: Ion species measurements

The technique for measuring average ion mass and ion species ratios, discussed in this chapter, was pioneered by Hala and Hershkowitz[1] at the University of Wisconsin-Madison. Their experiments focused on measurements of noble gas ion ratios under varying neutral gas ratios.

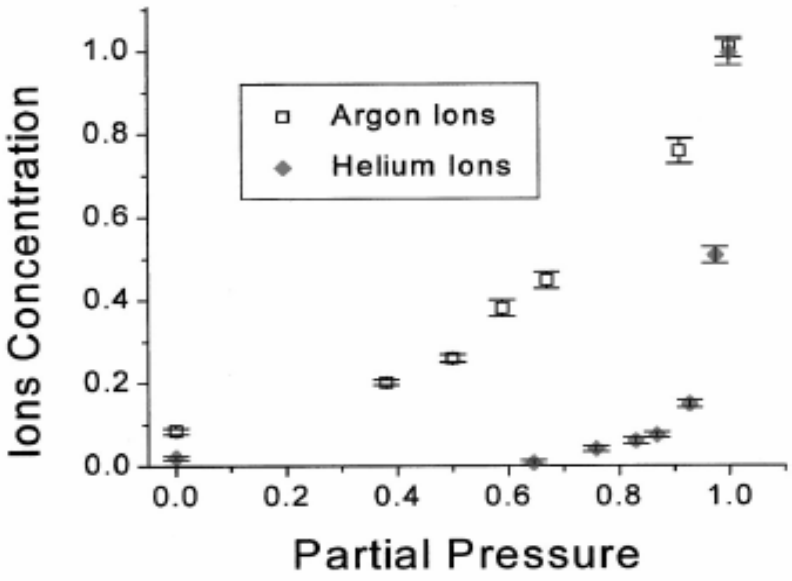

Figure 4.1-1: Argon and He Ion Ratios Compared to Partial Pressure with Respect to Xe

In particular He/Xe ion ratios, and Ar/Xe ion ratios were measured for varying neutral gas ratios. The data is shown in Figure 4.1-1. The ion acoustic wave technique[2] was able to measure the relative concentrations of ions in the multi-species plasmas to within 5% accuracy.

This technique has now been applied to a single neutral gas species that forms multiple molecular ion species. The ion source region in the UW-IEC device consists of weakly ionized deuterium plasma that contains multiple molecular ion species. By applying population dynamics techniques that utilize the atomic physics properties of ionization, recombination, and dissociation it has been shown that weakly ionized deuterium plasmas, like the IEC source region, form varying concentrations of D^+, D_2^+, and D_3^+. Using the ion acoustic wave technique put forth by Hala and Hershkowitz, the concentrations predicted by Emmert have been verified.[3]

Hershkowitz and co-workers have used utilized phase velocity measurements on ion acoustic for a variety of other experiments as well.[4] Most notably, examining a mildly collisional plasma with this technique leads to the finding that each species enters the plasma sheath at the same velocity, namely a concentration-weighted drift velocity that satisfies the Bohm criteria, where c_j, n_{j1}, and m_j represent the sound speed, ion density, and ion mass of each species in the multi-species plasma respectively.

$$c_1 = c_2 = c_3 = \sqrt{\frac{kT_e}{n_e}\left(\frac{n_{11}}{m_1} + \frac{n_{21}}{m_2} + \frac{n_{31}}{m_3}\right)} \tag{4-1}$$

These techniques used to measure ion acoustic wave phase velocities in these experiments were invaluable for the completion of this work.

4.1-b: Rate Equation Model of the IEC source region

The ion species measurements reported in this section were performed in conjunction with a model constructed by G.A. Emmert employing zero dimensional rate equations to determine the composition of the ions crossing the outer grid (anode). In this model the source region has a volume V, anode grid area A_g, wall area A_w, and is filled with deuterium gas. Electrons are emitted from filaments at an energy E_p (and speed v_p). These electrons are referred to as primary electrons; they have a density n_p. Ionization processes produce colder electrons with density n_e and temperature T_e. Because of the strongly negative potential between the cathode and anode, electrons are confined to the source region and do not penetrate very far into the intergrid region. A sheath is set up at the anode grid that extracts ions from the source region plasma and accelerates them towards the cathode. The primary electrons in the source region induce ionization and dissociation of the deuterium gas, ionization of the neutral deuterium atoms, and dissociation of the molecular ions. The plasma in the source region is composed of D^+, D_2^+, and D_3^+ ions; impurity ions are neglected. The density of the ith ion species is written as n_{i1} and the ion mass as m_i, where i =1 denotes D^+, i=2 denotes D_2^+, and i=3 denotes D_3^+ ions. The neutral atomic D species are denoted with density n_{10} and mass m_1, and neutral molecular D_2 species with density n_{20} and mass m_2. The atomic and molecular physics interactions considered in the rate equation calculations are compiled in Table 4-1. The cross sections and reaction rates are taken from published sources and the references and details of the calculation can be found in work by Boris and Emmert[3].

Table 4-1. Atomic and molecular processes considered.

Process	Interaction	cross section or reaction rate
1. Ionization of D_2	$e + D_2 \rightarrow D_2^+ + 2e$	σ_1
2. Dissociation of D_2	$e + D_2 \rightarrow 2D + e$	σ_2, α_5
3. Ionization of D	$e + D \rightarrow D^+ + 2e$	σ_3
4. Dissociation of D_2^+	$e + D_2^+ \rightarrow D^+ + D + e$	α_4
5. Dissociative ionization of D_2	$e + D_2 \rightarrow D^+ + D + 2e$	σ_5
6. Dissociative recombination of D_2^+	$e + D_2^+ \rightarrow 2D$	α_1
7. Interchange reactions producing D_3^+ ions	$D_2 + D_2^+ \rightarrow D_3^+ + D$	α_2
8. Dissociative recombination of D_3^+ ions	$e + D_3^+ \rightarrow D_2 + D$	α_3

The rate equation model made the following predictions regarding the ion species mixture in the source region of the HOMER IEC device. Using the assumption that each species enters the sheath at their own Bohm velocity, the resulting ion mix is calculated to be 74% D_3^+, 22% D_2^+, 4% D^+ for the ion density in the source region, and 69% D_3^+, 25% D_2^+, 6% D^+ for the ion current extracted through the anode grid. This mixture changed slightly if it was assumed that the different ion species enter the sheath with the concentration weighted drift velocity referenced in equation 4-1, then the resulting ion mix is 71% D_3^+, 23% D_2^+, 6% D^+ for both the ion density and the extracted ion current. The choice for the assumption concerning the ion drift velocity at the sheath edge does not greatly affect the results; the D_3^+ ions dominate the ion mixture in the source region with both assumptions. Varying the parameters over reasonable ranges did not seem to make much difference to the basic conclusion that D_3^+ dominates the ion mix. The multi-

species ion acoustic wave measurements detailed below corroborated the finds of the zero dimensional rate equation model.

4.2 Theory of the Multi-species Ion Acoustic Wave

In order to experimentally measure the ion mixture in the source region, a method to measure the concentration-weighted reduced ion mass of the source plasma was devised by utilizing the characteristics of multi-species ion acoustic waves. Since the source region of the UW-IEC device consists of a filament-assisted DC discharge, the source plasma can be treated as a cold, non-magnetized plasma. By measuring the phase velocity of ion acoustic waves propagated in the source region, a concentration-weighted reduced ion mass can be obtained for the plasma, provided that the electron temperature of plasma is known. This measured, concentration-weighted reduced ion mass can then be compared with the predicted ion mass from the 0-dimensional rate equation calculation that generates the initial source region mix for the coupled integral equations above.

The general dispersion relation for ion acoustic waves in an *n* species plasma is given herein. For a general electrostatic wave in a collisionless, non-drifting plasma of *n* ion species, the dispersion relation is given by

$$1 = \frac{\omega_{pe}^2}{\omega^2 - (kv_{th,e})^2} + \sum_{j=1}^{n} \frac{\omega_{pj}^2}{\omega^2 - (kv_{th,j})^2} \qquad (4\text{-}2)$$

where the plasma frequency and thermal velocity of the *j*th ion species in the plasma is represented by ω_{pj} and $v_{th,j}$, respectively, and ω_{pe} and $v_{th,e}$ represents the plasma frequency

and thermal velocity of the electrons, respectively. The primary electrons produced by emission from the filaments have a much lower density than the thermal electrons, so we neglect them in the dispersion relation. If cold ions are assumed, then the dispersion relation simplifies to

$$1 = \frac{\omega^2{}_{pe}}{\omega^2 - (kv_{the})^2} + \sum_{j=1}^{n} \frac{\omega_{pj}^2}{\omega^2} \tag{4-3}$$

For ion electrostatic waves such as those considered here, the phase velocity of the wave, ω / k, will be significantly lower than the electron thermal velocity, $v_{the} = \sqrt{2kT_e / m_e}$; this allows Eq. (4-3) to be simplified to

$$1 = -\frac{\omega^2{}_{pe}}{(kv_{the})^2} + \sum_{j=1}^{n} \frac{\omega_{pj}^2}{\omega^2} \tag{4-4a}$$

which can be re-expressed as

$$1 + \frac{1}{(\lambda_D k)^2} = \sum_{j=1}^{n} \frac{\omega_{pj}^2}{\omega^2} \tag{4-4b}$$

Since the plasmas dealt with in the context of the IEC source region are filament-assisted DC discharge plasmas, where the Debye length, $\lambda_D = \sqrt{\varepsilon_o kT_e / ne^2}$, is on the order of 1mm, and the k of the propagated wave was typically 100 m^{-1}, the ratio $(\lambda_D k)^{-2} >> 1$. Thus we can re-express Eq. (4-4b) as follows,

$$\frac{1}{(\lambda_D k)^2} \approx \sum_{j=1}^{n} \frac{\omega_{pj}^2}{\omega^2} \tag{4-5}$$

This leads to the following real solution for the dispersion relation

$$\frac{\omega}{k} = \sqrt{\sum_{j=1}^{n} c_{sj}^2} \tag{4-6}$$

In this expression the terms $c_{sj} = \sqrt{n_j kT_e / n_e M_j}$ are the concentration-weighted ion acoustic velocities of the individual plasma species. The dispersion relation can be re-expressed in terms the square of the phase velocity v_{ph},

$$v_{ph}^2 = \sum_{j=1}^{n} n_j kT_e \Big/ n_e M_j \tag{4-7}$$

Consequently, a concentration-weighted reduced ion mass can be obtained from the phase velocity of the ion acoustic waves,

$$M_R = \frac{1}{\sum_{j=1}^{n} n_j \Big/ n_e M_j} = \frac{kT_e}{v_{ph}^2} \tag{4-8}$$

4.3: Experimental Method

The measurements of the concentration weighted reduced ion mass were performed in the source region of the HOMER IEC device using two techniques to measure the ion acoustic wave phase velocity. The first technique involves measuring

the group velocity and frequency of the ion acoustic wave. The phase velocity was then calculated from the wavenumber that is implied by the measured group velocity and wave frequency. The second technique involves directly measuring the frequency and wavenumber by sampling the plasma perturbation, induced by a continuous sine wave, at varying distances from the wave source. The first technique, the group velocity method, is less accurate but allowed for useful measurements when the cathode was in operation. The second technique is a more accurate method for measuring the ion acoustic wave but suffers from signal to noise difficulties when the cathode is operation.

4.3-a: Group Velocity Technique

The experimental setup for the group velocity technique is shown below in Figure 1. In this configuration a wave pulse on a 150 cm^2 excitation grid initiates a perturbation that travels through the plasma to the Langmuir probe. The time of flight of the perturbation between the probe and excitation grid is measured using the Tektronix oscilloscope, with the signal being heavily averaged to reduce high frequency noise. This technique measures the group velocity of the ion acoustic wave, shown below for an *n* species plasma.

$$v_g = \frac{d\omega}{dk} = \sqrt{\sum_{j=1}^{n} c_{sj}^2} \qquad (4\text{-}9)$$

Since the ion acoustic wave is a linear wave the group velocity and phase velocity are the same. Thus the phase velocity can be inferred from the measured group velocity. When using this technique it is important to restrict the amplitude of the excitation signal to less

than kT_e/e. This ensures that the wave will be linear, as pseudo-ion waves will propagate when this condition is exceeded.[5] This effect is illustrated in Figure 4.3-1. Note that when the kT_e/e is exceeded by the excitation signal the group velocity of the wave becomes non-linearly dependent on the excitation signals amplitude. Under these conditions the phase velocity of the wave can no longer be inferred from the group velocity.

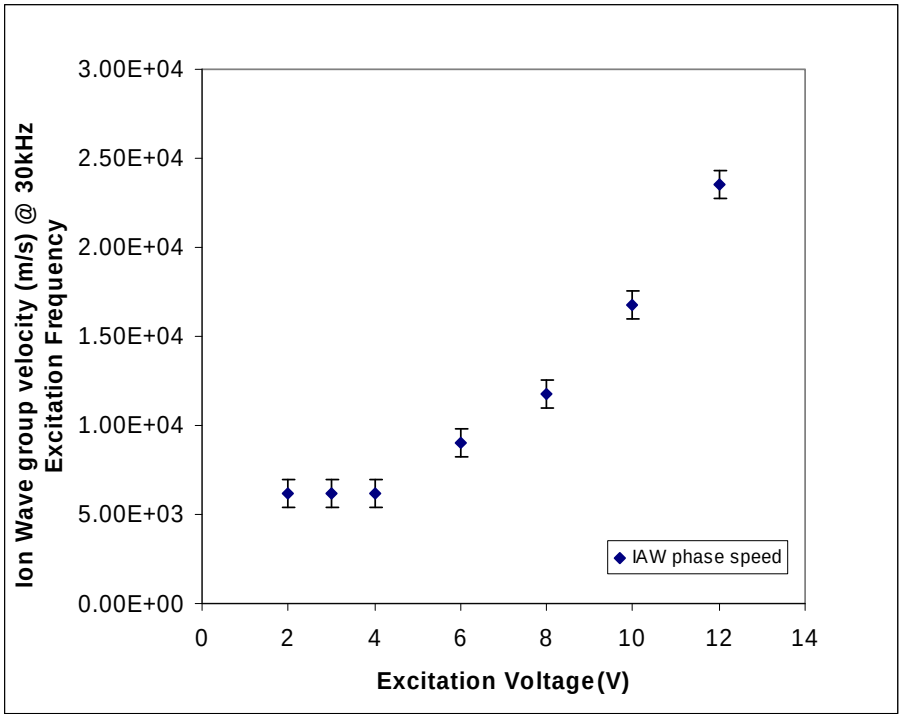

Figure 4.3-1: The above figure illustrates how the group velocity of the excited ion wave becomes non-linear at excitation voltages above kT_e/e. In this case kT_e was 2 eV - 3 eV.

The electron temperature is then measured using the Langmuir probe circuit shown in Figure 4.3-2b and thus the reduced weighted ion mass calculated. The difficulty with this technique stems from the possibility that the launch point of the wave pulse may be

substantially different from the position of exciter mesh. This leads to significant errors in v_g calculations based on the time of flight of the wave pulse.

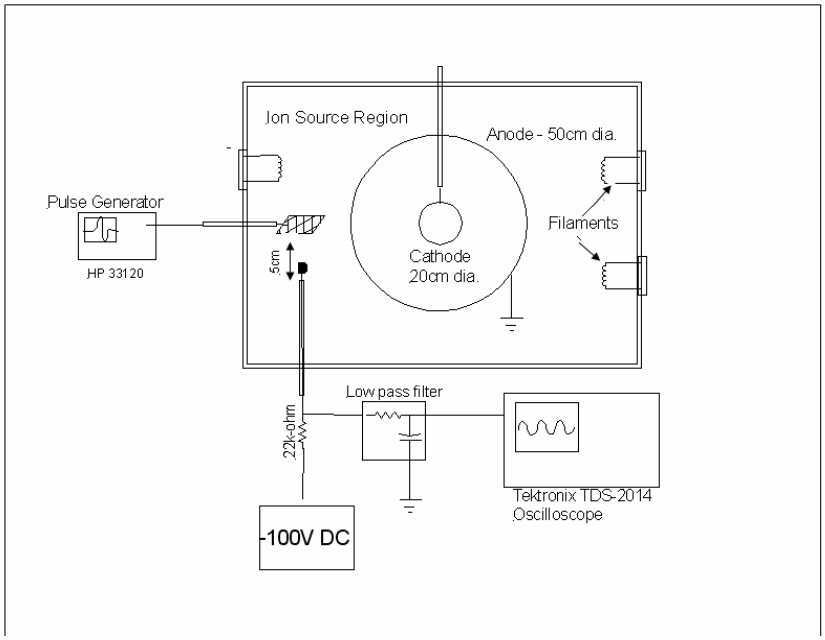

(a)

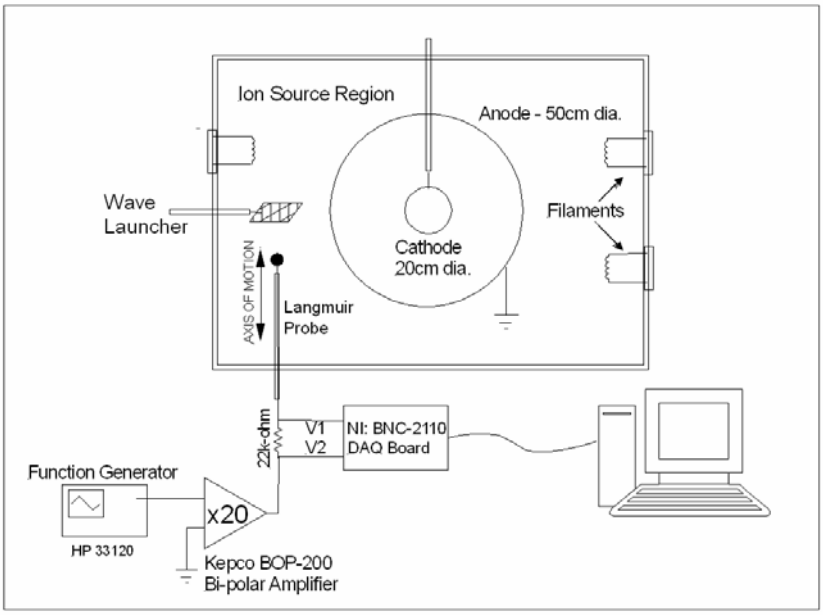

(b)

Figure 4.3-2: The above figure shows the experimental setup for (a) the measure of the received ion acoustic wave signal at 5cm from the pulsed wave source, and (b) the setup for measuring the electron temperature as a function of distance from the wave source.

The main advantage realized by utilizing the group velocity technique was the detection of ion acoustic waves with the cathode in operation. As will be discussed later, high voltage on the cathode perturbs the source region density such that it becomes so diffuse that it is difficult to detect the ion acoustic wave signal using the continuous wave method, which relies on a signal to noise ratio sufficient to measure the phase shift of the ion acoustic wave at varying distances from the wave generation source. The group velocity technique only requires a signal large enough for detection, allowing a relaxation of the signal to noise requirements.

4.3-b: Continuous Wave Technique

The high voltage system was not in operation during these experiments. This is because the potential from the cathode creates islands of negative potential within the holes in the anode grid. The islands act essentially like fingers of negative potential that reach into the source and perturb the nominally quiescent plasma that exists there in the absence of the high voltage on the cathode. These potential islands would substantially complicate the interpretation of ion acoustic wave data taken in the source region by locally perturbing the plasma potential and plasma density in the affected regions. In addition the cathode pulls ions from the source region, significantly reducing the overall plasma density in the source region, to the point where the signal to noise ratio for received ion acoustic waves becomes a concern.

The method used for obtaining a measurement of the concentration-weighted reduced ion mass is detailed below. A Langmuir probe, moveable along the designated

axis, can be used to sample the ion acoustic wave at varying distances from the excitation source, as shown in Fig. 4.3-3a.

(a)

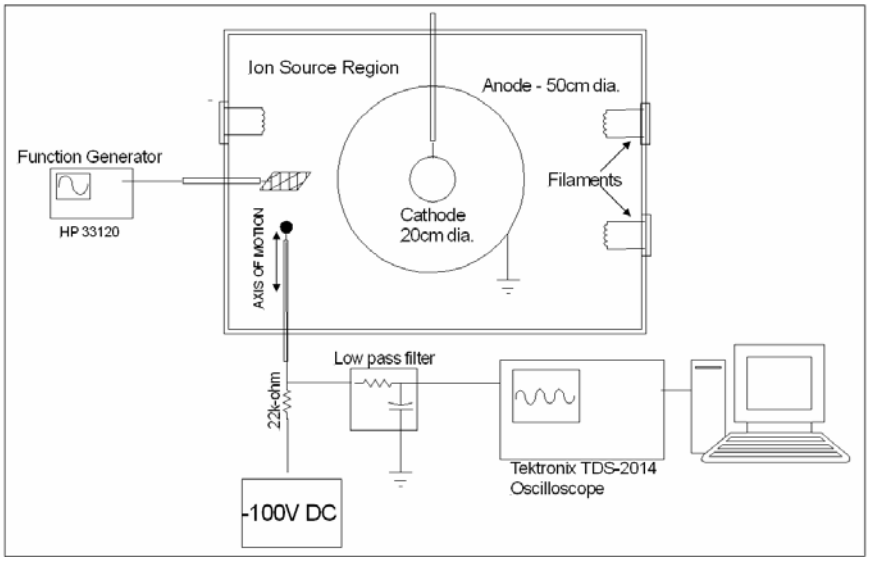

(b)

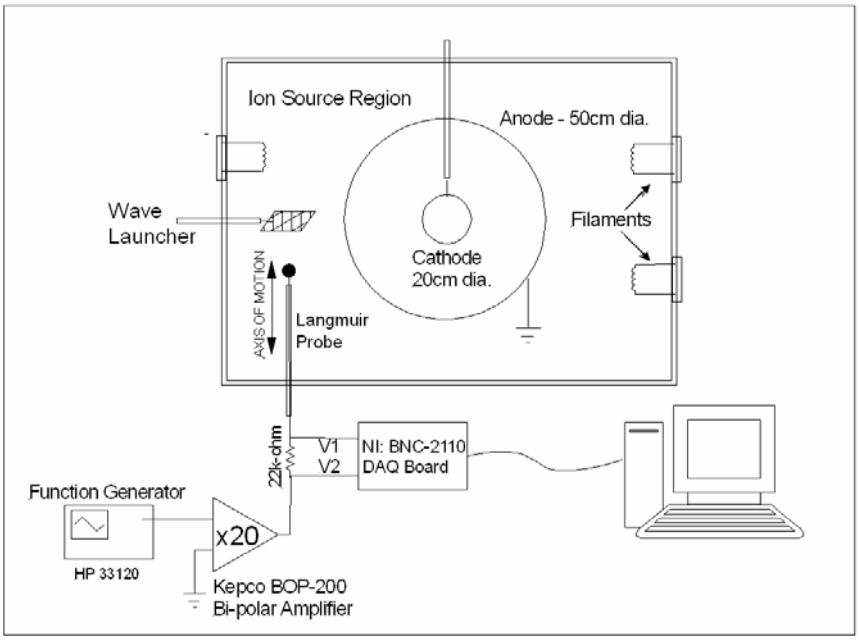

Figure 4.3-3: The above figure shows the experimental setup for (a) the measure of the received ion acoustic wave signal as a function of distance from the continuous wave source, and (b) the setup for measuring the electron temperature as a function of distance from the wave source.

The excitation source utilizes a continuous sine wave signal which is propagated through the plasma by a 150 cm^2 wave launcher made of a stainless steel mesh. Since the excitation signal is a continuous wave the received signal on the Langmuir probe will have a quantifiable phase shift from the source signal at varying distances from the wave launcher. This was done by holding the probe at a constant bias of -100 V and sampling the wave along the axis, as shown in Fig. 4.3-3a. By measuring the rate at which this phase shift changes with increasing distance from the excitation source the wave number, *k*, of the ion acoustic wave can be directly measured[6]. The oscilloscope used to analyze the received signal also provides the frequency of the ion acoustic wave, thus the phase velocity is easily calculated. The phase shift of the received signal from the excitation for varying distance from the wave launcher is plotted in Fig. 4.3-4.

In addition to sampling the ion acoustic wave signal, the Langmuir probe was also used to measure the electron temperature at varying distances from the excitation source. The experimental setup for measuring the electron temperature is shown in Figure 4.3-3b. In order to reduce noise on the received signal the received waveform is first sent through a low pass RC filter. In addition to the low pass filter, a 128 trace average of the received signal is taken using a Tektronix TDS-2014 Oscilloscope. This serves to further reduce high frequency components in the signal. With a direct measurement of the phase velocity of the ion acoustic wave the concentration-weighted reduced ion mass can easily be obtained.

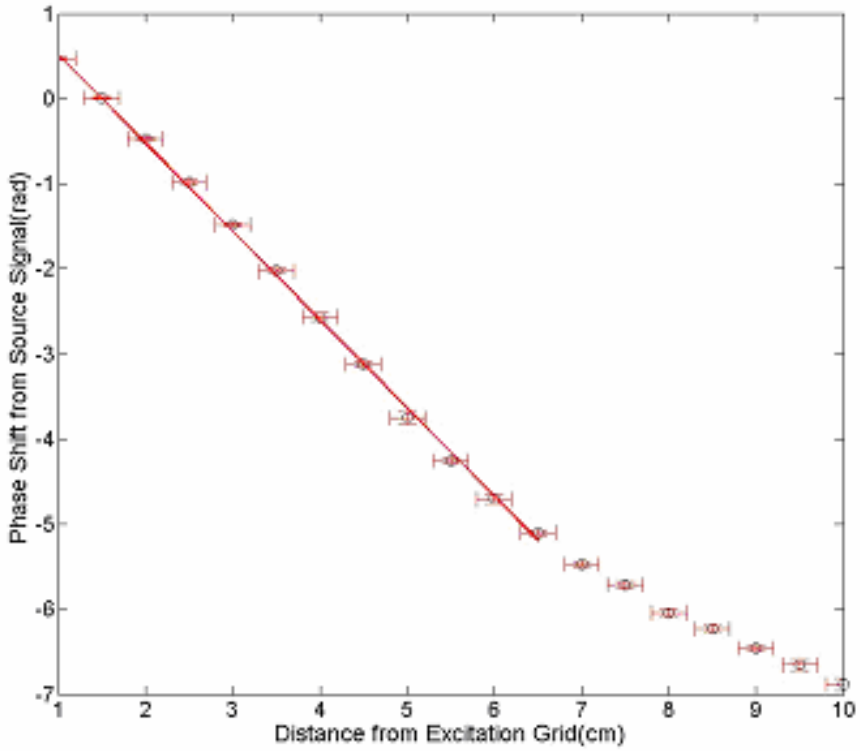

Figure 4.3-4: The above data corresponds to the phase shift of a 100 kHz wave moving through a plasma with a nominal electron temperature of 2.7 eV. This leads to a calculated weighted reduced ion mass of 5.9 amu ±0.5 amu. The neutral gas pressure for this data set was 3.0 mTorr.

4.4: Experimental Results and Comparison to Theory

4.4-a: Continuous Wave Technique Results

From the phase velocity of the wave and measured electron temperature in the IEC source region a concentration-weighted reduced ion mass can be calculated using Eq. (4-8). Fig. 4.4-1 shows the variation of M_R with neutral gas pressure and electron temperature. The measured values are compared with the M_R values predicted from the ion concentrations calculated by the rate equation model described in Sect. II. The comparison is generated by using the measured parameters of filament bias, electron temperature, and neutral gas pressure from the experimental data points as inputs into the rate equation calculation. Two versions of the rate equation calculation were executed;

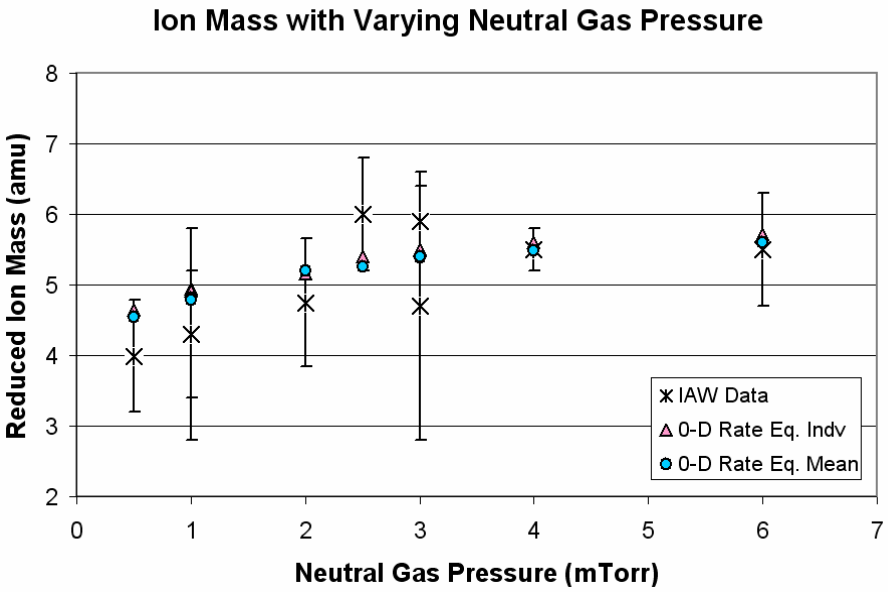

(a)

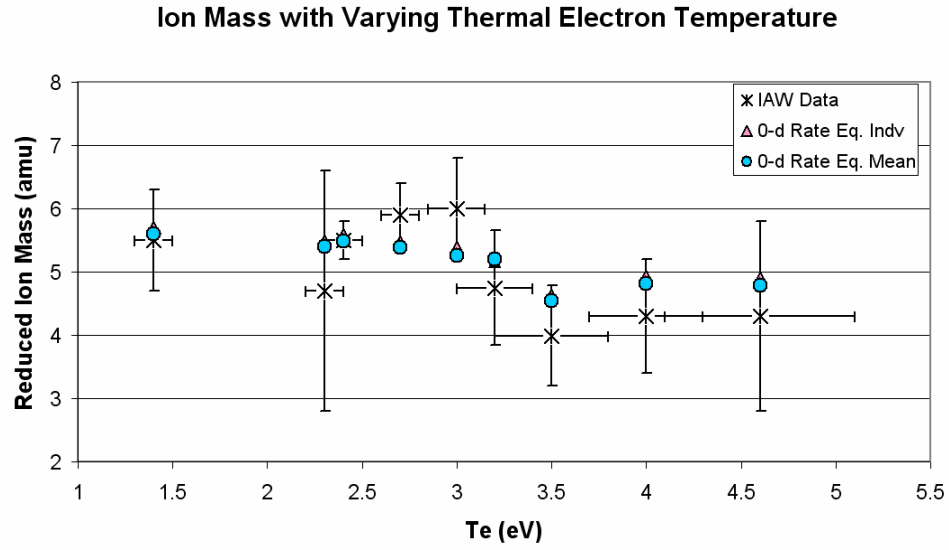

(b)

Figure 4.4-1: Comparison of experimental and theoretical concentration-weighted reduced ion mass. (a) At low neutral gas pressure the ion species mix contains a significant fraction of D_2^+, whereas at high neutral gas pressure D_3^+ is the dominant ion type. (b) low electron temperature plasmas contain mostly D_3^+; the fraction of D_3^+ is reduced as the electron temperature increases.

the first version assumed molecular ion flow out of the source plasma at the ion sound speed of the individual ion species. The second version assumed ion flow out of the source plasma at the concentration-weighted mean ion acoustic velocity, as indicated in

the work by Hershkowitz and co-workers[7]. In both cases the calculated ion species concentrations were used to determine the concentration-weighted reduced ion mass for comparison to the measured values. The error in the measured values is due primarily to the error in the v_{ph} measurement in conjunction with the error in the measurement of kT_e. In general, the agreement between the rate equation analysis and experiment was quite good at lower electron temperatures and high neutral gas pressures. The calculated values fell within error of the experiment for most measurements and the calculated molecular ion concentrations were generally able to reproduce the trends observed in the experimental data. In general, the M_R of the source plasma was larger (nearer to 6 amu) at low electron temperature and high neutral gas pressure, and smaller (nearer to 4 amu) at high electron temperature and low neutral gas pressure. It is reasonable to infer that the higher M_R values correspond with conditions conducive to high concentrations of D_3^+ ions. Conversely the lower M_R values correspond to conditions where more evenly distributed mixtures of D_3^+, D_2^+, and D^+ ions are present.

Khachan and Collis[8] have measured H_2^+ and H_3^+ in an IEC device operating on hydrogen; their measurements yielded a mixture of 20% H_3^+ in the cathode region. We expect that the fraction of H_3^+ in the cathode region will be significantly reduced by collisional attenuation between the source region and the cathode region, so their results are not in disagreement with our results.

4.4-b: Group Velocity Results

Using the group velocity technique described above approximate measurements of the weighted reduced ion mass in the IEC source were obtained with the cathode in

operation. This is the main advantage of the group velocity technique. Since it only requires the experimenter to be able to detect a pulse perturbation using the Langmuir probe receiver. This is much easier than having to resolve the wave characteristics of the received signal on the Langmuir probe, as is the case in the continuous wave technique. The measured values of M_R for varying electron temperature in the IEC source region are shown in Figure 4.4-2. The figure compares measurements taken with and without a multipole magnet configuration around the HOMER IEC device. As described in the section on the multipole configuration, the magnets allow for more effective use of the primary electrons off the filaments, thus leading to higher plasma densities and consequently lower electron temperatures.

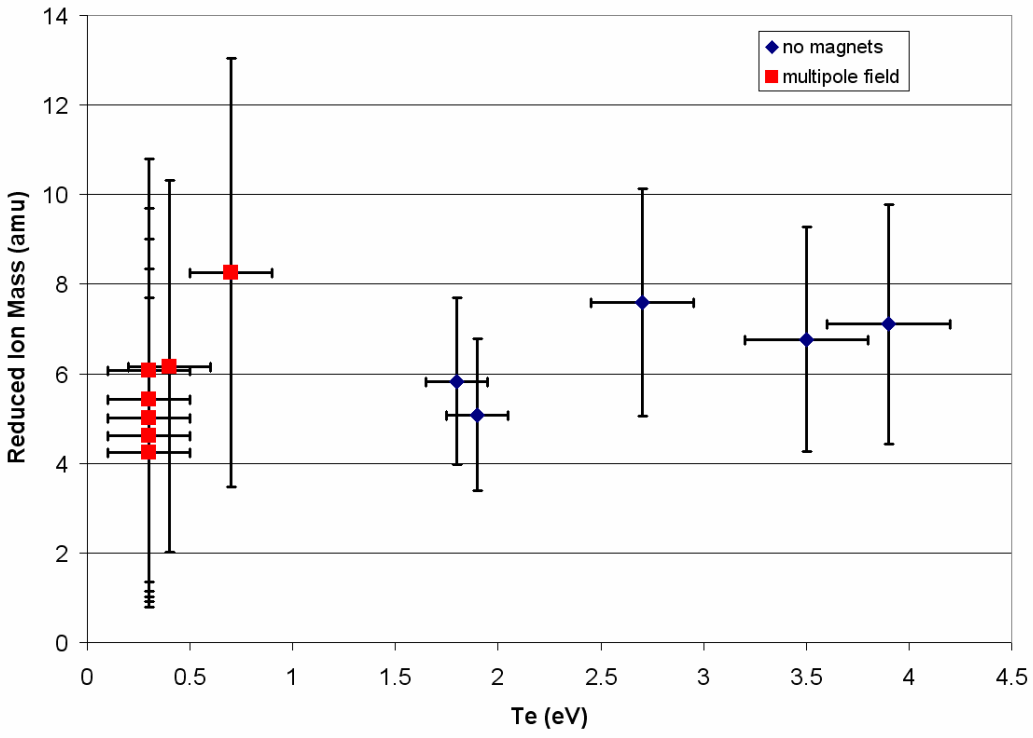

Figure 4.4-2: This figure shows how the variance of the electron temperature in the source region affects the measured weighted reduced ion mass. The higher degree of uncertainty in the data stems from the uncertainty in the propagation distance of the wave pulse. This was assumed to be ±5mm.

Figure 4.4-3 shows the measured values of M_R for varying cathode voltages. The cathode current in this case was held constant at 30mA. Above 70kV the source region plasma density was too depleted to measure the ion acoustic wave perturbation. Nonetheless the data indicates that the source region remains largely D_3^+ even with the cathode in operation.

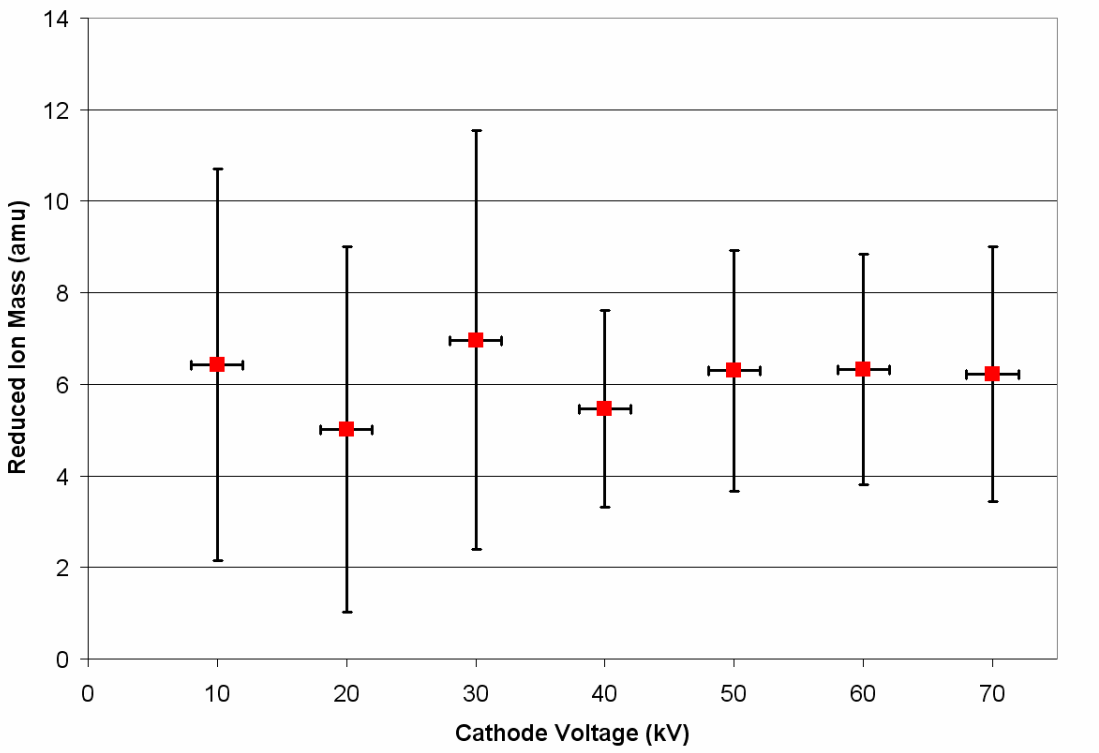

Figure 4.4-3: This figure shows the dependence of the weighted reduced ion mass with cathode voltage at 30mA cathode current. Once again the uncertainty stems from the ±5mm uncertainty assumed in the propagation distance of the wave pulse.

Admittedly, however, the uncertainty in these measurements is significant, on the scale of ±3 amu. The data is useful in that it gives some idea as to the composition of the IEC source region during operation of the device. Langmuir probe measurements confirmed

that the electron temperature of the source plasma did not change appreciably with the cathode in operation. Since the plasma parameters in the source region do not change drastically with the addition cathode voltage, it is reasonable to assume that the results from the continuous wave technique should apply to the source conditions when the IEC is in operation. Since the group velocity data is not perceptibly different from the continuous wave results, the conclusions drawn from comparing the 0-d rate equation calculation to continuous wave data can, with reasonable confidence, be carried over to source region conditions with the cathode in operation.

4.5: Conclusions

Generally the source region of the IEC device is made up of mostly D_3^+ ions with minority contributions from D_2^+ and D^+ ions. This mixture is maintained both with and without the cathode in operation. Rate equations have been used to determine the ion species mix in the source region of IEC devices. Experimental measurements of the concentration-weighted reduced ion mass in the UW-IEC device are reasonably consistent with those calculated from the ion species mix obtained from the rate equation analysis. Thus we find the rate equation model to be a good predictor of the source plasma conditions during normal high voltage operation of the UW-IEC device. Quantitative knowledge of the species composition of the ions leaving the source region and entering the intergrid region is important for understanding the molecular processes occurring in the intergrid region, the composition and energy spectrum of the fast ions near the cathode, the generation of fast neutral atoms and molecules by charge exchange processes, and the resulting fusion reaction rate. Changes to the source region that modify

the ion species composition offer the possibility of improving the performance of IEC devices.

Chapter 4 References

[1] A. M. Hala and N. Hershkowitz, "Ion acoustic wave velocity measurement of the concentration of two ion species in a multi-dipole plasma", *Rev. Sci. Instr.* 72, 5, 2279 (2001).

[2] H. Ikezi, Y. Kiwamoto, and K. E. Longrenn, "Ion acoustic wave response to an impulse disturbance", *Plasma Physics*, 15, 1141-1147 (1973)

[3] D. R. Boris and G. A. Emmert, "Composition of the source region plasma in inertial electrostatic confinement devices", *Physics of Plasmas*, 15, 083502 (2008)

[4] D. Lee, N. Hershkowitz, and G. Severn, "Measurements of Ar^+ and Xe^+ velocities near the sheath boundary of Ar–Xe plasma using two diode lasers", *Appl. Phys. Lett.* 91, 041505 (2007).

[5] I. Alexeff, and W. D. Jones, "Pseudowave Excitation in Plasmas Via a Grid", *Physical Review Letters*, 21, 13, (1968)

[6] X. Wang and N. Hershkowitz, "Two species ion flow in the plasma pre-sheath", *Phys. Plasmas* 13, 053503 (2006).

[7] D. Lee, L. Oksuz, and N. Hershkowitz, "Exact Solution for the Generalized Bohm Criterion in a Two-Ion-Species Plasma", *Phys. Rev. Lett*. 99, 155004 (2007)

[8] J. Khachan and S. Collis, "Measurements of ion energy distributions by Doppler shift spectroscopy in an inertial-electrostatic confinement device", *Phys. Plasmas* 8, 1299 (2001).

Chapter 5: Fusion Ion DOppler Shift Diagnostic (FIDO)

5.1 Previous Work

Charged particle detectors have been an important diagnostic tool in IEC research for nearly two decades. The first use of this diagnostic was by Nadler[1] at what is now Idaho National Lab, to measure potential structures with in an IEC device with a collimated proton detector. Thorson used a similar technique to map the fusion reaction profile in the IEC device at the University of Wisconsin – Madison[2]. Thorson's work was the first to indicate that the vast majority of D-D fusion taking place in the UW-IEC device was the result of interactions between fast neutrals from charge exchange and background gas. A schematic of Thorson's experimental setup and a sample data set are shown in Figure 5.1-1. Using an Abel inversion Thorson was able to calculate that over 75% of the fusion events are distributed over the volume of the IEC device rather than within the core.

Thorson's work was followed on by Ashley, Cipiti, and Murali[3, 4] at the University of Wisconsin-Madison who used a charged particle detector to further diagnose the source regimes in an IEC device. Their approach involved using a large, 1200 mm^2, charged particle detector in conjunction with movable eclipse discs of varying sizes to determine the contribution to the total fusion rate of varying sections of the UW-IEC device.

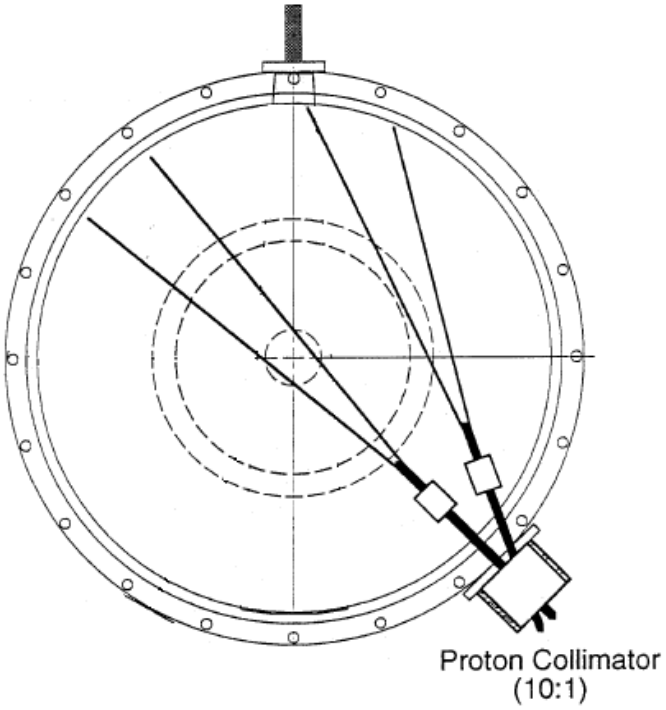

(a)

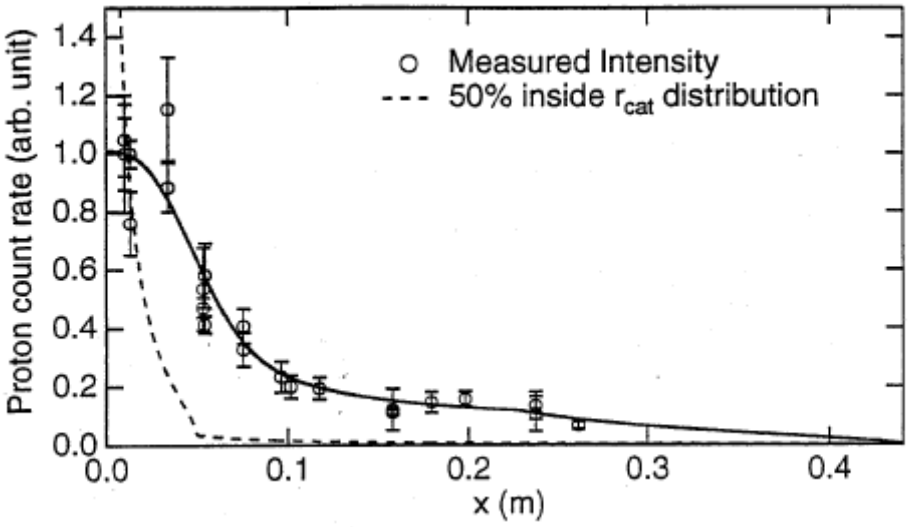

(b)

Figure 5.1-1: (a) Diagram of Thorson's experimental setup (b) collimated proton detector measurements at varying radii within the UW IEC device[2].

The eclipse disc experiments, shown in Figure 5.1-2, illustrated the significant difference between the source regimes for D-D and D-^{3}He fusion. By the varying the position and size of the eclipse disc the contribution to the total fusion rate from volume

source reactions, core reactions, and embedded fusions in the grid wires was determined. The contributions from these distinct source regimes for D-D and D-^{3}He fusion are shown in tables 5.1-1 and 5.1-2.

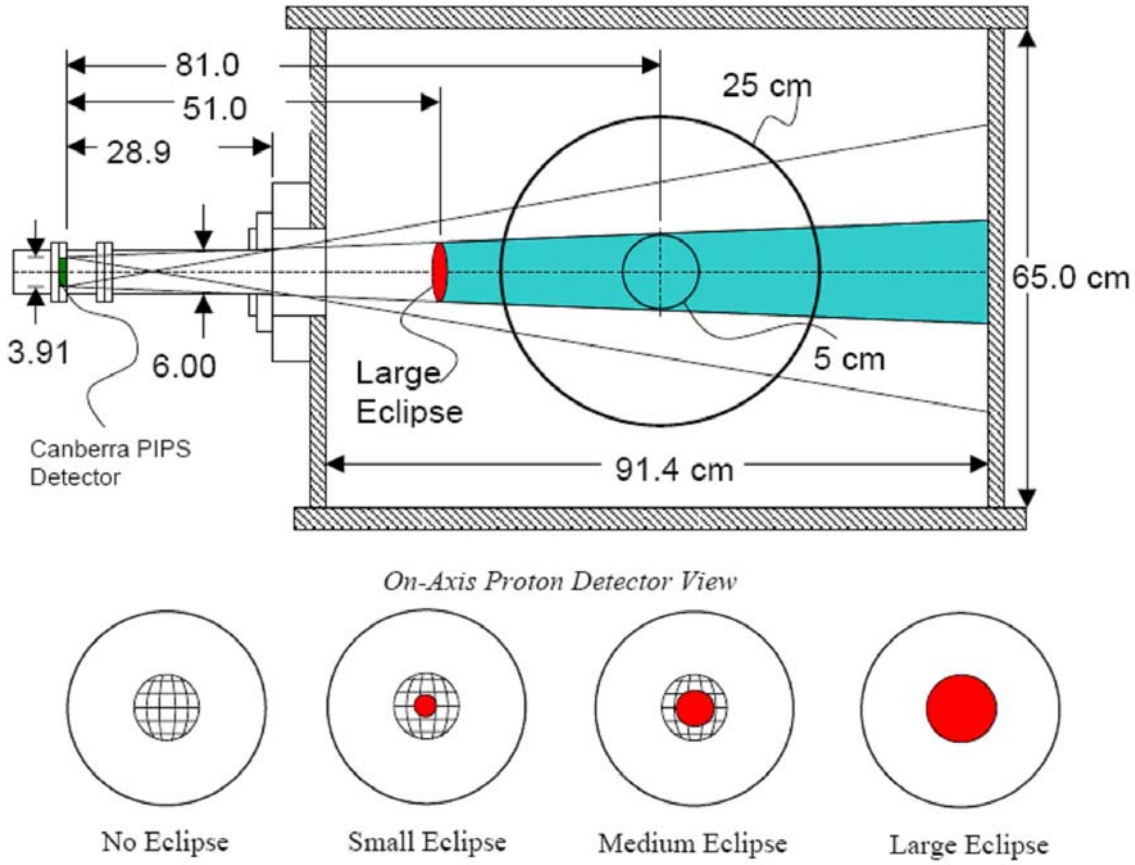

Figure 5.1-2: The eclipse disc diagnostic shown with varying eclipse disc sizes[4].

	Converged Core	Embedded	Volume
Raw Counts	74%	14%	12%
Total Rate	22%	8%	70%

Table 5.1-1: Results of eclipse disc and off-axis experiments on D-D fusion reaction including raw counts collected in solid angle view of detector and the corresponding contribution from total fusion reactions in entire device[4].

	Converged Core	Embedded	Volume
Raw Counts	10%	90%	Negligible
Total Rate	5%	95%	Negligible

Table 5.1-2: Results of eclipse disc and off-axis experiments on D-^{3}He fusion reactions including raw counts collected in solid angle view of detector and the corresponding contribution from total fusion reactions in entire device[4].

The work done by Thorson and by Ashley, Cipiti, and Murali used charged particle detectors to make significant contributions to the understanding of where fusion reactions occur within the IEC for two different fuel cycles. Similar work has also been performed by Masuda, Fujimoto, and Yoshikawa[5 6] at Kyoto University in Japan. The remainder of this chapter will focus on using charged particle detectors to obtain the energy spectra of the fusion reactants within the IEC, a previously unperformed study.

5.2: Theory of Fusion Product Doppler Shift

When nuclear fusion occurs between two deuterium nuclei the D(d,p)T branch of the reaction produces a 3.02 MeV proton and a 1.01 MeV triton due to the 4.03 MeV Q value of the reaction. However, these energies are will be shifted by kinetic energy of the center of mass of the deuterium reactants, plus a small contribution from the kinetic energy that goes into to the fusion event. In the IEC experiment the detected protons and tritons from D-D fusion carry with them a Doppler shift resulting from the center of mass energy of the deuterium reactants.

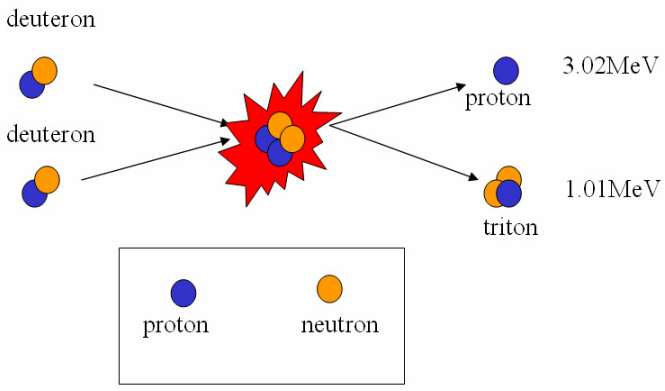

Figure 5.2-1: Representation of the D(d,p)T Fusion Reaction

Most of the fusion events that occur in the HOMER device occur between a fast ion or fast neutral and a neutral deuterium molecule that is part of the background gas pressure in the device. Thus the manner in which the center of mass velocity of the deuterium reactants is added to the velocity of the fusion products follows the law of cosines. The velocity imparted to the fusion product from the Q value of the fusion reaction, plus a small correction for the reacting ion energy, is denoted v_f. The velocity imparted to the fusion product from center of mass velocity of reacting particles is denoted, v_{cm}. The total velocity of the fusion product is denoted v_t, and the angle between v_{cm} and v_f is denoted Θ.

$$v_t = \sqrt{v_f^2 + v_{cm}^2 \pm 2 v_{cm} v_f \cos\Theta} \qquad (5\text{-}1)$$

The addition of v_{cm} and v_f in this manner creates a sphere of possible v_t values where each variation of the angle Θ creates a differential ring in velocity space of thickness $2\pi v_{cm} \cos\Theta\big|_{\Theta}^{\Theta+\Delta\Theta}$. A vector diagram of this is shown in Figure 5.2-2. The area of the ring traced out in velocity space by varying Θ is proportional to the number of reactions that have that geometrical orientation of v_{cm} and v_f. Hence there will be comparatively fewer particles with parallel and anti-parallel v_{cm} contributions and more with perpendicular orientations. A simulated spectrum of D-D fusion protons from a mono-energetic beam of deuterium impacting immobile deuterium neutrals is shown in Figure 5.2-3.

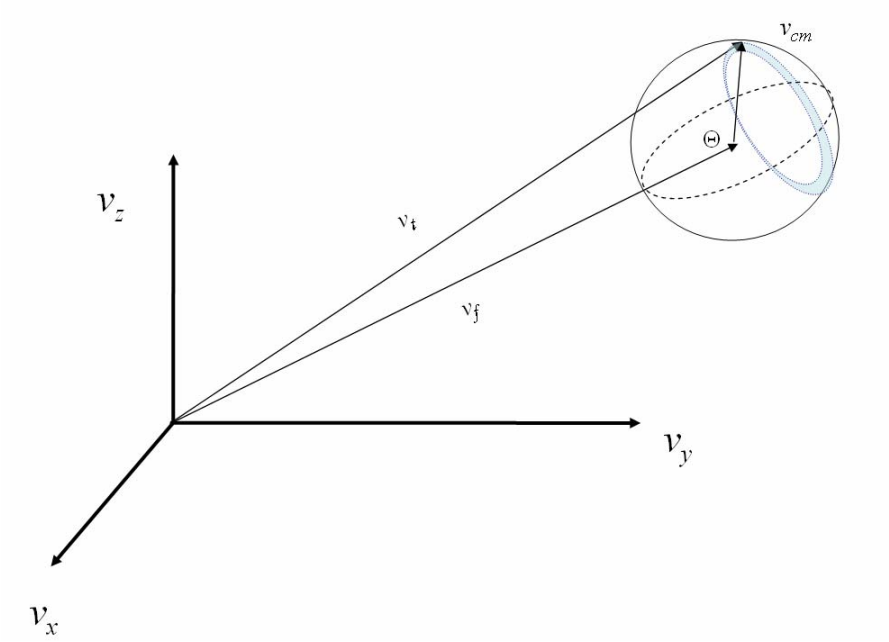

Figure 5.2-2: This illustrates the sphere in velocity space traced out by the v_t velocity vector of the fusion product. It also shows how each specific angle of Θ creates a differential ring on the velocity sphere. This implies, geometrically, why there will be fewer fusion products with parallel and anti-parallel Doppler shifts from the center of mass velocity of the reactants.

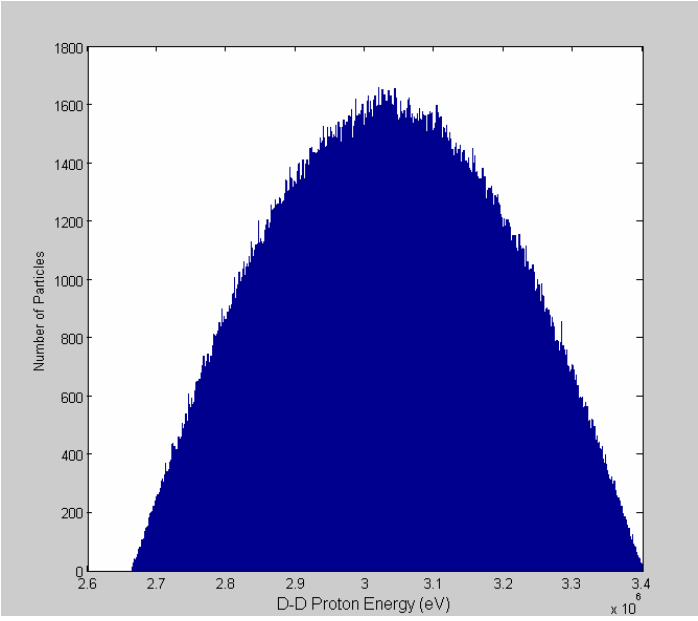

Figure 5.2-3: This represents a hypothetical distribution of D-D fusion protons from a mono-energetic deuterium beam with 90keV of energy incident on a cold background population of deuterium.

This special case illustrates how the proton energy distribution forms a cosine distribution with bounds defined by:

$$v_t = \sqrt{v_f^2 + v_{cm}^2 \pm 2 v_{cm} v_f} \qquad (5\text{-}2)$$

For a real IEC system, v_{cm} will not be a single value but instead take the form a distribution of velocities due to the atomic and molecular physics interactions that take place between the accelerated ions from the source region and the neutral gas that fills the IEC vacuum vessel. Because ions and fast neutrals within the IEC will have energies ranging from thermal energies up to the cathode energy, a description of the distribution of v_{cm} is far more difficult. The v_{cm} distribution function is further complicated because the distribution will almost certainly vary with radius throughout the IEC device. Since the cross section for D-D fusion is a function of the center of mass energy between reacting deuterium nuclei, the number of fusion events will vary as a function of radius from the center of the potential as well. Formalism for this problem is introduced in the publication[7] [8] that details the molecular version of Emmert and Santarius' integral equation code for calculating fusion rates inside the HOMER IEC device. The reader is directed to this work if a more in-depth description of the radial variation of fusion rates in an IEC is desired.

A simpler problem has been addressed in the next section. By applying an integral equation code developed by Emmert and Santarius the fast deuterium energy distribution at the HOMER cathode has been obtained. Fusion proton spectra were then

generated using a Monte Carlo technique which sampled from the calculated deuterium energy distribution and known D-D fusion cross sections.

5.2-a: Predictions of D-D Fusion Product Spectra Using a Monte Carlo Method

To utilize the Monte Carlo method a probability distribution function for the occurrence of a particular phenomenon is required. In the case described above, where a 0-d mapping between an energy distribution of fusion reactants, to a corresponding fusion products energy distribution is sought, it is necessary to know the probability of a fusion reactant's energy being in the range *[E, E+ΔE]*, and to know the probability of fusion for a particle in the afore-mentioned energy range. The source code is available in Appendix A of this thesis.

A probability distribution function, *p(x)*, is a measure of the relative likelihood of observing *x*. For example, the likelihood of observing a deuterium ion within an IEC device having energy between *[E, E+ΔE]*, can be described by a probability distribution function *p(E)*. Generally *p(x)* is normalized such that:

$$\int_{x\min}^{x\max} p(x)dx = 1 \qquad (5\text{-}3)$$

Here *x max* and *x min* define the domain of interest for the occurrence of phenomenon *x*. For Monte Carlo applications, the normalized probability distribution function must be integrated to present the cumulative distribution, *c(x)*, defined by:

$$c(x) = \int_{x\min}^{x} p(x')d(x') \qquad (5\text{-}4)$$

By the definition of *p(x)*, the range of *c(x)* will always fall between 0 and 1. Thus, by inverting *c(x)* (interchanging the domain and range) a sampling function is obtained for use with a random number generator. Using this sampling function to evaluate a random number between 0 and 1 (defined by the variable *rnd*) will give back a value between *x max* and *x min.*

$$x = c^{-1}(rnd) \tag{5-5}$$

An example of this progression from *p(x)* to a sampling function is illustrated below, with a hypothetical deuterium ion spectrum, in Figures 5.2-4 through 5.2-5.

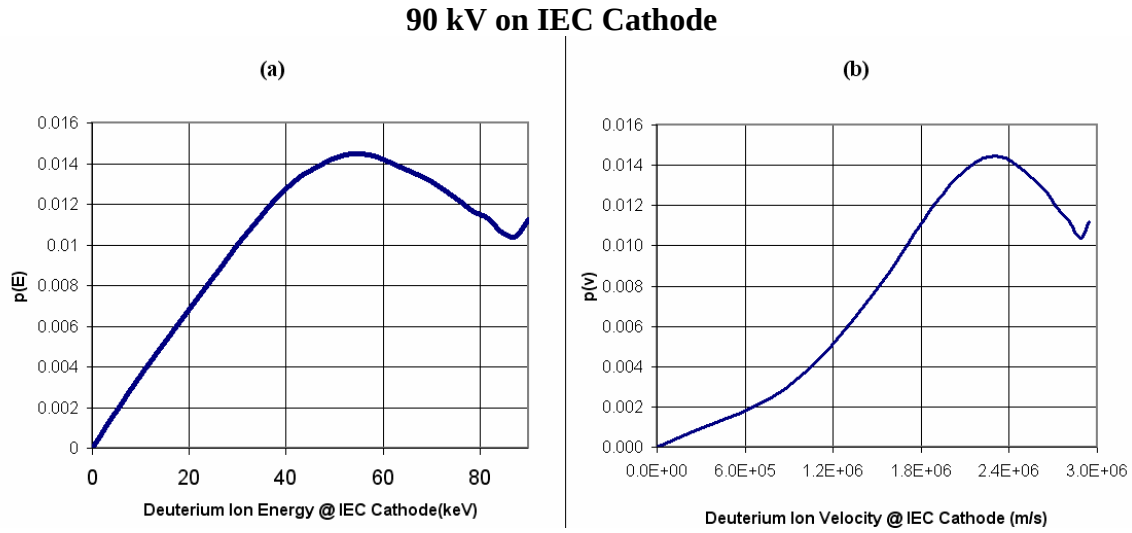

Figure 5.2-4: (a) p(E) is the probability distribution function for deuterium ion energy as simulated by the atomic version of Emmert & Santarius' integral equation code. (b) p(v) is the probability distribution function for deuterium velocity as simulated by the atomic version of Emmert & Santarius' integral equation code.

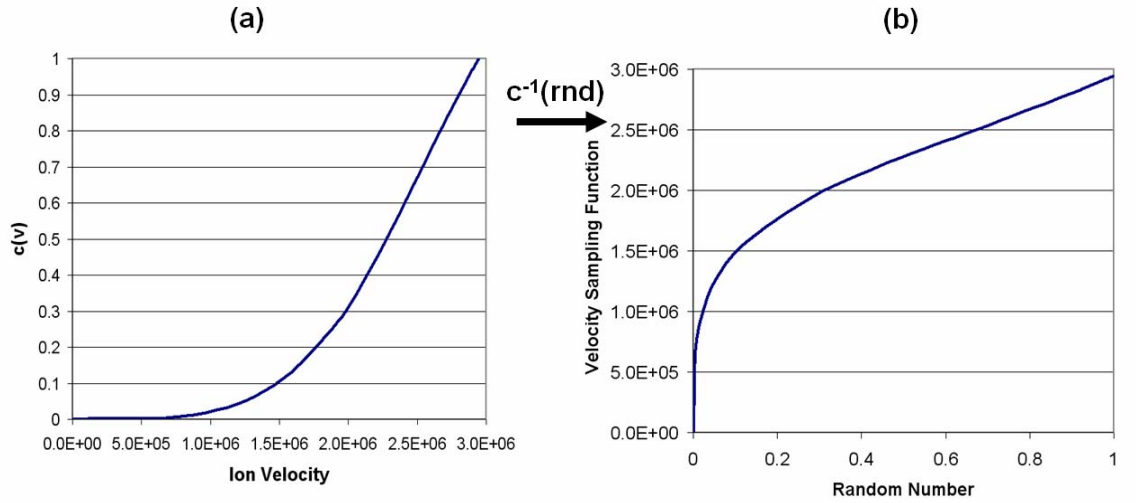

Figure 5.2-5: (a) shows the cumulative velocity distribution function for p(v) from Figure 5.2-4. (b) shows the velocity sampling function found by inverting c(v).

By supplying random numbers to the sampling function $c^{-1}(rnd)$ a reproduction of the structure of *p(x)* can be achieved, at least to within the statistical error inherent to number of samples taken.

In situations where the cumulative distribution function is not easily inverted one can resort to a technique known as the *rejection method.* In this case random number generators are scaled to produce random values between $xmin \leq rnd(1) \leq xmax$ as well as between $0 \leq rnd(2) \leq max(p(x))$. If $rnd(2) \leq p(\cdot rnd(1))$ then the event is counted as occurring at the prescribed value of *x*, otherwise, the event is rejected. This is not as efficient as inverting a cumulative distribution function, but it can be useful when the inversion is non-trivial.

These techniques have been applied to the atomic version of the integral equation code written by Emmert and Santarius to describe the behavior of deuterium between the HOMER anode and cathode. Using the above Monte Carlo techniques, probability distribution functions for both the deuterium energy spectrum and the fusion cross section

predicted the proton energy distribution created by the deuterium energy distribution from Figure 5.2-4. Figure 5.2-6 illustrates the result of the Monte Carlo calculation.

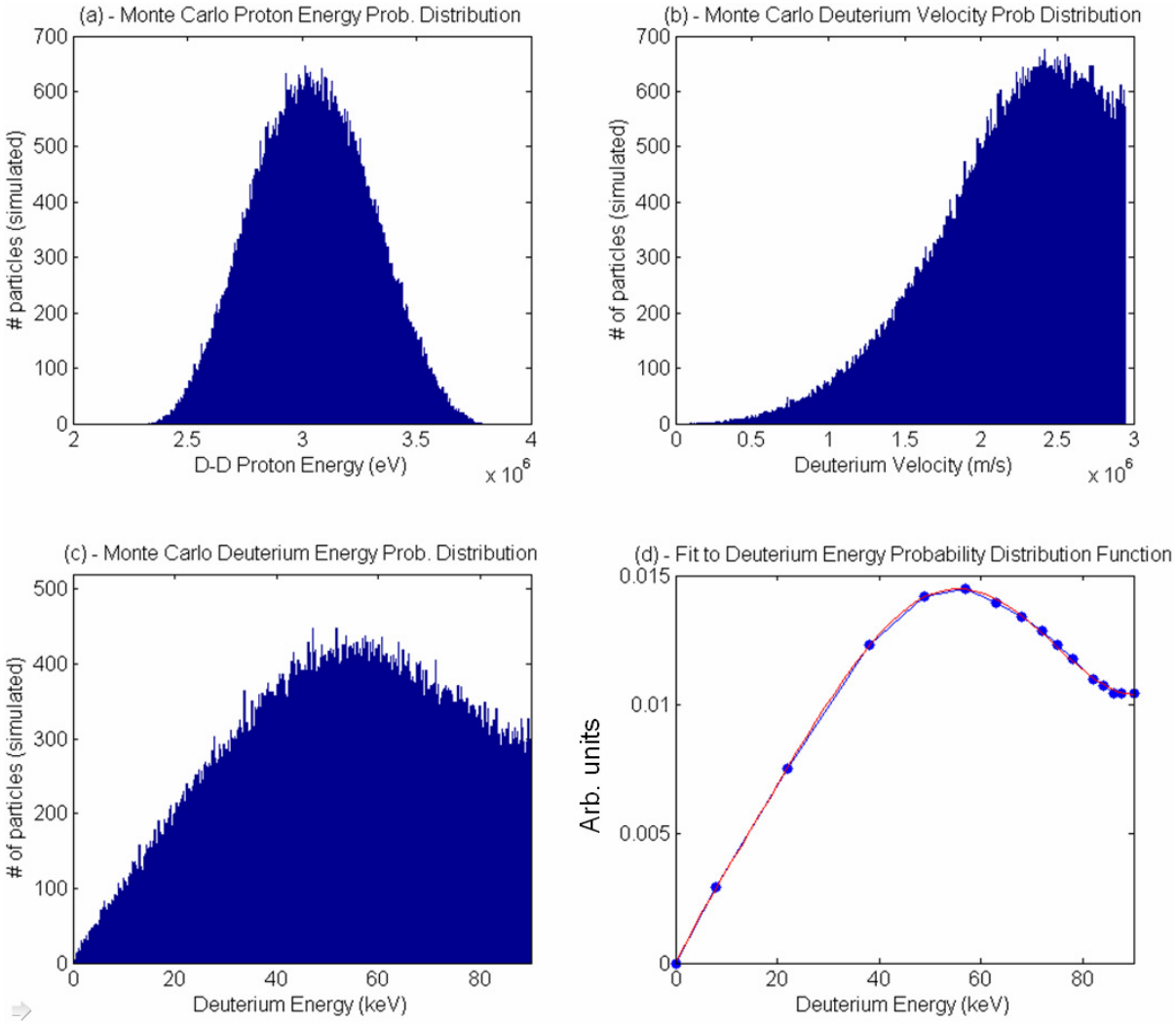

Figure 5.2-6: (a) The proton energy distribution resultant from the deuterium energy spectrum in Figure 5.2-4. (b) Monte Carlo calculated deuterium velocity spectrum (c) Monte Carlo calculated deuterium energy spectrum (d) fit to the deuterium energy spectrum at the HOMER cathode generated by the atomic version of the Emmert & Santarius integral equation code. [7]

As evidenced by a comparison of figures 5.4-4 (a) & (b) to 5.4-5 (c) & (d), the Monte Carlo calculation very accurately mimics the deuterium spectrum generated by the atomic version of the integral equation code. The resulting proton energy distribution also seems

reasonable, as its shape compares well with experimental results from the proton detector installed on the HOMER IEC device.

The FIDO diagnostic discussed later in this thesis constrains the view factor of a silicon charged particle detector to allow only parallel and anti-parallel contributions from the center of mass velocity of reactants to be detected. Simulation of this effect appears in Figure 5.2-7 and again shows good agreement with experimental measurements from the FIDO diagnostic.

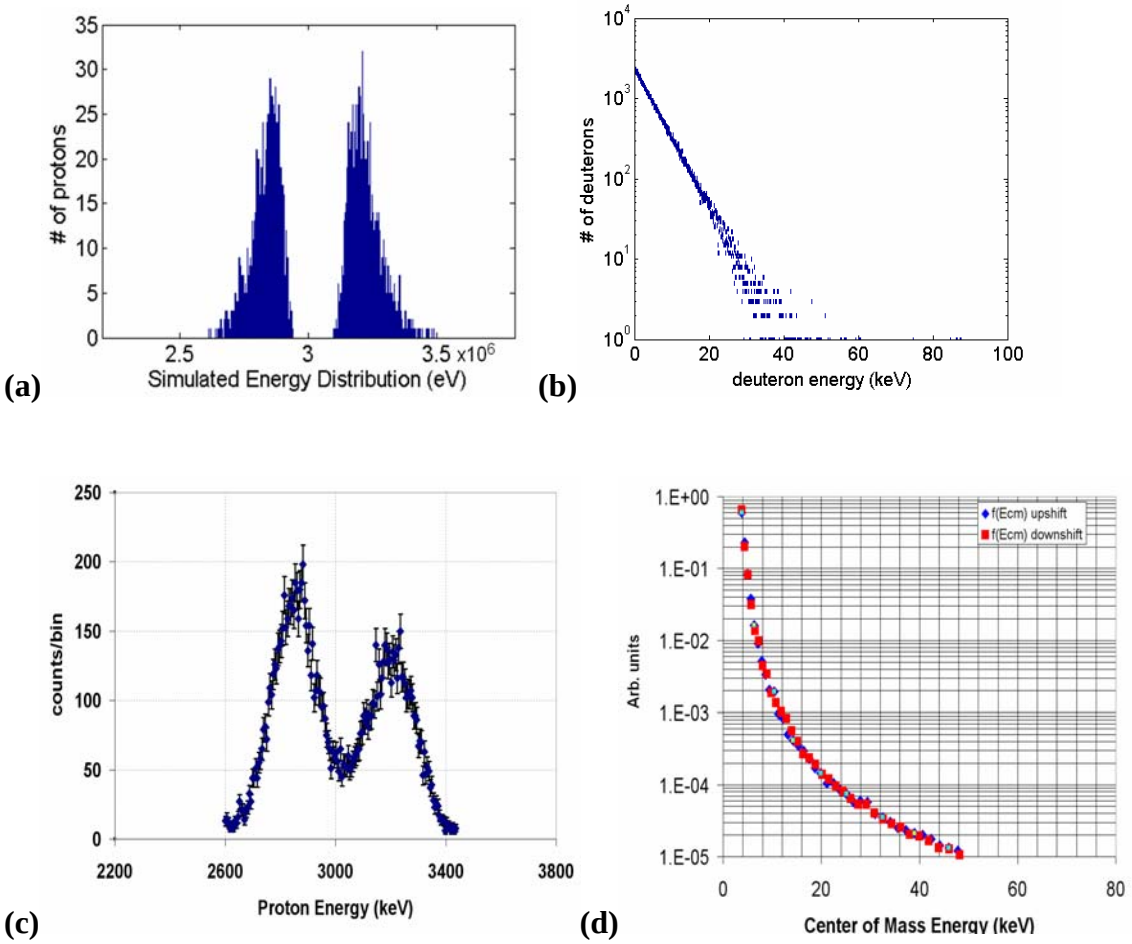

Figure 5.2-7: Shows (a) proton energy distribution resultant from (b) the given deuteron energy distribution. In addition the only parallel and anti-parallel contributions from the center of mass energy of the reactants have been allowed to contribute to the proton spectrum. This yields double peaked structure shown in (a). Raw data from the FIDO diagnostic (c) corresponds well with the modeled distribution. The distribution shown in (d) is derived from the raw data in (c).

5.3: Experimental Setup of the Fusion Ion DOppler Shift Diagnostic (FIDO)

As evidenced by the Monte Carlo calculation in the previous section, the center of mass velocity of fusion reactants imparts a significant shift to the velocity and likewise the energy of detected fusion products. Unfolding the magnitude of the energy shift is complicated, however, by the random orientation of the angle between v_{cm} and v_f vectors. This problem can be solved geometrically however, and it is greatly simplified by the predominantly radial directionality of the deuterium ions and fast neutrals in an IEC system. By constricting the view of the charged particle detector observing the fusion product ions to a very narrow column through the IEC device, the parallel and anti-parallel components of the velocity sphere in Figure 5.2-2 can be isolated from the rest of the fusion product spectrum (See Figure 5.3-1). Constricting the view factor of the detector achieves this by narrowing the acceptance cone of the detector to the point where fusion products with significant perpendicular velocity components will not make it to the detector.

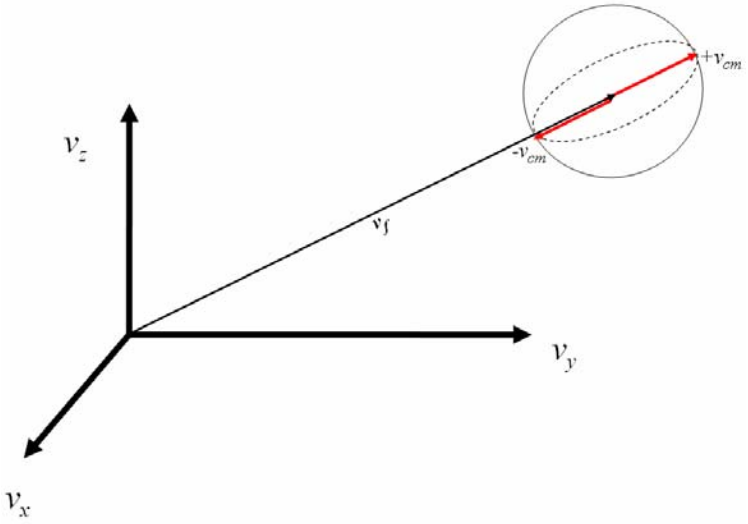

Figure 5.3-1: The parallel and anti-parallel components of the total velocity vector of a fusion product

A schematic of the actual experiment is shown in Figure 5.3-2. The diameter of each of the irises shown in the schematic is 1cm. The separation between the two irises is 15cm. This geometry only allows fusion products with a perpendicular velocity component of 1/15 their parallel velocity component (1/225 the parallel energy component) to enter the detector.

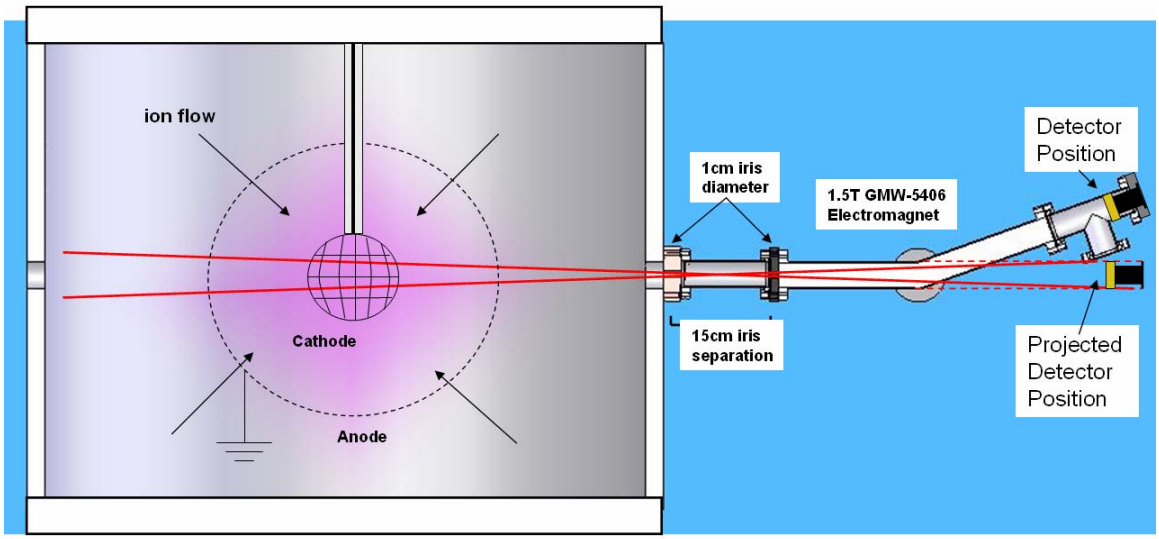

Figure 5.3-2: A schematic of the FIDO diagnostic is shown to illustrate the how the diagnostic geometry enhances of the detection of fusion products with only parallel and anti-parallel velocity components.

In general for this setup, the perpendicular energy component allowed to enter the detector will scale as,

$$E_{\perp} = E_{\parallel}\left(\frac{d_{iris}}{R_{iris}}\right)^2 \qquad (5\text{-}6)$$

where d_{iris} and R_{iris} represent the diameter of the irises and separation between the irises respectively.

In addition to the geometry of the diagnostic, the configuration of the HOMER IEC device also contributes to weighting the allowed protons toward parallel and anti-parallel v_{cm} shifts. The spherically convergent configuration of the electric fields in HOMER encourages the ions accelerated in the device to take up radial trajectories. Thus by simply limiting the field of view of the detector to a chord through the center of the device, we have essentially eliminated all ion velocities but those parallel and anti-parallel to the detector.

It should be noted however, that charge exchange processes are dominant in the moderate pressure operation regime (>0.01mtorr) of HOMER. Thus the angular deflection of fast neutrals created via charge exchange must be considered. According to Fasted and Han[9] charge exchange results in an angular deviation, Θ, of the fast neutral from its original ion trajectory by the following relation,

$$\sin^2\left(\frac{\Theta}{2}\right) = \frac{M_1 + M_2 + m}{4M_2}|q| \qquad (5\text{-}7)$$

where M_1 is the mass of the impacting ion, M_2 is the mass of the impacted neutral, m is the electron mass, and q is related to the energy defect of the charge exchange reaction by the following expression.

$$q = \frac{\Delta E}{E} + \frac{m}{M_1} \qquad (5\text{-}8)$$

In the above expression ΔE is the energy defect, and E is the center of mass energy of the impacting ion. Taking 10 eV as the energy defect for a charge exchange reaction between a 10 keV D_3^+ ion, and a neutral D_2 molecule yields of deviation angle Θ of 50 mrad. This implies that angular deviation of charge exchange neutrals should be insignificant for ion energies typical in HOMER[10]. Thus the fast neutrals from charge exchange should follow the radial path taken by the ions that birthed them. This implies that all the high velocity deuterium in an IEC device will have a predominantly radial trajectory. Therefore the geometry of the FIDO diagnostic will only admit fusion products to the detector if the v_{cm} component of their total velocity is in the parallel or anti-parallel direction.

5.3-a: Suppression of X-ray Noise in FIDO

The FIDO diagnostic also allows for the suppression of Bremsstrahlung radiation, in HOMER, produced primarily by electrons impacting the wall of the vacuum vessel. In the past, this has hampered attempts to measure the fusion product energies due to the intense flux of X-rays incident on charged particle detectors that have a direct line of sight into the chamber volume. The previous geometry is shown in Figure 5.3-3.

With the FIDO diagnostic, the charged particle detector is no longer in the line of sight to the chamber volume. Fusion products are re-directed up a 20 degree bending arm by a 1.5T GMW-5406 Electromagnet. Since X-rays do not scatter in the same way as visible light, and are more likely to penetrate through the steel bending arm, the X-ray flux on the charged particle detector will be substantially reduced.

(a)

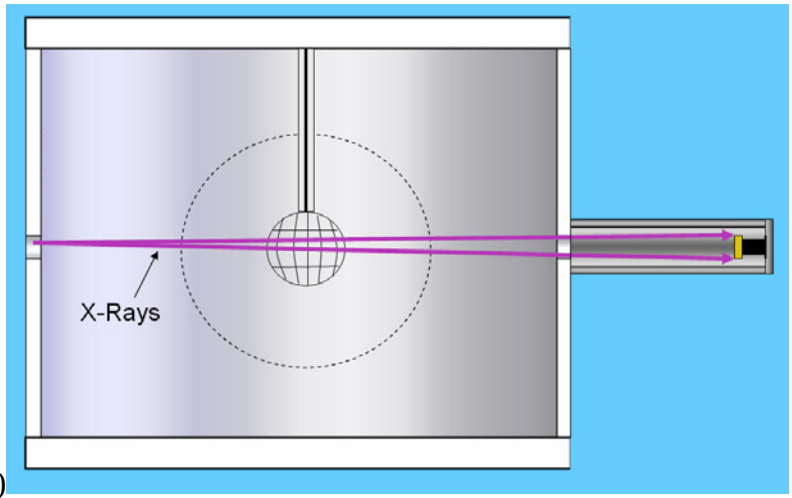

(b)

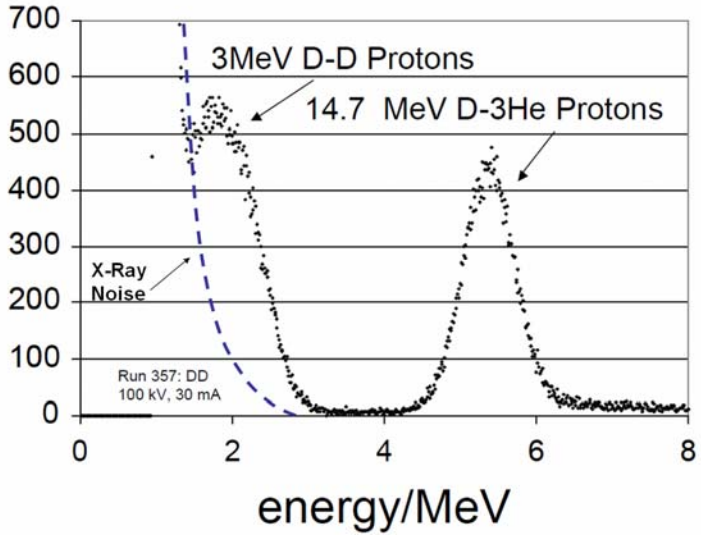

Figure 5.3-3: This illustrates how the Bremsstrahlung X-ray source on vacuum chamber walls of HOMER can adversely affect charge particle detectors by overwhelming them with X-ray noise (a) shows the previous proton detector geometry and (b) shows a characteristic D-D & D-3He proton spectrum from the previous configuration[11]

According a simulation of the FIDO geometry using MCNP 5, the flux of X-rays on the charged particle detector will be reduced by a factor of $3x10^{-6}$ compared with the geometry in Figure 5.3-3. Figure 5.3-4 illustrates how FIDO protects the silicon detector from the incoming X-ray flux from HOMER.

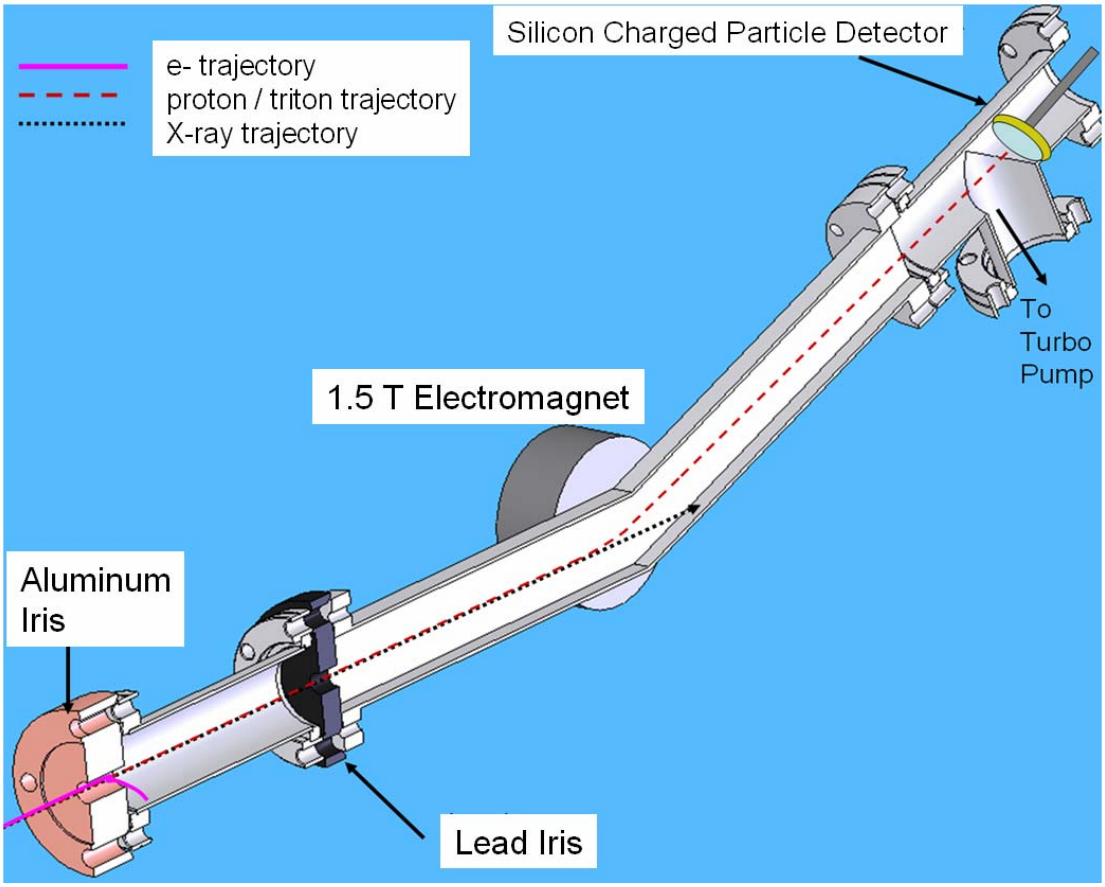

Figure 5.3-4: Above is a detailed schematic of FIDO illustrating how only fusion products from the D(d,p)T fusion reaction are allowed into the charged particle detector. Electrons are deflected by a 400 gauss permanent magnet at the Al iris.

A possible augmented design of FIDO, to further reduce X-ray noise in the silicon detector, is to add a lead wrapped X-ray beam dump just beyond the 20 degree bending section of the arm. This will eliminate the possibility of low angle scattering of X-rays into the FIDO detector, a problem that still prevents effective operation of the diagnostic in very high X-ray radiation fields.

5.3-b: Suppression of Noise from Visible Light in FIDO

Since FIDO relies on a silicon charged particle detector to examine the characteristics of fusion product energy spectrum, pollution from visible light is also an

issue that must be addressed. To eliminate signal from visible light pollution a 300nm thick reflective coating was added to the Ortec Ultra Series charged particle detectors used in the FIDO diagnostic, to make them light tight. The thickness of the coating was chosen to eliminate penetration from optical wavelength photons, but also to not adversely perturb the energy spectra of the fusion products of interest, as they would have to traverse this light shield as well. Figure 5.3-5 shows the effect of the light shield on mono-energetic 500keV tritons.

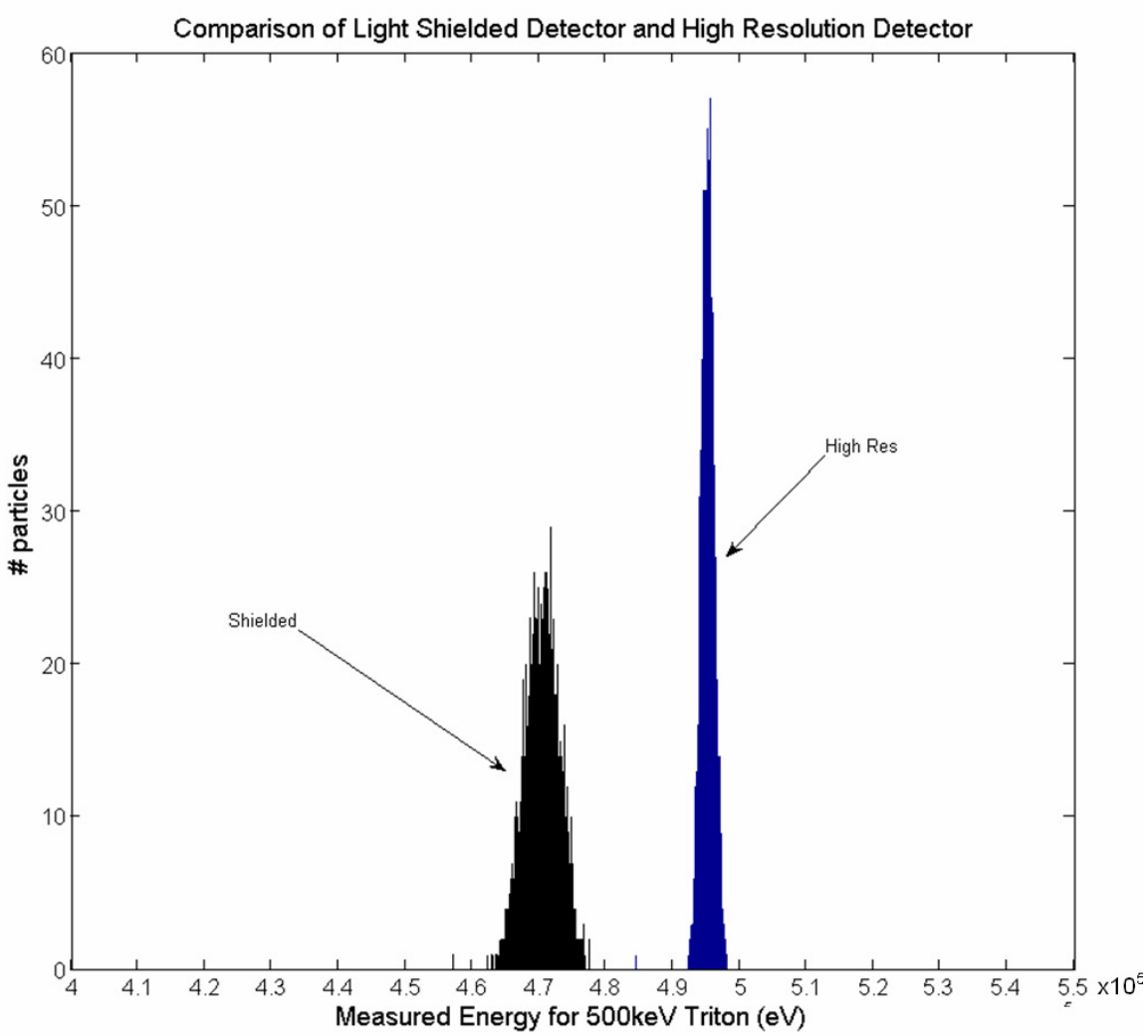

Figure 5.3-5: Shows the simulated detected energy spectra for 500keV tritons incident on an Ultra Series unshielded detector compared with an Ultra Series shielded detector with a 300nm reflective coating. The unshielded detector is denoted "High Res" in the figure. Spectra simulated using SRIM 2006.[12]

The above figure shows that a mono-energetic 500keV triton will only be down shifted by 30keV with the 300nm thick reflective coating in place. This is quite tolerable given the benefits of eliminating noise from visible light in HOMER. Previous attempts at eliminating signal from visible light in the FIDO diagnostic relied on shielding the Ultra Series detector with a 10μm thick aluminum shield. This effectively eliminated any signal from visible light but also completely eliminated the possibility of detecting tritons from the D(d,p)T fusion reaction, and noticeably broadened the 3.02MeV protons. The 30keV shift from reflective coating on the light tight detectors is obviously preferable.

5.3-c: Suppression of Noise from Deuterium Ions

The light tight detector was quite effective at preventing visible light from entering the detector. Below 50 kV cathode potentials, the signals were essentially noise free and both tritons and protons could be detected However, the 10 μm aluminum shield provided significantly improved noise reduction over the 300nm coating at cathode voltages over 50 kV. Between 40 kV and 50 kV there was an abrupt 10^4 increase in the noise level.

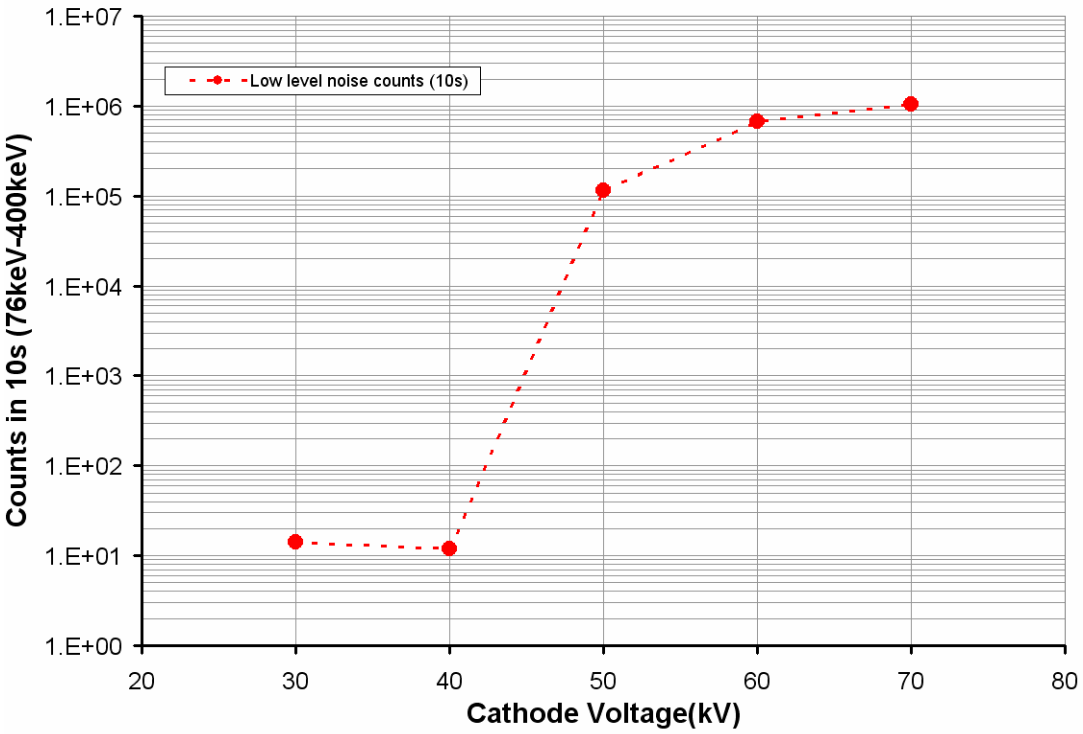

Figure 5.3-6: The effect of increasing cathode voltage on low level MCA noise at 1.2 mTorr and 30 mA of cathode current.

The transition stems from deuterium anions created in the IEC device streaming outward due to acceleration by the cathode potential. The details of the negative ion spectra are given in Chapter 6 of this thesis. The mechanism through which these deuterium anions can reach the charged particle detector is through charge transfer reactions that occur in the magnetic field of the FIDO bending arm. The current density of anions in the bending arm was measured to be ~1 mA/cm^2. If even a minute fraction of this particle flux undergoes the necessary charge transfer to access the charged particle detector it will be registered as an enormous signal. Charged particle detectors are typically saturated when measuring signals that exceed 10^6 counts/s. A deuterium ion current density of only ~1pA/cm^2 is required to achieve saturation. This would require

that only one out of every billion anions be re-directed into the detector to account for the low level noise.

The deuterium anion energy spectra generally have a median energy of one half the cathode voltages. The 300 nm thick coating on the front of the charged particle detectors used in FIDO is penetrated by the deuterium anions once their energy exceeds ~20 keV. Figure 5.3-7 shows a comparison between the measured low level noise signal in the detector and a simulation of the energy / incident ion deposited in the charged particle detector. The simulation was performed using the SRIM Monte Carlo charged particle implantation software package[12]. The simulation data points multiply the number of ions that traverse the light shield by the energy each ion deposits in the Si. This value is then divided by the total number of ions in the simulation.

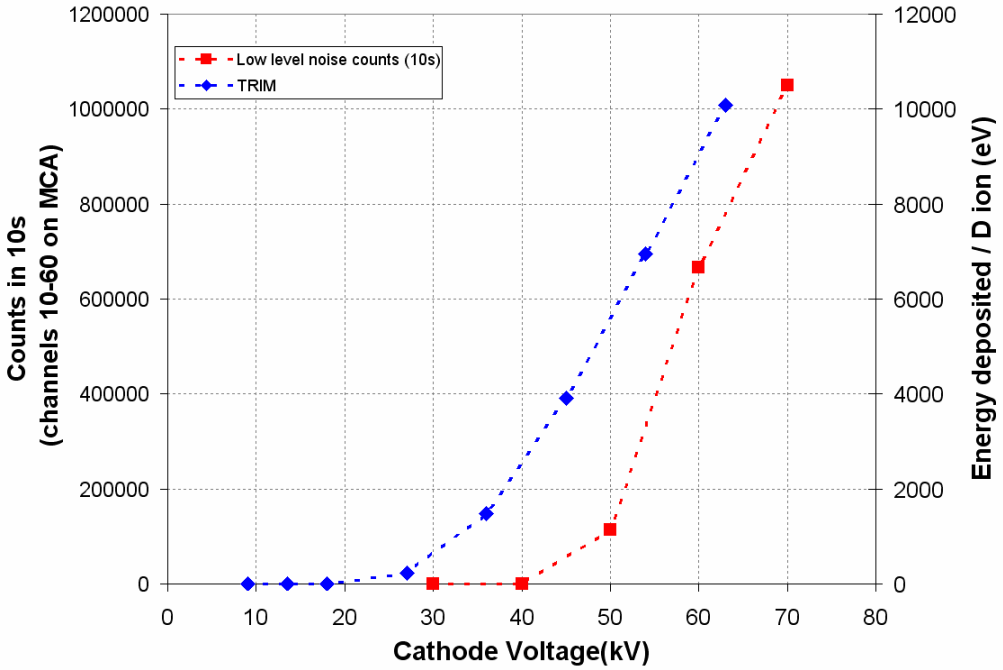

Figure 5.3-7: Compares the low level noise data at varying cathode voltages, 1.2 mTorr and 30 mA to a TRIM simulation of deuterium anions from the IEC traversing the 300 nm light shield and depositing energy into the silicon charged particle detector. The simulation data points multiply the number of ions that traverse the shield by the energy each ion deposits in the Si. This value is then divided by the total number of ions in the simulation.

The simulation and experimental data scale similarly with the transmission energy differing slightly between the experiment and the simulation. The assumption was made that the 300 nm light shield was in fact 300 nm. If the actual coating was slightly thicker (~50 nm) than the specified 300 nm this would significantly change the transmission energy and could account for some of the discrepancy between the experiment and simulation. In addition, the silicon detector will see a spectrum of deuterium ion energies whereas in the simulation only the mean energy of measured deuterium anion spectra was used. This could also contribute to the discrepancy between the experimental data and the TRIM simulation.

5.4: Experimental Results – Fusion Ion DOppler Shift Diagnostic

The FIDO diagnostic allows for the isolation and measurement of the parallel and anti-parallel components of the Doppler shifted proton energy distribution from the HOMER IEC device. Because the diagnostic isolates the parallel and anti-parallel components of v_{cm} imparted to the fusion product velocity, it is relatively straightforward to unfold the line averaged velocity spectrum of the deuterium reactants that create the detected fusion products (See Figure 5.4-1).

To unfold the velocity spectrum from the fusion product spectrum recall from Section 5.3 that the total kinetic energy of the fusion products from a D-D fusion reaction is given by:

$$E_t = \frac{1}{2} m_p v_t^2 = \frac{1}{2} m_p \left(v_f^2 + v_{cm}^2 \pm 2 v_{cm} v_f \cos\Theta \right) \qquad (5\text{-}9)$$

From equation (5-10) it is straightforward to calculate the center of mass velocity associated with the number of counts in each energy bin of a proton energy spectrum. The upshifted and downshifted portion of the proton spectrum shown in Figure 5.4-1a is plotted against v_{cm} in Figure 5.4-2. The number of counts in each velocity bin can then be divided by the fusion cross section associated with that center of mass velocity. The D(d,p)T fusion cross section is shown in Figure 5.4-3. This technique was used generate the line averaged velocity spectrum plotted in Figure 5.4-1b.

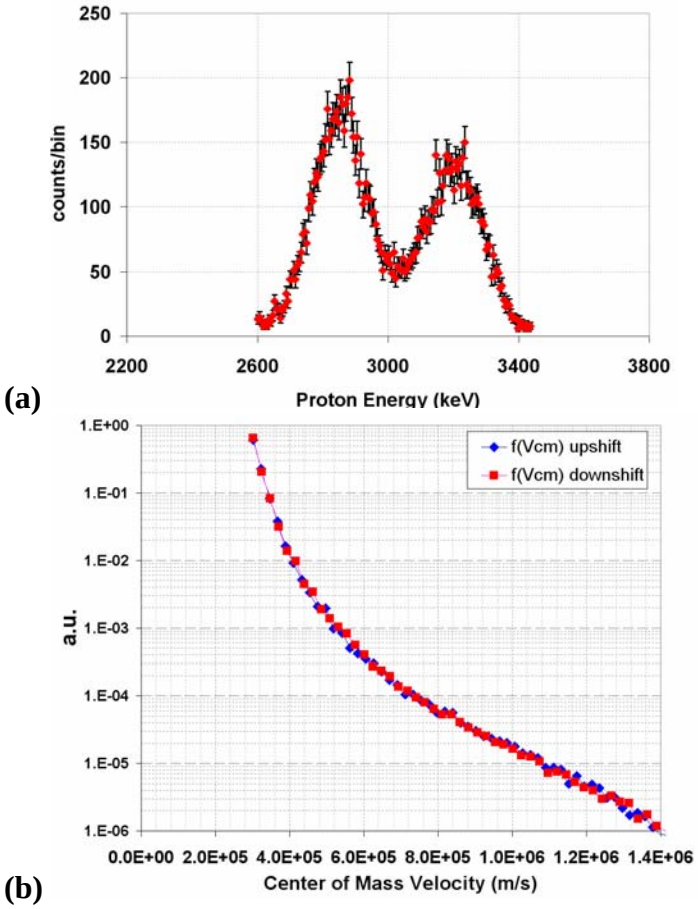

Figure 5.4-1: An experimentally measured D-D proton energy spectrum (a) at 70 kV cathode voltage, 30 mA cathode current, and 1.25 mTorr neutral gas pressure. At right (b) is the center of mass velocity spectra of the deuterium reactants resulting from the upshifted and downshifted portions of the proton spectrum above.

The charged particle detector used in FIDO measures this quantity, and thus allows for calculating v_{cm} since v_t and v_f are known through measurement and the Q value of the D-D fusion reaction. Since $\cos\Theta \approx 1$ for the FIDO geometry the following simple expression can be used for the total velocity.

$$v_t = v_f \pm v_{cm} \tag{5-10}$$

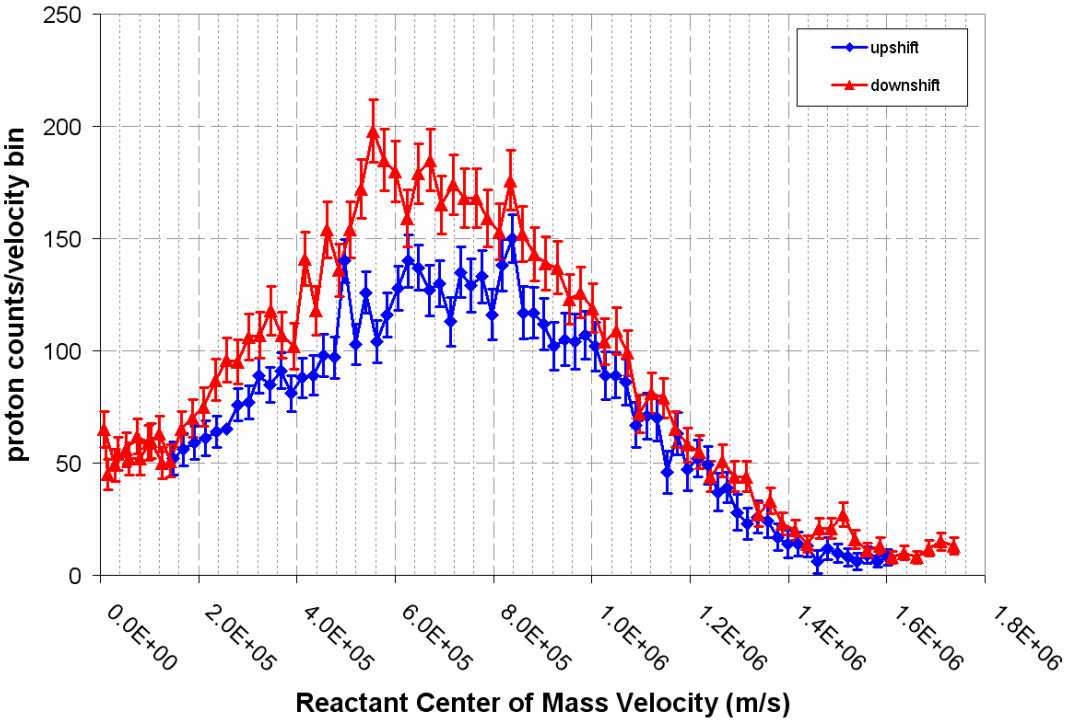

Figure 5.4-2: The upshifted and downshifted components of the experimentally measured D(d,p)T proton energy spectrum from Figure 1 (70 kV, 30 mA, 1.25 mTorr) are plotted against the center of mass velocity of deuterium reactants.

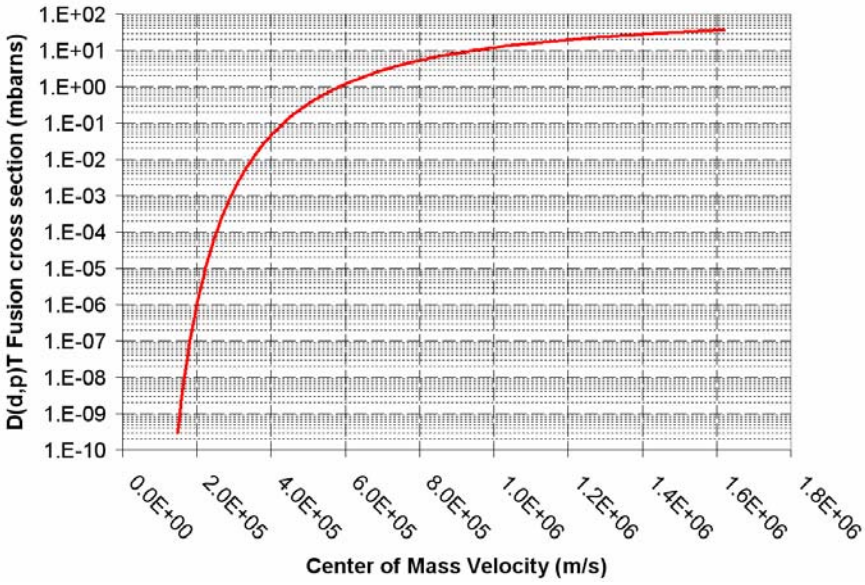

Figure 5.4-3: D(d,p)T fusion cross section for varying center of mass velocity[13]

For a two-body collision, in which nearly all the energy is with the incoming particle, the center of mass velocity and center-of-mass kinetic energy are defined as follows where m_1, and m_2 represent the masses of the incoming and stationary particles respectively. Similarly v_1 is the velocity of the incoming particle and v_2 is zero.

$$v_{cm} = \frac{m_1 v_1}{m_1 + m_2} \tag{5-11}$$

The kinetic energy of the system in center of mass coordinates is given below:

$$E_{cm} = \frac{1}{2}(m_1 + m_2)v_{cm}^2 = \frac{1}{2}\frac{m_1^2 v_1^2}{(m_1 + m_2)} \tag{5-12}$$

The energy available for fusion to occur, E_{fus}, is given by:

$$E_{fus} = \frac{1}{2}\frac{m_1 m_2 v_1^2}{(m_1 + m_2)} \equiv \frac{\mu_{12} v_1^2}{2} \tag{5-13}$$

Where μ_{12} is the reduced mass of the system.

For the molecular deuterium species mixture in the HOMER IEC device three discrete center of mass energies are possible, if all fusion reaction products are assumed to originate from reactions with background neutral gas. The reactions shown only regard the reacting deuteron from the background gas molecules as the energies imparted to the system during a fusion reaction will likely dissociate the deuterium molecules before the fusion event takes place.

$$E_{cm} = \begin{cases} 2m_D v_{cm}^2 : & \mathrm{D}_3^+ \rightarrow \mathrm{D} \\ \frac{3}{2} m_D v_{cm}^2 : & \mathrm{D}_2^{+/-} \rightarrow \mathrm{D} \\ m_D v_{cm}^2 : & \mathrm{D}^{+/-} \rightarrow \mathrm{D} \end{cases} \qquad (5\text{-}14)$$

Since the identity of the reactants cannot be determined from the FIDO diagnostic data sets the spectra must be plotted against v_{cm} and the cross section is calculated assuming $m_1 + m_2 = 2m_D$, essentially taking the center of mass energy only between the two reacting deuterons. Using the technique outlined in this section the center of mass velocity spectra of the deuterium reactants in the HOMER IEC device are mapped for a variety of experimental parameters. Cathode voltage, cathode current, cathode/anode geometry, and background neutral gas pressure were all varied to ascertain their effect on the deuterium velocity spectra.

5.4-a: Voltage Scan

A voltage scan was performed on the HOMER IEC device so as to observe the effect of varying cathode voltage on the deuterium velocity spectrum. The neutral gas pressure in HOMER was maintained at 2.5 mTorr, and the cathode current was held constant at 30 mA. The spectra obtained by varying the cathode voltage from 50-100 kV are shown below in Figure 5-4-4.

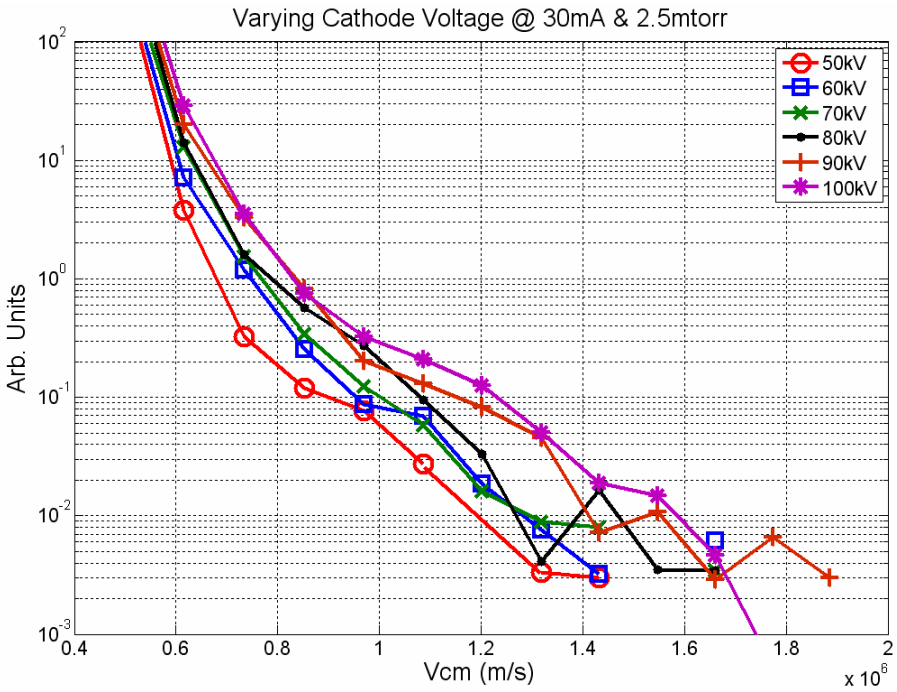

Figure 5.4-4: Voltage scan between 50 kV and 100 kV with the cathode current and background neutral gas pressure held constant at 30 mA and 2.5 mTorr respectively. The vast majority of deuterons remain at velocities well below the maximum.

The spectra shown in Figure 5.4-4 are derived from proton spectra which have been normalized for varying count times. This was done due to the significantly longer count times necessary to obtain good statistics on the lower voltage runs. As the voltage is increased both the average velocity, v_{mean}, and the peak velocity, v_p, of the deuterium spectra increase.

5.4-b: Current Scan

Scans of the cathode current were performed at neutral gas pressures of 2.5 mTorr and 0.5 mTorr. The cathode current was varied between 15 mA and 60 mA in the 2.5 mTorr case and between 15 mA and 70 mA in the 0.5 mTorr case. This data is shown in Figures 5.5-5a and 5.5-5b respectively.

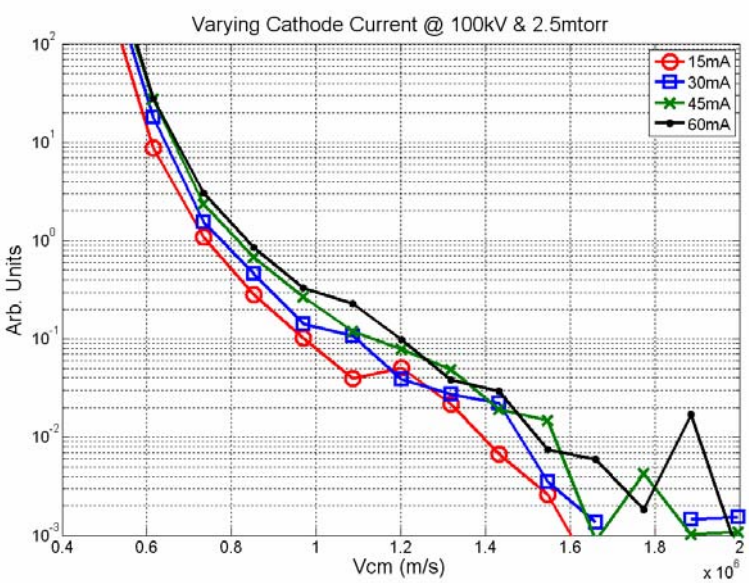

(a)

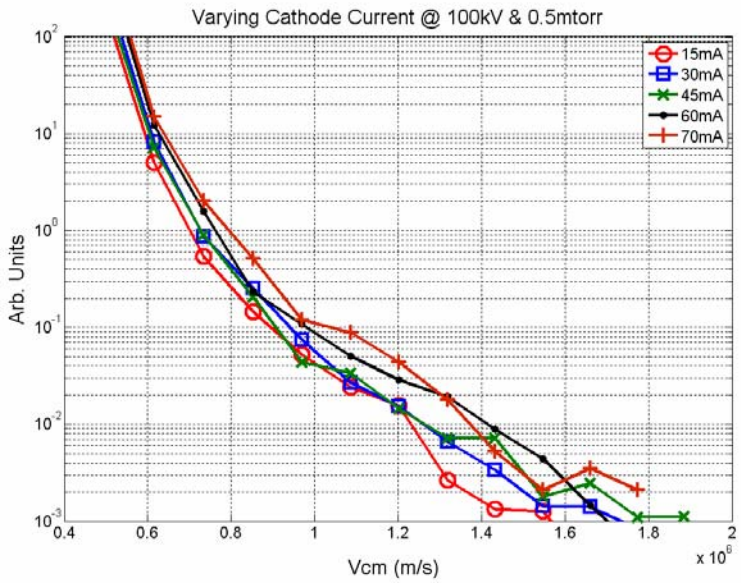

(b)

Figure 5.4-5: Cathode current scan at a background neutral pressure of (a) 2.5 mTorr, (b) 0.5 mTorr, and cathode voltage of 100 kV. The relative number of particles in each velocity group tends to increase with cathode current.

The current scan data at both pressures shows a relatively uniform increase in the number of particles in each velocity bin. This correlates well with the linear increase observed in the fusion rate as the cathode current in increased (See Figure 5.4-6).

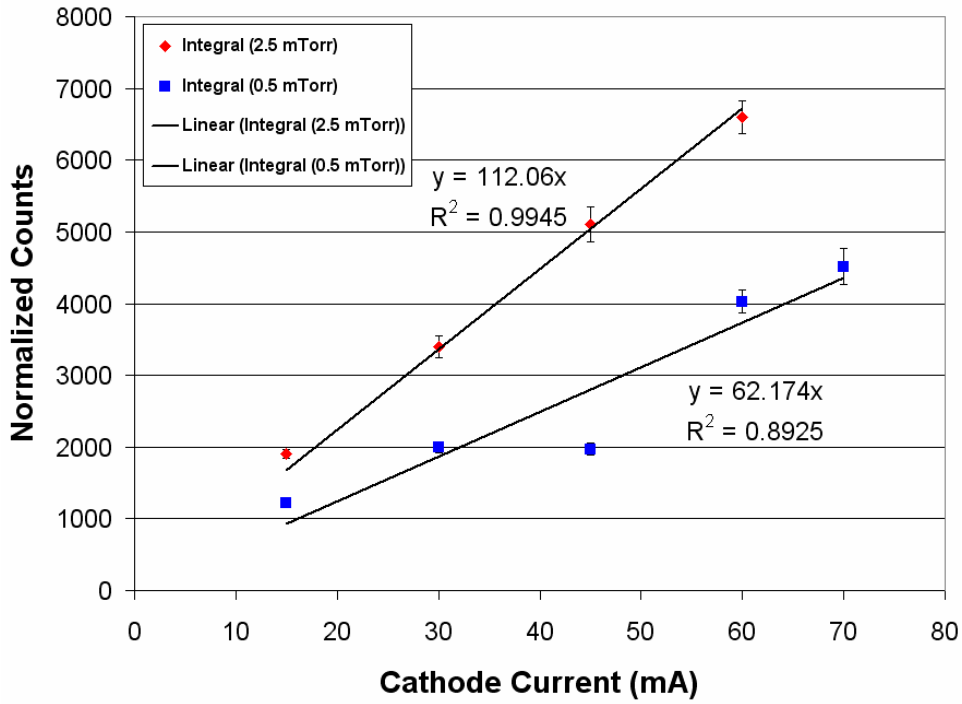

Figure 5.4-6: Shows time normalized integrations of the proton spectra collected at varying cathode current. The cathode voltage was held at 100 kV. A 2.5 mTorr and a 0.5 mTorr case were examined.

This linear scaling with current is also in good agreement with neutron rates measured on the HOMER IEC device[14]. The slower rate of increase in the 0.5 mTorr case relative to the 2.5 mTorr case is due to the decreased number of background gas targets at the lower pressure.

5.4-c: Pressure Scan

Neutral gas pressure was varied within the HOMER IEC device while the cathode current and cathode voltage were held constant so as to ascertain the effect of varying chamber pressure on the velocity spectra of the reacting deuterons within the device. Shown in Figure 5.4-7 are the velocity spectra for the reacting deuterons at neutral gas pressures between 0.25 mTorr and 3.5 mTorr.

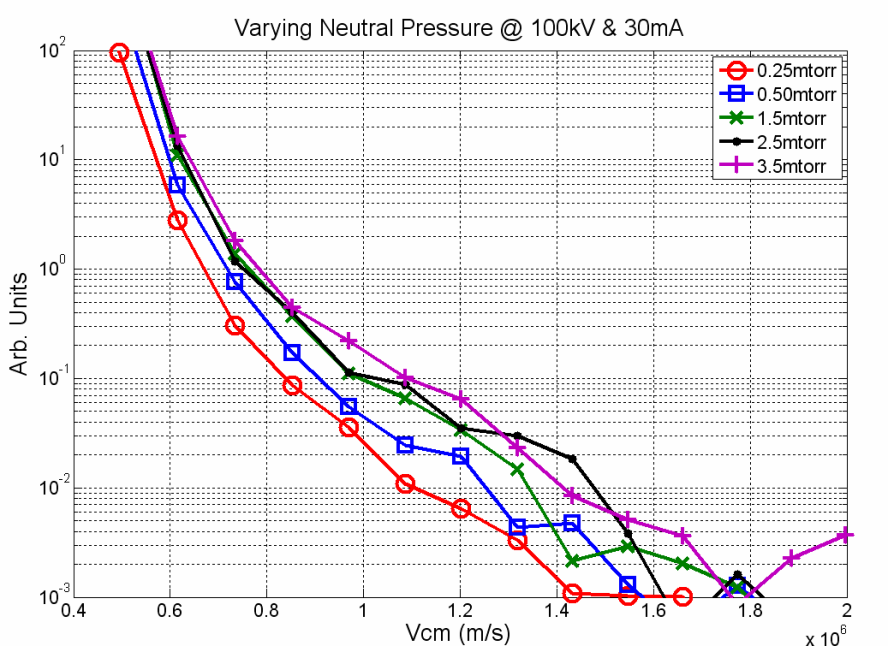

Figure 5.4-7: Deuterium velocity spectra at neutral gas pressures between 0.25 mTorr and 3.5 mTorr. Cathode voltage and cathode current are held at 100 kV and 30 mA respectively. The relative intensity of the spectra increases substantially between 0.25 mTorr and 1.5 mTorr. Above 1.5 mTorr the intensity of the velocity spectra appear to approach saturation.

At pressures between 0.25 mTorr and 1.5 mTorr changes to the background neutral pressure result in significant changes in the intensity of the deuterium velocity spectra. As the pressure is increased the number of fast deuterons available for fusion increases with the spectra intensity saturating above 1.5 mTorr. This is reflected in the fusion rate recorded by both the FIDO proton detector and neutron detector used with the HOMER IEC device. (See Figure 5.4-8.)

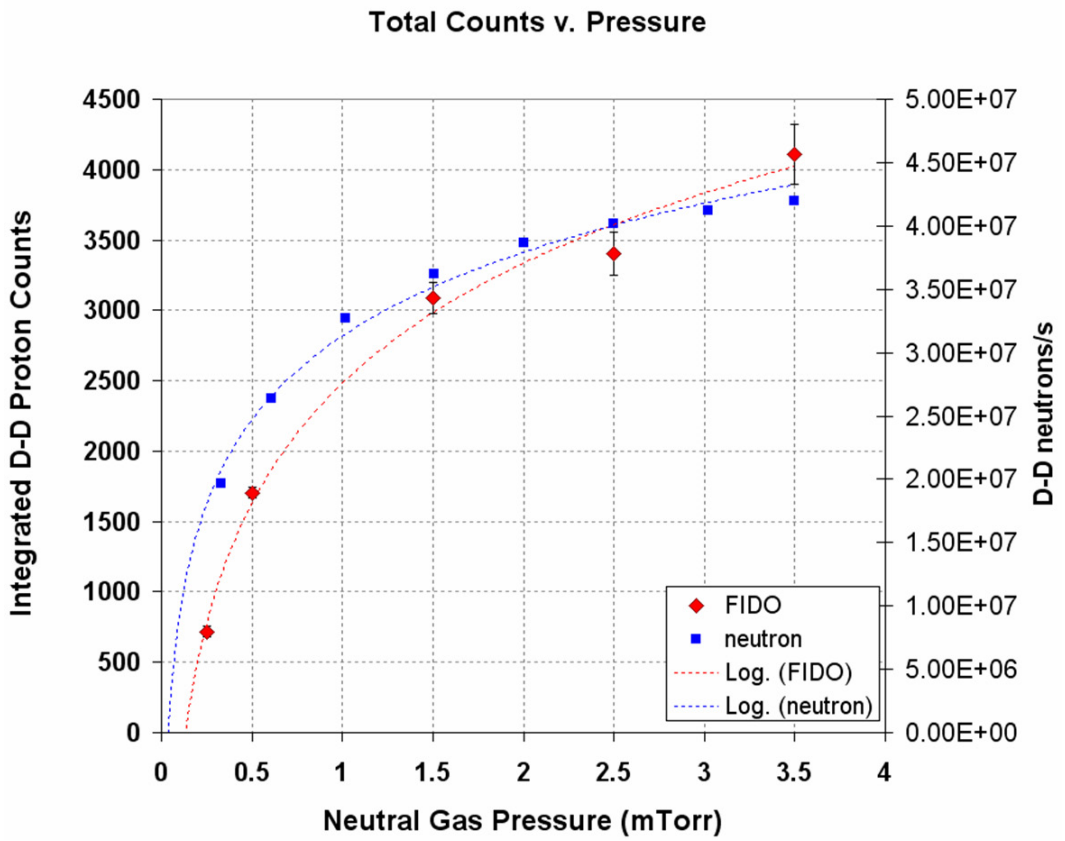

Figure 5.4-8: Integrated, time normalized, proton counts from the FIDO detector reflecting how the fusion rate within the FIDO line of sight scales with background neutral pressure. Scaling of the $D(d,n)^3He$ reaction rate in HOMER with varying neutral gas pressure is also shown. Both sets of data were taken at 100 kV, and 30 mA.

Another feature of the deuterium spectra shown in Figure 5.4-7 is the relative increase in the number of higher velocity particles as background pressure is increased. Close examination of Figure 5.4-7 shows that the gain in the number of deuterons at high velocity ($>8x10^5$ m/s) is measurably larger than the gain in the number of deuterons in the lower velocity groups. This feature is shown quantitatively in Figure 5.4-9 where the increase in the number of particles / velocity bin for a pressure increase from 0.25 mTorr to 2.5 mTorr is plotted for each velocity bin individually. The lower velocity groups see a factor of 6 increase in intensity over this pressure range, whereas the higher velocity groups see factors of 8-20 increases over the same pressure range.

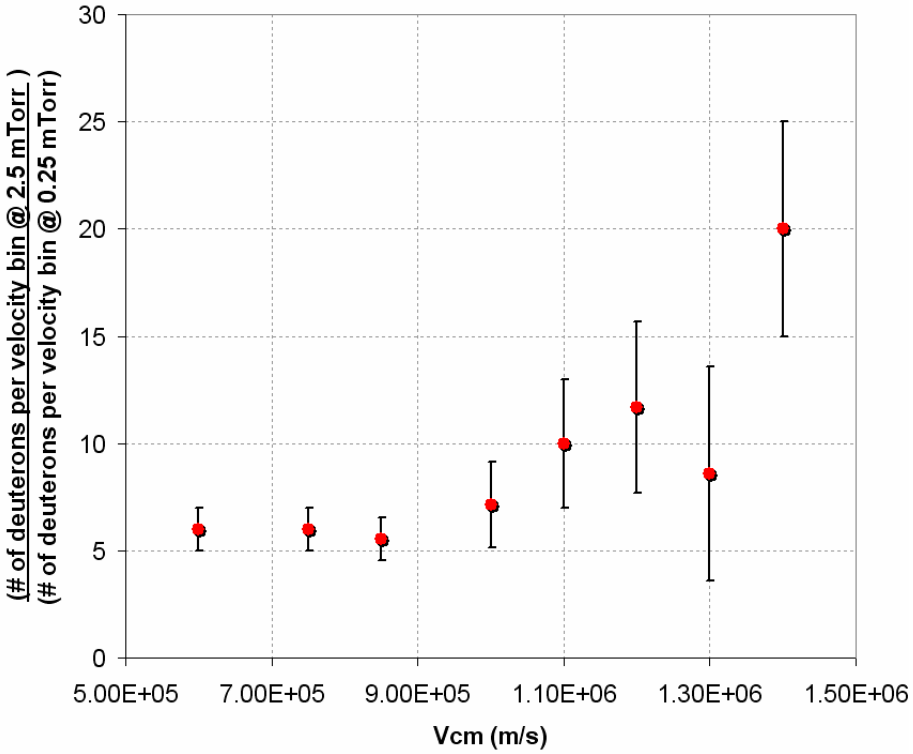

Figure 5.4-9: Ratio of the number of deuterons per velocity bin @ 2.5 mTorr to the number of deuterons per velocity bin @ 0.25 mTorr plotted for each velocity bin of the deuterium spectra in Figure 5.4-7.

This observed hardening of the deuterium velocity spectra at higher background pressures is the opposite of what would be expected in the context of positive ions traversing a gas target with charge exchange neutral formation being the dominant processes. In this context one would expect a higher charge exchange neutral production rate which should soften the spectra.

Explanation for this phenomenon is the increased production rate of deuterium anions, or negative ions, at higher background neutral pressure. See Chapter 6.3 for a detailed description of the deuterium anion measurements in IEC devices. The processes that govern deuterium anion formation in IEC devices are charge transfer and electron attachment. Charge transfer reactions occur at energies in the hundreds to thousands of eV range, and involve a transfer of electrons to form negative deuterium ions from fast

positive deuterons interacting with thermal deuterium gas molecules. Electron attachment occurs via thermal electrons attaching to vibrationally and rotationally excited neutral gas molecules. Both of these processes are dependent on the background neutral gas density, and since negative ions are accelerated more quickly by the cathode potential than positive ions they attain higher energies. This explains the hardening of the spectra observed at higher neutral gas pressures.

The hardening of the spectra can also be observed in the raw proton counts measured by FIDO. Shown in Figure 5.4-10 is a succession of plots depicting Gaussian fits to the double peaked proton spectra obtained by FIDO at 100 kV and 30 mA. Through the progression from 0.25 mTorr to 2.5 mTorr background pressure an additional high energy contribution to the Doppler shifted proton spectra becomes apparent. In Figures 5.4-10c through 5.4 -10f, this higher energy contribution is fit by an additional high energy Gaussian. This is accounted for by the increased contribution from deuterium anion fusions as neutral gas pressure is increased. The energy of the anion peak is well correlated with the energy of deuterium anions directly measured for these experimental parameters. Further detail can be found Chapter 6. Although the deuterium anions have higher energy than the positive ions and fast neutrals their trajectories within HOMER are directed outward, thus they have a much reduced path length relative to the positive ions which are confined by the cathode potential. This accounts for their relatively minor contribution to the fusion rate. In addition, negative ions are likely to be a minority fraction of the current in the HOMER IEC device, diminishing their contribution to the fusion rate.

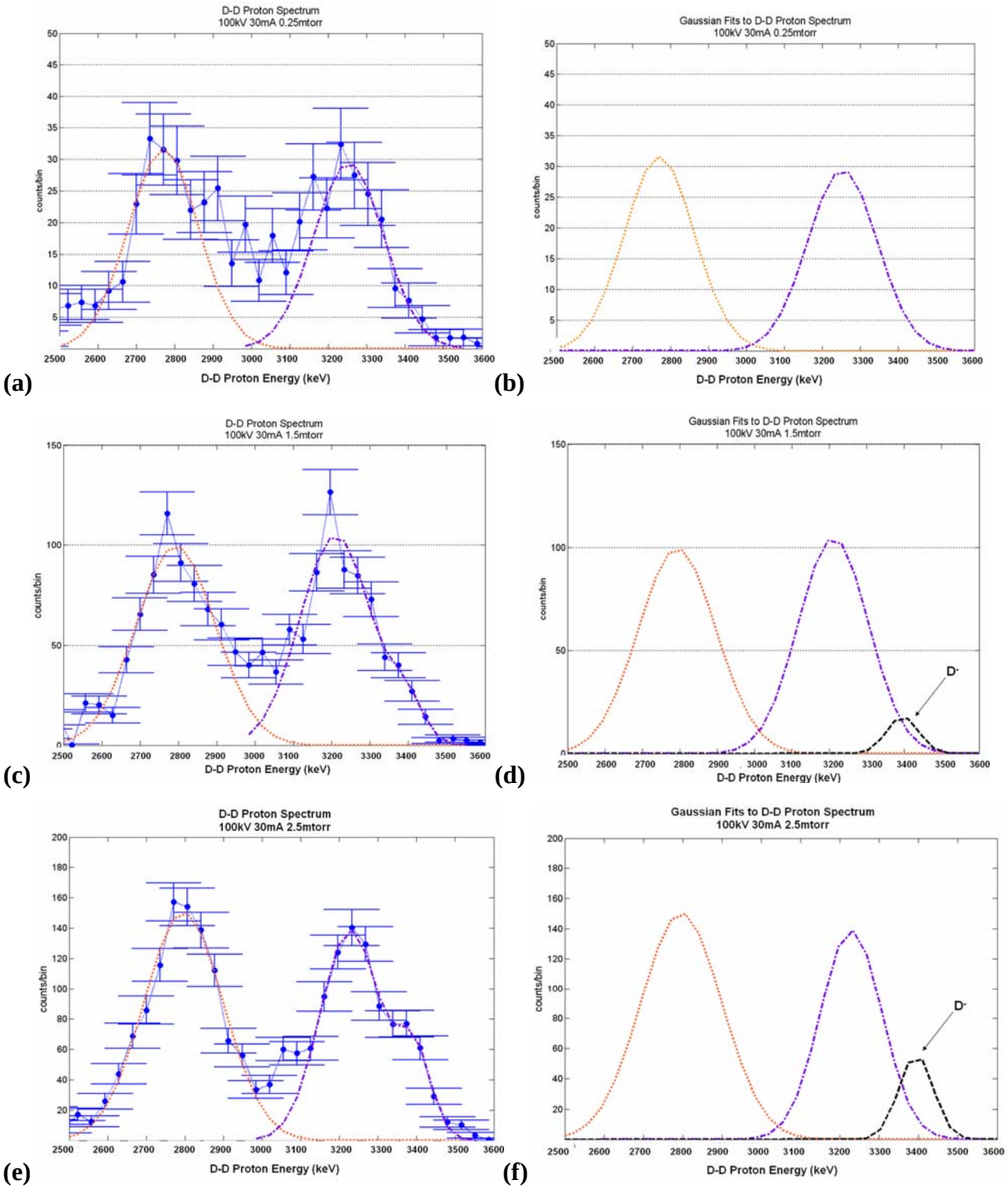

Figure 5.4-10: FIDO proton spectra taken at 100 kV cathode voltage, and 30 mA cathode current. The pressure is varied from 0.25 mTorr for (a) and (b), to 1.5 mTorr for (c) and (d), to 2.5 mTorr for (e) and (f). Images (b), (d), and (f) depict the Gaussians used to fit the raw data in (a), (c), and (e) respectively.

Further evidence that the high energy peak in the Figure 5.4-10 proton spectra originates from fusing deuterium anions comes from the magnitude of the Doppler shift for the alleged anion part of the spectra. Doppler shifted protons measured at 3.4 MeV such as those in Figure 5.4-10 are consistent with D-D center of mass energies of 50 keV. The Doppler shift is consistent with measured velocity spectra of deuterium anions detailed in Chapter 6 of this thesis. Negative ions with the energy spectra measured in Chapter 6.4 would produce the Doppler shifts observed in Figure 5.4-10 if the accelerated deuterium anions were to strike background gas and cause fusion.

Figure 5.4-11 shows 100 kV, cathode current scans at 2.5 mTorr and 0.5 mTorr background pressure. By integrating the Gaussian fits in Figure 5.4-10 the contributions from positive ions and negative ions have been isolated and plotted below. Figure 5.4-11a shows scaling with current for the fast neutral and positive ion peak. For a factor of five increase in pressure the current dependence increases by roughly a factor of two. Figure 5.4-11b shows that the anion peak contribution increases in proportion with the pressure increase (increasing by a factor of 5 for a factor of 5 increase in background pressure). This is consistent with fusions from negative ions undergoing a single pass through the background gas in HOMER. Since the positive ions, which account for the larger of the two peaks in the FIDO spectra, re-circulate through the system their longer path length makes them less dependent on background gas pressure. Figure 5.4-12 shows how the number of fusions from positive ions/fast neutrals and anions scale relative to each other in HOMER. Anions make their maximum contribution to fusion at around 2.5 mTorr beyond which their contribution levels off. This is also consistent with the data from direct measurements of the deuterium anion flux emanating from HOMER.

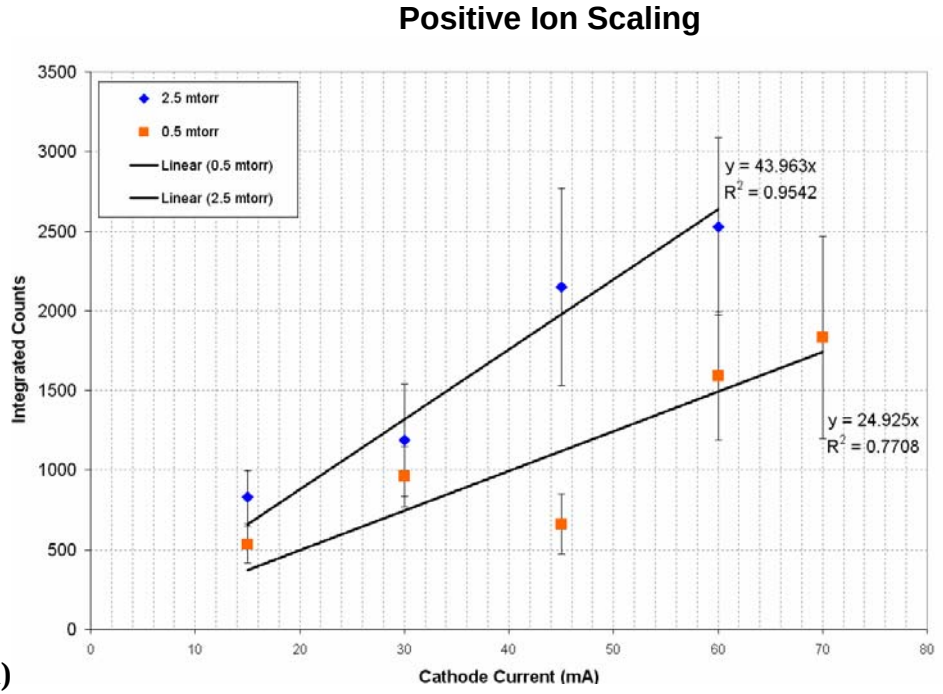

(a)

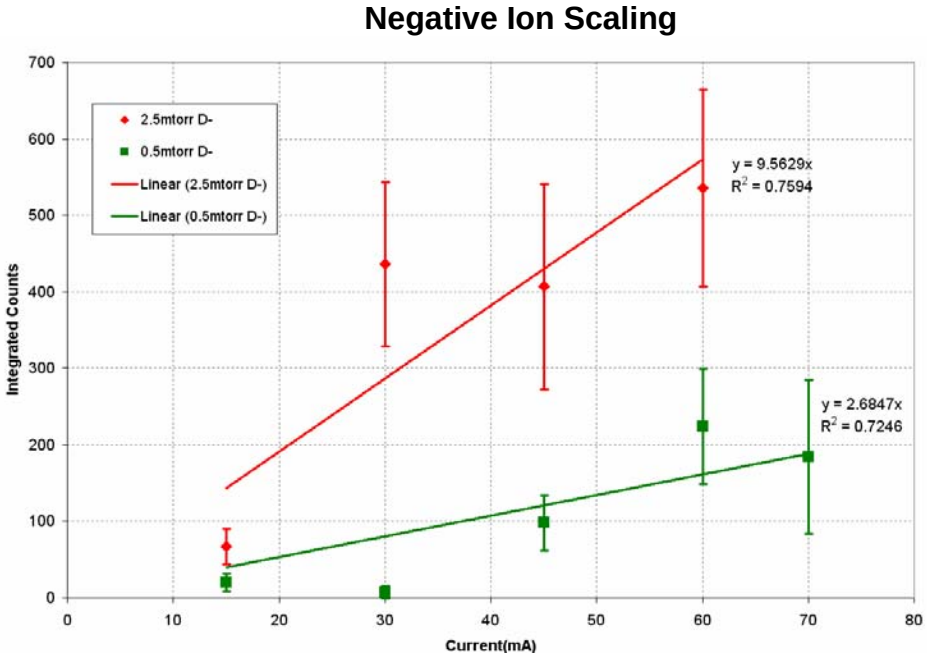

(b)

Figure 5.4-11: Scaling of integrated D-D proton counts with cathode current of the (a) positive ion/fast neutral peak for background pressures of 0.5 mTorr and 2.5 mTorr, compared with the scaling with cathode current of the (b) anion peak for the same background pressures.

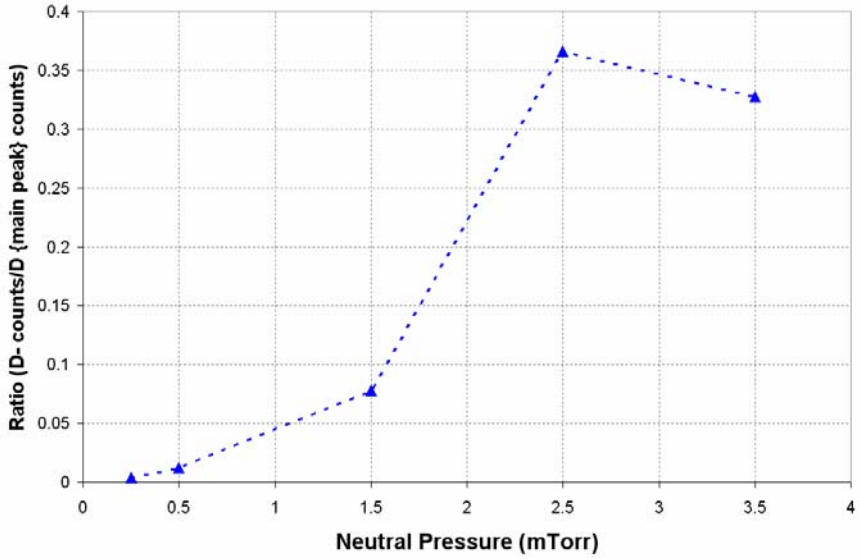

(a)

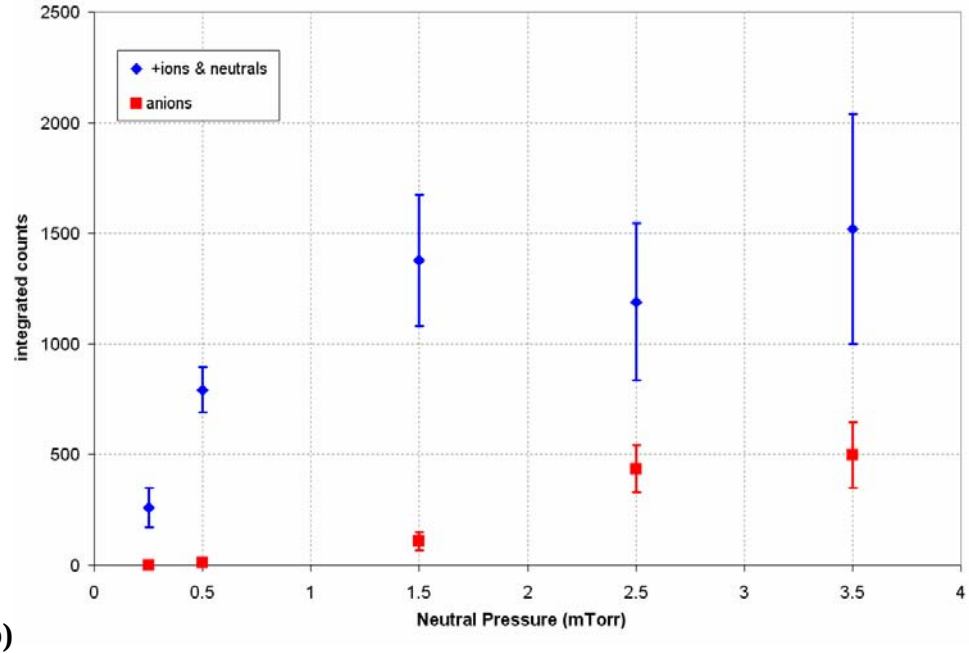

(b)

Figure 5.4-12: (a) Ratio of the number of counts in the D^- peak over the number of counts in the positive ion/fast neutral peak of the FIDO proton spectra. (b) Plot of the time normalized integrated counts for FIDO data sets taken at 100 kV cathode voltage, 30 mA cathode current, and varying background pressure.

Figure 5.4-12 shows that deuterium anions account for between 30% - 40% of the fusions that occur in the HOMER IEC device when the background pressure is greater than 2.5 mTorr. This is consistent measurements of the deuterium anion current that indicate anions make up a few percent of the total current with the HOMER IEC device. Since they are higher energy than the positive ions, however, it is expected that the anions would contribute more to the total fusion rate. It should be noted that the FIDO diagnostic is oriented along a suspected channel of deuterium anions. The FIDO diagnostic is aligned along the same chord through the device as the magnetic deflection energy analyzer described in Chapter 6. It is possible that this would lead to a higher percentage of fusions from anions along the FIDO diagnostics line of sight. Nonetheless the contribution of deuterium anions to the fusion rate in the HOMER IEC is significant.

5.4-d: Grid Geometry Scan

The grid geometry was also varied as part of the parametric studies performed with the FIDO diagnostic[10]. The separation between the cathode radius and the anode radius was found to have a measurable effect on both the fusion rate in the HOMER IEC device as well as the deuterium energy spectra obtained with the FIDO diagnostic. In the grid configuration study the cathode diameter was held constant at 20 cm and the anode diameter was varied. Anode diameters of 30 cm, 40 cm, and 50 cm were tested at 75 kV and 90 kV voltages on the cathode. The cathode current was held constant at 45mA, and all the measurements were taken with the a background neutral pressure of 1.25 mTorr.

Below in figures 5.4-13 through 5.4-15 the FIDO velocity spectra for the conditions mentioned above are shown. The figures show a trend toward hardening of

the deuterium velocity spectra as the anode diameter is increased from 30 cm to 50 cm. This behavior is clearly visible in both the 75 kV and 90 kV case. In figure 5.4-15 the raw proton energy spectra are shown to illustrate how the relative number of proton counts in each energy group changes as the anode diameters are altered. The up-shifted portion of the proton spectra in figure 5.4-15 have been normalized to each other, so the number of up-shifted counts in each spectrum is the same.

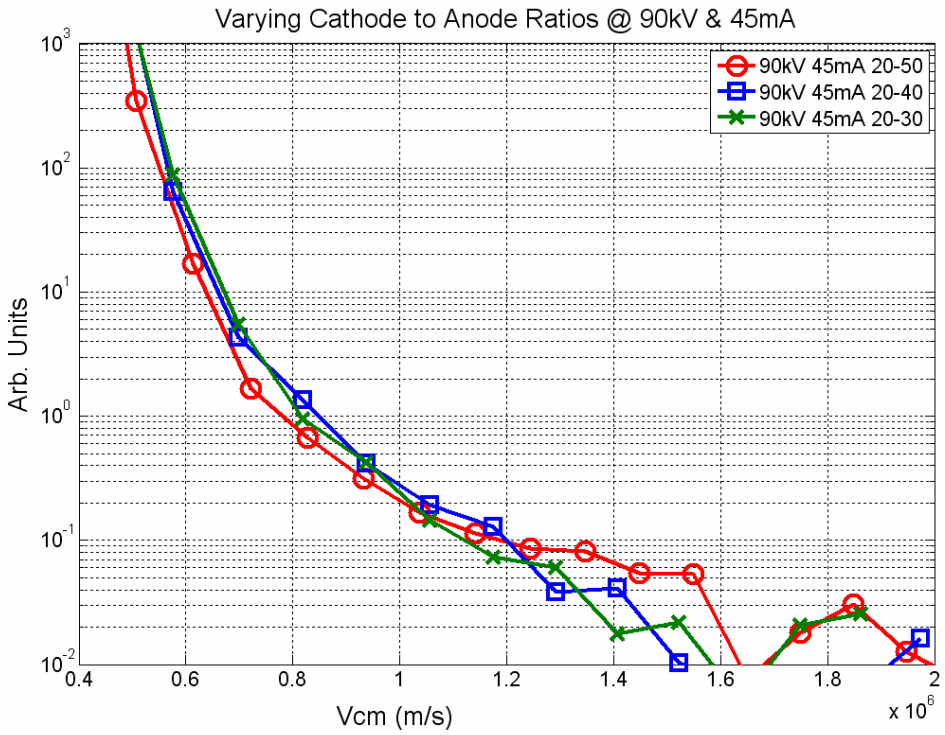

Figure 5.4-13: Deuterium velocity spectra for 30 cm, 40 cm, and 50 cm anode diameters at 90 kV, 45 mA, 1.25 mTorr.

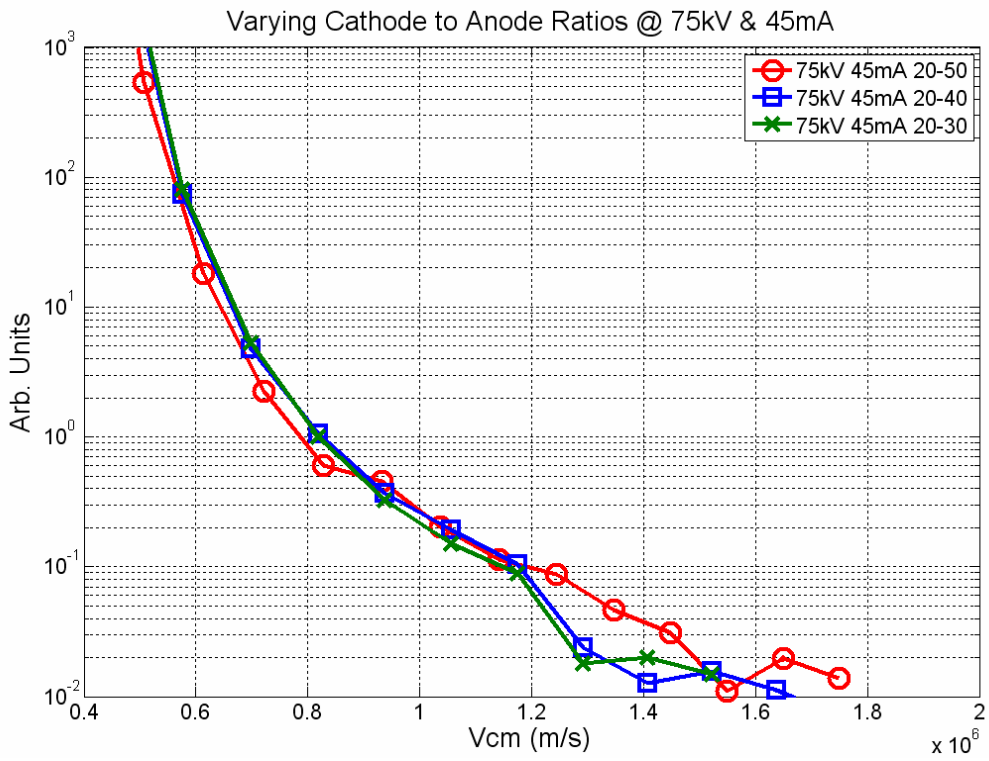

Figure 5.4-14: Deuterium velocity spectra for 30 cm, 40 cm, and 50 cm anode diameters at 75 kV, 45 mA, 1.25 mTorr.

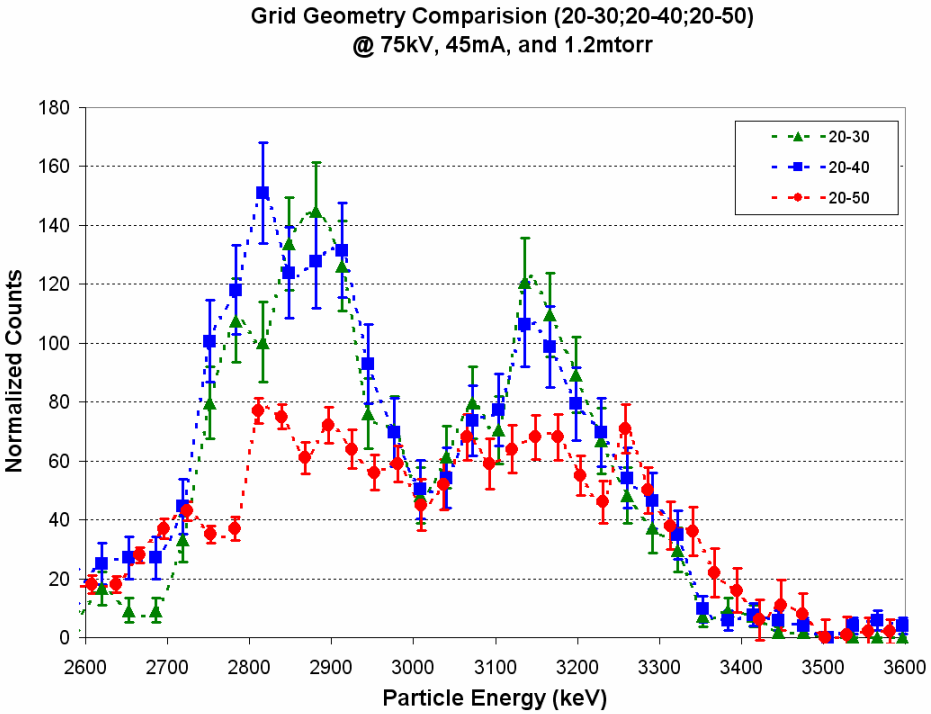

Figure 5.4-15: Proton energy spectra for 30 cm, 40 cm, and 50 cm anode diameters at 75 kV, 45 mA, 1.25 mTorr.

The reason for the hardening of the deuterium spectra with larger grid separations is related to the molecular ion species mix in the source region of HOMER. Since the source region contains mostly D_3^+ ions only 1/3 of the cathode energy is given to each deuteron in the molecular ion. When the grids are close together the path length over which the D_3^+ ions can dissociate is relatively short. As the grid separation is increased the likelihood of the molecular ions dissociating (or undergoing charge transfer) into lighter ions D_2^+, D^+, and D^- becomes larger. Figure 5.4-16 shows the attenuation of D_3^+ ions as the molecular ion traverses varying fractions of cathode to anode separation.

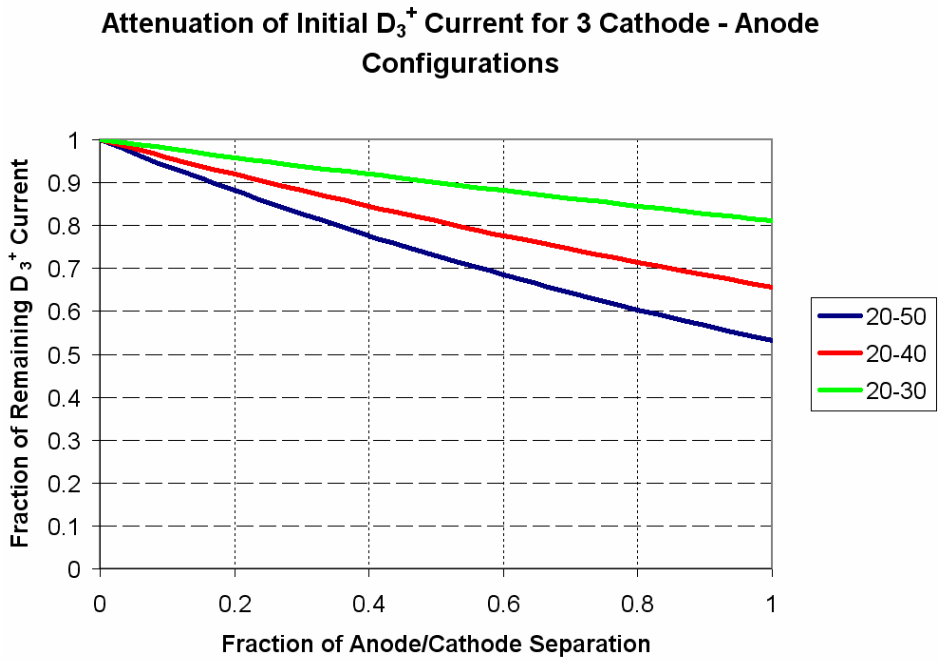

Figure 5.4-16: Shows calculated attenuation of D_3^+ ions through dissociation at varying fractions of the anode to cathode separation distance. The most dissociation occurs in the 20-50 case due to the longer path length.

These lighter ions are able to attain a higher kinetic energy/nucleon as a result of larger grid separation. As one might expect, the hardened deuterium spectra result in higher neutron rates at wider grid separations. This effect is shown in Figure 5.4-17.

The smaller grid separations were originally meant to overcome the scavenging of ion kinetic energy by charge exchange reactions. It is likely that as grid separation increases, the neutron rates will again decrease as softening of the spectra from charge exchange overcomes the effect of dissociating the molecular ions from the source region. This was observed by Radel and Wehmeyer[15] when variations on the cathode geometry were performed in 2006.

The study of the separation between the electrodes helped to advance the understanding of how the spherical IEC chambers operate and the extent to which the various molecular ions have an effect upon the fusion rates in the device. The study led to an operating configuration that has up to 50 percent higher neutron rates compared to the previously implemented configuration.

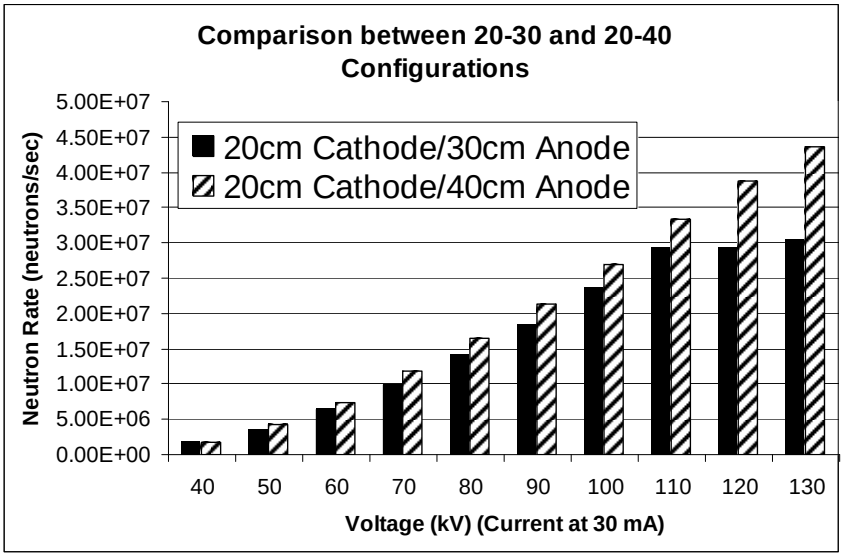

(a)

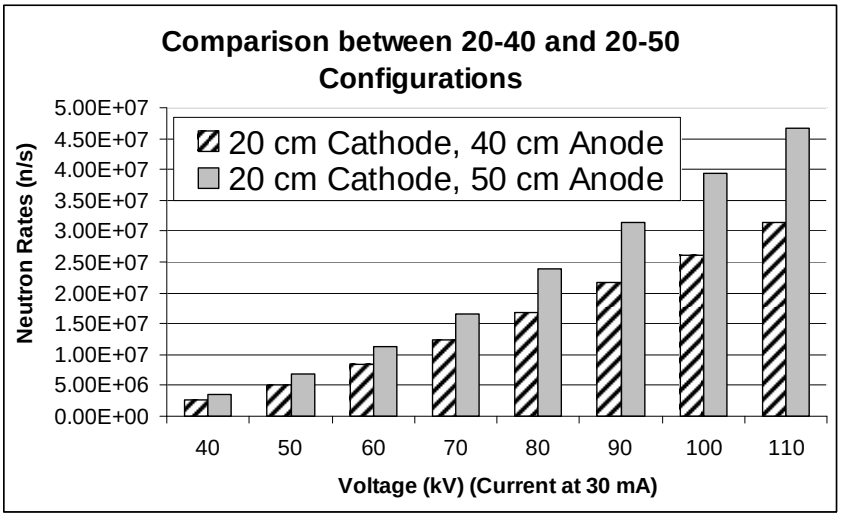

(b)

Figure 5.4-17: (a) Neutron rate comparison for the 20-30 grid configuration and the 20-40 grid configuration. (b) Neutron rate comparison between the 20-40 grid configuration and the 20-50 grid configuration.

5.4-e: Fraction of Wall Fusion Observed in HOMER

Close observation of the proton spectra obtained from the FIDO diagnostic reveals a repeating discrepancy between the number of up-shifted and down-shifted proton counts. In virtually all the proton spectra taken with the FIDO diagnostic the down-shifted proton peak contains between 5%-20% more proton counts than the up-shifted peak. This discrepancy indicates that FIDO is observing more fusions in which

v_{cm} is directed away from the detector, than fusions in which v_{cm} is directed toward the detector. This is clearly shown in Figure 5.4-1, and the integrals of the two peaks are shown below in Figure 5.4-18.

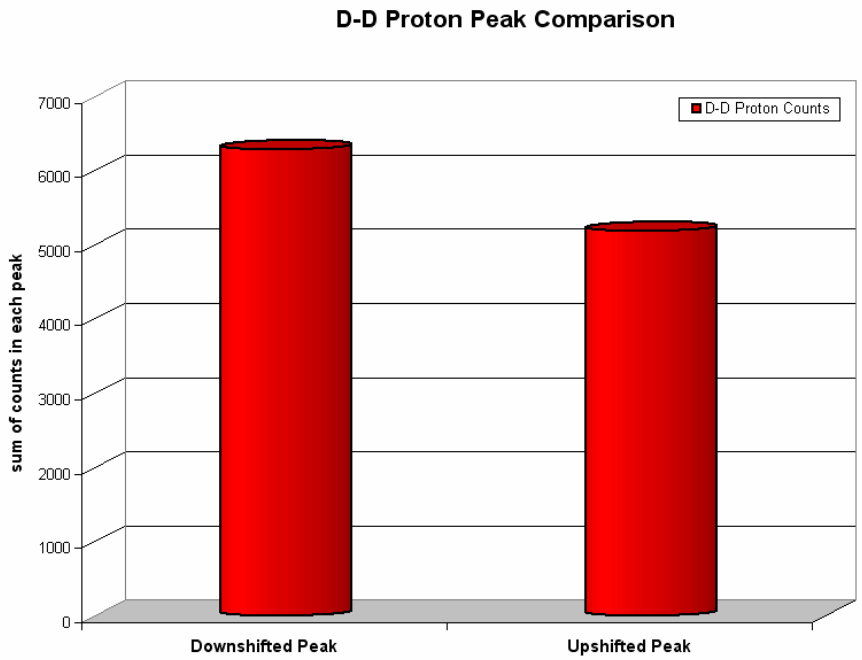

Figure 5.4-18: Comparison of the integrated up-shifted and down-shifted portions of the D-D proton spectrum shown in Figure 5.4-1.

An explanation of the discrepancy between the up-shifted and down-shifted portions of the proton spectra is provided by the fraction of fusion events that occur in the wall of the HOMER IEC device. The FIDO diagnostic is situated to view a portion of the wall on the opposite side of the chamber from the diagnostic port. Thus it is capable of observing fusion events that occur on the far side of the chamber but not the near side. This provides a reasonable explanation for the increased counts in the down-shifted portion of the spectra since fusion events that occur in the far wall will necessarily have a v_{cm} component directed away from the FIDO detector. If the up-shifted counts in the D-D proton spectra are taken to be representative of the beam-background fusion reactions occurring the volume of the chamber then the additional 5%-20% of counts

seen in the down-shifted portion of the spectra may indicate that approximately 5%-20% of the fusion events that occur in HOMER occur in the vacuum chamber wall. This is qualitatively consistent with experiments done by Rusch and Radel in 2007 to coat the chamber wall in Titanium so as to increase deuterium retention in the wall. Their efforts resulted in a 30% increase in neutron rates.

Chapter 5 References

[1] J. H. Nadler, Y. B. Gu, G. H. Miley, "Potential Profile Measurements Using a Collimated Proton Detector" *Review of Scientific Instruments*, 63, 10, 4810-4812 (1992)

[2] T. A. Thorson, Ion flow and fusion reactivity characterization of a spherically convergent ion focus – PhD Thesis – University of Wisconsin – Madison (1996)

[3] Ashley, Kulcinski, Santarius, S. K. Murali, G. R. Piefer, B. B. Cipiti., R. F. Radel, J. W. Weidner, "Recent Progress in Steady State Fusion Using D-^{3}He," *Fusion Science and Technology*, 44, 564 (2003).

[4] S. K. Murali, B. B. Cipiti, J. F. Santarius, G. L. Kulcinski, "Study of Fusion Regimes in an Inertial Electrostatic Confinement Device Using the New Eclipse Disk Diagnostic" *Physics of Plasmas*, 13, 053111 (2006)

[5] K. Masuda, K. Yoshikawa, T. Ohishi, S. Ogawa, H. Zen, T. Takamatsu, "Spatial Distribution of D-D/D-^{3}He Advanced Fuels Fusion Reactions in an Inertial Electrostatic Confinement Device" *Proceedings of the 21st IAEA Fusion Energy Conference* (2006)

[6] Fujimoto, T., Oishi, T., Zen, H., Masuda, K., Yoshikawa, K. "Intensity Distribution of D-^{3}He Fusion Reaction Rate in an IEC Device" *Fusion Engineering*, SOFE 2007

[7] G.A. Emmert and J.F. Santarius, "Atomic and Molecular Effects on Spherically Convergent Ion Flow I: Single Atomic Species" (submitted to *Physics of Plasmas*, 2009)

[8] G.A. Emmert and J.F. Santarius, "Atomic and Molecular Effects on Spherically Convergent Ion Flow II: Multiple Molecular Species" (submitted to *Physics of Plasmas*, 2009).

[9] Fan C**,** Hasted J. B., *Advances in Electronics and Electron Physics*, vol. 13, 63-68 (1960) (Academic Press)

[10] D Bordenave-Montesquieu, D Blanc and R Dagnac "Angular distribution of neutral particles produced by charge exchange in high energy H_3+, D_3+ and D_2H + on H_2O molecule collisions" *J. Phys. B: Atom. Molec. Phys.*, vol. 7, No. 9, 1974

[11] R.P. Ashley, G.L. Kulcinski, J.F. Santarius, S. Krupakar Murali, G.R. Piefer, B.B. Cipiti, R.F. Radel, and J.W. Weidner, *Fusion Science and Technology*, Vol. 44, p. 564 (2003)

[12] computer code SRIM 2006 – available at www.srim.org

[13] H. M. Bosch, G. M. Hale, "Improved Formulas for Fusion Cross-Sections and Thermal Reactivities" *Nuclear Fusion*, **32**, 4, (1992)

[14] D.C. Donovan, D. R. Boris, G. L Kulcinski, J. F. Santarius “OPTIMIZATION OF AN IEC FUSION DEVICE TO INCREASE STEADY-STATE D-D NEUTRON GENERATION RATES” Proceedings of 2008 TOFE meeting

[15] A.L. Wehmeyer, R.F. Radel, and G.L. Kulcinski, "Optimizing Neutron Production Rates from D-D Fusion in an Inertial Electrostatic Confinement Device," September 2004 [presented at the 16th ANS Topical Meeting on Fusion Energy, 14-16 September 2004, Madison WI] (see also UWFDM-1249).

Chapter 6: Negative ions in IEC devices

6.1: Previous Work

Hydrogen anions are a much studied subject that holds important implications for ion sources involved in high energy accelerators, ion beam surface treatments, as well as neutral beam injection schemes for fusion plasmas.[1, 2] The literature on negative ion formation in hydrogen extends back to the 1950's when the first concepts for hydrogen anion sources were explored.[3, 4]

There are two processes of hydrogen anion formation that are particularly relevant for IEC devices, namely electron attachment and charge transfer. Electron attachment, as the name implies, involves the attachment of a thermal electron to a neutral hydrogen gas molecule in an excited vibrational state[5], thus producing a negatively charged hydrogen molecule. The formation of this H_2^- molecular ion is typically followed by its near instantaneous dissociation into H^- and an H atom. However, recent work has shown that metastable states of these hydrogenic molecular anions exist with lifetimes on the order of several to hundreds of μs.

Charge transfer in hydrogen occurs at much higher energies than electron attachment, and involves a transfer of two electrons from background neutral gas to a positive ion moving through the neutral gas at high energy (~100 to ~$1x10^4$ *eV*). This process was among the first means to produce negative ions by simply accelerating positive ions to the *keV* energy range and passing them through a gas target.

The dynamics of negative ions in an IEC potential well help to explain some of the phenomena observed recently in the field of IEC research. Most notably work by both the University of Illinois Urbana-Champaign[6], and the University of Sydney[7] in

Australia have shown experimental results that indicate the outward flow of ions and charge exchange neutrals in IEC devices. The work by Miley et al[8] mentions the phenomena of beamlets of charged particle flow that appear correlated with gaps in the IEC cathode wires. Anions in an IEC would be focused into the gaps between grid wires by the potential perturbations near the cathode. This effect would enhance any already existing ion flow through the grid channels by producing a beamlet of negative space-charge.

The work by Khachan et al. focused on optical spectroscopy measurements of charge exchange neutrals that indicated net outward flow of the fast neutrals in the University of Sydney IEC device. The neutralization of outward flowing deuterium anions would produce this effect, and help to explain the net blue shift observed in the Doppler shift measurements performed by Shrier, Khachan, Bosi, Fitzgerald, and Evans[9]. The work indicates an increasing blue shift with increasing radius. This is consistent with deuterium anions forming through electron attachment and charge transfer and varying radii throughout the device. The total current of anions should be largest nearest the chamber wall as anion current has had the maximum path length to accumulate anions.

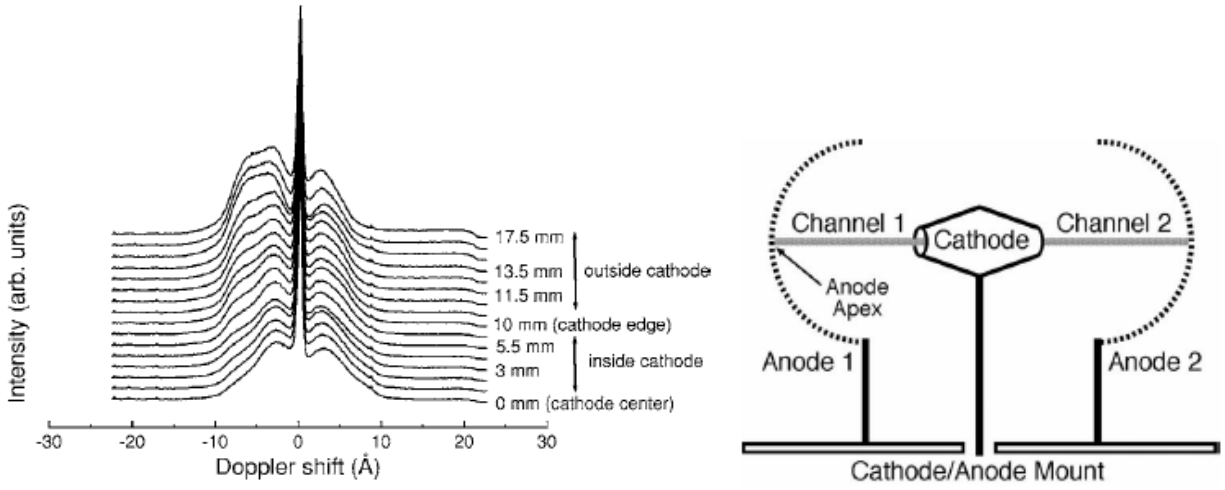

(a) **(b)**

Figure 6.1-1: (a) Doppler shift measurements at increasing distances from the center of a (b) double ring cathode. Plasma conditions were -10 kV on the cathode, and 15 mTorr background pressure[9].

6.2: Theory of negative ion formation

6.2-a: Dissociative Thermal Electron Attachment to Hydrogen

Thermal electron attachment to hydrogen molecules results in the dissociation of a hydrogen molecule into an H^- anion and neutral H atom. The time frame for this dissociation can range from a few *fs* to a few *ms*, depending on the rotational and vibrational states of the hydrogen molecule in question[10]. Amidst a population of thermal electrons ($kT \leq 1\ eV$) the dissociative attachment reaction is such that hydrogen anions can become a significant fraction of the charge carriers in a low temperature plasma. (See Figure 6-2-1.) However, for long-lived meta-stable molecular anions to form, the molecule must be in highly excited angular momentum states. Modeling work done by Čížek, Horáček, and Domcke indicates that long-lived meta-stable states exist for H_2^- when the angular momentum quantum number of the molecular system, J, is greater than 25. Similar conditions exist for long lived D_2^- formation[13], with J values in

the range of 35-40. When these conditions are met, meta-stable lifetimes exceeding hundreds of μs are possible.

$$D_2 + e \rightarrow D_2^{-(m)} \rightarrow D^- + D \qquad (6\text{-}1)$$

the meta-stable lifetime τ = ~1 μs to ~1 *ms.*

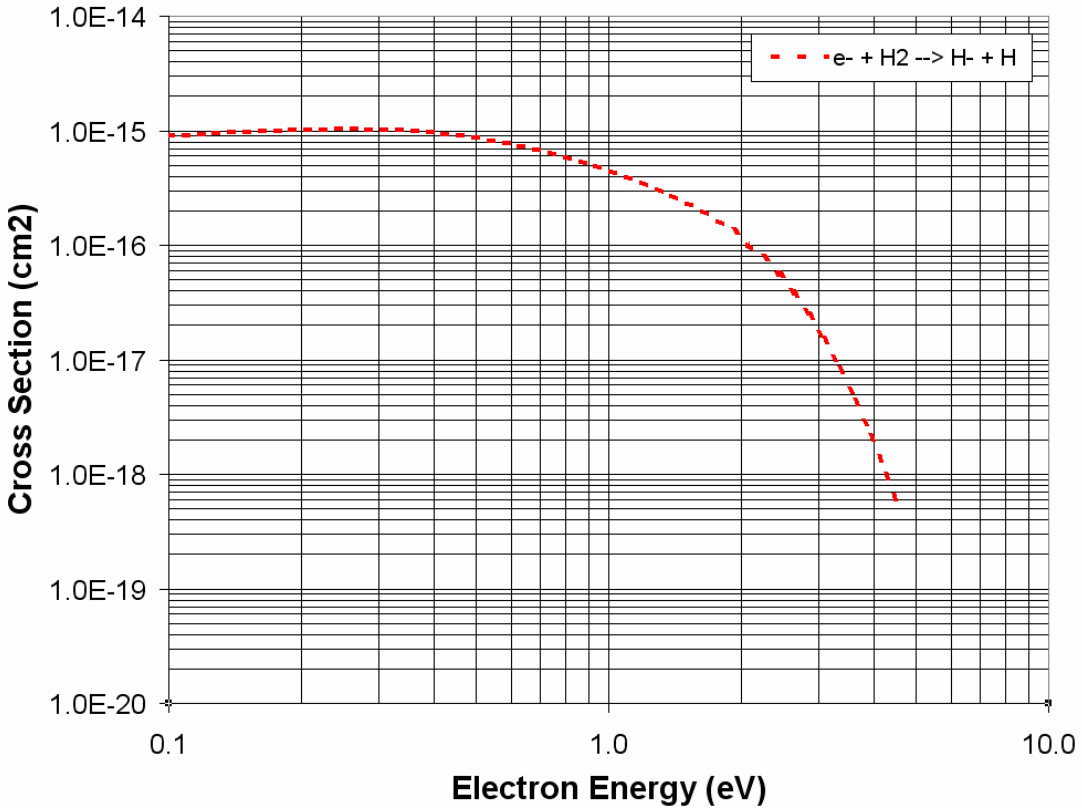

Figure 6-2-1: Dissociative attachment cross section for hydrogen [12]

In IEC devices the cathode region provides the necessary conditions for negative hydrogen ions to be produced through dissociative attachment. The neutral gas in glow discharge type IEC devices is dispersed throughout the volume of the device so there is ample neutral gas located near the cathode. In addition there is an abundant supply of

thermal electrons produced from secondary emission at the cathode wires from positive ion impact. Also, cathode wires are typically heated by ion impact to temperatures in the 1200 K range, which provide a means to excite the background hydrogen gas into the excited rotational states necessary for the formation of molecular hydrogen anions. It may also be the case that sputtering of implanted hydrogen from the cathode wires could account for the production of excited hydrogen molecules that are susceptible to electron attachment. In either case, the J states of the hydrogen molecules produced near the cathode could be high enough to produce molecular hydrogen anions.

6.2-b: Charge Transfer of Hydrogen Ions in IEC Devices

As mentioned previously, charge transfer is fundamentally different from electron attachment in that it occurs between positive ions and background neutral gas at higher energies of a few keV. Positive deuterium ions form three species, D^+, D_2^+, and D_3^+, all of which can undergo charge transfer to produce deuterium anions when traversing a gas target. Examples are shown below:

$$D_3^+ + D_2 \rightarrow D^- + 2D^+ + 2D \quad (6\text{-}2)$$

$$D_2^+ + D_2 \rightarrow D^- + 2D^+ + D \quad (6\text{-}3)$$

$$D^{fast} + D_2 \rightarrow D^- + D^+ + D \quad (6\text{-}4)$$

$$D^+ + D_2 \rightarrow D^- + 2D^+ \quad (6\text{-}5)$$

Observations of positive hydrogen and deuterium ion beams passing through gas targets of the same species indicate that a few percent of the beam current can be H^- or D^- ions upon exiting a gas target of sufficient thickness[11, 12]. In IEC devices, positive ions will undergo continuous oscillations within the spherically symmetric potential well. This

leads to an effective path length through the background neutral gas that can be much larger than the device dimensions. The positive ions in a gridded IEC device will eventually undergo one of four processes as they oscillate in the IEC potential well:

1. The positive ion will be lost to a collision with the cathode grid.
2. The positive ion will undergo nuclear fusion with either background gas or another ion.
3. The positive ion will undergo a charge transfer reaction that creates a fast neutral and a positive ion. The fast neutral can also produce an anion in a subsequent reaction; however the mean free path for this to occur is a few meters.
4. The positive ion will undergo a charge transfer reaction, or series of charge transfer reactions that create a fast negative ion along with a cold positive ion.

The likelihood of producing negative ions through charge transfer is qualitatively significant provided that the grid transparency is sufficiently high to ensure that interactions with the background gas are more likely than interactions with the cathode.

6.3: Experimental Setup – Deuterium anion detection in the HOMER IEC device

The detection of deuterium anions in the UW-IEC device was accomplished with two separate diagnostics:

1. A magnetic deflection experiment, in which a variable electromagnet was used to measure the energy of negative ions with a specific charge to mass ratio streaming from the center of the UW-IEC device.

2. A current collection plate with secondary electron suppression (Faraday trap) coupled with a weak permanent magnet tuned to deflect electrons emitted from the cathode but allow the detection of negative ions born within the anode of the UW-IEC device.

The magnetic deflection energy analyzer was able to measure the energy spectra of negative ions in the UW-IEC device to a resolution of ±1 keV. The Faraday trap was used as a means of confirming the presence of deuterium anions and to examine the manner in which the negative ion current scales with the operation parameters of the UW-IEC device.

6.3-a: Magnetic Deflection Energy Analyzer

The magnetic deflection energy analyzer diagnostic (Figure 6.3-2) operates by first collimating the divergent flux of deuterium anions emanating from the IEC into a narrow beam with a pair of 2 *mm* diameter lead irises. This beam of deuterium anions is then passed through a variable electromagnet which causes the beam to deflect in a direction perpendicular to both the velocity of the beam and the applied magnetic field. The angle of the deflection of an incoming particle, with charge q and mass m, when passing through a constant magnetic field, $\vec{B}$, is given by the following expression:

$$\sin\theta_d = \frac{at}{v} \qquad (6\text{-}6)$$

where $a \equiv \left| \frac{q}{m} \vec{v} \times \vec{B} \right|$ is the magnitude of the acceleration due to the magnetic field, *t* is the time spent in the magnetic field, and *v* is the velocity of the ion. The time *t* can be defined as $t = l/v$, where *l* is the path length of the particle in the region of significant and nearly constant magnetic field. The acceleration due to the constant magnetic field can be expressed as:

$$a = \frac{qpB}{m^2} \tag{6-7}$$

where *p* and *B* are the magnitudes of the ion momentum and magnetic field respectively. Thus equation 6-6 can be re-expressed as:

$$\sin\theta_d = \frac{qlB}{p} \tag{6-8}$$

Equation 6-8 indicates that the deflection angle, θ_d, is dependent on the charge to mass ratio, the spatial extent of the magnetic field, and magnitude of the magnetic field.

Once the anions have been deflected by the electromagnet they will continue towards the detector until they encounter a smaller lead iris with a diameter of 100 μm. This iris samples a narrow portion of the resulting fan-shaped beam of anions, consequently isolating a narrow band of the velocity spectrum of deuterium anions emanating from the IEC device. A silicon charged particle detector is used to detect the portion of the beam passing through the lead iris. Counts from the silicon charged

particle detector are collected by a single channel analyzer (SCA). The count rate in the SCA was recorded as a function of applied magnetic field from a GMW 5403 electromagnet with a 76 mm diameter cylindrical cross section magnet pole. The magnetic field was measured using a F.W. Bell 5070 gauss-meter with the transverse magnetic field probe mounted to the side of the bending section of the experiment. Spectra as a function of magnetic field were obtained using this setup. The SIMION[13] charged particle optics software package was then used to simulate deuterium anion trajectories in the magnetic field produced by the GMW 5403 electromagnet. Thus for the magnetic field settings applied during the experiments the energy of anions directed into the charged particle detector could be calculated, yielding a measure of $\text{number of ions}/(\text{keV}\cdot\text{amu})$. The calibration curve for the magnetic deflection energy analyzer is shown in Figure 6.3-1.

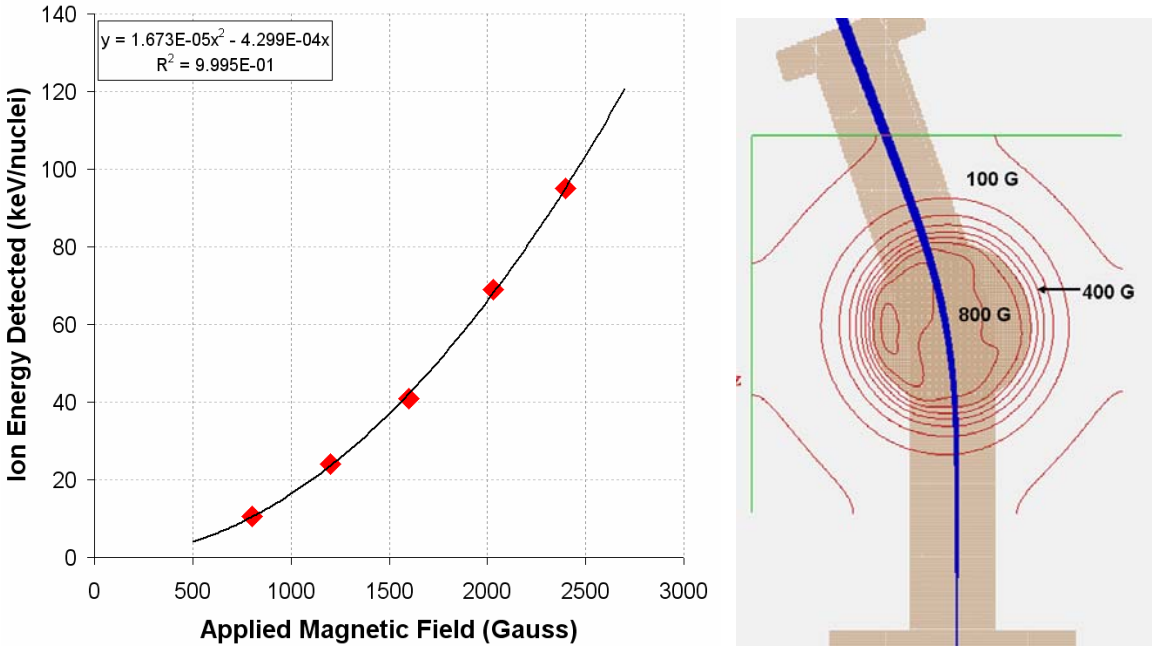

Figure 6.3-1: The anion energy to applied magnetic field calibration curve for the magnetic deflection energy analyzer. The calibration function is shown in the top left of the graph. To the left is an image from SIMION of a 10.5 keV D^- ion traversing the simulated magnetic field configuration.

The small iris allows the acquisition of high resolution energy spectra of the deuterium anions. Energy resolution of ±1 keV was achieved using this technique. Energy spectra showing clear structure are shown in the following sections. The energy resolution was determined using the SIMION code to determine the ΔE necessary to account for a 0.1 mm change in the position of anion beam impact on the detector face.

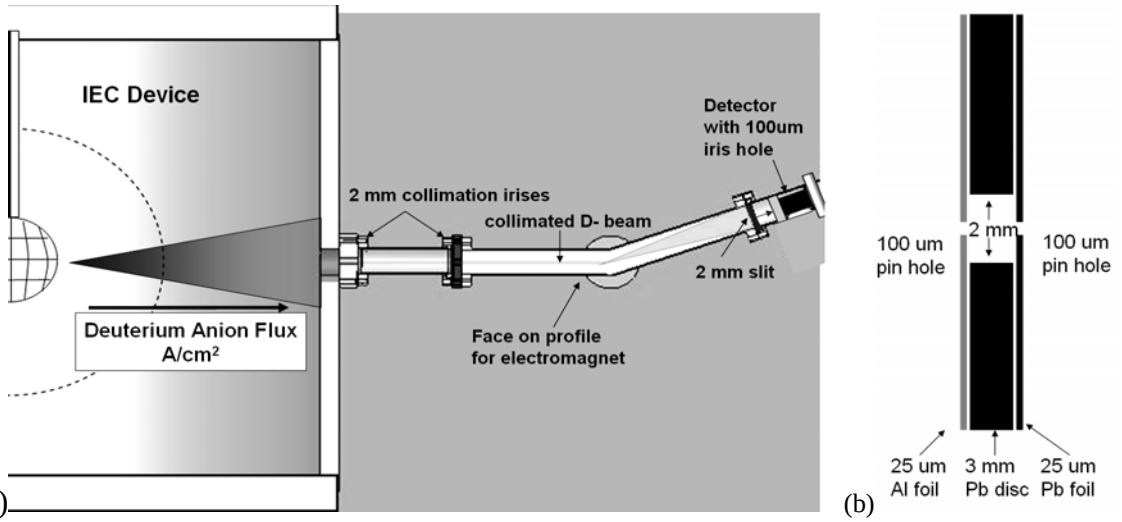

Figure 6.3-2: (a) shows schematic of the magnetic deflection energy analyzer. (b) Shows a closeup of the construction of the 100 μm iris hole (not to scale) used to both limit particle flux to the detector and narrow the energy resolution of the diagnostic. The 100 μm iris sits on the face of the detector.

6.3-b: Faraday Trap Diagnostic

The Faraday trap diagnostic operates by collecting negative ions on a 0.7 cm^2 aluminum current collection plate and suppressing the emission of secondary electrons from the plate with a transparent steel mesh biased to -50 V relative to the collection plate. With the UW-IEC device in operation this configuration resulted in a negative current corresponding to the collection of electrons and negative ions diverging from the center of the UW-IEC device.

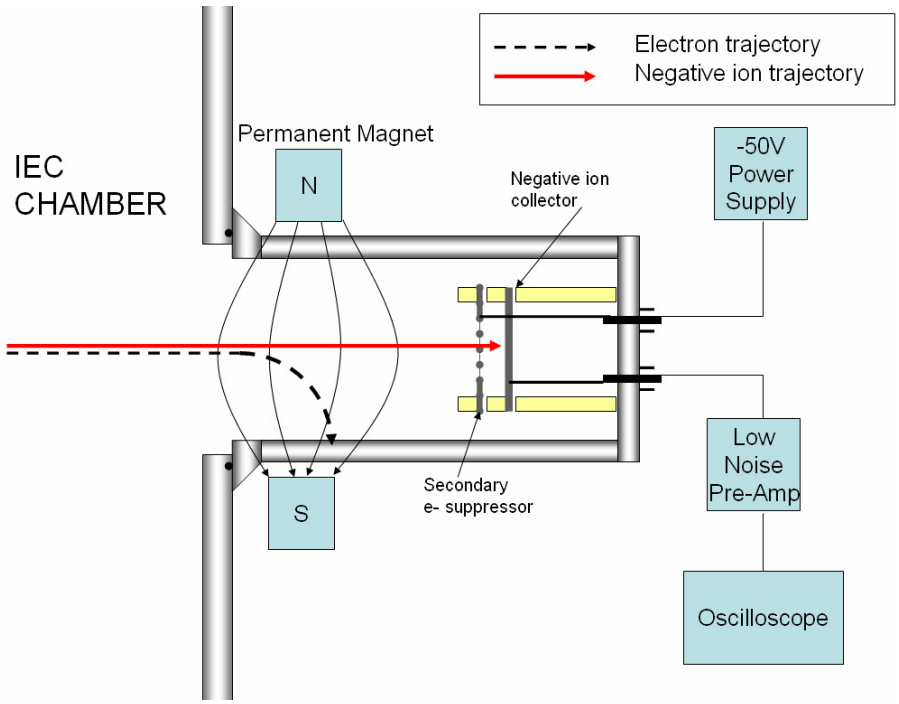

Figure 6.3-3: Shows a schematic of the Faraday trap diagnostic illustrating differing negative ion and electron trajectories. The negative ion collector plate and secondary electron suppressor grid are isolated from the chamber and each other by ceramic standoffs. The magnetic field magnitude is ~100 gauss.and the magnetic field's orientation has been rotated by 90º to show the spatial extent of the magnetic field.

In order to isolate the negative ions from the high energy electrons a weak permanent magnet with a ~100 gauss field was utilized to deflect the high energy electrons away from the collection plate while leaving the trajectory of the negative ions relatively unperturbed. This is illustrated in Figure 6.3-3.

The secondary electron suppressor grid is isolated from the negative ion collector plate by ceramic standoffs, and both of these metallic components are isolated from the chamber by additional standoffs. The ceramic standoffs are configured as alumina columns to minimize the area over which secondary electrons are can be produced on the ceramic surface, near the charge collection plate. Secondary electrons can be produced

from oblique angle fast neutral impact on the insulator. The negative ion current collected by the Faraday trap is fed to a Stanford Research Systems SR-570 Low Noise Current Pre-Amplifier through isolated BNC feedthroughs. The pre-amplifier provides +5 V of bias to drive the negative ion signal collection. The amplifier is able to measure negative ion currents a fraction of a nanoamp reliably on the 1 nA/V amplification setting. This signal is then fed to a Tektronix TDS-220 oscilloscope. This allowed the total negative ion current to be measured in addition to the spectral measurements made with the magnetic deflection energy analyzer diagnostic. The Faraday trap diagnostic took measurements at two locations on the UW IEC device. These are shown below in Figure 6.3-4.

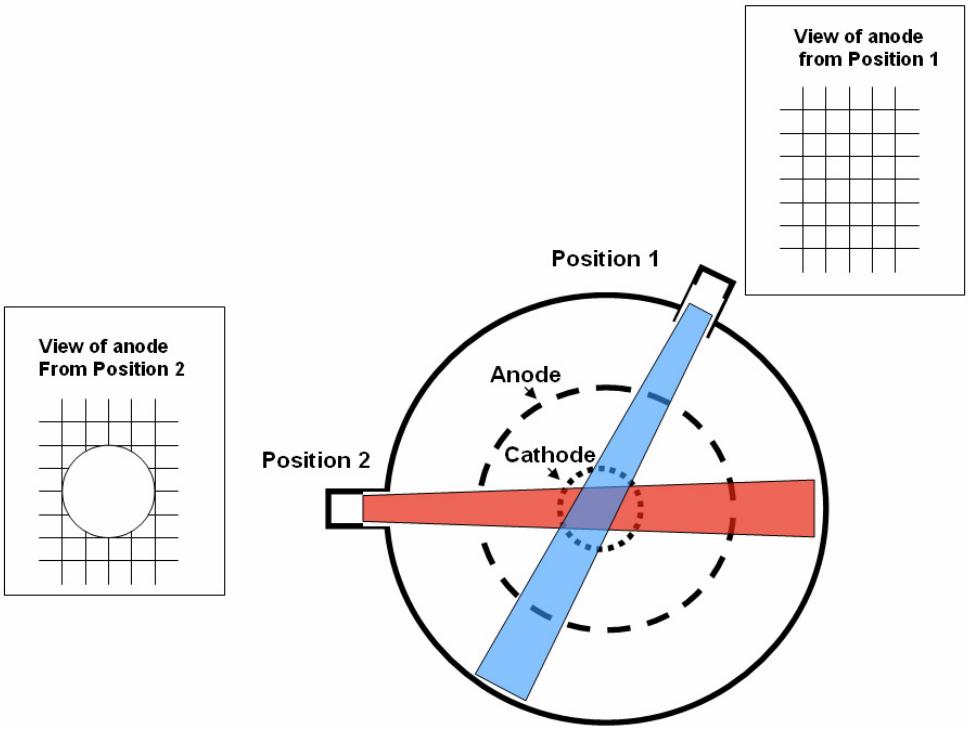

Figure 6.3-4: Shows the two positions and corresponding lines of site on which the Faraday trap diagnostic was oriented. Top down view of the cylindrical vacuum vessel of the HOMER IEC device.

The two locations collected vastly different amounts of the negative ion current emanating from the UW IEC device. Position 1's view of the device was moderately obstructed by a cross in the anode wires, whereas position 2 was aligned for its view to be roughly centered through an anode and cathode channel. The resulting data obtained from these two positions will be detailed in following sections.

6.4: Experimental Results

6.4-a: Magnetic Deflection Energy Analyzer

The energy analyzer diagnostic was used to examine the effects of cathode voltage and background pressure on the structure of the deuterium anion energy spectra. In all the spectra there was structure indicating the presence of negative ions produced from the variety of processes mentioned previously, charge transfer and thermal electron attachment. Figure 6.4-1 shows the voltage scan performed on the UW IEC device with the cathode current and background pressure held constant at 30 mA and 2 mTorr, respectively. The spectra are shown offset from each other on the y-axis to illustrate the manner in which the spectra evolve as the cathode voltage is changed. The structure of the spectra can be fit by a five Gaussian structure. The three main Gaussian peaks can be accounted for by charge transfer processes involving positive molecular deuterium ions moving at high energy in the intergrid region. The smaller peak at nearly the full cathode energy, and the smaller peak at ½ the cathode energy, originate from thermal electron attachment to excited background gas near the hot cathode. An enhanced view of the 100 kV case is shown in the upper right hand corner of Figure 6.4-1.

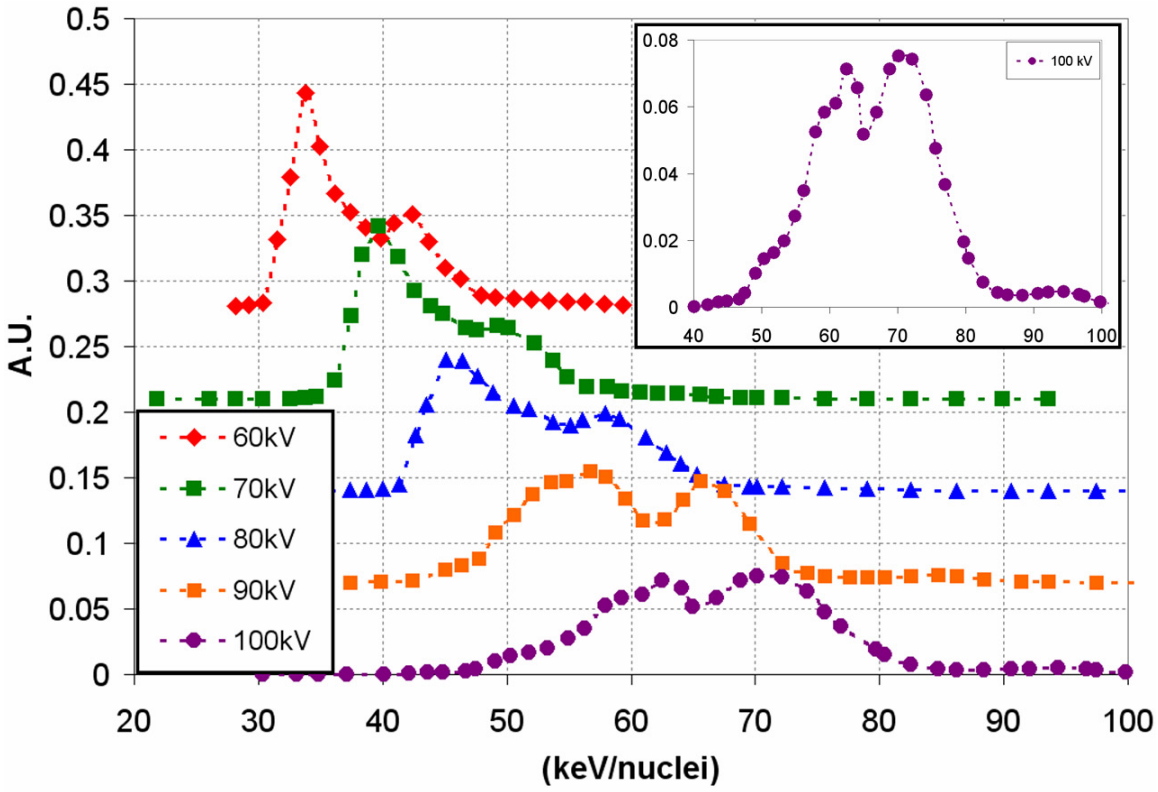

Figure 6.4-1: The deuterium anion spectra are plotted for several cathode voltages offset by 0.07a.u. for every 10 kV. These show a clear hardening of the spectra with increasing cathode voltage. In addition the spectra change from being dominated by D_3^+/D^- at lower voltages (60 kV – 80 kV) charge transfer ions to being dominated by D^+/D^- charge transfer ions at higher voltages (90 kV-100 kV). Error bars from counting statistics are negligible on the scale shown. Detail of 100 kV data set shown in upper right.

Detailed views of the 90 kV and 100kV cases from Figure 6.4-1 are shown in Figure 6.4-2 and 6.4-3. Close observation of the 90 kV spectrum (Figure 6.4-2) shows five peaks discernable in the data. In Figure 6.4-2 these peaks are denoted “gauss1”, “gauss2”, “gauss3”and “gauss4”. The “gauss1” through “gauss3” peaks result from charge transfer reactions which occur in the intergrid region where D_3^+ to D^-, D_2^+ to D^- and D^+ to D^- reactions respectively, occur through the electron transfer processes described earlier in this chapter. The “gauss4” peak results from D^- formed via thermal electron capture near the cathode of the HOMER IEC device. These anions are detected with the full cathode

energy. The "gauss5" fit is accounted for by metastable D_2^- from thermal electron attachment.

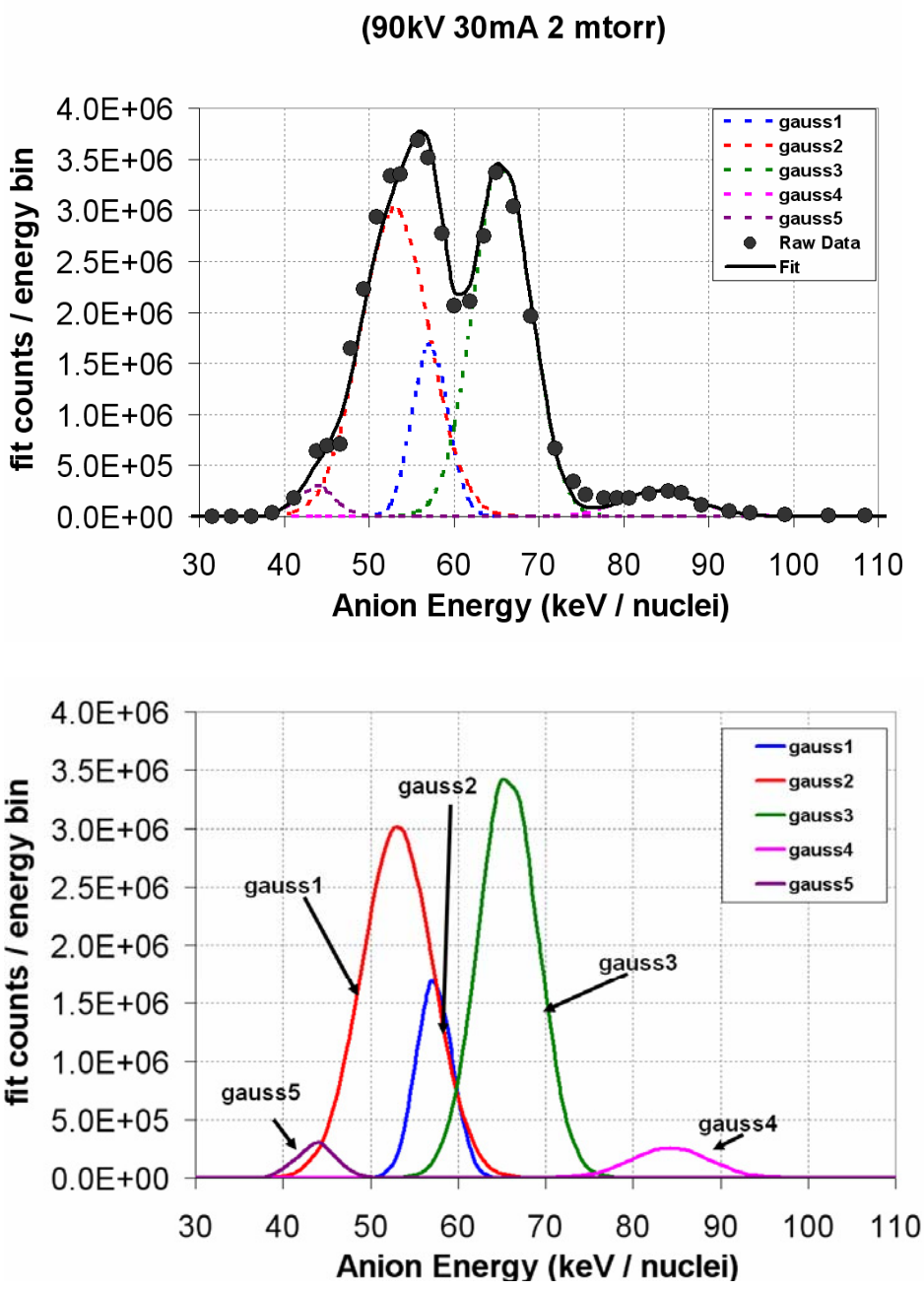

Figure 6.4-2: Detailed view of the 90 kV, 30 mA, 2 mTorr, data set from the voltage scan in Figure 6.4-1. It shows the 4 Gaussian least squares fit used to accurately replicate the structure from the data set. The fits "gauss1", through "gausss3" account for deuterium anions produced through D_3^+/D^-, D_2^+/D^- and D^+/D^- charge transfer reactions respectively. The "gauss 4" fit is accounted for by D^- formed at the cathode via thermal electron attachment to background neutral gas. The "gauss5" fit is accounted for by meta-stable D_2^- formed via thermal electron attachment at the cathode.

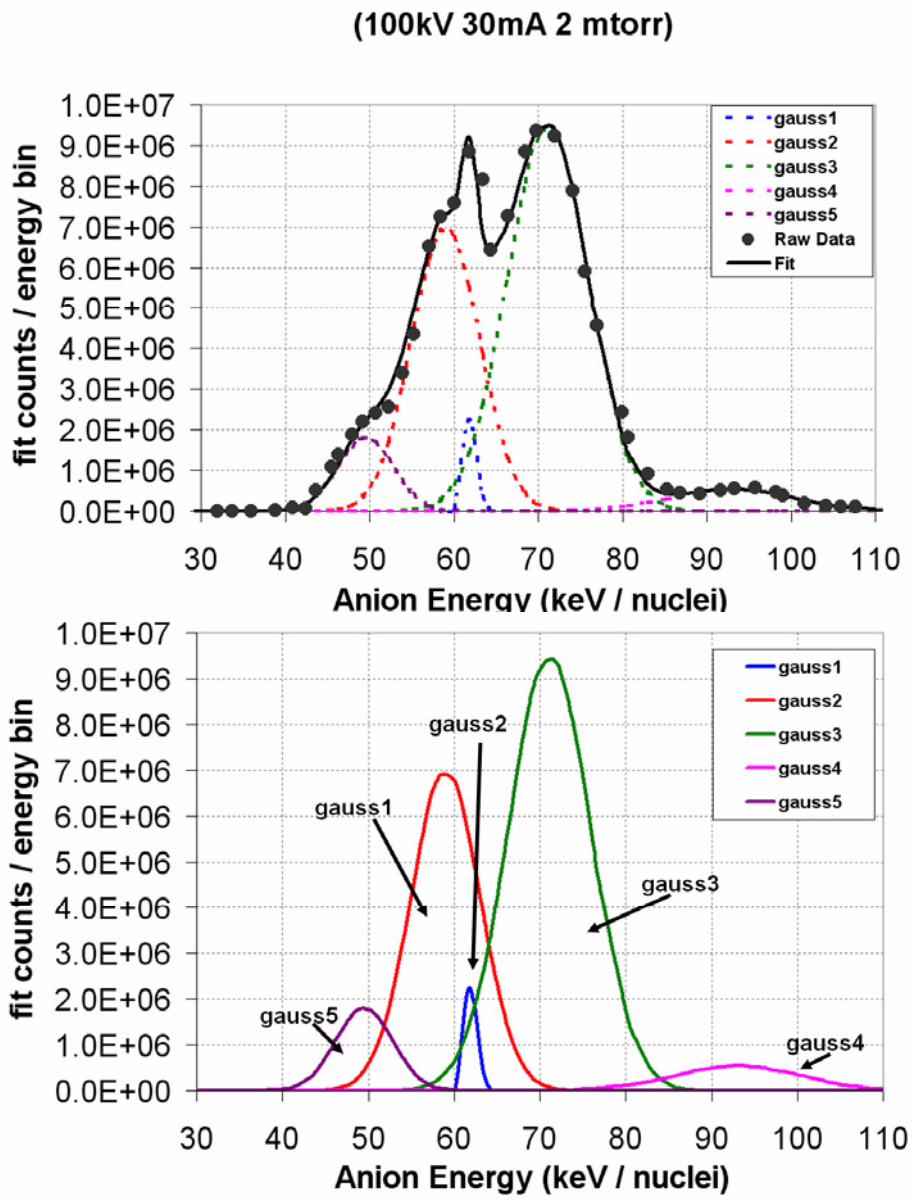

Figure 6.4-3: Detailed view of the 100 kV, 30 mA, 2 mTorr, data set. It shows the 5 Gaussian least squares fit used to accurately replicate the structure from the data set. The fits "gauss1", "gausss2" and "gausss3" account for deuterium anions produced through D_3^+/D^-, D_2^+/D^- and D^+/D^- charge transfer reactions respectively. The "gauss 4" fit is accounted for by D^- formed at the cathode via thermal electron attachment to background neutral gas. The "gauss5" fit is accounted for by meta-stable D_2^- formed via thermal electron attachment at the cathode.

Figure 6.4-3 also illustrates the five peaks discussed from Figure 6.4-2 with a larger ½ energy peak that indicates a more significant contribution from what appear to be D_2^- ions. The "gauss5" peak implies the presence of these molecular anions. A less

distinct form of this half cathode energy peak is indicated around 45 keV/nuclei in Figure 6.4-2 as well. This half energy peak is also consistent with molecular deuterium anions (D_2^-) formed in the cathode region.

Recent theoretical work by Čížek, Horáček, and Domcke[13] presents an explanation for reported experimental observations of molecular hydrogenic anions. They suggest that diatomic hydrogen or deuterium molecules in high angular momentum states can undergo thermal electron capture and retain the electron in a metastable state with a substantial mean lifetime (~1 μs – ~1000 μs). The work corroborated experimental results by Ober, et. al.[14] and Golser, et. al.[15] that measured long lived metastable molecular anion states for deuterium and hydrogen. The mean lifetime of these metastable states varied from ~1 μs to ~1000 μs. The distance of the anion detector from the cathode indicates that the detected D_2^- had a minimum lifetime of ~0.5 μs. This is consistent with the experimental and theoretical results mentioned previously.

This previous work provides a reasonable explanation for the signature of D_2^- ions in the energy spectra measured by the magnetic deflection energy analyzer. The cathode of the UW device reaches temperatures in the range of 1200 K. In this temperature regime, the production of metastable molecular deuterium anions seems reasonable, since the neutral gas near the cathode wires would likely be in excited rotational and vibrational states. In the presence of these excited neutral gas molecules is an abundance of thermal electrons created by secondary and thermionic electron emission from the cathode wires. Qualitatively, this implicates the cathode region of the UW IEC device as an ideal place for molecular deuterium anions to form. If D_2^- ions are formed near the cathode the lifetimes of these metastable states are sufficient to allow the molecular

anions to be accelerated out of the device and into the energy analyzer's charged particle detector before the molecular ion dissociates. Thus it is reasonable to expect the presence of the molecular deuterium anions within a gridded IEC device.

Figures 6.4-2 and 6.4-3 indicate that both charge transfer and thermal electron attachment are important processes within the HOMER IEC device. A schematic of the charge transfer process is shown in Figure 6.4-4a. In this figure the initial incoming D_3^+ ion undergoes a charge transfer after it has acquired 30 keV of kinetic energy from the potential well. Upon undergoing charge transfer the resulting D^- anion still has 10 keV of radially inward directed kinetic energy. This is because the kinetic energy of the initial D_3^+ ion is divided between three nuclei. Thus the D^- anion continues to a position in the potential well with -40 kV of potential. The D^- anion is then accelerated out of the device with 40 keV of kinetic energy, which can be detected in the magnetic deflection energy analyzer. Figure 6.4-4b illustrates the process of thermal electron attachment that can occur with excited gas molecules near the cathode. With the formation occurring in the region of relatively flat potential within the cathode the anions are able to attain full energy as they are accelerated out of the system by the anode-cathode potential difference. However, the magnetic deflection energy analyzer measures the kinetic energy/amu of the anions. Thus a full cathode energy D_2^- ion will be measured at the same deflection angle as a D^- ion with half the cathode energy. This accounts for the "gauss5" peak in Figure 6.4-3 (centered at 50 keV/nuclei). Thermal electron attachment also accounts for the full cathode energy peaks present in the other spectra (6.4-1 and 6.4-6). The full energy peak was a repeatable feature of every data set taken with the magnetic deflection energy analyzer.

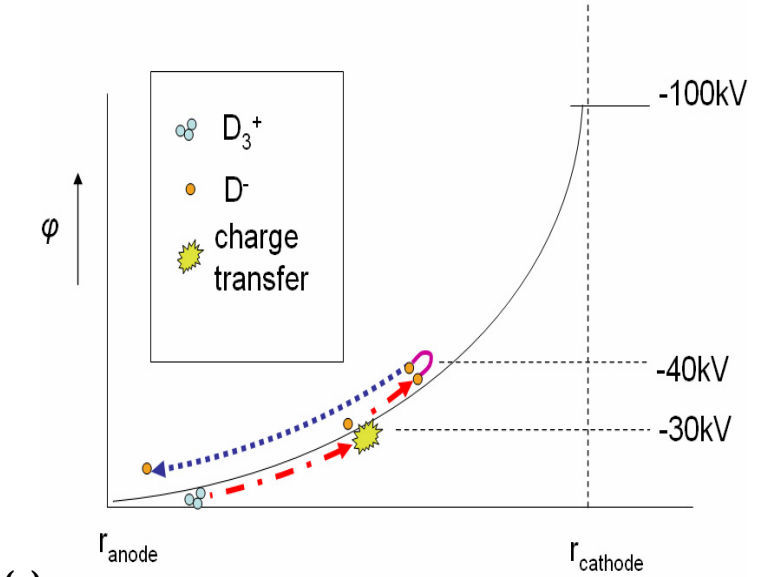

(a)

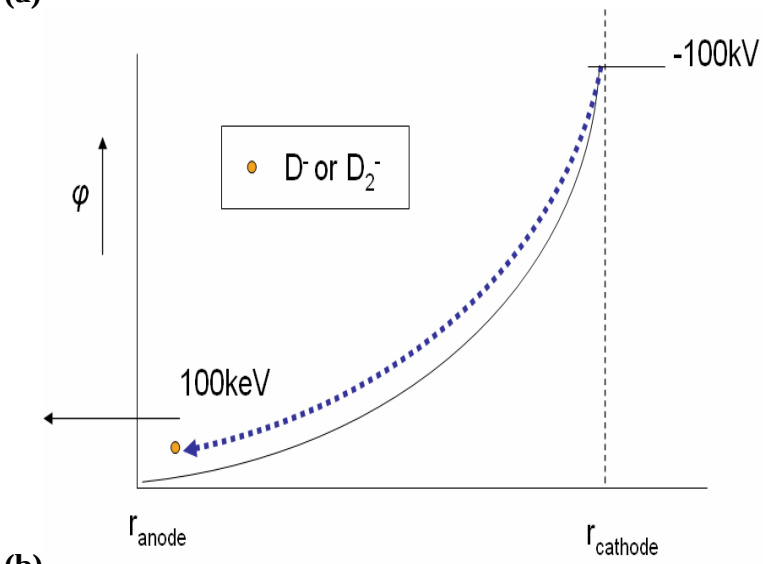

(b)

Figure 6.4-4: Illustrates examples of the resulting deuterium anion energies from (a) charge transfer reactions in the intergrid region of the UW IEC device, and (b) thermal electron attachment near the cathode of the UW IEC device. Note that the anions resulting from the thermal electron attachment will have 100 keV/anion so a D^- ion will have 100 keV and a D_2^- ion will have 50 keV/nuclei with the cathode at 100 kV.

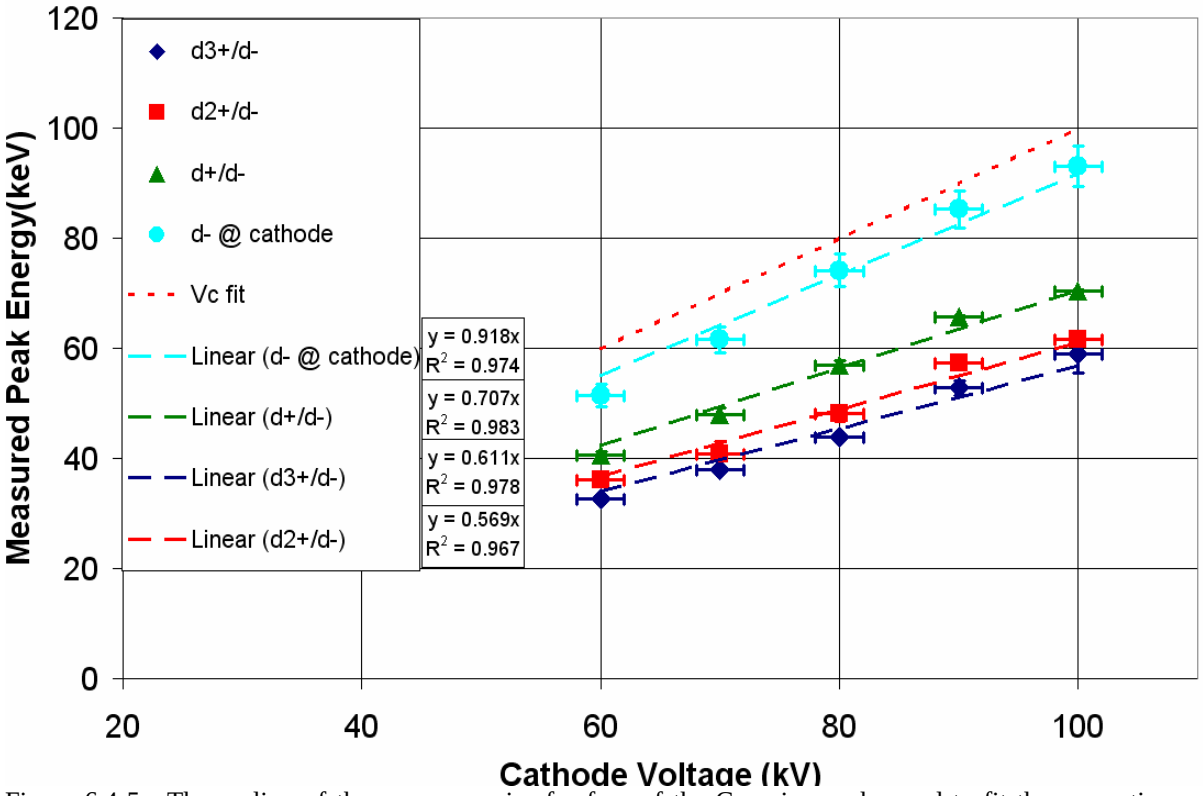

Figure 6.4-5: The scaling of the mean energies for four of the Gaussian peaks used to fit the magnetic deflection energy analyzer data is shown. The cyan colored data ● is associated with the D^- peak. The scalings of the charge transfer peaks are shown at left and are color coded.

As the voltage on the IEC cathode is changed the negative ions peaks, in the magnetic deflection energy analyzer, undergo shifts in their detected energy. Most notably the position of the thermal electron attachment peaks scale with the cathode voltage (See Figure 6.4-5). The other three, more prominent peaks in the anion spectra are accounted for by the D_3^+/D^-, D_2^+/D^- and D^+/D^- charge transfer reactions respectively. Consequently, if it is assumed that the detected anions have not interacted appreciably with the background gas on the way out of the IEC, the energy of the positive molecular ions that birthed the anions can be calculated. The results of these calculations are shown in Table 6.4-1.

Cathode Voltage (kV)	D3+/D-	±	D2+/D-	±	D+/D-	±
60	24.5	0.2	24.0	0.6	20.3	0.4
70	28.5	0.3	27.2	2.3	24.0	0.8
80	32.9	0.3	32.0	1.4	28.5	0.5
90	39.6	1.0	38.2	0.4	32.9	0.2
100	44.3	2.6	41.0	0.4	35.2	0.1

Table 6.4-1: Calculated positive deuterium ion energies based deuterium anion energy spectra for varying cathode voltages in the HOMER IEC device. D_3^+/D^-, D_2^+/D^- and D^+/D^- refer to which charge transfer reactions are responsible for the peaks.

The deuterium anion spectra indicate that the positive ions that undergo charge transfer uniformly attain 30-40% of the kinetic energy of the cathode potential before becoming anions. This indicates that the most energetic ions in the IEC device are actually the negative ions. However, the positive ions still seem to contribute more to nuclear fusion since they are confined in the cathode's potential well for multiple passes while the anions are accelerated out of the system in a single pass.

A scan of the background neutral gas pressure was also performed on the UW IEC device with results shown in Figure 6.4-6. The pressure scan was performed with the cathode voltage and cathode current held constant at 90 kV and 30 mA, respectively. The charge transfer peaks are most prominent in this data set, and the data indicates that the charge transfer peaks are significantly affected by changes in neutral gas pressure. At low pressures (0.35 mTorr to 1 mTorr) the D^+ to D^- peak dominates the spectra. At high pressures (2 mTorr to 3.75 mTorr) the D_3^+ to D^- peak dominates the spectra. Between these two pressure regimes is a transition region. This is most likely linked to changes in the molecular ion species mix in the source region plasma as the pressure is varied[16].

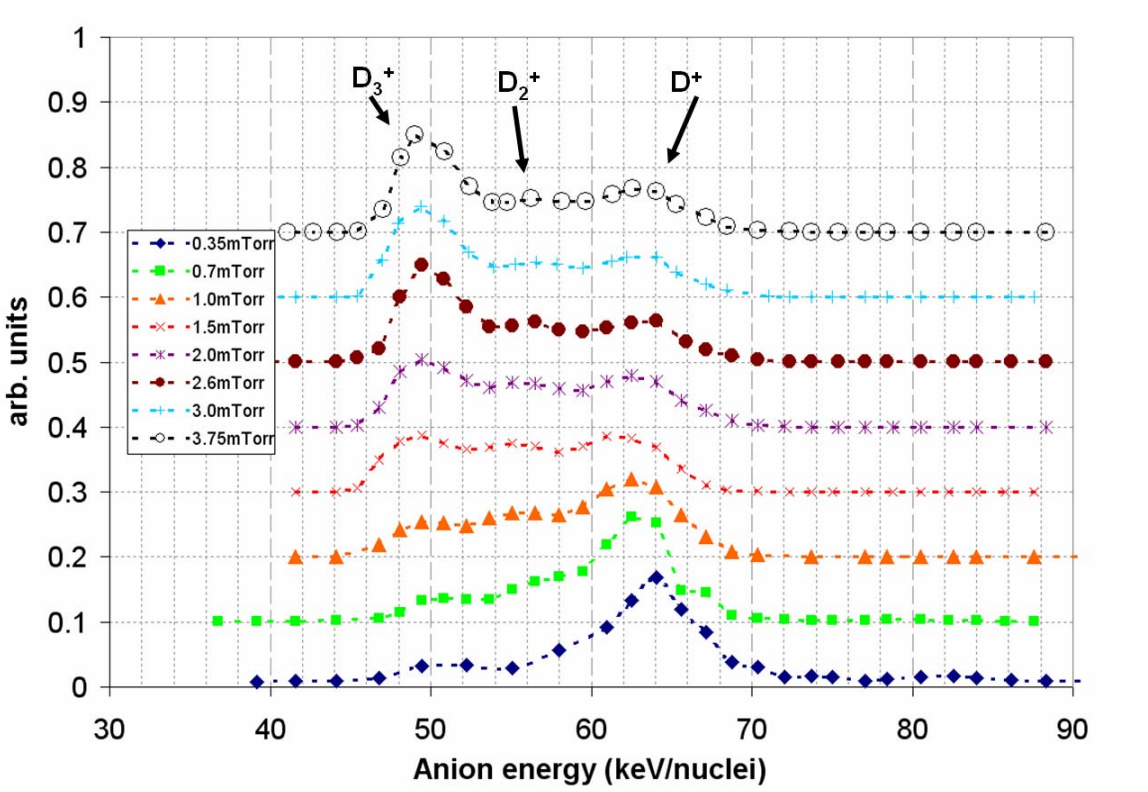

Figure 6.4-6: Pressure scan with cathode voltage and cathode current held constant at 90 kV, and 30 mA respectively. Note that the ratio of the D_3^+ / D^- peak to the D^+ / D^- peak changes dramatically over the scan. Each successive data set is offset by 0.1 arbitrary units.

The energy spectra obtained by the magnetic deflection energy analyzer indicate that the anion creation processes of charge transfer and thermal electron attachment are significant to the operation of IEC devices in which a substantial background neutral pressure (>0.1 mTorr) is present.

6.4-b: Faraday trap experimental results

The Faraday trap diagnostic was able to show that negative ions were being collected by showing that negatively charged particles were still impacting the collector plate even in the presence of a 100 G magnetic field. The UW IEC device is capable of

generating electrons with a maximum energy of 200 keV. It is not possible for electrons of this energy to both traverse the 100 gauss magnetic field and maintain a trajectory that intersects the Faraday trap collector.

Measurement of the fraction of the current into the Faraday trap due to deuterium anions and electrons, respectively, were performed by measuring the collector current with and without the deflection field in place. The deflection field was then increased to 400 G to show that the negative ions were not substantially perturbed by the presence of the deflection field.

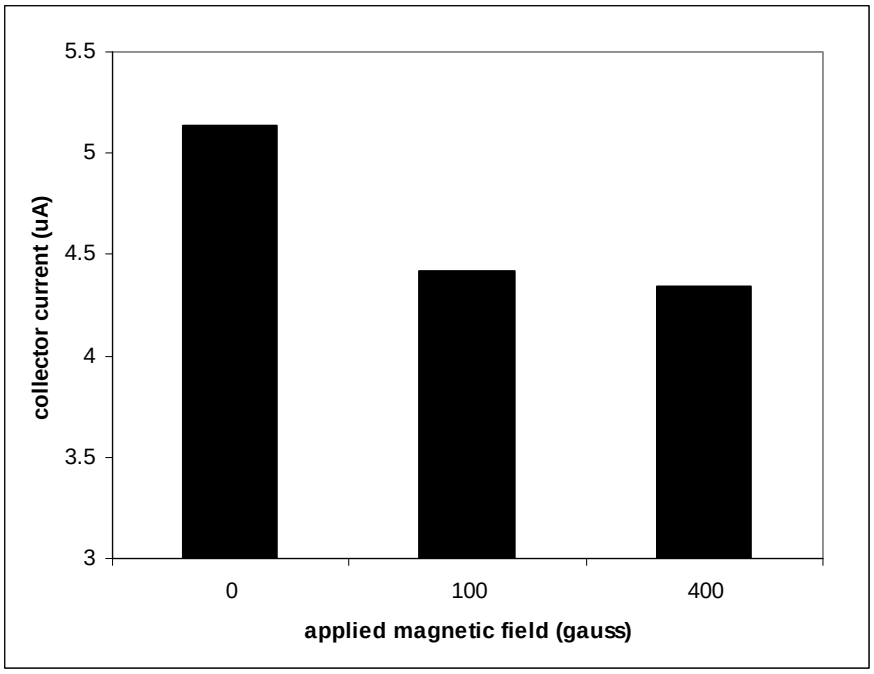

Figure 6.4-7: Varying the applied magnetic field prior to the collector plate in the Faraday trap illustrates how electrons are easily deflected with a modest magnetic field of 100 G. IEC conditions were 80 kV on the cathode, 30 mA of cathode current, 2 mTorr of background pressure.

Figure 6.4-7 illustrates the effect of changing the applied magnetic field from 0 G, to 100 G, to 400 G. The 0 – 100 G change results in an 18% decrease to collector current,

effectively accounting for the fraction of the current resulting from secondary electrons from the cathode. The 100 – 400 G change results in a 2% decrease in collector current, illustrating that the remaining negative ions should be essentially unperturbed by the initial 100 G field used to deflect the secondary electrons. This data also gives the surprising result that, at least along the field of view of the Faraday trap, secondary electrons make up a relatively minor portion (18%) of the diverging current in the device. This may be an effect of channels of electron and anion current caused by the cathode geometry and their relative position with respect to the collection region of the Faraday trap diagnostic. Potential perturbations brought about by the discrete nature of the cathode grid wires in a gridded IEC device may also play a major role in determining the flow of charged particles, particularly negative charged particles. Figure 6.4-8 shows a schematic of potential perturbations around the grid wires of a cylindrical IEC cathode, and the spherical cathode of the present study will have analogous 3-D perturbations.

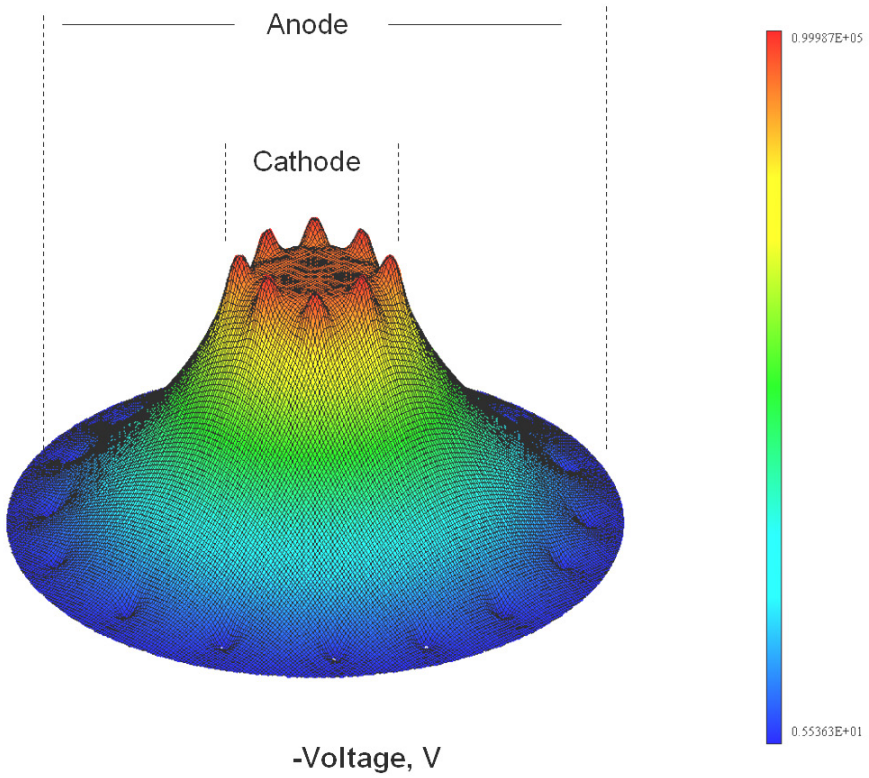

Figure 6.4-8: The schematic above shows a 2-D cylindrical representation of the potential profiles between an IEC cathode and anode with -100 kV on the cathode. The perturbations near the cathode in the 2-D representation are ~5-10 kV. These perturbations will be reduced in a 3-D geometry but will still substantially effect cold anions and electrons born near the cathode.

The variations in potential near the grid wires can act as a mechanism to focus anions and electrons born near them in the relatively field free region within the cathode. Such focusing would result in channels of negative charged particle flow. The spatial extent of such channels would be on the order of the holes formed by the cathode wires. The beams should have a focal length dependent on the mass of the charged particles being focused, the cathode voltage and the cathode geometry. Thus it is possible that the position of the Faraday trap did not provide a full measure of both the anion and electron current leaving the device. The mapping of these ion flow channels should be the subject of future work.

The Faraday trap was also used to parameterize the deuterium anion current when varying cathode voltage, and neutral gas pressure in the UW IEC device. These characteristics were examined at Faraday trap positions one and two to get a qualitative picture of the uniformity of the anion current. The deuterium anion current and the electron current were found to be highly non-uniform between positions one and two. At position 1 no electron current was measured compared to ~0.75 μA at position 2. Similarly the deuterium anion current measured at position 2 was a factor of 5 higher than at position 1. Qualitatively this suggests the presence of a channel of negative ion and electron current closer to position 2. At position 2 the collector current varied between 2 μA and 6 μA nominally. An estimate of the total deuterium anion current in the system can be calculated by assuming the collector plate was perfectly aligned with the suspected anion micro-channel and that all the current in the micro-channel was collected by the Faraday trap. Since the UW IEC cathode used in this experiment has 230 such channels in total a rough estimate of the total anion current is approximately 0.5 mA – 1.5 mA.

Parametrics of the deuterium anion current were performed for varying cathode voltage, cathode current and neutral gas pressure. Thus for this particular line of sight through the chamber scaling laws for varying conditions could be obtained. In all of the parametric studies it should be noted that the collected current represents the flux of anions that actually gets through the background neutral gas to the detector. The anion flux may vary significantly with radius, and this would not be discernable from the Faraday trap diagnostic in its current configuration.

6.4-a-i. Pressure Scan

A pressure scan of the deuterium anion current was performed with the cathode at 100 kV. The cathode current was held constant at 30 mA over the course of the experiment and the neutral gas pressure was varied between 0.5 mTorr and 4 mTorr. This represents the standard operation regime of the UW IEC device. The data for the pressure scan is shown in Figure 6.4-9.

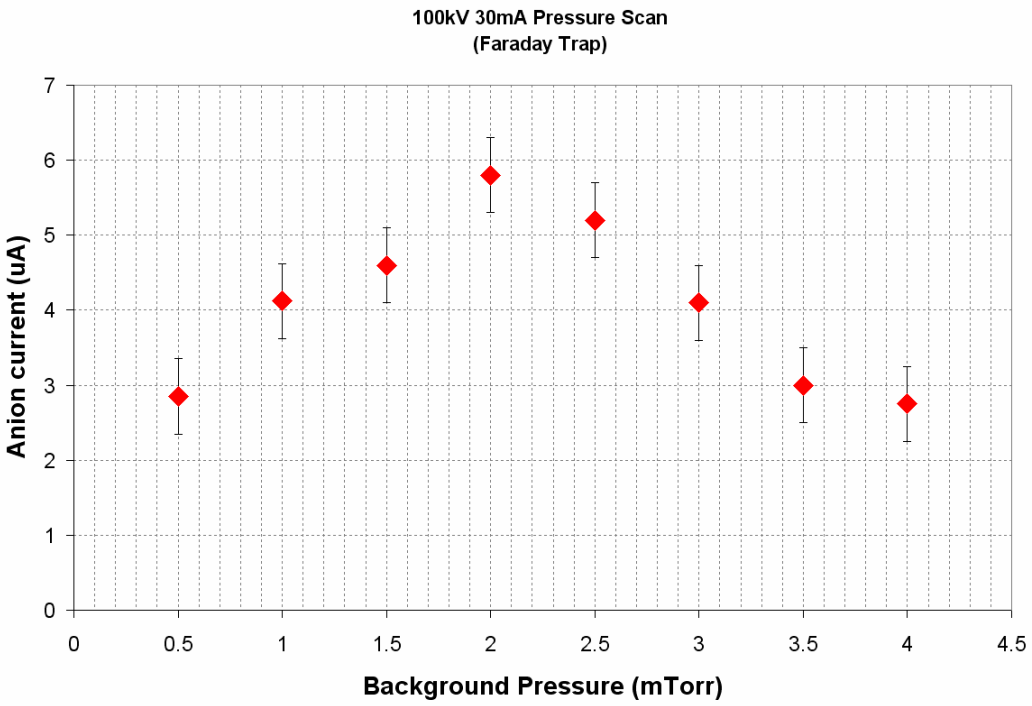

Figure 6.4-9: The pressure scan illustrates how the deuterium anion current detected in the Faraday trap has a maximum for 2 mTorr of background gas. This is due to increasing neutral pressure resulting increasing anion creation up to 2 mTorr with further increases in background pressure resulting in attenuation of the anion flux to the detector.

The anion flux to the collector peaks at 2 mTorr, followed by decreasing detected current at higher pressures. The likely interpretation of this peak is that from 0.5 mTorr to 2 mTorr the increased pressure serves as a source for anion creation, leading to greater anion flux detected at the collector of the Faraday trap. At pressures greater than 2 mTorr

the increased gas pressure begins to attenuate the anion flux incident on the collector plate. Thus the measured current decreases. This experiment was repeated at positions 1 and 2 with similar scaling found at both positions.

6.4-a-ii. Voltage Scan

The voltage scan performed using the Faraday trap showed significant variability between the two positions. In position 1 the collector received between 0.5 – 1.5 μA of current with a peak current between 40 – 50 kV on the cathode. Moving the collector to position 2 resulted in roughly a factor of five increase in collected current and a dramatically different profile to the collector current and voltage curve. (See Figure 6.4-10) What is clear from this data is that the deuterium anion flux is highly dependent on the chamber geometry with the dominant factor, most likely, being the cathode wire orientation. Potential variations due to non-uniformities in the cathode (namely grid wires) can result in perturbations that will focus the negative ions, and secondary electrons, into channels. It is likely that position 1 is outside one of these channels and that position 2 is better aligned with one of the potential channels generated by the cathode.

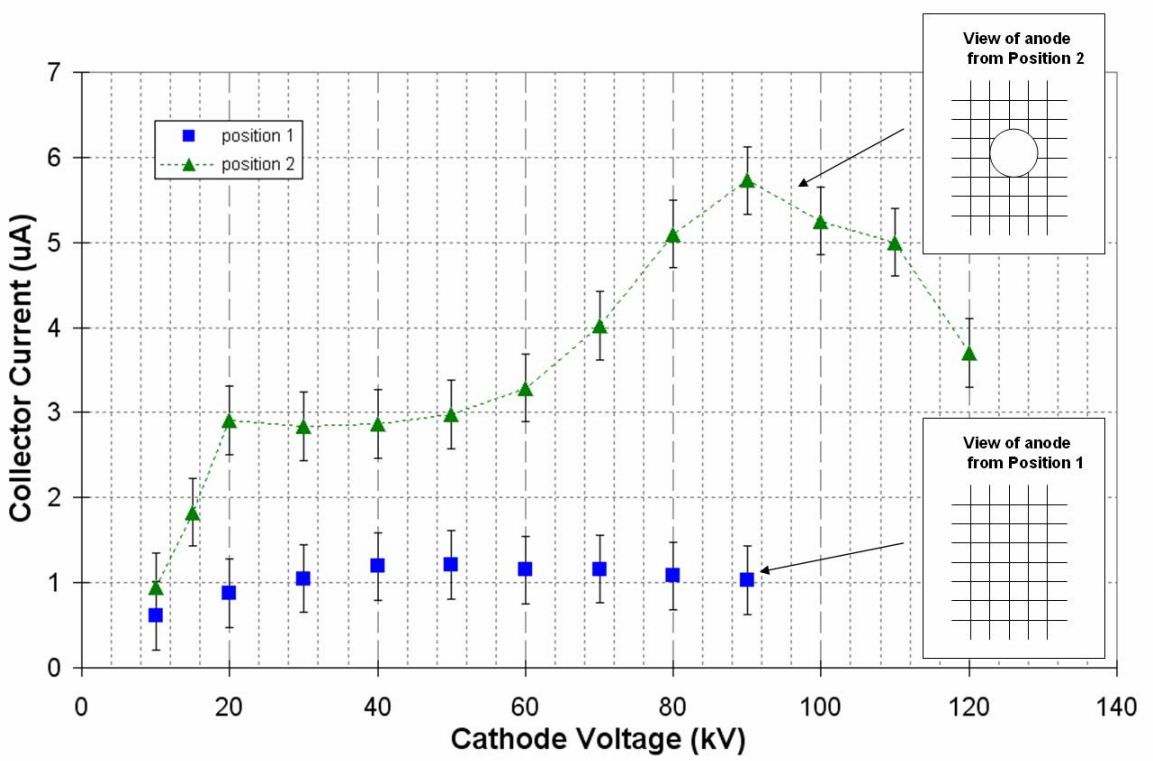

Figure 6.4-10: Position 1 shows a sub-linear dependence of Faraday trap collector current on voltage, with a maximum between 40-50 kV. Position 2 shows a greater than linear dependence of collector current on voltage with a maximum at 90 kV. At both positions the cathode current was 30 mA and the background pressure was 2 mTorr.

The rollover of anion current with voltage may be related to two separate factors. First, as voltage is increased the positive ions undergoing charge transfer are accelerated to energies past the peak of the charge transfer cross section (~60keV for D_3^+ ions). A second possibility is that the focusing effect of the grid wires optimally focuses the deuterium anion flux onto the collector plate at near 90 kV on the cathode. Above and below this value the negative ion flux is either under-focused or over-focused, resulting in a lower current measured by the Faraday trap. It may be that both of these effects are contributing to the scaling observed in the voltage scan.

These assertions require further experiments to more definitively map the deuterium anion current in the UW IEC device. A detailed mapping of the beam

channels with a multi-channel array of Faraday cups would answer many of the questions regarding the geometry of the anion and electron flux. Such an experiment would also quantitatively assess the contributions of the anions and electrons to total cathode current in the UW IEC device.

6.4-a-iii. Current Scan

A current scan was done at position 2 and indicated a mostly linear dependence of the collected anion current up to an apparent threshold, at which point the collected current would plateau and cease to increase with further increase in cathode current. This is shown in Figure 6.4-11. Since the deuterium anion current is being measured over a very small fraction of the total solid angle of the chamber, it is difficult to discern what is causing the scaling observed in the voltage, pressure, and current scans detailed above.

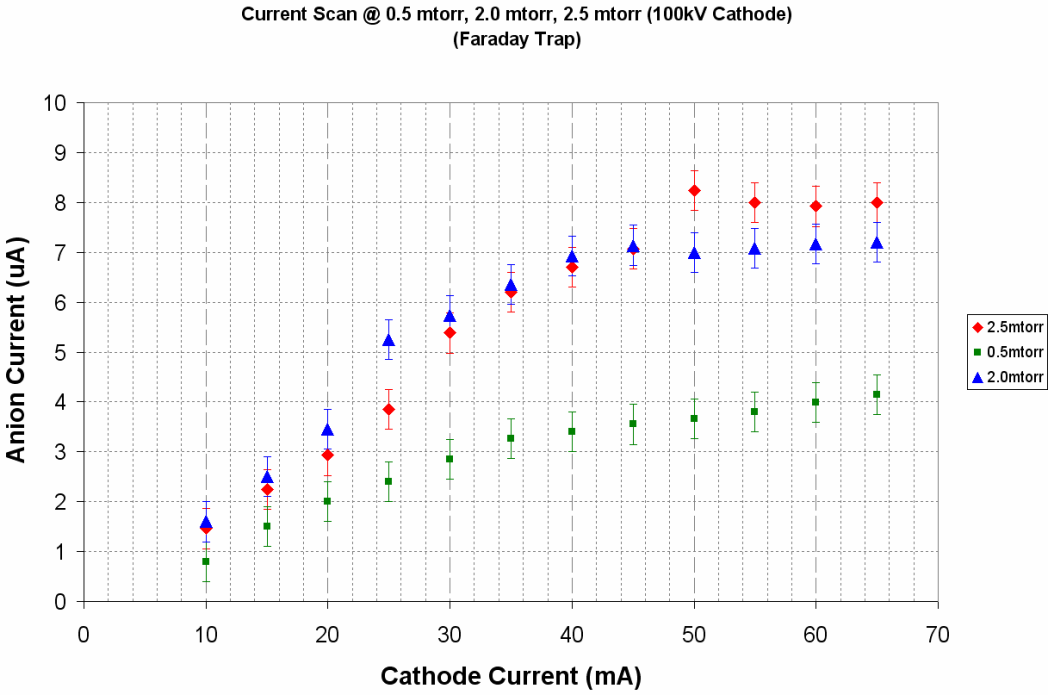

Figure 6.4-11: Shows the dependence of anion current measured on the collector to changes in cathode current. The traces appear to have a knee that occurs at varying cathode current depending on the neutral gas pressure.

The geometry of the cathode wires will likely play an important role in focusing or de-focusing the channels of deuterium anions present in the device. In addition, if the channels are well focused, the space charge of the anion and electron beams may play a role in the behavior observed by the Faraday trap as well. If space charge phenomena are being observed then self neutralization of the beam may be a contributing factor. This would explain some of the dependence on background neutral gas pressure (for the cathode current scan in particular) observed with the Faraday trap diagnostic.

These assertions require further experiments to more definitively map the deuterium anion current in the UW IEC device. A detailed mapping of the beam channels with a multi-channel array of Faraday cups would answer many of the questions regarding the geometry of the anion and electron flux. Such an experiment would also quantitatively assess the contributions of the anions and electrons to total cathode current in the UW IEC device.

In summary, using a magnetic deflection energy analyzer, deuterium anions resultant from both charge transfer and thermal electron attachment processes have been measured in the UW IEC device. In addition, with 90 kV and 100 kV potentials on the cathode, long lived molecular deuterium anions have been measured with metastable lifetimes of at least 0.5 μs. These molecular anions were detected with the full cathode energy indicating that they originated near the hot cathode at the center of the IEC device.

A Faraday trap diagnostic was used to corroborate the data from the magnetic deflection energy analyzer and to make measurements of deuterium anion current at two positions around the UW IEC device. This diagnostic indicated that the deuterium anion

current was highly variable with angular position, indicating a strong dependence on device geometry. In addition a total anion current of ~1mA, out of 30 mA of total current, was calculated from the Faraday trap measurements. Further work is recommended to more definitively map the angular dependence of deuterium anion intensity.

Nonetheless, 1 mA of deuterium anion current would be a significant contribution to the total ion current of the system with typically assumed values of ~1/3 of the cathode current (or 10-15 mA in the cases detailed in this section). The data reported here supports the data from the FIDO diagnostic reported in Chapter 5.4 indicating that as much as 30% of the D-D fusion in the IEC device may result from accelerated deuterium anions.

Chapter 6 References

[1] Ian G. Brown, in The Physics and Technology of Ion Sources, edited by Ian G. Brown, (Wiley, New York, 2004)

[2] J. Peters, "Negative ion sources for high energy accelerators" Rev. Sci. Instrum., 71, 1069 (2000)

[3]Stier, Barnett, "Charge Exchange Cross Sections for Hydrogen Ions in Gases" Phys. Rev., 103, 4 (1956)

[4] Phillips, Tuck, Rev. Sci. Instrum., 27, 97,(1956)

[5] R. K. Janev, W. D. Longer, K. Evants, Jr., and D. E. Post, Jr., in Elementary Processes in Hydrogen-Helium Plasmas, Springer, Berlin, (1987)

[6] G. H. Miley, "Inertial Electrostatic Confinement Approach to Fusion Power" Proceedings - Symposium on Fusion Engineering, 1419 -1422 (1995)

[7] J. Khachan and S. Collis, "Measurements of ion energy distributions by Doppler shift spectroscopy in an inertial-electrostatic confinement device" Physics of Plasmas, 8, 4 (2001)

[8] G. H. Miley, Y. Gu, J. M. DeMora, R. A. Stubbers, T. A. Hochberg, J. H. Nadler, and R. A. Anderl, "Discharge Characteristics of the Spherical Inertial Electrostatic Confinement (IEC) Device" IEEE TRANSACTIONS ON PLASMA SCIENCE, 25, 4 (1997)

[9] O. Shrier, J. Khachan, S. Bosi, M. Fitzgerald, and N. Evans, "Diverging ion motion in an inertial electrostatic confinement discharge" PHYSICS OF PLASMAS 13, 012703 (2006)

[10] M. Čížek, J. Horáček, W. Domcke, "Long-lived anionic states of H2, HD, D2, and T2," Phys. Rev. A, 75, 012507 (2007)

[11] S. K. Allison, "Experimental Results on Charge Changing Collisions of Hydrogen and Helium Atoms and Ions at Kinetic Energies above 0.2 keV," Rev. Mod. Phys., 30, 4, (1958)

[12] S. F. Philp, "Negative Hydrogen and Deuterium Ion Beams," J. Appl. Phys., 31, 9, (1960)

[13] computer code SIMION® Version 8, Scientific Instrument Services, Inc.

[14] O. Heber, R. Golser, H. Gnaser, D. Berkovits, Y. Toker, M. Eritt, M. L. Rappaport, and D. Zajfman, “Lifetimes of the negative molecular hydrogen ions: H2−, D2−, and HD−” Phys. Rev. A, 73, 060501 (2006)

[15] R. Golser, H. Gnaser, W. Kutschera, A. Priller, P. Steier, A. Wallner,. M. Cízek,. J. Horácek, W. Domcke, “Experimental and theoretical evidence for long-lived molecular hydrogen anions H2- and D2,” Physical Review Letters, v 94, n 22, p 1-4, June 10, (2005)

[16] D. R. Boris and G. A. Emmert, “Composition of the source region plasma in inertial electrostatic confinement devices,” Physics of Plasmas, 15, 083502 (2008)

Chapter 7: Fusion Product Time Of Flight Diagnostic (FPTOF)

7.1: Previous Work

The Fusion Product Time of Flight (FPTOF) diagnostic relies heavily on the noise reduction methods used in the FIDO diagnostic described in Chapter 5 of this thesis. Without the energy spectroscopy capability of FIDO, and its ability to detect both protons and tritons from D-D fusion reactions, the time-of-flight technique would not be possible in the context of an IEC device. The time of flight technique relies on precise temporal measurement of particle arrival times at detectors placed 180^{o} apart on either side of the origin point of a fusion event. This technique is used in a variety of applications outside of fusion research. In particular, inertial confinement fusion research[1] and medical imaging technology make use of the time-of-flight technique. In the context of inertial confinement fusion the the time of flight of the D-T neutrons are measured relative to pellet implosions. The 14.1 MeV neutron energy is altered by scattering interactions within the high energy density imploded pellet. The resulting energy spectrum of the D-T neutrons, recorded in the varying time-of-flight of the neutrons, provides information about the temperature of the imploded ICF fusion pellet. Thus, while ICF utilizes time-of-flight techniques to measure energy distributions, coincidence techniques are not part of the ICF time-of-flight applications.

Time-of-flight techniques are regularly used in position emission tomography applications (TOFPET). The first use of TOF techniques to enhance PET scanning occurred in the early 1980s[2]. The advantage of TOFPET techniques over traditional PET techniques is their ability to use the arrival times of the positron annihilation gammas to

calculate the point of origin within the patient of the annihilation reaction[3]. This allows TOFPET scanners to more effectively deal with the signal degradation associated with PET imaging through large quantities of human tissue. State of the art TOFPET scanners are capable of timing resolution of ≤0.3 ns, and new advances in scintillator technology promise to enable even higher resolutions[4]. This provides spatial resolution that is on par with traditional PET scanners (~ 4-6 mm). The main advantage of TOFPET scanners is their significantly enhanced signal to noise characteristics.

In the context of locating the origin of fusion reactions within an IEC reactor vessel, spatial resolution of a few millimeters (such as the resolution achieved in PET applications) would be a dramatic improvement over previous attempts to spatially resolve the location of fusion reactions within such a device. Currently the FPTOF diagnostic described in this work has attained 2 cm resolution. However multiple avenues for improvement exist to enhance this spatial resolution by a factor of ten or more. In addition to providing much more precise spatial resolution than previous techniques, FPTOF gives a more direct measurement of spatial location, whereas other techniques require inversion of data taken along chords and, therefore, depend on plasma profile assumptions. Thus, coupling the time-of-flight technique to the energy resolution of the FIDO diagnostic represents significant progress in the ability to diagnose the physical processes taking place within an inertial electrostatic confinement device.

7.2 Fundamentals of Fusion Product Time of Flight Diagnostic

The products of D-D fusion reactions travel in exactly opposite directions in the center-of-mass system in order to conserve the momentum of the reaction. In the lab

frame, there will be a slight shift caused by the reacting ion velocities, but the trajectories will still be nearly opposed. As a result, particle detectors placed 180º apart on the wall of the cylindrical reaction vessel will detect the fusion products associated with reactions occurring along the line of sight between the two detectors. The easiest reaction to detect is the D(d,p)T branch of the D-D fusion reaction, since both reaction products are charged particles of relatively moderate energy. When a D-D fusion reaction occurs on the line of sight between the two charged particle detectors, the proton and triton associated with the fusion reaction will arrive at their respective detectors at different times, due to the difference in velocities of the two products. These arrival times will be referred to as t_p and t_T for the proton and triton respectively. It should be noted that the dimensions of the HOMER IEC device are such that the proton will always arrive before the triton if the fusion reaction occurs in the cylindrical vacuum vessel. The energies of the two particles are measured by the two charged particle detectors, thus the velocities of the fusion products are known. With this information it is possible to calculate the origin point of the fusion products to a high degree of accuracy. A schematic of the setup described above is shown in Figure 7.2-1.

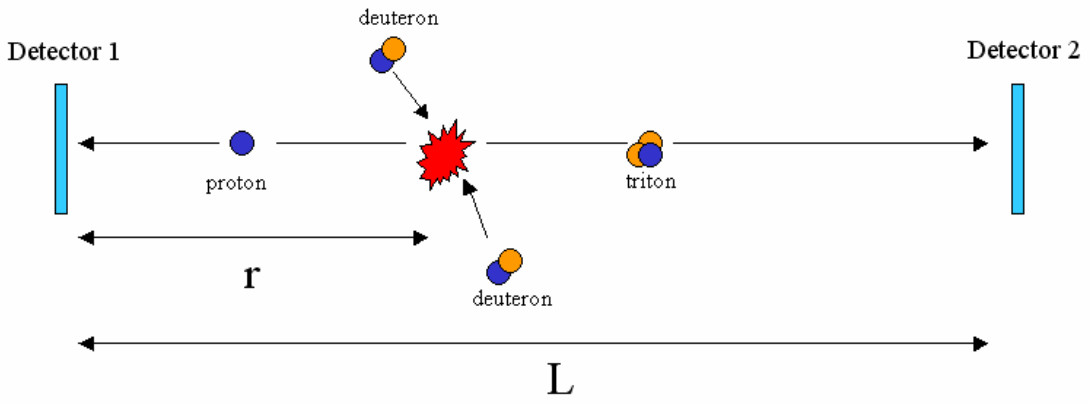

Figure 7.2-1: A schematic of a fusion product time of flight setup for determining spatial location of D-D fusion reactions between two charged particle detectors.

Here r is the distance between detector 1 and the fusion reaction, and L is the distance between the two detectors. To describe how the distance r is calculated we must define t_p as the time required for the proton to reach detector 1, and t_T as the time required for the triton to reach detector 2. The velocities of the proton and triton respectively, defined in terms of their fusion product energy (E_p and E_T) and mass (m_p and m_T), are:

$$v_p = \sqrt{2E_p / m_p}$$
$$v_T = \sqrt{2E_T / m_T} \qquad \text{(7-1a \& b)}$$

The arrival time difference, Δt, can be measured by the setup in Figure 7.2-1 and is described by:

$$\Delta t = t_T - t_p = \frac{L - r}{\sqrt{2E_T / m_T}} - \frac{r}{\sqrt{2E_p / m_p}} \qquad \text{(7-2)}$$

With this information we can construct an expression that gives the position where the fusion reaction occurred, in terms of known or measurable quantities. This expression is:

$$r = \frac{\left(\frac{L}{v_T} - \Delta t\right)}{\left(\frac{1}{v_p} + \frac{1}{v_T}\right)} \qquad (7\text{-}3)$$

It should be noted that the procedure described above for determining the location of the D(d,p)T fusion reaction does not account for the complexities added by the Doppler shift imparted to the fusion products from the reacting deuterons. In order to account for this, it is necessary to differentiate between the reactant center of mass energy imparted to the fusion products and the fusion product energy derived from the Q-value of the fusion reaction.

Using the notation established previously in equations 7-1 through 7-3 let E'_p = 3.02 MeV and E'_T = 1.01 MeV = ($Q - E'_p$). From here the components of the final velocities of the fusion products derived from the Q value of the reaction can be defined as follows, where m_p and m_T are the masses of the proton and triton respectively, and u_p and u_T are the components of the total velocity derived soley from the Q value of the fusion reaction.

$$u_p = \sqrt{\frac{2E'_p}{m_p}} \tag{7-4}$$

$$u_T = \sqrt{\frac{2E'_T}{m_T}} = \sqrt{\frac{2(Q - E'_p)}{m_T}} \tag{7-5}$$

Including the center of mass velocity of the reactants (v_{cm}) gives the relation in equations 7-6 and 7-7, defined by the law of cosines (See chapter 5.2 for the cosine law description). The variables v_p and v_T are defined as the total velocities of the proton and triton respectively. The case below is for v_{cm} adding to the proton velocity and subtracting from the triton velocity.

$$v_p = \sqrt{u_p^2 + v_{cm}^2 \pm 2v_{cm}u_p \cos\Theta} \tag{7-6}$$

$$v_T = \sqrt{u_T^2 + v_{cm}^2 \mp 2v_{cm}u_T \cos\Theta} \tag{7-7}$$

Thus the total energy of the fusion products can be described as follows for both protons and tritons (*p/T*):

$$E_{p/T} = \frac{1}{2} m_{p/T} v_{p/T}^2 \tag{7-8}$$

In order to express the position of the fusion reactions in terms of only measured quantities the cosΘ and v_{cm} terms must be determined. In the case of the FIDO diagnostic this is straightforward since cosΘ ≈ 1 implying that $v_{p/T} = u_{p/T} \pm v_{cm}$. This is due to the irises present in the FIDO set that constrain the admitted protons and tritons to have Doppler shifts only parallel and antiparallel to the detector line of sight. However, it may

by desirable to remove these constraints to increase the count rates observed by the detectors. Thus we will solve for cosΘ and v_{cm} in the more general case where Θ is any angle. This can be done by squaring equations 7-6 and 7-7 and subtracting them.

$$v_p^2 - v_T^2 = u_p^2 - u_T^2 + 2v_{cm}(u_p + u_T)\cos\Theta \tag{7-9}$$

Solving for cosΘ yields the following:

$$\cos\Theta = \frac{\frac{1}{m_p}\left(E_p - E'_p\right) - \frac{1}{m_T}\left(E_T - E'_T\right)}{v_{cm}\left(u_p + u_T\right)} \tag{7-10}$$

The above expression can then be substituted in the expression for the total energy of either of the fusion products to solve for v_{cm}.

$$v_{cm}^2 = \frac{2}{m_p}\left(E_p - E'_p\right) - 2v_{cm}u_p\cos\Theta \tag{7-11a}$$

$$v_{cm}^2 = \frac{2}{m_p}\left(E_p - E'_p\right) - \frac{u_p}{u_p - u_T}\left(\frac{2}{m_p}\left(E_p - E'_p\right) - \frac{2}{m_T}\left(E_T - E'_T\right)\right) \tag{7-11b}$$

By substituting equations 7-10 and 7-11b into the appropriate locations in equations 7-6 and 7-7, expressions for the total velocities can be obtained that only rely on known or measured quantities. This then generalizes equation 7-3 to cases that involve Doppler shifted fusion products incident on the detector at non-zero angles off the line of sight.

This allows for a very high resolution spatial profile of the fusion events within HOMER. The ability of the experimental hardware to resolve the very short timescales between the arrival times of the protons and tritons in the charged particle detectors limits the spatial resolution in the FPTOF diagnostic.

7.3 FPTOF Experimental Setup

7.3-a: FPTOF Vacuum components and detection hardware

The FPTOF diagnostic is comprised of two identical bending arm configurations, each one similar to the FIDO diagnostic described in Chapter 5. The proton and triton trajectories, from a fusion reaction occurring along the line of sight between the two charged particle detectors, are bent at a 20º angle by two, 1.5 T, variable electromagnets. A diagram of the FPTOF diagnostic is shown in Figure 7.3-1.

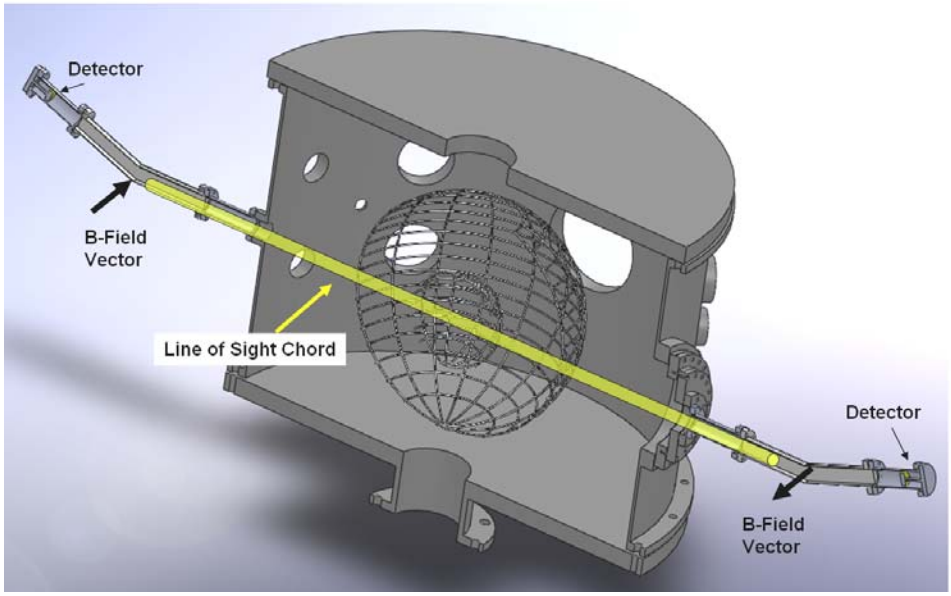

Figure 7.3-1: A schematic of the Fusion Product Time Of Flight diagnostic illustrating how the two silicon charged particle detectors are used to detect the location of fusion events along a line of sight through the HOMER IEC device.

Since a proton and triton from the same fusion reaction must obey conservation of momentum, the two particles will have identical in magnitude but oppositely directed momenta, except for the shift imparted to the fusion products from the center of mass velocity of the reacting deuterons. The center of mass velocity of the reacting deuterons will cause either a lab-frame up-shift or down-shift to the momentum of the particles in the direction of the center-of-mass velocity vector of the reacting deuterons. This will result in one of the detected fusion products having an up-shift in energy and momentum, while the other fusion product has a corresponding down-shift in energy and momentum. Because of this, the electromagnets used to divert the protons and tritons into their respective detectors must use different magnetic fields to account for the difference in momentum between the two fusion products. In order maintain different magnetic fields in the two magnets with one power supply, a shunt resistor circuit was used to siphon current away from one of the magnets thus reducing its magnetic field. A schematic of this circuit is shown in Figure 7.3-2.

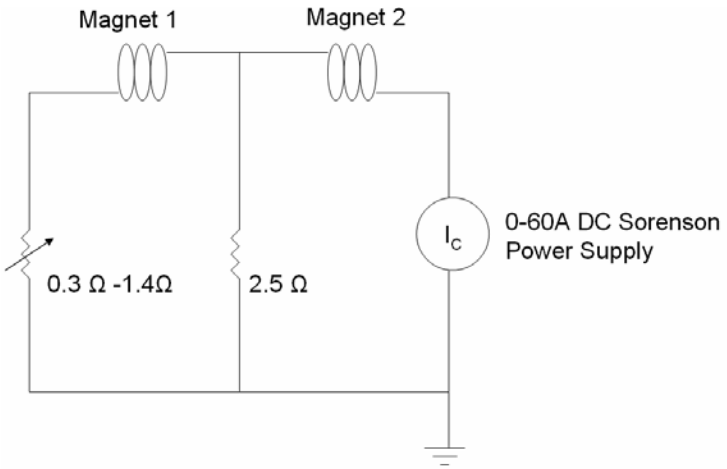

Figure 7.3-2: The current shunting circuit employed to obtain different magnetic fields in the FPTOF magnets employs a variable resistor to allow a 12-56% reduction in magnetic field for Magnet 1 in relation to Magnet 2.

The ability to independently control the magnetic field in the two arms of the FPTOF diagnostic is essential, because the difference in momentum between the proton and triton is large enough to prevent their detection in a system with the same magnetic field in both arms. This was shown using a SIMION simulation with the results displayed in Figure 7.3-3.

The 7700 G case shown in Figure 7.3-3 is representative of the magnetic field employed in the FIDO diagnostic since it allows the maximum number of fusion products to enter the detector. This field setting appears non-optimal for measuring fusion products from the same fusion reaction, however. The SIMION simulations indicate that the magnetic fields in the two time-of-flight arms should differ by ~2000 G in order to achieve optimal fusion product collection with the TOF technique.

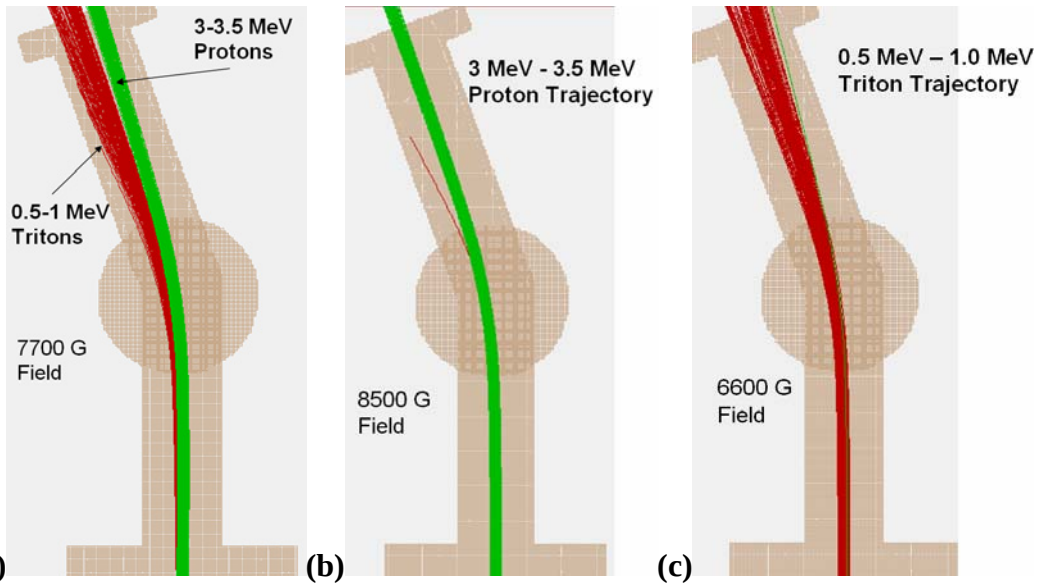

Figure 7.3-3: At (a) 7700 G up-shifted protons (3-3.5 MeV) and down-shifted tritons (0.5-1.0 MeV) from the same fusion reactions can miss either of the detectors since their trajectories diverge after crossing the magnetic field. For (b) 8500 G and (c) 6600 G fields respectively the fusion products can be directed effectively into in the charged particle detectors.

7.3-b: Nuclear Instrumentation Module Setup

In addition to the hardware discussed previously, the Nuclear Instrumentation Module (NIM) circuitry necessary to resolve the short time periods involved in the TOF measurements is also an essential component to the FPTOF diagnostic. The NIM circuitry used in the FPTOF diagnostic can resolve the difference in arrival times of the proton and triton to a resolution of ~2 ns. The uncertainty in measuring the Δt of the proton and triton limits the spatial resolution of the FPTOF in determining the spatial profile of fusion events within an IEC device. An uncertainly of 2 ns translates to ~2 cm of spatial resolution for the location of fusion events within the IEC chamber. There are several sources of timing uncertainty in collecting the TOF signals from the D-D fusion products. Some of these sources of error are effectively dealt with in the current generation of the FPTOF diagnostic while others require additional instrumentation upgrades. The two major sources of timing error in the FPTOF system are amplitude walk, and timing jitter.[5] These will be described separately below.

7.3-b-i: Timing Jitter

An example of what timing jitter from a pre-amplifier looks like is shown in Figure 7.3-4. The uncertainty in the timing arises from random voltage fluctuations in the signal generated by the pre-amplifier. Figure 7.3-4 shows a signal representative of common timing jitter observed in the Ortec® 142-B pre-amps used in the timing circuitry of the FPTOF diagnostic. Upgrading to a thermoelectrically cooled pre-amplifier should significantly decrease this effect in future generations of the FPTOF diagnostic.

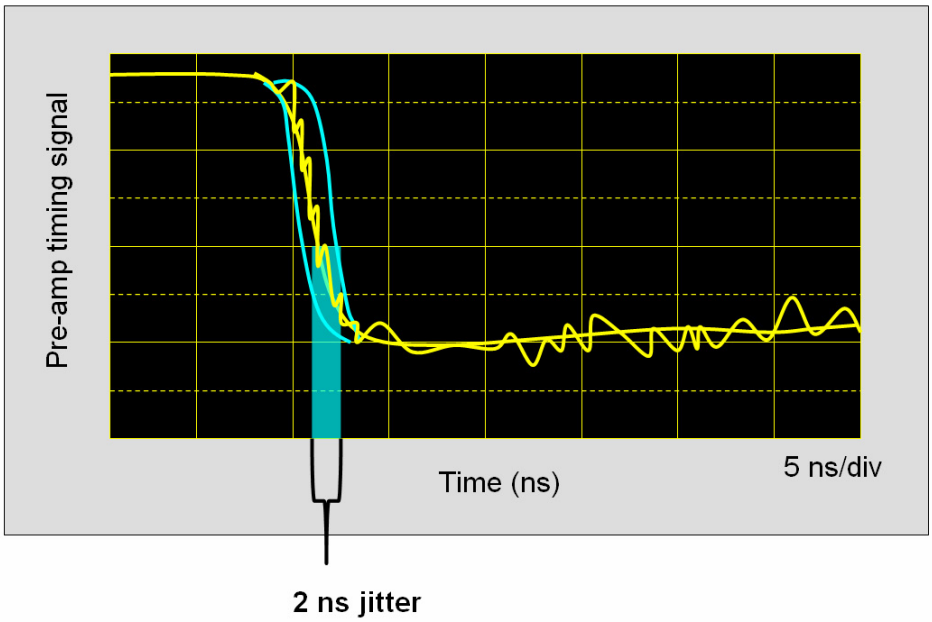

Figure 7.3-4: Timing jitter arises from random fluctuations in the voltage signal from the pre-amplifier. It is caused by broadband thermal noise in circuitry. The random voltage fluctuations translate into a time envelope depicted in blue above.

7.3-b-ii: Amplitude Walk

Amplitude walk is another phenomenon that affects the collection of the TOF data for the D-D fusion products. Amplitude walk occurs when two signals of different amplitudes are used to trigger timing logic pulses dependent on the triggering signal reaching a specified voltage level. Even if the two signals originate at the same time they can produce logic pulses at vastly different times due to the time differential in when the signals cross the voltage trigger level. This is illustrated in Figure 7.3-5. This phenomenon is of particular importance in the context of the FPTOF diagnostic since the proton and triton signals will inherently have different amplitudes due to their significantly different particle energies. The amplitude walk phenomenon can be dealt with by employing the constant fraction timing technique in which the uni-polar proton

and triton signal is converted into a bi-polar signal with a temporally consistent zero-crossing point. By timing off the zero crossing point, consistent logic timing pulses can be achieved. This technique in used in the NIM electronics for the FPTOF diagnostic.

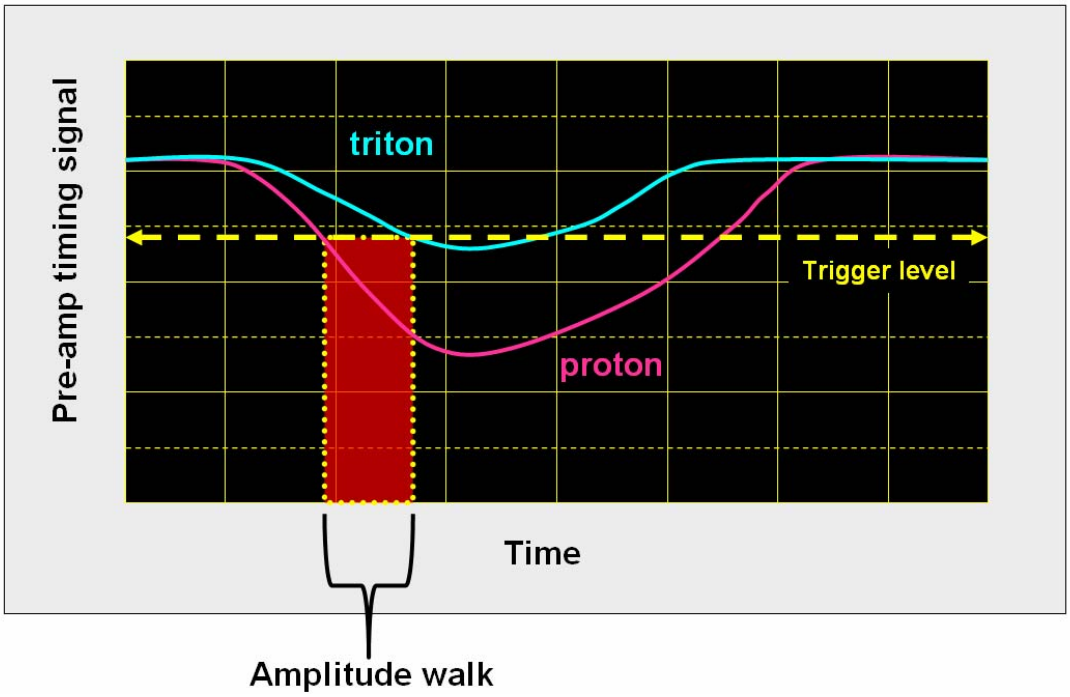

Figure 7.3-5: An example of amplitude walk with a characteristic proton (pink), and triton (blue) signal is shown above. Logic pulses associated with the above analog signals will be transmitted when the signals cross the trigger level.

7.3-b-iii: Timing Electronics Configuration

The NIM module timing electronics used in the FPTOF system use a variety of electronics modules to achieve the fast signal collection and to mitigate the sources of timing error discussed previously. A schematic of the current FPTOF system is shown Figure 7.3-6 and is described in this section.

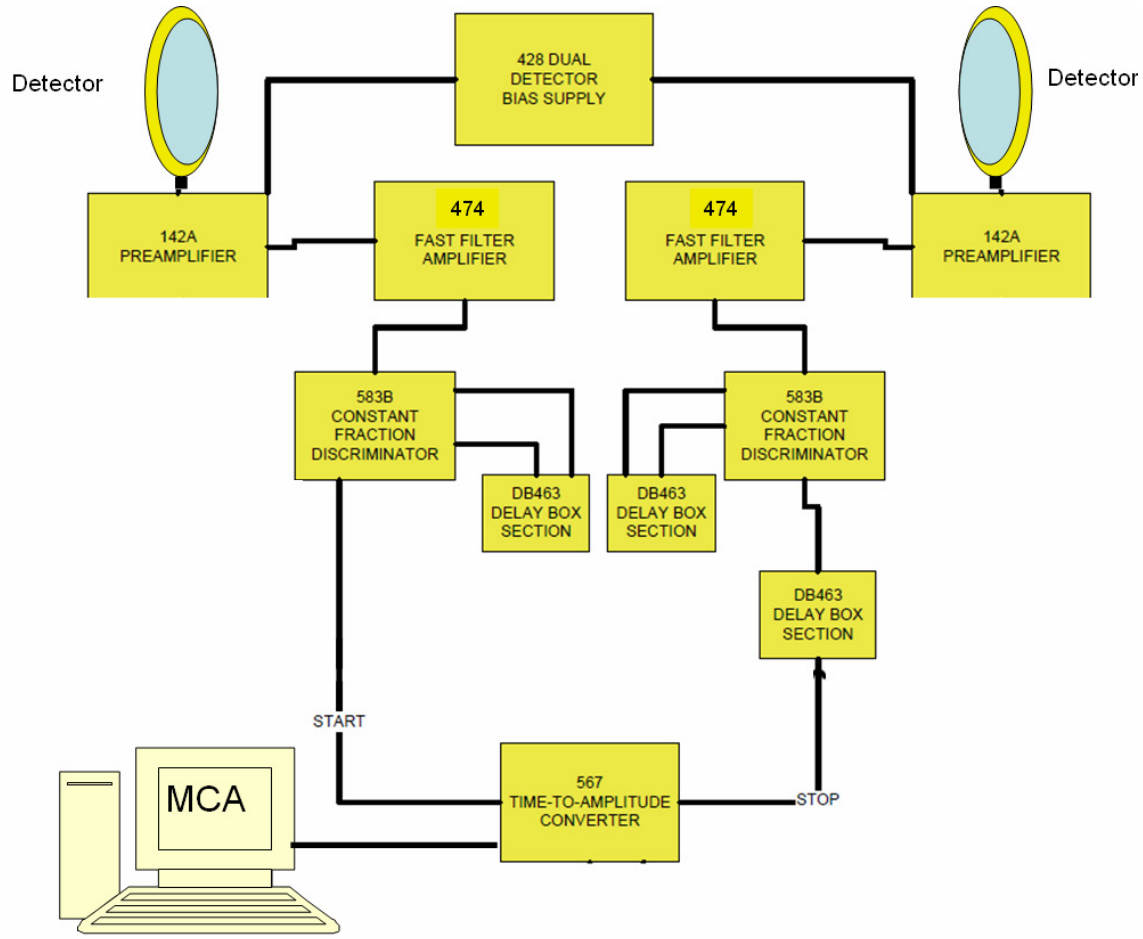

Figure 7.3-6: Block diagram for the FPTOF diagnostic's nuclear instrumentation module (NIM) electronics.

When a fusion event occurs within the HOMER IEC device a coincident proton and triton count will be detected within ~200 ns of each other, in two charged particle detectors located on opposite sides of the vacuum chamber. The protons and tritons generate current signals within the detectors of ~10 pA . These small current signals are then amplified in Ortec® 142 series pre-amplifiers. The timing jitter in these pre-amplifiers is ~2 ns as shown above in Figure 7.3-4. With the current suite of timing electronics the time jitter in the pre-amplifiers represents the limiting factor in spatial resolution for the FPTOF diagnostic.

The signals from the Ortec® 142 pre-amps are then sent to two Ortec® 474 timing filter amplifiers. These are fast rise time amplifiers that amplify the ~20 mV pre-amp signal to a ~1-3 V signal. The rise time of these amplifiers is ≤ 10 ns, although this is not the determining factor in the timing system. The repeatability of the amplifier output, for a given input signal, ultimately determines temporal resolution. This is because the Ortec® 474 timing amplifier signals are then passed into a pair of Ortec® 583b constant fraction discriminators. The constant fraction discriminator (CFD) effectively mitigates the amplitude walk phenomenon described in Figure 7.3-5. This NIM component provides the ability to consistently time off the same point on the incoming amplifier signal from the Ortec® 474 module. The CFD attenuates and inverts the Ortec® 474 signal. This smaller inverted signal is then added to a delayed replica of the incoming Ortec® 474 signal. The superposition of these two signals creates a bi-polar signal with a zero-crossing point that coincides consistently with the same point on the incoming Ortec® 474 fast amp signal. A fast timing logic pulse is emitted from Ortec® 583b CFD when the zero-crossing point is measured. The process of creating the timing logic pulse from the Ortec® 474 fast amp signals is shown in Figure 7.3-7. The fast timing logic pulses reduce the amplitude walk between the two amplifier signals to ≤75 ps.

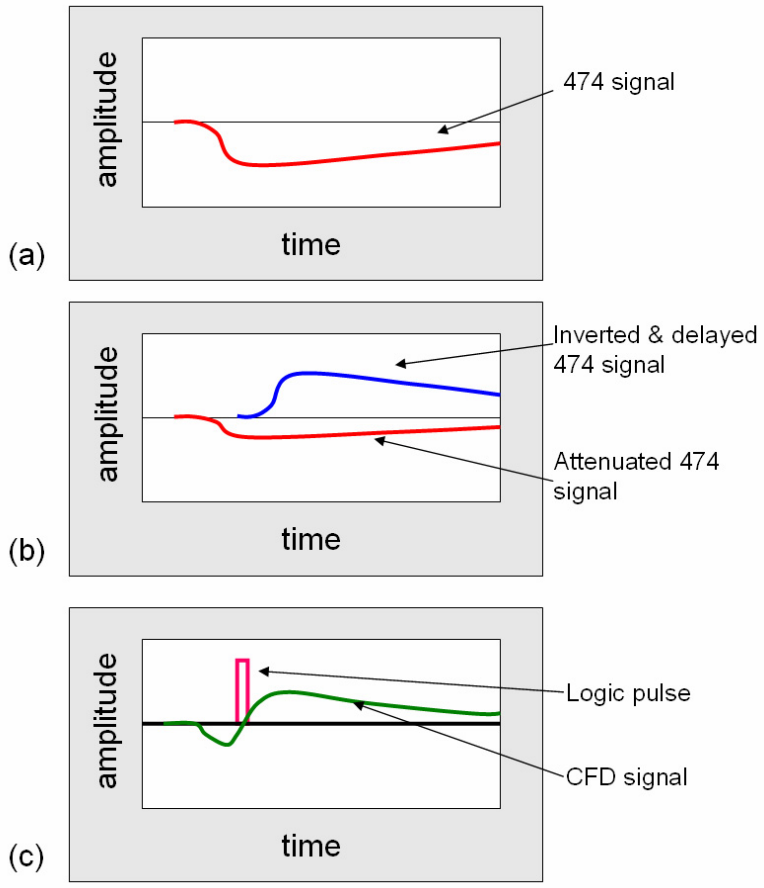

Figure 7.3-7: The progression through which a 583b constant fraction discriminator (CFD) changes a (a) Ortec® 474 fast amp signal into the (b) superposition of two CFD generated signals, in order to produce (c) a consistent timing logic pulse.

From the CFDs, the logic pulses are then used as the start and stop pulses for an Ortec® 567 Time to Amplitude Converter. The Ortec® 567 TAC converts the time delay between a start and stop pulse to an output voltage between 0-10 V. For the time scales being measured with the FPTOF diagnostic the temporal resolution of the Ortec® 567 TAC is ≤50 ps. By sending the TAC output pulses to an MCA a histogram of the number of counts for given time delay can be achieved. Mapping this histogram to a spatial profile of the fusion reactions with the line of sight of the two charged particle detectors is straightforward.

7.4 FPTOF Experimental Results

The implementation of the FPTOF diagnostic, as described above, was recently achieved in the UW-IEC lab. Consequently only a few data sets currently exist using the FPTOF technique. Nonetheless this data is invaluable as it is the first time that a spatial profile of the fusion reactions within an IEC device has been performed without the use of Abel inversion or a similar unfolding technique. A single spatial profile has been taken on the HOMER IEC device under conditions of 50 kV on the high voltage cathode, 30 mA of cathode current, and 2 mTorr of background neutral deuterium pressure. The raw data of this spatial profile is shown in Figure 7.4-1.

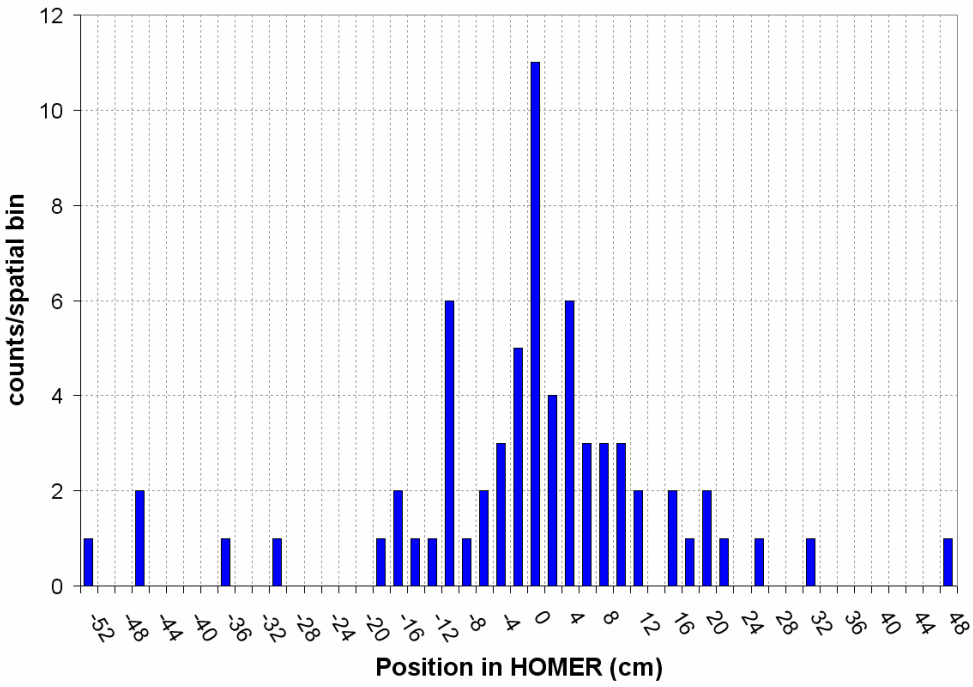

Figure 7.4-1: At 50 kV, 30 mA, 2 mTorr background pressure, the data shows the number of counts recorded in each spatial bin of the cylinder viewable by both charged particles detectors of the FPTOF diagnostic.

The data shown in Figure 7.4-1 was obtained by using the FPTOF diagnostic to measure the delay in arrival time between the proton and triton of a D-D fusion reaction in the manner described previously in this chapter. This data proves the principle of the FPTOF diagnostic to be valid and an effective means of measuring the spatial profile of fusion reactions within an inertial electrostatic confinement device.

It should be noted that measurements of the energy of the fusion products were not performed in conjunction with the timing measurements. The energy spectra from the FIDO diagnostic were used to account for the ~10% shift in fusion product energy imparted by the Doppler shift from the deuterium reactants. The average shift in energy from the Doppler shift was found to be 200 keV when the cathode was at 50 kV. This 200 keV energy shift was added or subtracted appropriately to the fusion products detected in the FPTOF diagnostic. The Doppler shift does not significantly affect the temporal or spatial resolution of the FPTOF setup, although a significant increase in temporal resolution will make the Doppler shift a relevant concern.

The data in Figure 7.4-1 shows a distinct weighting of the fusion reactions toward the center of the device. This is consistent with the geometric convergence of fast deuterium ions and neutrals which would lead to a fusion reaction profile weighted toward the origin. A plot of the normalized number of fusion reactions measured per unit volume within HOMER is shown in Figure 7.4-2.

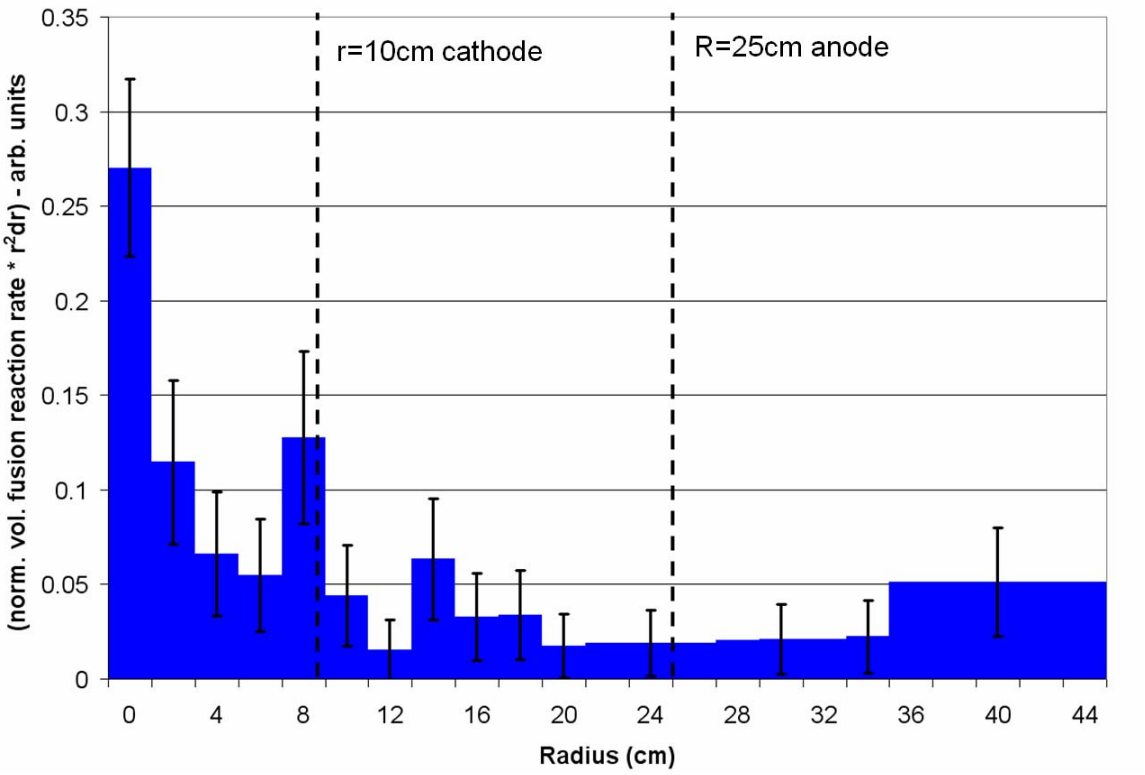

Figure 7.4-2: Normalized profile of reactions per unit volume weighted by the spherical shell volume of each radial bin. The experimental conditions for this data set were 50 kV, 30 mA, 2 mTorr.

This data set was taken with a 10 cm radius cathode and 25 cm radius anode as the electrodes in the HOMER IEC device. Figure 7.4-2 shows >50% of the fusion reactions occurring within the cathode radius. This data disagrees somewhat with previous work by Thorson[6] and Cipiti[7], although it should be noted that Thorson's and Cipiti's work used techniques with less spatial resolution than the FPTOF diagnostic. Table 7.4-1 shows a comparison between the results of the FPTOF diagnostic and those obtained from Thorson and Cipiti. It should be noted that Thorson's and Cipiti's work was performed on grid geometries with 5 cm cathode radii. The FPTOF work was performed on a 10 cm radius cathode. To account for this the number counts recorded by the FPTOF diagnostic within 10 cm and 5 cm is shown in the table 7.4-1.

Author	Percentage of Counts within Cathode Radius	Cathode Radius	Anode Radius
D. R. Boris	~50%	10 cm	25 cm
B. B. Cipiti	22%	5 cm	25 cm
T. A. Thorson	10%	5 cm	25 cm
D. R. Boris	~40%**	5 cm**	25 cm

Table 7.4-1: Conclusions regarding the percentage of fusions which occur within the cathode radius of the HOMER IEC device. (** This entry indicates that 40% of the counts occur within 5 cm of the grid origin. The cathode radius in this case remains 10 cm.)

The spatial profiling in both of their measurements relied on the Abel inversion technique, which is heavily dependent on assumptions made about the spatial profile and the resolution of the diagnostic used for measurement. It should also be noted that the data shown in Figure 7.4-1 must be verified and expanded to a wider range of operating conditions and grid geometries. Nonetheless Figure 7.4-2 shows that the data from the FPTOF diagnostic measures a reactivity profile that is significantly more centrally focused than Thorson's or Cipiti's data previously indicated.

The work detailed in this chapter is the first direct measurement of the fusion reaction spatial profile within an IEC device. The preliminary data from this diagnostic indicates a substantially more centrally peaked reaction profile than previously identified. This diagnostic, with further development, promises to be an important tool in identifying varying modes of operation within IEC devices.

Chapter 7 References

[1] M.A. Russoto, R.L. Kremens, Review of Scientific Instruments, 61, 10, 3125-3127 (1990)

[2] E. Tanaka, "Recent Progress on Single Photon and Positron Emission Tomography – From Detectors to Algorithms," IEEE Transactions on Nuclear Science, Vol. NS-34, 1 (1987)

[3] G. Muehllehner and J. S. Karp, "Positron Emission Tomography," Phys. Med. Biol., 51, R117-R137) (2006)

[4] W. W. Moses, "Recent Advances and Future Advances in Time of Flight PET" Nuclear Instruments and Methods in Physics Research A, 580, 919-924 (2007)

[5] G. F. Knoll, *Radiation Detection and Measurement*, John Wiley and Sons Inc., New York, NY, (2000)

[6] T.A. Thorson, R.D. Durst, R.J. Fonck, A.C. Sontag, "Fusion Reactivity Characterization of a Spherically Convergent Ion Focus," Nuclear Fusion, Vol. 38, No. 4 (1998)

[7] B. B. Cipiti, The Fusion of Advanced Fuels to Produce Medical Isotopes Using Inertial Electrostatic Confinement – PhD Thesis – University of Wisconsin – Madison (2004)

Chapter 8: Conclusions

The important conclusions of this thesis are discussed below. The direct conversion of high energy protons to electricity via the use of silicon PIN junction diodes was shown to be possible, however the conversion efficiency was low (< 1%) and the device was highly sensitive to radiation damage. The mixture of ions in the source region of the HOMER IEC device was shown to be dominated by D_3^+ molecular ions for a range of neutral gas pressures and electron temperatures. The energy distribution of the reacting deuterons within the HOMER IEC device has been measured for the first time by measuring the Doppler shift imparted to D-D fusion products by the center-of-mass velocity of the deuterium reactants. Negative ions have been measured within the HOMER IEC device for the first time, and they have been shown to be at least 3%-4% of the total measured current in the device. Also, for the first time, the time of flight of D-D fusion products has been used to calculate the spatial profile of fusion reactions within an IEC device. Spatial resolution of 2 cm was achieved. More details on these general conclusions are given below.

8.1: Direct Conversion of High Energy Protons

It has been shown that silicon PIN junction radiation cells are capable of converting the kinetic energy of high energy protons to electricity.

1. The conversion efficiency of the silicon PIN junction radiation cells was demonstrated to be ~0.5%.
2. The maximum power output obtained from the silicon radiation cell used in this work was 40 $\mu W\text{-}cm^{-2}$.

3. Both the power output and the radiation cell efficiency were shown to be extremely sensitive to radiation damage occurring within the PIN junction. Both the power output and conversion efficiency of the device dropped by a factor of 100 after experiencing a proton fluence of only 1×10^{11} protons-cm^{-2}.

The prospect for using a solid state device to convert fusion protons to electricity depends on finding a way to mitigate the damage produced by high energy protons as they traverse the PIN junction. In addition to the problem of end of trajectory proton damage, the efficiency of conversion must be increased for this concept to be a relevant energy conversion technology.

8.2: Ion Species Measurement in the IEC Source Region

Experimental measurements of the concentration-weighted reduced ion mass in the source region of the HOMER IEC device are reasonably consistent with the calculated ion mix in the source region obtained through rate equation analysis.

1. Both the experimental results using ion acoustic waves and the 0-D rate equation analysis agree that the source region of the HOMER IEC device contains mostly D_3^+ ions with lesser concentrations of D_2^+ and D^+.
2. The density weighted reduced ion mass of the system varied between 5.9 ± 0.5 amu and 4.0 ± 0.8 amu corresponding to calculated D_3^+ fractions of ~95% and ~50% respectively.
3. Measurements performed with the cathode at high voltage show that the high D_3^+ concentrations persist with the cathode in operation.

8.3: Fusion Ion DOppler Shift Diagnostic

Using the FIDO diagnostic the following has been shown regarding the deuterium energy spectrum within the HOMER IEC device.

1. The deuterium energy distribution within HOMER is dominated by low energy deuterons with energies between 10 – 20 keV, for cathode voltages between 50 kV and 100 kV. These deuterons are presumably charge exchange neutrals born at low energy relative to the cathode voltage.
2. Increasing the cathode voltage within the HOMER IEC device results in an increase in the mean velocity and peak velocity of the deuterium energy spectra.
3. Increasing the cathode current while maintaining voltage and pressure constant results in a relative increase in the number of deuterons in each velocity group within the spectrum. Generally the shape of the deuterium spectrum remained similar for all currents and the number of counts in the integrated proton spectra scaled linearly with current. This correlates well with the observed linear increase in neutron rates as cathode current is increased in HOMER.
4. Increasing the background neutral pressure within HOMER, at 100 kV cathode voltage and 30 mA of cathode current, resulted in a significant increase in the number of deuterons in each velocity group when pressure was varied between 0.25 mTorr and 1.5 mTorr. The number of counts in the integrated proton spectra between 0.25 and 1.5 mTorr increased by a factor of four. From 1.5 – 3.5 mTorr the deuterium velocity spectrum changed comparatively little, and the total number of counts in the proton spectra increased by only 30%. This is consistent with the neutron rate scaling as pressure is scanned in HOMER.

5. Increasing the pressure in HOMER also seemed to cause a trend toward hardening of the deuterium energy spectra. This is counterintuitive; however, the explanation for this phenomenon is the increased production of high energy deuterium anions as background pressure is increased. The hardening of the deuterium energy spectra was correlated with the appearance of an additional peak of highly Doppler shifted counts in the raw D-D proton spectra between 3.3 – 3.5 MeV. The large Doppler shift of these counts and the manner in which they scaled with pressure indicate a contribution to D-D fusion by high energy (1/2 - 2/3 the cathode energy) deuterium anions. The data indicates that these deuterium anions could account for up to 30-40% of the fusion rate within HOMER, with 100 kV of and 30 mA on the cathode.
6. Changing the geometry of the cathode and anode radii had an effect on the deuterium energy spectra as well. Cathode – anode configurations of 20 cm-30 cm, 20 cm-40 cm, and 20 cm-50 cm were examined. From these experiments it was shown that the 20-50 configuration had a hardened energy spectrum relative to the other two configurations with 3x – 6x more deuterons in the highest velocity group in the deuterium spectra (between $1.2x10^6$ and $1.6x10^6$ m/s). This was correlated with a 30% increase in neutron rates between the 20-30 and 20-50 configurations.

8.4: Negative Ions in IEC devices

Negative ions have been identified as being a significant component of the total current measured in the HOMER IEC device. A magnetic deflection energy analyzer and a Faraday trap diagnostic have been used to independently confirm the presence of the deuterium anions within HOMER. The magnetic deflection energy analyzer measured the energy spectra of the deuterium anions and concluded:

1. Deuterium anions resulting from charge transfer processes taking place in the intergrid region of HOMER are responsible for a major component of the anion current. From the anion energy spectra, charge transfer anions appear to account for 90-95% of the anion current. These anions are created by positive molecular ions from the IEC source region changing charge to become negative ions within the intergrid region.
2. Deuterium anions resulting from thermal electron attachment within the IEC cathode region are also present within the HOMER IEC device. They appear to account for 5-10% of the anion current. D^- ions formed in the cathode are measured with the full cathode energy. Metastable D_2^- ions formed in the cathode region are measured with the full cathode energy as well, however on a per nucleon basis these molecular anions have half the cathode energy.
3. The molecular D_2^- ions have a metastable lifetime of at least 0.5 μs within the HOMER IEC device, while traversing $2x10^{-3}$ Torr-m of neutral gas. They were only measurable at cathode voltages > 90 kV.

With the Faraday trap diagnostic, deuterium anion current densities as high as 8.5 $\mu A/cm^2$ have been measured at the wall of the UW-IEC device, 40 cm from the surface of the device cathode with a detector assembly of admittance area 0.7 cm^2.

8.5: Fusion Product Time of Flight Diagnostic

The Fusion Product Time of Flight (FPTOF) diagnostic has been implemented on the HOMER IEC device. It has successfully demonstrated the ability to generate spatial profiles of the fusion reactions occurring within the HOMER IEC device by directly measuring the location of fusion events. Preliminary results from this diagnostic indicate a fusion reactivity profile peaked toward the origin of the device with at least 50% of the fusion occurring within the cathode radius.

8.6: Summary

In summary, this thesis details the development of 4 different plasma diagnostics that were previously unavailable to the UW – IEC lab. The ion acoustic wave diagnostic measured the source region ion species concentration for the first time at the UW-IEC lab. The FIDO diagnostic performed the first measurements of the reacting deuterium velocity spectra in the HOMER IEC device by utilizing Doppler shifted D-D fusion protons. A magnetic deflection energy analyzer, based on the FIDO diagnostic, and a Faraday trap, were used to make the first measurements of deuterium anions in an IEC device. The FPTOF diagnostic was used to make the first direct measurements of the spatial profile of fusion reactions within an IEC device.

Chapter 9: Recommendations and Future Work

Recommendations for improvements to both the Fusion Ion DOppler diagnostic and Product Time Of Flight diagnostic will be treated in this chapter. In addition recommendations for future experiments will also be commented on for these two diagnostics. Recommendations for additional experiments regarding the phenomenon of deuterium anion production within IEC devices will also be addressed in this chapter.

9.1: FIDO and FPTOF diagnostics

Recommendations for improvements to the FIDO (Fusion Ion DOppler) diagnostic will affect the FPTOF (Fusion Product Time Of Flight) diagnostic by default; therefore they have been included together. Future changes to both of these diagnostics should focus on improvements to the design of the FIDO bending arms, the silicon charged particle detectors, and the FPTOF electronics and data acquisition hardware.

9.1-a: FIDO Improvements and Future Work

The main improvement that can be made to the FIDO bending arm involves augmenting the design of the existing charged particle detectors. Currently, charged particle detectors with 300 nm light shielding coatings are in use on the FIDO and FPTOF diagnostics. This 300 nm coating is not sufficient to prevent the penetration of fast deuterons. These fast deuterons can be directed into the detector through charge transfer reactions that occur within the bending arm magnetic field and result in charged particle trajectories that intersect the face of the charged particle detectors. The simplest solution to this noise problem is to thicken the shielding on the surface of the detectors to ~1 μm. This would prevent deuterons up to 200 keV from penetrating the silicon

detector and greatly reducing the signal to noise ratio of the diagnostic. It also would not significantly degrade the energy resolution of the detectors.

With these improvements to the FIDO diagnostic it is recommended that the diagnostic be employed on other IEC devices besides HOMER. The Six Ion Gun Fusion Experiment (SIGFE) and the Helios device are the next logical candidates for use of the FIDO diagnostic. It may also be desirable to employ the FIDO diagnostic on a Polywell device, such as the one being constructed in Santa Fe, NM by the EMC2 Corporation.

9.1-b: FPTOF Recommendations and Future Work

It is recommended that the augmentations to the NIM (Nuclear Instrumentation Module) electronics on the FPTOF diagnostic be pursued so as to further enhance the temporal and spatial resolution of the diagnostic. This can be done by coupling the timing data to the energy of the particle events detected by the silicon charged particle detectors of the FPTOF diagnostic. Coupling the energy and timing measurements allows for much higher spatial resolution. This is because the Doppler shift imparted to the velocity of the fusion products by the center of mass velocity of the deuterium reactants can be taken into account. By implementing this technique, the uncertainty in the fusion products velocity, and therefore the position from which it originated, can be significantly reduced. This leads to enhanced spatial resolution for the FPTOF diagnostic. In addition to enhancing the spatial measurements, deuteron energy spectra can be obtained for each spatial bin of the diagnostic by recording the Doppler shifted proton energy distribution in each of the spatial bins. With proper statistics this powerful tool will allow diagnosis of how the deuteron energy spectrum evolves radially within an IEC device.

This leads into the next recommendation; that higher resolution timing amplifiers and lower noise, actively cooled, pre-amplifiers be employed to enhance the spatial resolution to the point where space charge induced potential well structures are observable by the FPTOF diagnostic. It has been hypothesized that virtual anode and cathode structures may form within the cathode of an IEC device with dimensions of few millimeters. These should be resolvable if the temporal uncertainty in the system is decreased to ~100 ps as this would allow for spatial resolution of less than 1 mm. The ability to resolve reaction rate profiles on this scale would be invaluable, particularly for the SIGFE system, which may be capable of producing the potential structures mentioned previously.

9.2: Deuterium Anions

With regard to the phenomena of deuterium anions present in IEC devices it is recommended that studies to be done to better characterize the spatial distribution of the anion current density within IEC devices. Along this line of research it is also recommended that the effect of varying the cathode geometry be investigated to determine how the shape of the cathode affects the anion current density. An array of Faraday traps, similar in function to the one described in Chapter 6 of this thesis, be used to undertake this study.

It may be that an IEC – like device, with modified cathode geometry, would be useful in applications such as anion thrusters or anion sources for neutral beams. Studies regarding the optimization of deuterium anion production within IEC devices should be undertaken to determine the viability of such applications.

Also, it is recommended that magnetic deflection energy analyzer be modified to use a Faraday cup coupled to an electron multiplier for collection of the anion signal. This would replace the silicon charged particle detector and eliminate the possibility X-ray noise in the magnetic deflection energy analyzer.

The likely presence of the deuterium anions within the cathode region of the HOMER IEC device implies that these negative ions may have a profound effect on any formation of potential structures within the core of an IEC device. Both theoretical and experimental investigations into this phenomenon are recommended. This should be done by using the magnetic deflection apparatus to isolate the portion of the deuterium anion energy spectra resultant from thermal electron attachment in the cathode. Parametric studies can then be undertaken to understand what affects the deuterium anion population within the cathode region.

Chapter 10: Implications of this Work

The work conducted in this thesis has implications for several research endeavors currently underway within the Fusion Technology Institute. In particular the research presented in this thesis has significant implications regarding the direct conversion of high energy charged particles using semiconductors, ion sources for inertial electrostatic confinement, IEC, fusion devices, the energy spectra of the reactants within IEC devices, the spatial profile of fusion reactions with IEC devices, and also the contribution to fusion from negative deuterium ions within IEC devices.

10.1: Direct Conversion of High Energy Protons to Electricity

The work detailed in this thesis indicates that using silicon PIN junction diodes to convert high energy protons to electricity will not provide adequate conversion efficiency, at the present time, to be a viable means of power conversion. The conversion efficiency of measured in this work of ~0.5% needs to be improved for this technology to be useful. Other materials, such as SiC, could provide increased conversion efficiency. This has been demonstrated in betavoltaic devices. However, the theoretical maximum conversion efficiency remains too low for a radiation cell conversion scheme to be useful as the sole means of power conversion in fusion power reactor. It may eventually be a viable concept for topping and bottoming cycles however.

Even if the efficiency is substantially increased the sensitivity of such devices to radiation damage will likely preclude their use as a means to convert high energy protons to electricity. A possible solution to the radiation damage issue involves actively annealing the devices to heal the damage from the protons. This would likely have to be

done very often since fluences as low as $1x10^{11}$ protons/cm^2 will completely disable the device. The device cannot be operated at the annealing temperature since these temperatures will cause large parasitic thermally generated currents to dominate the high energy proton generated current. Thus it is unclear whether there is a path forward for this technology in light of the difficulties of operating radiation cells under a high energy proton flux.

10.2: Source Region Plasma Characteristics

This thesis indicates that the source region of the HOMER IEC device is dominated by molecular ion species. This occurs because of the low ionization fraction present in the HOMER IEC source region. In order to reduce the amount of D_3^+ and D_2^+ changes must be made to the ion source used in the device. Specifically, changes must be made that greatly increase the ratio of plasma ions to background neutral gas. Work has already been performed in this area by Dr. Greg Piefer of Phoenix Nuclear Labs in Middleton WI, and Mr. Brian Egle of the UW-Fusion Technology Institute. Both of their research focuses on the use of ion source regions separated from the main IEC chamber by regions of differential pressure. The separate ion sources provide for the possibility of tuning the source's ion species mixture without substantially affecting the fusion target density within the IEC device. This work would also allow for lower pressure operation of IEC devices. This is desirable since it reduces the frequency of interactions between fast deuterium ions and background gas.

10.3: FIDO diagnostic

The FIDO diagnostic has shown that the energy spectrum of energetic deuterons within the HOMER IEC device contains very few deuterons at or near the cathode energy, at least for background gas pressures between 0.25 – 4 mTorr. This work indicates that charge exchange processes, which dominate at energies of a few keV, are largely responsible for this effect. The heavily degraded energy spectra shown in the FIDO data indicate that the dominant processes within HOMER are atomic and molecular physics reactions occurring at low energy relative to the cathode voltage. While this degraded energy spectrum is undesirable it also appears that the vast majority of the fusion events occurring within HOMER are from interactions between energetic deuterons and thermal background gas. Thus, a reduction in the background gas density will simply lead to lower fusion rates. In order to attain significant amounts of fusion while maintaining an energetic ion population with nearly the full cathode energy, the ion source region must be separated from the main IEC chamber and the IEC chamber must be differentially pumped with respect to the ion source. With low neutral gas pressure in the main IEC chamber (<0.25 mTorr), the only way to attain similar fusion rates to those in HOMER involves accessing a beam – beam fusion configuration. This could be done with ion optics as has been done in SIGFE device.

10.4: FPTOF Diagnostic

The FPTOF diagnostic has shown, through time of flight measurements that the HOMER IEC device produces a spatial profile of fusion reactions that is peaked towards the origin. This indicates some kind of geometric focusing both the ions and charge

exchange neutrals within the HOMER system. This diagnostic has already shown the ability to perform spatial measurements of the fusion reaction profile with resolution that previously was not possible (±2 cm). With upgrades to this diagnostic it would be possible to remotely look for indications of space charge structures within the SIGFE device. This capability would greatly enhance the understanding of the physics going on within the core of IEC devices.

10.5: Deuterium Anions

The discovery of negative ions within the HOMER IEC device opens up the possibility for new applications of IEC devices and signals the need for negative ion formation to be considered in the modeling of IEC devices. This thesis indicates that negative ions represent a significant fraction (3-4%) of the charged particle flux within IEC devices. If this could be optimized, perhaps through novel grid geometries, IEC devices may prove useful in space thruster applications. Negative ions are significantly easier than positive ions to neutralize, thus a simple negative ion thruster could hold a significant advantage over other positive ion based thruster concepts. A great deal more work must be done on this concept, but simple gridded IECs may prove to be a viable alternative to the current generation of station-keeping thrusters.

Appendix A: Improved Electron Confinement in HOMER with a Multipole Magnetic Field Configuration

A-1. Motivation for Multi-pole Configuration

The University of Wisconsin Inertial Electrostatic Confinement Experiments has, for the last several years, relied upon a simple filament-assisted DC discharge configuration to initiate formation of plasma for fusion research. The current configuration consists of a set of six 200 W light-bulb filaments biased to between -50 V and -200 V. A heating supply provides the power necessary to initiate thermionic electron emission from the tungsten filaments and the negative bias forces the emitted electrons away from the filament. These hot electrons provide a mechanism for ionizing the fuel gas in the UW-IEC device. Ultimately this configuration is an inefficient use of the electron emission current since the mean free path for electron collisions with neutral gas molecules is significantly greater than the dimension of the IEC vacuum vessel.

A method to improve the confinement of the primary electrons off the hot tungsten filaments is to utilize a multiple dipole magnet configuration. By adding strips of permanent magnets around the circumference of the IEC vacuum vessel, with alternating north and south alignments, a series of line cusps is created (See Figure A-1).

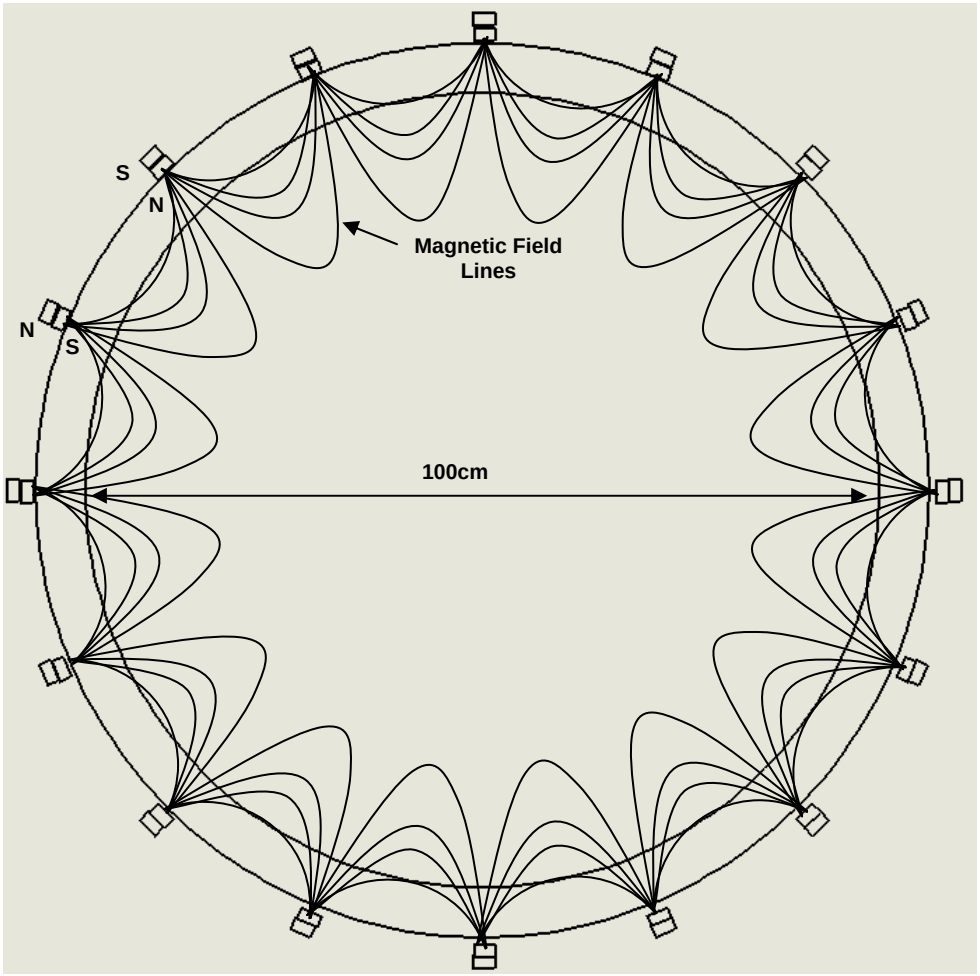

Figure A-1: Multiple dipole configuration showing the magnetic field geometry inside HOMER with the existing 16 magnet configuration.

The line cusps essentially act as a magnetic mirror utilizing the adiabatic invariance of the magnetic moment. The magnetic moment is defined in terms of the mass of the confined particles[1], *m*, the magnitude of the magnetic field, *B*, and the particle velocity perpendicular to the magnetic field, $v_{\perp}$.

$$\mu = \frac{m v^2{}_{\perp}}{2B} \qquad \text{(A-1)}$$

Thus, as a confined particle moves towards regions of higher magnetic field its $v_{\perp}$ must reduce to maintain invariance of the magnetic moment. This results in reflection of some

of the charged particles near the wall of the vacuum vessel, where the magnetic field is greatest. Within the velocity space defining the velocities of the charged particles in the system, there are velocity-space loss cones around the line cusps. These loss cones correspond to the regions where charged particles are on trajectories that are excessively parallel to the magnetic field lines. Charged particles on trajectories within the loss cone of the line cusps do not possess enough perpendicular velocity to be reflected by the magnetic fields present at the wall of the device. Despite the presence of these loss cones, confinement of electrons can be greatly increased using a multiple dipole configuration.[2]

The cylindrical configuration of the UW-IEC device is compatible with a multiple dipole configuration for the purposes of electron confinement. The configuration works best when the ends of the cylindrical system are augmented to prevent electron losses. This can be done with either an additional series of line cusps placed along the face of the end of the vacuum vessel, or by biasing the end of the vacuum vessel electrostatically to reflect the primary electrons emitted from the filaments. Even without augmenting the ends of the cylindrical vacuum chamber the UW-IEC device has experimentally shown a 30% increase in electron confinement with the addition of a multi-pole magnet configuration around the vacuum vessel.

A-2. SIMION Simulation of Electron Confinement in a Multipole Device

Using the commercially available charged particle optics software package SIMION®[3] the IEC device has been simulated to show how electron confinement is affected with the additions of a multipole magnet configuration and electrostatic end

caps. Figures A-2 through A-4 illustrate the effect that adding a multipole magnet configuration and electrostatic end caps to IEC device has on electron confinement. The effect of having the high voltage cathode at the center of the device is also accounted for in these simulations. The simulations assumed -100 kV on the cathode in the center of the device. The cathode has the effect of reflecting the primary electrons from the filaments just within the anode of the device. The cathode and anode dimensions in the simulation were a 20 cm cathode surrounded by a 40 cm anode. The simulations track the path of 100 eV electrons from their origin at the filament position until their trajectory intersects a solid surface. The simulation only treats one filament placed below the mid-plane of the IEC device. This is a standard position for one of the hot tungsten filaments in the IEC device.

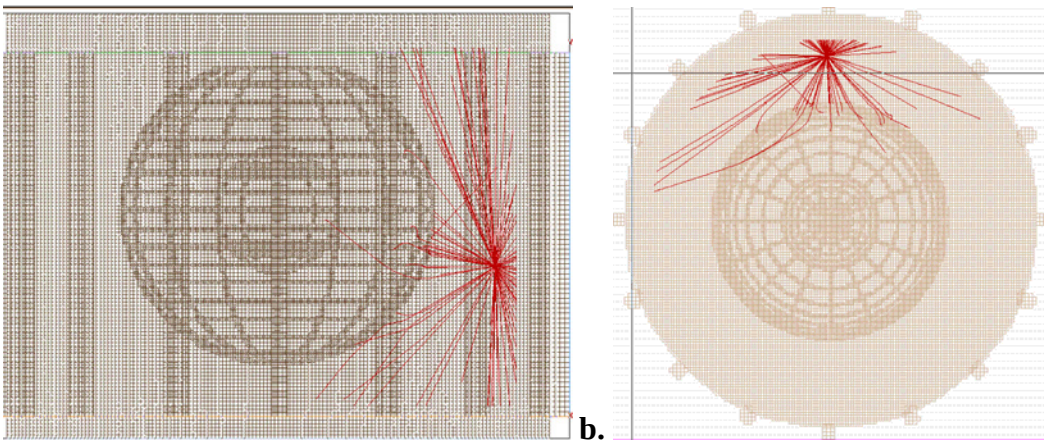

Figure A-2: This configuration shows the electron trajectories for 100 eV electrons with no magnetic field, and no electrostatic end caps. The cathode voltage is -100 kV. **a -** side view, **b –** top view

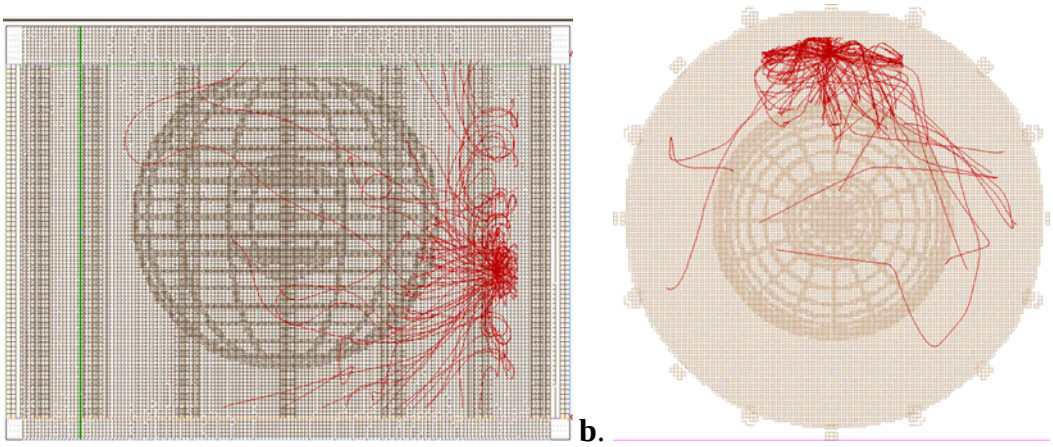

a. **b.**

Figure A-3: This configuration shows the electron trajectories for 100 eV electrons with a 1500 G magnetic field, and no electrostatic end caps. The cathode voltage is -100 kV. **a -** side view, **b –** top view

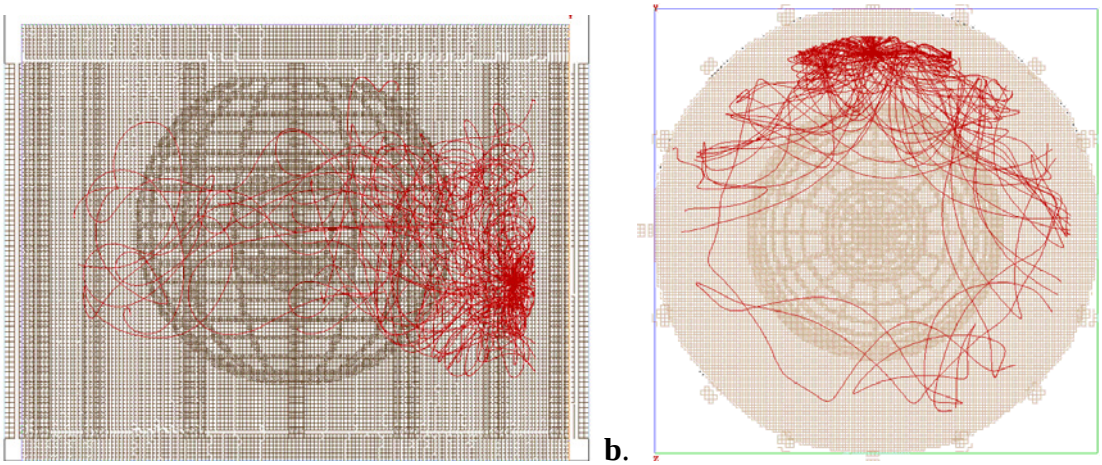

a. **b.**

Figure A-4: This configuration shows the electron trajectories for 100 eV electrons with a 1500 G magnetic field, and -150 V electrostatic end caps. The cathode voltage is -100 kV. **a** - side view, **b** – top view

As is clear from these qualitative figures the path length of the electron trajectories is significantly increased by adding the multipole configuration to the IEC device. The electron path length seems to lengthen even further with the addition of the electrostatic end caps, which keep the primary electrons from intersecting the top and bottom of the device. A quantitative presentation of the electron path length for the three configurations is shown in Figure A-5. It also seems that the electrons are far more evenly distributed throughout the source region with addition of the multipole

configuration. This should lead to more uniform ion flow as ionization from the primary electrons will occur more uniformly within the source region.

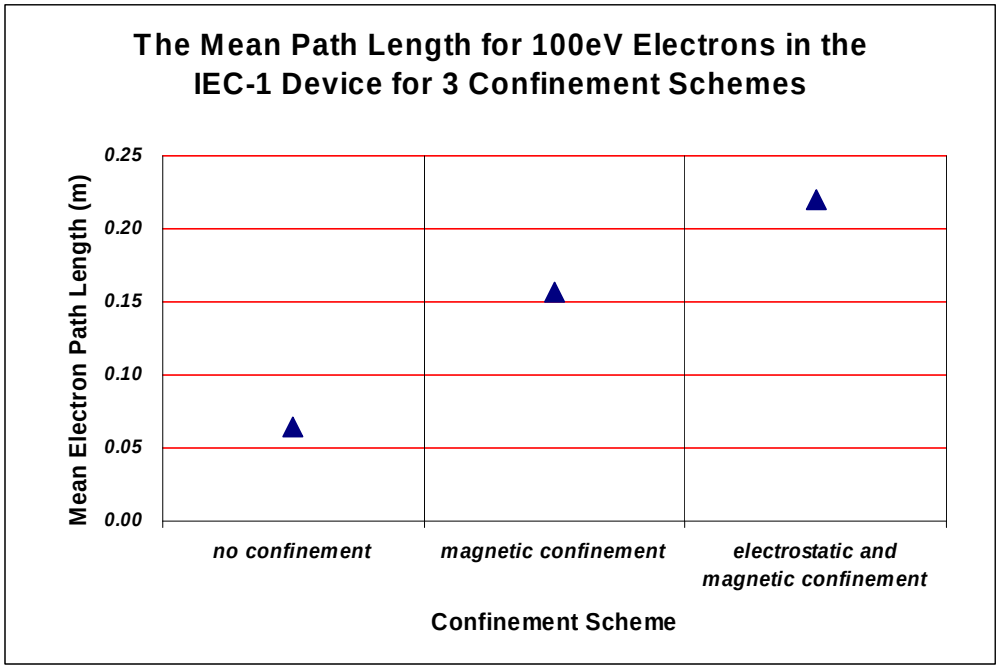

Figure A-5: The mean path length of 100eV electons in the IEC device is shown above for three different confinement schemes.

In Figure A-5 "no confinement" refers conditions detailed in Figure A-2, "magnetic confinement" refers to the conditions detailed in Figure A-3, and "electrostatic and magnetic confinement" refers to the conditions detailed in Figure A-4. By adding the multipole magnet configuration electron path length increased by a factor of 2.4 over the configuration with no electron confinement mechanisms. Adding electrostatic caps as well as a multipole magnet configuration increased the electron path length by a factor of 3.4 over the configuration with no electron confinement mechanisms. These simulations

show that significant gains in electron confinement can be made in the IEC device by adding the electrostatic caps and magnetic multipole configuration detailed above.

A-3. Increased Plasma Density in HOMER with Multipole Configuration

Indeed the multipole configuration has been tested in the IEC device and compared with the previous IEC configuration in which there were no electron confinement mechanisms. The multipole configuration tested was identical to the one detailed in the SIMION™ simulations above. Sixteen magnetic strips were attached to the circumference of the IEC device consisting of alternating north and south poles facing the interior the IEC. The resulting increase in plasma density, for varying cathode voltages, is shown below in Figure A-6. The filament power is held constant throughout the experiment with cathode voltage varied.

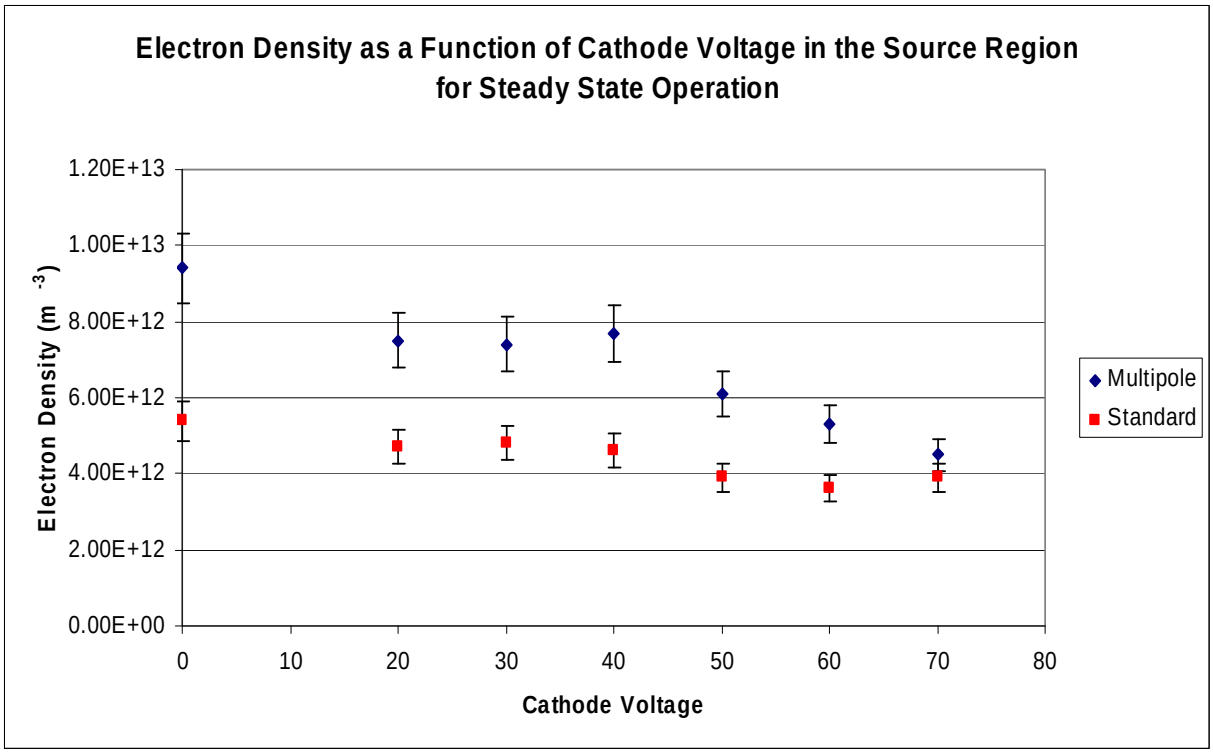

Figure A-6: Measured electron density as function cathode voltage with and without the multipole magnet configuration surrounding the IEC device.

From the data in Figure A-6 it is clear the multipole configuration leads to a consistently higher electron density in the IEC device for a variety of cathode conditions. In Figure A-7 the cathode current is examined with and without the multipole configuration in place.

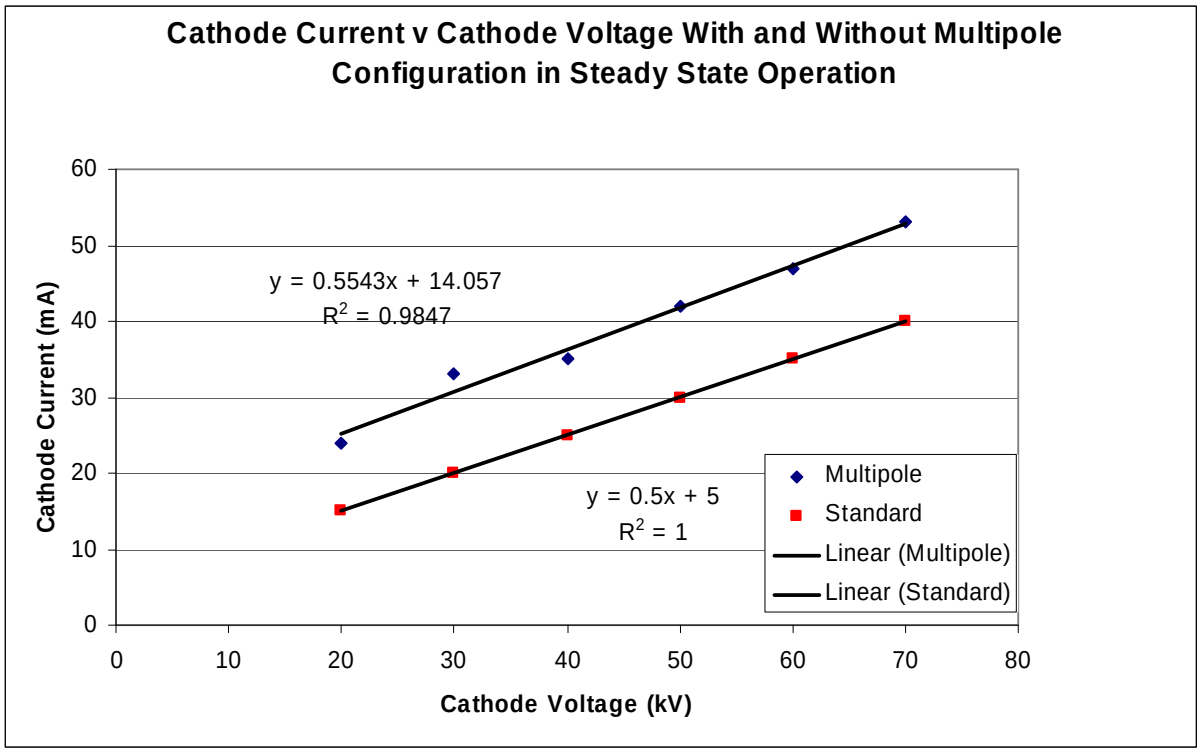

Figure A-7: Cathode current as function cathode voltage for constant filament power with and without a multipole magnet configuration surrounding the IEC device.

The increase in cathode current over the cathode voltage range in this data set is between 35% and 60%. This is a significant increase, and with the data from Figure A-6, it shows that electron confinement has clearly been augmented by the addition of the multipole magnet configuration.

Appendix – A References

---

[1] F. F. Chen, *Introduction to Plasma Physics and Controlled Fusion,* New York, NY, Plenum Press (1974)

[2] M.A. Lieberman and A. Lichtenberg *Principles of Plasma Discharges and Materials Processing*, Hoboken NJ, John Wiley & Sons Inc. (2005)

[3] Computer code – SIMION Version 8.0 Scientific Instrument Services Inc.

Appendix B – 0-d Monte Carlo simulation of D-D proton spectra from HOMER

Written in Matlab Version 7

```
%This program creates proton energy spectra that take into account the
%dopplar shift associated with energetic reactants in fusion reactions and
%creates a spectrum for the fusion products.  The reactants are "a" and "b"
%and the product is "c".

%The output file generated by the program is compatible with TRIM.dat
%format for SRIM 2006.  This allows the fusion product spectrum to be used
%as input to the ion implantation software SRIM.

%Ea,Eb,ma,mb,Ec,and mc denote the Energy and masses of the reactants and
%product respectively in eV and amu. Note Ec is the unshifted energy of
%the fusion product.     ^^^^^^^^^^

%----------------------------Center of Mass Velocity-----------------------
e=1.6e-19;%conversion from eV to J
amu=1.6605e-27;%conversion from amu to kg
mr=2;     %-----|--reactant
mrsi=mr*amu;   %|
Ep=3.02e6;     %|------  These convert the energies and masses given in eV
mp=1;          %|--product      and amu to J and kg (SI units)
Epsi=Ep*e;     %|
mpsi=mp*amu;%---|

%Solid Angle in Velocity Space Detectable
a=180; %0 for only parallel and anti-parallel fusion products
       %180 for a complete angular spread
rad=a*pi/180;
f=2*rad/pi;%This is the multiplier that goes into the portion of the code
%         that determines the detected particle energy distribution.
M=rand(2e6,5);%RANDOM NUMBER MATRIX FOR MONTE CARLO REJECTION METHOD
%The columns of M will used in the following calculations:
%M(:,1)-for random deuterium energy
%M(:,2)-rejection parameter for D energy distribution function
%M(:,3)-rejection function for fusion event
%M(:,4)-used to determine parallel and antiparallel fusion product
%M(:,5)-  "          "          "         "

%----------------------------Bosch-Hale X-section fit----------------------
%Bosch, Hale "NUCLEAR FUSION" Vol. 32, #4, (p611-631), 1992

A1=5.5576e4;
A2=2.1054e2;
A3=-3.2638e-2;
A4=1.4987e-6;
A5=1.8181e-10;
B1=0;
B2=0;
B3=0;
B4=0;
Bg=31.3970;
```

```
%These coefficients will go into the S(E) function defined later in the
%script.  They produce the cross section fit for the D(D,p)T reaction

%----------------------------Energy SpectrumMatrix-------------------------
%This section of code requires that column vectors are created from the
%Xcel Spreadsheet [90kV-d-ionspectrum.xls]- The names of the column vectors
%must be used in filling the 16x4 ionspec matrix.

format short e
ionspec=zeros(16,4);

for n=1:16
    ionspec(n,1)=cumDistFunc(n,1);%Cumulative Distribution function
    ionspec(n,2)=sqrt(1e3*e*2*Edeut(n,1)/(mrsi));%Velocity Range (m/s)
    ionspec(n,3)=distFunc(n,1);%Velocity Distribution Function
    ionspec(n,4)=Edeut(n,1)*1000*e;%Energy Range (J)
end

%This polynomial fit provides a usable sampling function
p=polyfit(ionspec(:,1),ionspec(:,2),6);

%This is a polynomial fit of the distribution function distFunc
p1=polyfit(ionspec(:,4)/(1000*e),ionspec(:,3),6);

X=linspace((ionspec(1,4)/(1000*e)),(ionspec(16,4)/(1000*e)),50);%This is the x
%    values for the polyfit to distFunc
Y=p1(1,1).*X.^6+p1(1,2).*X.^5+p1(1,3)*X.^4+p1(1,4).*X.^3+...
    p1(1,5).*X.^2+p1(1,6).*X.^1+p1(1,7);
[fitmax,I]=max(Y);%This is the maximum value of the Dist Function

Q=fitmax %Gives a little head room over the max Dist Function value.


productz=1;
allparticles=length(M(:,1));
%Matrix of values that makes up the TRIM.dat format for SRIM
%NOTE:length(allparticles) must be <= 99999 for compatibility with TRIM.dat
format
A=zeros(allparticles,9);
A(:,7)=1;   %Directionality - 1 --> perpendicular incidence
A(:,1)=11111;  %placeholder value-non essential
A(:,2)=productz;   %Atomic number of simulated particle

%_____________________________________________________________________________

%CROSS SECTION FUNCTION

Ed=1;%This is a place holder-it will be changed in the following for loop
S=(A1+Ed*(A2+Ed*(A3+Ed*(A4+Ed*A5))))/(1+Ed*(B1+Ed*(B2+Ed*(B3+Ed*B4))));
xs=S/(Ed*exp(Bg/Ed));%This is the cross section function in (mBarns)

%These are the max values for 90keV COM energy-they are used in the
%rejection statement to determine if fusion occured.

Smax=(A1+(ionspec(16,4)/(1000*e))*(A2+(ionspec(16,4)/(1000*e))*(A3+(ionspec(16,4
)/(1000*e))*...
```

```
(A4+(ionspec(16,4)/(1000*e))*A5))))/(1+(ionspec(16,4)/(1000*e))*(B1+(ionspec(16,
4)/(1000*e))*(B2+...
    (ionspec(16,4)/(1000*e))*(B3+90*B4))));
xsmax=Smax/((ionspec(16,4)/(1000*e))*exp(Bg/(ionspec(16,4)/(1000*e))));


%_____________________________________________________________________

VCM=zeros(allparticles,1);
ED=zeros(allparticles,1);
for k=1:allparticles %This loop contains 2 rejection criteria to determine
                     %if (A)The D-ion fits the distribution function and
                     %   (B)The D-ion actually fuses to produce a proton.
    dfun=p1(1,1)*(M(k,1)*(ionspec(16,4)/(1000*e)))^6+p1(1,2)*(M(k,1)*...

(ionspec(16,4)/(1000*e)))^5+p1(1,3)*(M(k,1)*(ionspec(16,4)/(1000*e)))^4+p1(1,4)*
...

(M(k,1)*(ionspec(16,4)/(1000*e)))^3+p1(1,5)*(M(k,1)*(ionspec(16,4)/(1000*e)))^2+
...
        p1(1,6)*(M(k,1)*(ionspec(16,4)/(1000*e)))^1+p1(1,7);
    if Q*M(k,2)<=dfun %(A)If this is true the particle fits the distribution
                      %function-now we check to see if it fuses to create a
                      %D-D proton.
        %COM velocity in (m/s)
        VCM(k,1)=sqrt(2*M(k,1)*ionspec(16,4)/mrsi);
        %Changes energy input to B-H Cross Section function
        Ed=ionspec(16,4)*M(k,1)/(1000*e);
        ED(k,1)=Ed;
        S=(A1+Ed*(A2+Ed*(A3+Ed*(A4+Ed*A5))))/...
            (1+Ed*(B1+Ed*(B2+Ed*(B3+Ed*B4))));
        xs=S/(Ed*exp(Bg/Ed));
        %(B)If this is true a D-D proton is produced with the
        %appropriate energy.
        if xsmax*M(k,3)<=xs
            if M(k,3)>0.5
                A(k,3)=(mpsi/(2*e))*((2*Epsi/(mpsi))+...
                (VCM(k,1))^2+2*VCM(k,1)*sqrt(2*Epsi/(mpsi))*...
                ((acos(1-2*(f*M(k,5))))/pi));
            else
                A(k,3)=(mpsi/(2*e))*((2*Epsi/(mpsi))+...
                (VCM(k,1))^2-2*VCM(k,1)*sqrt(2*Epsi/(mpsi))*...
                ((acos(1-2*(f*M(k,5))))/pi));
            end
        end

    end
    %This creates a row of energies for the TRIM.dat file in units of eV
end

%The next set of for loops counts the non-zero entries of the ED,VCM, and
%A(:,3) vectors.  These values can be used to determine the efficiency of
%the the monte carlo code.

counter1=0;
counter2=0;
```

```
counter3=0;



for w=1:allparticles
    if A(w,3)~=0
        counter1=counter1+1;
    end
    if VCM(w,1)~=0
        counter2=counter2+1;
    end
    if ED(w,1)~=0
        counter3=counter3+1;
    end
end

%With counter1..counter3 we can now define new vectors for VCM, Ed, and
%A(k,3) that are the correct size.

VCMa=zeros(counter2,1);
EDa=zeros(counter3,1);
A1=zeros(counter1,1);

%countera..counterc correspond to counters that signal the loop below to
%populate the new vectors whenever a nonzero entry from vectors VCM,ED, or
%A(:,3) are encountered

countera=0;
counterb=0;
counterc=0;
Efficiency=counter3/length(allparticles)

for v=1:allparticles
    if A(v,3)~=0
        countera=countera+1;
        A1(countera,1)=A(v,3);
    end
end
for y=1:allparticles
    if VCM(y,1)~=0
        counterb=counterb+1;
        VCMa(counterb,1)=VCM(y,1);
    end
end
for z=1:allparticles
    if ED(z,1)~=0
        counterc=counterc+1;
        EDa(counterc,1)=ED(z,1);
    end
end
```

```
%PLOTTING

subplot(221)
hist(A1(:,1),1000)
subplot(222)
hist(VCMa(:,1),1000)
subplot(223)
hist(EDa(:,1),1000)
subplot(224)
plot(ionspec(:,4)/(1000*e),ionspec(:,3))
hold on
plot(X,Y,'r')

dlmwrite('dopplar spectrum.txt',A,'delimiter','\t','roffset',9);
%Creates output file compatible with TRIM
```

Appendix C: High Energy Charged Particles in Silicon Detectors

Within any crystalline material there exist electron energy levels that continuously repeat between lattice positions known as energy bands. These energy bands define the energies at which electrons can exist with in the crystal lattice of a specific material. In semiconductors and insulators the nominal minimum energy band is called the *valence band*. Electrons in the valence band can be thought of as being bound to their lattice sites and not free to move throughout the crystal. Generally, the next highest energy band is known as the *conduction band*, and electrons that acquire the energy to jump into the conduction band can move freely throughout the crystal. In metals electrons can freely access the conduction band, thus metals have high electrical conductivities. In semiconductors and insulators a forbidden energy gap, typically between 0.5 eV – 5 eV must be overcome for an electron to exist in the conduction band. This energy gap is known as the *band gap.*

If an electron is provided the energy necessary to overcome the band gap in an insulator or semiconductor that electron will migrate freely through the material either by diffusion processes, or by response to the presence of an electric field. The electron leaves in its place a *hole*, or a volume of net positive charge that can also migrate through the material. The electron, and resulting hole then move through the material until they reach the material boundary, or recombination occurs[1]. For detailed description of electron/hole motion in semiconductors see Reference 1.

As is the case with most semiconductor devices, dopant materials are added to regions of charged particle detectors so as to provide either an excess or a depletion of valence electrons to that portion of the material. The dopant typically is an element with

either one more valence electron (called a donor) or one less valence electron (called an acceptor) than the bulk semiconductor. The portion of the semiconductor doped with material that possesses excess valence electrons is referred to as n-type, whereas the portion of the semiconductor doped with material that possesses a depletion of valence electrons is called p-type. An example of this would be Silicon, doped with Phosphorus, being n-type material, and silicon doped with boron would be considered p-type material.

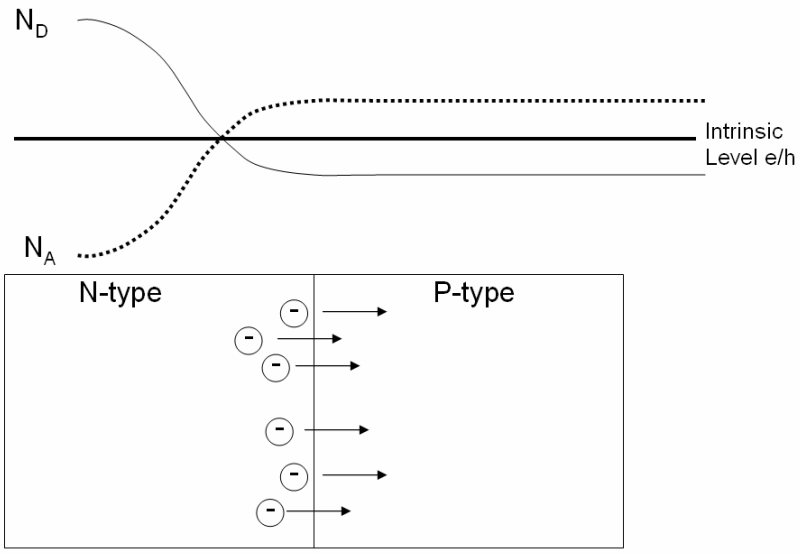

Figure C-1: N_D and N_A are the concentrations of donors, with excess electrons relative to the bulk, and acceptors, with less electrons relative to the bulk, respectively across the p-n junction shown in the graphic above.

When an excess of holes and electrons are present in adjacent regions of the semiconductor the system will come into thermal equilibrium through the motion of the charges across the p-n junction. (See Figure C-1) Valence electrons from the n-type region will migrate across the junction to fill holes in the p-type region. This occurs due to the discontinuity of in the concentrations of electrons and holes at the junction between the p and n type materials. This will create a region of negative space-charge in the p-

type region and a region of positive space charge in the n-type region. (See Figure C-2) Here we define a 1-dimensional approximation of the space-charge density as *ρ(x)*. This region of space charge accumulation is known as the *depletion region.*

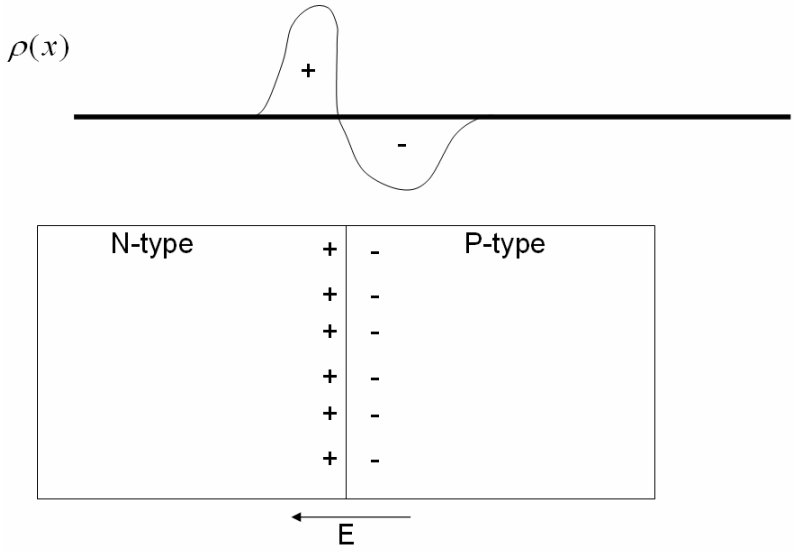

Figure C-2: A representation of the charge density, *ρ(x)*, configuration at the p-n junction along with the induced electric field from the configuration is shown above.

The electric potential difference across the junction is given by Poisson's equation:

$$\nabla^2 \varphi(\vec{x}) = -\frac{\rho(\vec{x})}{\varepsilon} \qquad \text{(C-1)}$$

In the 1-dimensional approximation this reduces to the following, where E is the magnitude of the electric field across the p-n junction.

$$\frac{d^2\varphi(x)}{dx^2} = -\frac{dE}{dx} = -\frac{\rho(x)}{\varepsilon} \qquad \text{(C-2)}$$

Clearly, if the charge density is known it is possible to solve for the potential drop across the p-n junction. This potential drop is typically known as the *contact potential* or the *built-in voltage* (V_{bi}).

The built-in voltage drop is typically between ~0.1 – 2 V for most semiconductors, so it is capable of moving charge carriers generated in the junction to the electrical contacts at the boundaries of a semiconductor device. In essence, this is how photovoltaic cells operate. In the context of charge particle detection however the built-in voltage drop is insufficient for effective measurement. This is due to the small active area created by the *depletion region* created at the p-n junction, and the high capacitance of the junction (see below). The small active area and relatively small electric field present in the *depletion region* makes the unbiased p-n junction highly inefficient at moving charge-carriers (electrons and holes), generated within semiconductor material, to the electrical contacts at the boundaries of the device. In addition to this detrimental effect the high capacitance, of an unbiased junction leads to a prohibitively high signal-to-noise ratio. The capacitance per unit area, *c*, of a p-n junction is given by:

$$c = \frac{\varepsilon}{d} \qquad \text{(C-3)}$$

where *d*, is the width of the *depletion region* of the p-n junction. Because this region is small (~1μm), only a small fraction of the total diode, the capacitance is quite high. Reverse biasing the p-n junction can extend the *depletion region* across the entire depth of the detector. This significantly reduces the capacitance of the device and greatly alleviates the signal to noise issues faced by the unbiased junction. Similarly the greatly enhanced electric field of the additional voltage drop, provided by the external bias, moves charge carriers to the boundaries of the device far more quickly, and efficiently than in an unbiased junction. (See figure C-3)

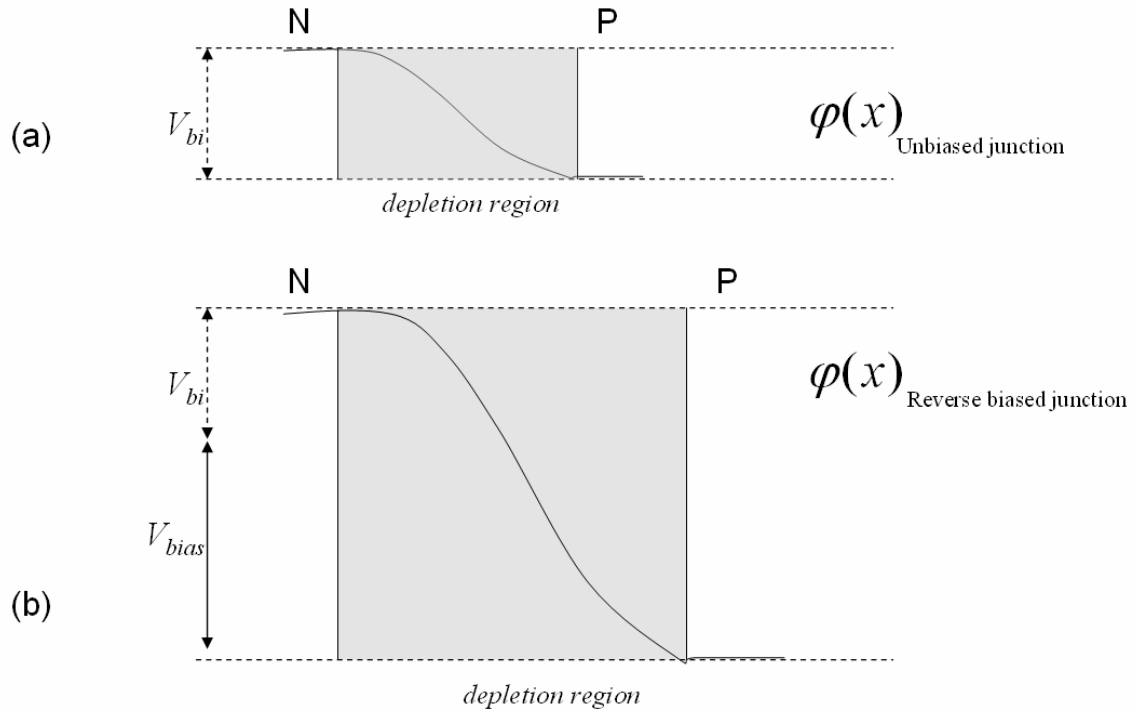

Figure C-3: (a) Illustrates the built in voltage drop of an unbiased p-n junction (b) illustrates the enhancement in voltage drop achieved by reverse biasing the p-n junction. Note the steeper slope of the reversed bias case indicating a higher electric field across the depletion region.

Radiation induced charge carrier production from a single high energy charged particle intersecting a p-n junction can be quantified by the following expression, where *e* is the electronic charge, E_{pair} is the energy required to create an e^-/hole pair (3.62 eV in Si),[2] and E_p is the energy of the incident charged particle.

$$N = \frac{eE_p}{E_{pair}} \qquad \text{(C-4)}$$

The number of electron/hole pairs, *N*, created by a single charged particle event in the junction must be cleared from the junction before the next incident particle impacts the detector junction. This is why the reverse biasing of the detector is important, since it provides a means to quickly clear the charge carriers produced by the detected radiation to contacts at either end of the detector junction. Without the applied electric field a large

fraction of the generated charge carriers would be lost to recombination before the signal could reach the detection circuitry.

Of some note is the difference between the band-gap energy, E_g, in Si (1.1 eV) and the e-/hole pair creation energy (3.62 eV). This is due to heat losses as the high energy charged particle traverses the detector. Thus only about 1/3 of the charged particles energy goes into producing electron hole pairs. An empirical relation developed by Klein generalizes this phenomenon to all semiconductor materials.[2]

$$E_{pair} = 2.8E_g + \varepsilon \qquad (0.5eV \le \varepsilon \le 1.0eV) \qquad \text{(C-5)}$$

The data in figure C-4 illustrates this relation for a variety of semiconductor materials.

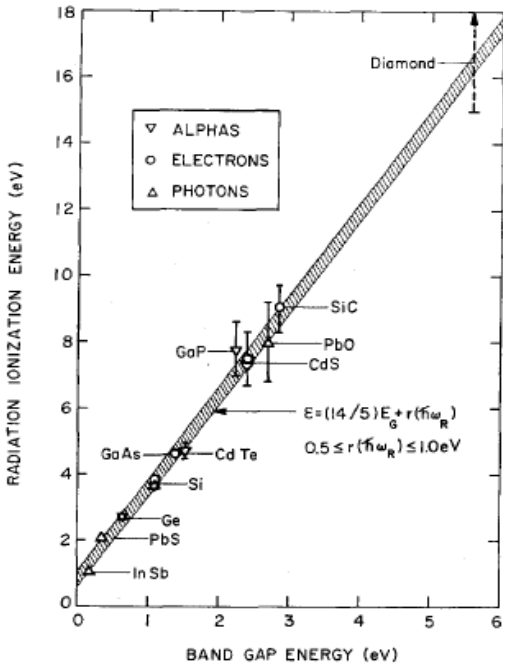

Figure C-4: Electron/hole pair production energy for various Semiconductors.[2]

Once these charge carriers created by the incident high energy charged particles traverse the p-n junction standard nuclear instrumentation electronics can be used to

transform the minute signal from the charged particle detector into a usable signal, usually between 0-10V. If, however, there are additional processes producing electron/hole pairs in the semiconductor junction, these noise signals will also be amplified by the nuclear instrumentation amplifiers. This can lead to significant signal to noise difficulties especially in the unique environment of inertial electrostatic confinement devices.

C-1: Sources of Noise in Semiconductor Charged Particle Detectors

C-1a: Thermal Noise

Thermal noise is the result of thermally excited electron hole pairs forming within the depletion region of the p-n junction. These charge carriers are detected as a constant low energy signal in the detector. Reverse biasing a charged particle detector will reduce, but not eliminate, the thermal noise present in the detector. Thermal noise contributes to broadening of actual radiation signals detected within the p-n junction. Typically this broadening is on the order of 10keV for a silicon detector. This low level noise is always present in a charged particle detector and usually does not have a significant detrimental effect on the spectra acquired using the detector. Excessive heat can lead to problems with thermal noise so it is important to keep semiconductor detectors isolated from substantial heat sources.

C-1b: Visible Light

Any charged particle detector exposed to visible light will generate a signal current due to the excitation of electron/hole pairs by the incident photons. In the ideal case, a charged particle detector will be in a completely dark environment where light pollution is a non-issue. With respect to IEC devices at UW, multiple light sources are available to contribute to light pollution. Tungsten filaments used to light the plasma in the IEC device as well as plasma discharges initiated by fast electrons and ions can pose significant noise problems for charged particle detectors that are not properly shielded from these light sources. Fortunately visible light can be shielded by very thin reflective coatings on the order of 100nm in depth. These coatings can be applied to semiconductor charged particle detectors with little effect on the high energy charged particles of interest.

C-1c: X-Rays

X-Rays are a more troublesome source of noise than visible light, due to their greatly enhanced penetrating power. Thin, coatings are insufficient for shielding X-Rays. Coatings or barriers of sufficient thickness to attenuate X-Rays are generally far too thick to allow the passage of high energy charged particles.

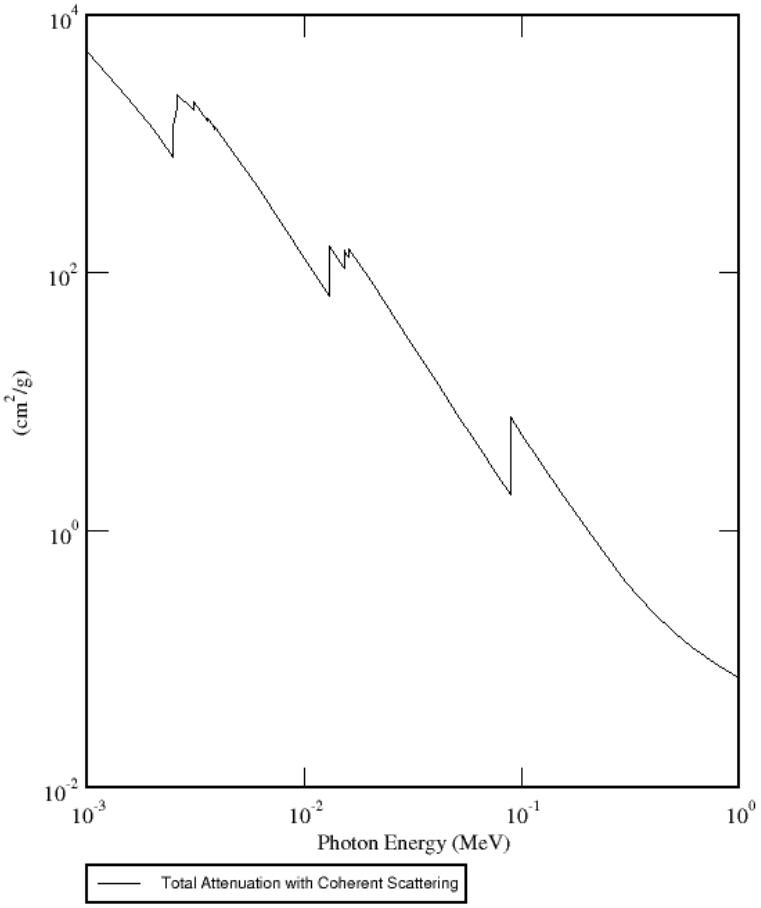

Figure 5: Mass attenuation coefficients for Lead. The X-Rays generated by the IEC device are a bremsstrahlung spectrum with a maximum energy equivalent to the cathode voltage. (100-200keV) [www.physics.nist.gov\PhysRefData – accessed 7/20/2008][3]

If the initial intensity of a monoenergetic beam of x-rays is denoted I_0 and the intensity of the beam after passing through a lead shield of thickness x is denoted I then the attenuation of the x-ray beam can be defined as follows:

$$\frac{I}{I_0} = \exp\left(\frac{\mu x}{\rho}\right) \qquad \text{(C-6)}$$

where ρ is the density of the shield material (with units g/cm^3), and μ is the mass attenuation coefficient of the material (with units cm^2/g). Lead has a density of 11.35 g/cm^3 and Figure 5 displays the mass attenuation coefficient for lead over a range of photon energies from 1keV to 1MeV. Clearly from this data, a lead shield of a few tens

of microns in thickness, necessary to allow the passage of high energy charged particles, will not be sufficient to appreciably attenuate a photon in the 10-200keV range typical in a radiation field generated by an IEC device, which regularly exceeds 10R/hr. Consequently measures must be taken to position a charged particle detector outside the line of sight of these x-rays if appreciable noise reduction is to be achieved.

Appendix C References

[1] M. Shur, *Introduction to Electronic Devices*, John Wiley & Sons Inc., New York, NY (1996)

[2] C.A. Klein, "Bandgap Dependence and Related Features of Radiation Ionization Energies in Semiconductors," *Journal of Applied Physics*, 39, 4, (1968) 2029

[3] www.physics.nist.gov\PhysRefData – accessed 7/20/2008